SPIM

Thèse de Doctorat

école doctorale sciences pour l'ingénieur et microtechniques

UFC UNIVERSITÉ DE FRANCHE-COMTÉ

Effet de la non-stœchiométrie en Li sur la performance des dispositifs à ondes élastiques à base de monocristaux de $LiTaO_3$ et $LiNbO_3$

Impact of Li non-stoichiometry on the performance of acoustic devices based on $LiTaO_3$ and $LiNbO_3$ single crystals

MINERVA GONZALEZ

SPIM

Thèse de Doctorat

école doctorale **sciences pour l'ingénieur et microtechniques**

UFC UNIVERSITÉ DE FRANCHE-COMTÉ

N° |_|_|_|

THÈSE présenté par

MINERVA GONZALEZ

pour obtenir le

Grade de Docteur de

l'Université de Franche-Comté

Spécialité : **Sciences pour l'ingénieur**

Effet de la non-stœchiométrie en Li sur la performance des dispositifs à ondes élastiques à base de monocristaux de $LiTaO_3$ et $LiNbO_3$

Thèse soutenue le 19 juillet 2016 devant le Jury composé de :

M. Matthieu CHATRAS	Président du jury	Professeur des Universités, Université de Limoges, Limoges
M. Marc P. DE MICHELI	Rapporteur	Directeur de recherche au CNRS, Université Côte d'Azur, Nice
M. Alexandre REINHARDT	Examinateur	Ingénieur-Chercheur, LCRF, CEA-LETI, Grenoble
M. Stéphane CHAMALY	Examinateur	Responsable Développement Produit RF, TDK Electronics France SAS, Sophia-Antipolis
M. Sylvain BALLANDRAS,	Examinateur	Président-Directeur-Général de la société frec|n|sys SAS, Besançon
M. Bernard DULMET	Co-directeur de thèse	Professeur des Universités, ENSMM, Institut FEMTO-ST, Besançon
Mme. Ausrine BARTASYTE	Directeur de thèse	Chaire d'excellence – Maître des Conférences, Université de Franche-Comté, Institut FEMTO-ST, Besançon

Remerciements

Tout d'abord, je voudrais remercier les membres du jury pour m'avoir fait l'honneur de juger mon travail. Merci à M. Matthieu Chatras, professeur des universités à l'Université de Limoges et M. Marc P. de Micheli, Directeur de recherche au CNRS à l'Université Côte d'Azur, Nice pour avoir accepté d'être les rapporteurs de mon manuscrit et pour leurs remarques pertinentes. Merci à M. Alexandre Reinhardt, Ingénieur de recherche au CEA-LETI, Grenoble et à M. Stéphane Chamaly, responsable développement produit RF à TDK Electronics France d'avoir accepté d'être membres du jury et pour leurs remarques, leurs questions et pour l'intérêt porté à mon travail.

J'exprime toute ma gratitude à ma directrice de thèse, Ausrine Bartasyte, qui m'a fait confiance pour mener à bien ce projet en collaboration avec la société TDK. Je lui suis très reconnaissante pour sa grande implication dans ce projet et pour toujours avoir dirigé mon travail avec enthousiasme et exigence, ce qui m'a permis de m'améliorer dans plusieurs domaines. Merci pour tout le temps consacré au suivi et à la révision de la thèse, pour sa disponibilité, pour ses conseils et son amitié.

Je tiens à remercier également à mon co-directeur de thèse, Bernard Dulmet, qui a eu la gentillesse de me prendre au cours de la deuxième année de thèse et qui m'a aidé à comprendre le « monde » des ondes élastiques, modèles théoriques, dispositifs, etc.., un domaine que je ne maitrisais pas auparavant. Merci pour son temps dédié aux explications, à la révision du manuscrit, pour ses conseils et son amitié.

Un grand merci à Sylvain Ballandras, qui a suivi mes travaux et qui a participé activement aux réunions du projet. Merci aussi pour son aide avec les simulations.

Je voudrais exprimer ma gratitude envers Jean Michel Brice pour m'avoir confié ce projet, ainsi qu'aux autres membres de la société TDK pour leur suivi, leur conseils et pour leur engament dans l'avancée de ces travaux. I want to thank to Ingo Bleyl and Claudia Kajiyama for the follow-up, their advice and their feedback allowed the progress of this project. Thanks for all the time spent in the review of presentations, proceedings and thesis.

Une grande partie du travail expérimental n'aurait pas été possible sans la contribution de plusieurs personnes. En commençant par mes collègues du département Temps-Fréquence, je remercie Florent Bassignot pour m'avoir appris la technique d'inversion de domaines, j'ai beaucoup apprécié travailler avec lui, toujours dans la bonne humeur. Merci également à Fabien Henrot, qui m'a beaucoup aidé pour la fabrication des « ridges » et merci pour son amitié.

Je voudrais remercier également à Thomas Baron pour m'avoir aidé en plusieurs occasions lorsque la polisseuse ne marchait pas ainsi qu'à la réalisation de certaines caractérisations et merci aussi pour ses remarques utiles avant la soutenance. Un grand merci à Jean-Michel Friedt et David Rabus pour m'avoir aidé à faire des caractérisations dans l'étuve. Merci également à Gilles Martin et à Valérie Pétrini pour m'avoir aidé à faire les connections électriques de mes dispositifs. Je voudrais remercier également William Daniau pour son aide avec les simulations et pour l'installation d'opensuse sur mes différents

ordinateurs. Un grand merci à Xavier Vacheret et à Jean Jacques Boy pour leur aide à la fabrication et caractérisation des résonateurs.

Merci à mes collègues du département MN2S qui ont participé de près ou de loin à cette thèse. Merci à Etienne Herth pour les caractérisations avec l'interféromètre, merci à Nicolas Martin et Jean Yves Rauch pour l'installation du four. Thanks to Stefania for all her help (AFM measurements, microscope, etc.). Thank you very much for your support and for your friendship. I wish you all the best in your last year.

Je remercie le personnel de la Centrale MIMENTO qui ont contribué à la réalisation de dispositifs : à Blandine Guichardaz pour les nombreuses découpes à la scie qu'elle a fait; à Ludovic Gauthier-Manuel pour le polissage et découpes des wafers; à Jean Claude Jeannot pour avoir eu la gentillesse de nous offrir le tout premier four, qui nous a permis de commencer nos traitements à haute température; à Laurent Robert pour toutes les gravures avec HF réalisées, à Franck Chollet pour m'avoir formé à l'utilisation de l'interféromètre Zygo avant même qu'il soit disponible à tout le monde.

Merci également au personnel du service commun et administratif de FEMTO-ST : à Betty Baudinot, qui a fait des pièces mécaniques pour moi, à Adrien Gaudet qui m'a dépanné en informatique plus d'une fois ; à Joëlle Berthelot, à Sandrine Pyon, à Cindy Pointelin, à Jocelyne Renaut, à Sarah Djaouti et à Fabienne Cornu pour les différents aspects de gestion.

Merci à mes collègues du TF et MN2S pour leur amitié et les moments de convivialités passés au labo ou dehors: Meddy, Loïc, Marc, David, Alexandre, Fabien, Florent, Nesrine, Lyes, Christophe, Stefania, Gautier, Xianlong et Anurupa.

Un grand merci aux personnes extérieures : à Pascal Boulet, de l'Institut pour avoir fait des mesures de DRX et pour m'avoir appris la méthode de raffinement de structures, à Brice Gautier pour avoir effectué des caractérisation avec le PFM sur mes substrats et je veux remercier spécialement à Samuel Margueron pour avoir eu la gentillesse d'effectuer des milliers de mesures par Spectroscopie Raman sur les cristaux et les poudres.

Je veux finir par remercier ma famille en France qui sont venus m'accompagner le jour de ma soutenance et à ma famille au Mexique, que malgré la distance m'a toujours soutenue moralement.

Llegar hasta aquí no hubiera sido posible sin el apoyo de mis padres y mis dos hermanos. Agradezco a mis padres y a mi hermano Eduardo por todo el esfuerzo que hicieron para que yo pudiera realizar estudios superiores. Gracias a sus enseñanzas yo comprendí que para conseguir mis objetivos es necesario mucha entrega y dedicación.

Finalement, je n'aurais pas pu arriver jusqu'ici sans l'aide précieuse de mon mari, Thomas, qui a su me comprendre et qui a tout fait pour que je puisse me dédier entièrement à la rédaction de ma thèse. Merci pour ton soutien, pour ton aide et pour m'avoir encouragé au cours de toutes ces années.

Je dédie ce manuscrit :
À Thomas
À mes parents
À mes frères

Table of contents

Abbreviations

36RY-X LT.- 36°rotated Y-cut X propagating Lithium Tantalate

3G.-Third generation

42RY- LT.-42° rotated Y-cut Lithium Tantalate

42RY-X LT.- 42°rotated Y-cut X propagating Lithium Tantalate

42RYX-LT.- Ridges perpendicular to x-axis in 42°Y-cut LT wafer

4G.-Fourth generation

AFM.- Atomic Force Microscope

Al.- Aluminium

AlN.-Aluminium Nitride

$AlPO_4$.- Berlinite

BAW.- Bulk Acoustic Wave

BEM.-boundary elements method

BIM.- boundary integral method

BW.-Bandwidth

CLN.- Congruent Lithium Niobate

CLN:Fe.- Congruent iron doped lithium niobate

CLT.- Congruent Lithium Tantalate

CLT:Fe.- Congruent iron doped lithium tantalate

C_m.- concentration in the middle depth

C_s.- concentration in surface

CTE.-coefficient of thermal expansion

CVD.- Chemical Vapor Deposition

CZ.- Czochralski method

D_c.- concentration dependent Li-diffusion coefficient.

DCCZ.- Double-crucible Czochralski method

E_a.- activation energy

E_c.- Electric Coercive Field

$E_{f.}$- forward poling

E_{int}.- Internal field

E_r.- reverse poling

E_{thr}.- electric field threshold

FBAR.-Film Acoustic Bulk Acoustic Resonators

FEM.-finite element method

FS.- fast shear

FWHM.- Full Width at Half Maximum

$GaAsO_4$.- Gallium arsenate

HBAR .-High Overtone Bulk Acoustic Resonator

HF.-Hydroflouric Acid

HVA.- High Voltage Amplifier

IDT.-Interdigital Transducer

IEF .-impedance element filter

IIDT.-Interdigitated Interdigital Transducer

IL.-Insertion loss

I_{pol}.- Poling current

k.- Boltzmann constant

K^2.- Electromechanical coupling coefficient

LFE.-Lateral Field Excitation

Li_2CO_3.-Lithium Carbonate

Li_2O.- content

Li_2O.-Lithium oxide

LiCl.- Lithium chloride

LN.- Lithium Niobate

LSAW.- Leaky surface Acoustic Wave

LT.- Lithium Tantalate

MgO:LN.- magnesium oxide doped lithium niobate

Nb_2O_5.- Niobium pentoxide

NSLN.- Near stoichiometric Lithium Niobate

NSLT.- Near stoichiometric Lithium Tantalate

PCB.-Printed Circuit Board

PPLT.- periodically poled lithium tantalite

P_s.- Spontaneous polarization

PTFE.-Polytetrafluoroethylene

PZT .- $Pb(Zr_xT_{1-x})O_3$ $(0 \leq x \leq 1)$

Q.- Quality factor

QE.-Quasi extensional

QS.-Quasi shear

R.- Radius of curvature

Ra.- Roughness Average

RF.- Radio frequency

RMS.- Root Mean Square

RW.- Rayleigh wave

SAW.- Surface Acoustic Wave

SiO_2.- Silicon dioxide

SLN.- Stoichiometric Lithium Niobate

SLT.- Stoichiometric Lithium Tantalate

SMA.- SubMiniature version A

SMR.-Solidly Mounted Resonators

SPM.- Scanning Probes Microscopes

SS.- slow shear

SSBW.- Surface Skimming Bulk Wave

sub CLN.-subcongruent lithium niobate crystals

Ta_2O_5.- Tantalum pentoxide

T_c.-Curie Temperature

TCF.- Temperature Coefficient of Frequency

TCF_p.- temperature coefficient of parallel frequency

TCF_s.- temperature coefficient of series frequency

TE.- thickness extension

TE.-Thickness extensional

TFE.- Thickness Field Excitation

TFE.-Thickness Field Excitation

T_m.- Taman temperature

TSSG.- Top-seeded solution growth

t_{stab}.- stabilization time

TTV.- Total thickness variation

VNA.-Vector Analyzer Network

VTE.- Vapor Transport Equilibration

VTE.- Vapor Transport Equilibration

VTE.-Vapour Transport Equilibration

$X_{Li2O.}$- mole fraction of lithium oxide

XRD.- X-Ray Diffraction

$X_{Ta2O5.}$-mole fraction of tantalum pentoxide

ZnO.- Zinc Oxide

ZX-LT.- Ridge parallel to x-axis in Z-cut LT wafer

ZY-LT.- Ridges normal to x-axis in Z-cut LT wafer

Introduction

Acoustic devices have been used since 1915. Then Paul Langevin and Constant Chilowski developed the first transducers for SONAR (Sound Navigation and Ranging) in submarines, exploiting the piezoelectric effect in quartz to generate acoustic waves in sea. Around 1920, the use of a piezoelectric plate as an electrically coupled acoustic resonator and its application to stable oscillators began to be developed. Today, the quartz resonator is widely employed for regulation of oscillator frequencies due to its high thermal stability.

In the 1960's the possibility to generate surface acoustic waves (SAW) on piezoelectric single crystals was demonstrated by White and Voltmer. They proposed the use of interdigitated transducers (IDT) which generate and receive the waves propagating in the piezoelectric substrate. Since this type of wave motion can be guided along the surface, it allows the possibility to increase the versatility of devices. Besides, the technology employed for fabrication of SAW devices enables its industrial production.

SAW technology has been extensively developed, increasing the application possibilities of a wide range of components, including delay lines, bandpass filters, resonators, oscillators, etc. These devices found application in many systems such as radars, communications equipment, radio, mobile phones, remote controls, car navigation systems, etc. Bulk acoustic waves (BAW) and SAW devices are complementary in the case of operational frequencies around 2 GHz. When higher frequencies are required, BAW devices are preferred. The SAW devices are widely used as passband filters in the radio frequency (RF) range in mobile phones due to their efficiency, compact size and their relatively low cost of production.

The most of RF filters are based on $LiTaO_3$ (LT) and $LiNbO_3$ (LN) as piezoelectric substrate due to their good acoustical properties. For example, a high electromechanical coupling factor (K^2), which allows to obtain a wide bandwidth and low losses required in the telecommunications systems. However, these materials present a significant sensitivity to temperature, defined by the Temperature Coefficient of Frequency (TCF), resulting in a frequency shift with the temperature during the operation of filters. The TCF of LT and LN crystals depends on the crystal cut and the direction of propagation of the waves. For example, the TCF of 42 RY-X LT and 128 RY-X LN single crystals is -40 and -75 ppm/°C, respectively.

Nowadays, the reduction of TCF, the increase of the stability at high power density, and the reduction of size are the main topics of research and development ongoing to improve the performance of SAW devices. At present, the value of TCF is improved by using the deposition of SiO_2 layers on devices. However, this technology has some drawbacks, for

example the increase of insertion losses and the deterioration of the electromechanical coupling factor. Another method consists in the implementation of a layer with inverted direction of polarization on the surface of crystal used for the SAW device. Thus, the domain boundary acts as an electric-field short circuit that diminishes the TCF but the K^2 decreases as well. However, the main disadvantage of this technique is the difficulty to control the thickness of the inverted layer, which is not suitable for the industrial production. Therefore, the exploration of alternative methods allowing the improvement of TCF without the deterioration of the other properties is an active research field.

On the other hand, it is known that the physical and structural properties of LT and LN single crystals depend on the Li content in the crystals. The Li_2O non-stoichiometry in LT and LN crystals affects the acoustical velocities. However, the effect of the Li_2O on TCF and stability at high power densities still needs to be clarified.

The objectives of this work are the improvement of TCF of LT crystals and the amelioration of stability at high power density of LN crystals without deterioration of other acoustical properties (K^2, insertion losses, etc.). For this purpose, the Li_2O concentration in LT and LN single crystals was modified by using the Vapor Transport Equilibration (VTE) method and the effect of Li_2O concentration on the performance of SAW devices was investigated. This project was carried out in FEMTO-ST Institute and it was financially supported by the National Association for Research and Technology (ANRT) and TDK Corporation.

This manuscript is organized in four chapters. In the 1st Chapter, I introduce some general concepts about piezoelectricity, ferroelectricity and the effect of Li stoichiometry on structural and physical properties of LT and LN single crystals. Then, the principles of surface and bulk acoustic wave devices (SAW and BAW, respectively) are presented with focus on the SAW filters. Finally, I present the context and the objectives of my thesis in more details.

In the 2nd Chapter, the methods used to modify the Li_2O concentration in single crystals (VTE) and to characterize the treated crystals are presented. The estimation of Li_2O concentration by means of Raman spectroscopy and X-Ray diffraction is described in details.

The VTE process was optimized by studying the influence of VTE parameters on the Li_2O concentration of crystals, its homogeneity and wafer warping. In the case of LT crystals, the VTE process takes place at temperatures above Curie temperature. Thus, after VTE treatment, the crystals are in polydomain state. Thus, the homogenous electrical poling is required, in order to obtain crystals with uniform polarization. The techniques used for electrical poling of Z-cut LT and 42 RY-LT crystals with different Li_2O concentrations are described in the 3rd Chapter.

The 4th Chapter presents the investigation of the effects of Li_2O concentration and ferroelectric domain state on the properties of SAW devices and on the elastic constants of LT crystals. The chapter starts from some theoretical considerations and simulations of BAW devices, in order to identify BAW configurations suitable for the investigation of the temperature dependence of C_{44} elastic constant, which mainly defines the frequency response of SAW filters based on 42 RY-X LT crystals.

Finally, in the last part, I give the general conclusions and the perspectives of this project.

Chapter 1

Acoustic wave devices based on $LiTaO_3$ & $LiNbO_3$ single crystals

1.1 Introduction

The acoustic wave devices investigated in this work are based on piezoelectric substrates, thus the concepts of piezoelectricity and ferroelectricity will be introduced firstly. The properties of $LiTaO_3$ and $LiNbO_3$, the materials used in this project, will be explained thereafter, as well as the effect of Li-non stoichiometry on structural and physical properties. After that, an introduction to the acoustic waves devices and their main principles will be revisited and finally, the motivation and the context of this work will be presented.

1.2 Piezoelectricity and ferroelectricity: generalities

1.2.1 Piezoelectricity and piezoelectric materials

Pierre Curie and Jacques Curie discovered piezoelectricity in 1880. They have shown that in some crystals, such as quartz, tourmaline and zinc blende, the application of a mechanical stress produce its electrical polarization. This is called *direct piezoelectric effect*. This effect also works in the opposite way. Hence, the *reverse piezoelectric effect* consists in the deformation of a material when an electric field is applied, and was discovered one year later by Gabriel Lippmann [1].

Piezoelectricity is present only in some materials, depending on its internal structure and more specifically on the symmetry of its unit cell (defined by point group). A required condition for piezoelectricity is that the crystal should be non-centrosymmetric, which is implied by the formation of electric dipoles (via the movement of ions) to produce a polarization. Crystals are classified according to the symmetry elements of their structure in 32 point groups. Among these, there are 21 groups non-centrosymmetric, of which 20 point groups are piezoelectric [2]. All materials with non-centrosymmetric structure are piezoelectric except for the cubic class 432.

The fundamental relations of piezoelectricity can be described mathematically in terms of the constitutive tensor equations relating the strain, S_{kl}, and the electric displacement (or electric flux density), D_i, with the stress, σ_{ij}, the electric field, E_i, and the temperature T as independent variables [3]:

$$S_{ij} = s_{ijkl}^{E,T}\sigma_{kl} + e_{kij}^{T}E_k + \alpha_{ij}^{E}\Delta T \qquad \textit{Eq. 1.1,}$$

$$D_i = e_{ikl}^{T}\sigma_{kl} + \varepsilon_{ij}^{\sigma,T}E_k + p_i^{\sigma}\Delta T \qquad \textit{Eq. 1.2,}$$

Where $s_{ijkl}^{E,T}$ – the isothermal elastic compliances at constant field, e_{ijk}^{T}- the isothermal piezoelectric coefficients, α_i^E – the electrically clamped thermal expansion coefficients, $\varepsilon_{ij}^{\sigma,T}$- the isothermal permittivity at constant stress, p_i^{σ}- the pyroelectric coefficients at constant stress.

The relation between the electric displacement, $\vec{D}$, and the polarization, $\vec{P}$, can be described corresponding to the equation:

$$\vec{D} = \varepsilon_0 \vec{E} + \vec{P} \qquad \textit{Eq. 1.3}$$

Where ε_0 is the permittivity of vacuum. The superscripts T, E and σ indicate that the parameters are measured at constant temperature, electric field and stress, respectively. The ability of a piezoelectric material to convert mechanical energy into electric, or vice versa, is given by the *piezoelectric coupling coefficient*, K^2, [4, p. 33], which can be expressed taking into account the elastic properties of the material.

$$K^2 = \frac{e^2}{\varepsilon C} \qquad \textit{Eq. 1.4}$$

The value of this coefficient should be high to ensure an efficient conversion of energy. In this case, this relationship takes into account only the properties of the piezoelectric material. However, the definition of coupling factor changes according to the type of wave that propagates in acoustic devices. Moreover, it is a very important parameter to take into account for the design of acoustic devices, as will be explained later.

Piezoelectric materials are used in a wide range of products, from the everyday use (telephones, lighters, speakers, watch, keyless door entry, sensors, printers, disc drives, etc.) until more specialized applications (ultrasound imaging, sonar, radars, temperature sensors, fuel injector, gyroscope, inkjet actuator, etc.) [5], [6]. Piezoelectric materials can be sorted in five main categories according to their physical form used in industry:

1) *Single crystals:* quartz, Topaz, tourmaline, Potassium sodium tartrate (Rochelle salt,), berlinite ($AlPO_4$), Gallium arsenate ($GaAsO_4$), Lithium Niobate (LN), Lithium Tantalate (LT) [7];
2) *Ceramics:* in industry the materials unavailable in the form of single crystals are used in form of sintered powders, for example the Barium Titanate ($BaTiO_3$), Potassium niobate ($KNbO_3$) and Lead zirconate titanate Pb (Zr_xT_{1-x})O_3 ($0 \leq x \leq 1$) also called PZT [7, p. 315];
3) *Thin films:* Aluminium Nitride (AlN), Zinc oxide (ZnO);
4) *Polymers:* Polyvinylidene Fluoride (PVDF), Nylon-11;
5) *Composites:* these materials can be found as piezoelectric ceramic in a matrix of polymers, for instance PZT/PVDF; $PbTiO_3$/Epoxy.

1.2.2 Ferroelectricity and ferroelectric materials

Ferroelectric materials represent a subgroup of piezoelectrics. Thus ferroelectric materials are necessarily non-centrosymmetric and they must have two important characteristics: i) spontaneous polarization, $\overrightarrow{P_s}$, even without application of an electric field and ii) the capability to reverse the direction of polarization [2].

The regions having uniform direction of polarization constitute *ferroelectric domains*. Two adjacent domains, having $+P_s$ and $-P_s$ are separated by a domain wall [8]. Direction of polarization in ferroelectrics can be reversed by the application of an external electric field, $\vec{E}$. During the polarization reversal, the applied electric field and the polarization are related by the hysteresis loop P(E), Fig. 1.1 [9]. First, the polarization increases linearly with the electric field, but the magnitude of E is not sufficient to change the polarization, this corresponds to segment *OA* in Fig. 1.1. At this stage, the polarization of domains is oriented in different directions. The polarization of domains will start to change the orientation with the further increase of the electric field, in order to approach as much as possible crystallographically the direction of electric field (AB). Once all the domains are aligned, the polarization reaches a saturation state (*BC*). When the electric field is reduced and switched in opposite direction ($-E_c$), the polarization of domains will be reversed, following the path C-D-F-G. If the electric field is reversed again, the domains will change their orientation, following the path G-H-C. This cycle corresponds to the hysteresis loop, the segment OD is called remanent polarization, P_r, and the value of P_s can be obtained by a linear extrapolation of the segment CB [10, p. 391]. The electric field necessary to reverse the direction of polarization of ferroelectric domains is the electric coercive field, E_c [11].

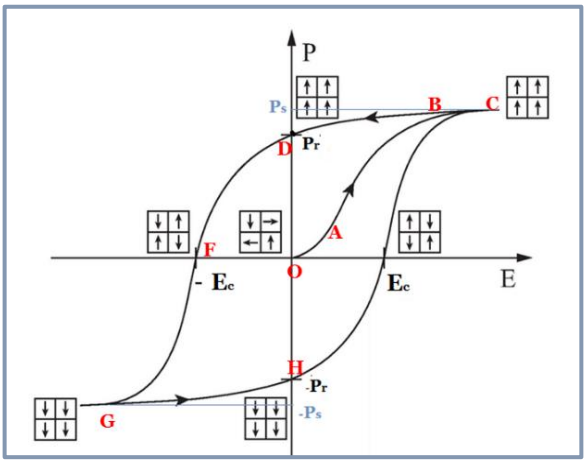

Fig.1.1 Ferroelectric hysteresis loop P (E) and evolution of domain structure during domain reversal [9].

Ferroelectric materials can be sorted in groups according to their unit cell structure in: a) the tungsten-bronze, b) the oxygen octahedral group, c) the pyrochlore group and d) bismuth layer structure group. Among these groups, the most important industrially are ABO_3 materials with perovskyte and ilmenite type structures because of their wide industrial applications [2]. Examples of ferroelectric perovskite materials are: $CaTiO_3$, $Pb(Zr_xT_{1-x})O_3$ (PZT) and $BaTiO_3$. These materials are used in dielectric capacitors, sensors, and in non-volatile memory devices, microphones, actuators, inkjet printers, nebulizers, transducers, filters, ultrasonic cleaners, etc. [2]. LN and LT have ilmenite structure and are ferroelectric at room temperature. LN and LT are well known for their low acoustic losses, high piezoelectric coupling coefficient, and for their electro-optic properties. Thus, they are widely used for fabrication of acoustic filters for cell phones and of optical devices such as optical modulators, Pockels cells, Q-switching devices, waveguides, optical switches, etc. At present, 70 % of radio frequency (RF) filters based on surface acoustic waves (SAW) are fabricated from LT and LN single crystals. The structural and physical properties of these two materials will be presented in the following sections.

1.3. Properties of $LiTaO_3$ and $LiNbO_3$

1.3.1 Structural properties

LN and LT are isostructural with space group R3c at room temperature (RT) as determined by Abrahams et al.[12], [13] The structure of lithium niobate and tantalate consists of planar sheets of oxygen atoms and of octahedral interstices filled by Li, Nb or Ta, and vacancies (Fig. 1.2) in the sequence *Li, Ta (or Nb), vacancy, Li, Ta (or Nb), vacancy.., etc*. The displacements of the cations with respect to the oxygen planes define the spontaneous polarization of LN and LT.

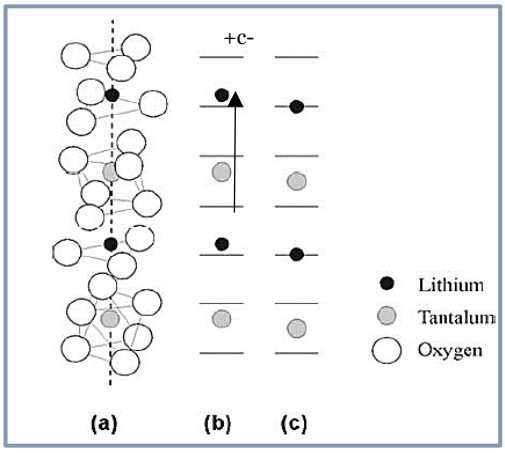

Fig. 1.2 Representation of the unit-cell of $LiTaO_3$ showing the position of Li and Ta atoms in Ferroelectric phase(a), transversal view of atom positions in ferroelectric phase (b), Li and Ta atom positions in the paraelectric phase (c) [14].

The Curie Temperature (T_c) is defined as the temperature at which ferroelectric materials become para-electric. Below T_c, displacement of cations with respect to the oxygen planes occurs (Fig. 1.2 b), which results in separation of charges and induces the spontaneous polarization. Above the Curie temperature, T_c, LN and LT are para-electric and non-polar as Li ions lie in the oxygen planes and the Nb/Ta ions are placed in the center between the oxygen planes (Fig. 1.2 c) [14]. In trigonal system, the conventional unit cell can be hexagonal or rhombohedral. In the case of LN and LT, the commonly used unit cell is of the hexagonal type, in which the threefold symmetry axis is along the c-axis and the basal planes is intersected by three mirror planes, which are 60° apart from each other.

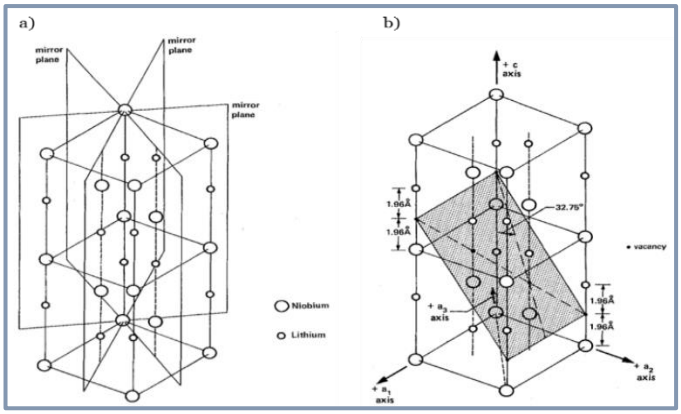

Fig.1.3 Unit cell of LN showing the three mirror planes of symmetry (a). Hexagonal unit cell of LN indicating the cleavage plane (01$\bar{1}$2) (b)

The a-axis of hexagonal cell is taken perpendicular to the mirror plane (Fig. 1.3) [15]. The lattice parameters are *a*=5.153Å et c=13.787Å for LT and *a*=5.15Å et c=13.865 Å for LN. Moreover, LN and LT present three cleavage planes (01$\bar{1}$2), ($\bar{1}$012) and (1$\bar{1}$02), which are shown on Fig.1.3 b [12], [13]. The change of the lattice parameters of LN and LT as a function of temperature is presented in Fig. 1.4 [16]. A linear temperature dependence of the *a*-lattice parameter in LT and LN single crystals has been observed (Fig.1.4 a). Thermal expansion of *c*-lattice parameter of LN and LT is nonlinear and changes its sign from positive to negative at around 550°c and 200 °C, respectively (Fig. 1.4 b).

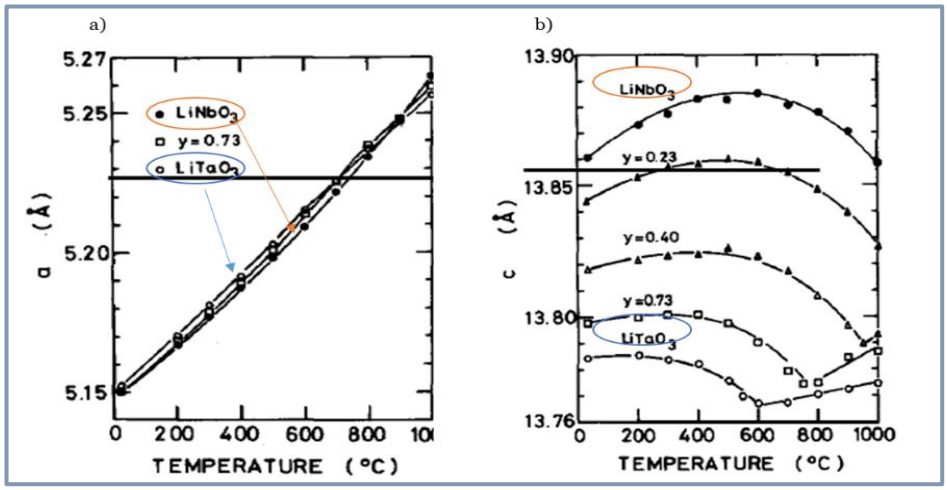

Fig. 1.4 Evolution of lattice parameters of LT and LN with temperature: a-lattice parameter (a) and c-lattice parameter (b) [15].

Many structural and physical properties of LT and LN depend on its stoichiometry and point defects, for this reason we will explain these concepts in the following text.

1.3.1.1 Non-stoichiometry and point defects

Commercially available LT and LN single crystal are produced by Czochralski technique [17]. More details about this method will be given in the Chapter 2. When LN and LT crystals are grown by using this technique, there is only one point where the compositions of the melt and the grown crystal are identical throughout the growing process. This point corresponds to the congruent composition, where liquid and solid phases are in equilibrium. The Fig. 1.5 a shows the phase diagram of Li_2O-Nb_2O_5 binary system, where it can be seen that the congruent melting point for LN is at ~1240 °C [18] at the composition of 48.38% mol of Li_2O[17]. The melting point of LT is 1650°C [19]and its congruent composition is 48.5-48.6 mol% [20]. The phase diagram of the Li_2O-Ta_2O_5 system is shown in Fig. 1.5 b [21]. According to the phase diagrams, single phases of lithium tantalate and lithium niobate exist over a wide compositional range (from 46.5 to 50.5 mol% of Li_2O). The Li non-stoichiometry can be defined as the molar ratio between Li and the total amount of cations X_{Li2O}=Li /[Li+(Nb or Ta), where X_{Li2O} corresponds to the molar fraction of Li_2O (mol%) within the crystal. Congruent crystals (CLT and CLN) have the same composition as the melt

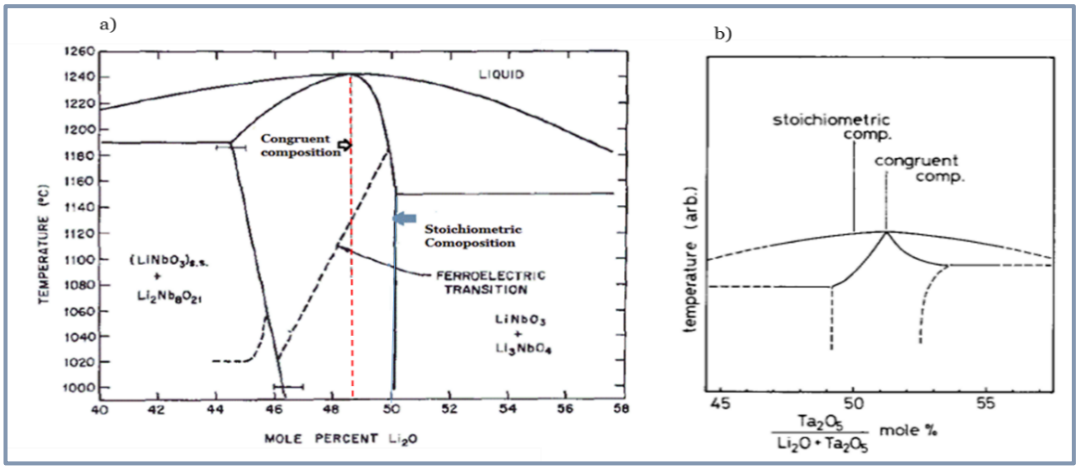

Fig. 1.5 Phase diagram of Li_2O-Nb_2O_5 (Fig. modified from Ref.[18]) (a) and phase diagram of Li_2O-Ta_2O_5 system (b) [21].

used for its growth. Whereas having X_{Li2O}=50%mol are called stoichiometric (SLT and SLN).

The deviation from stoichiometry in LN and LT is possible due to the formation of intrinsic defects of stacking faults of the crystalline structure. The defect model in CLN was widely investigated [22], [23]. According to these works, some amount of Nb^{5+} ions occupy the Li sites, leaving Li or Nb vacancies. There were proposal two defect models (illustrated in the Fig. 1.6):

i. *Nb-site vacancy model.*- In the case of CLN, the Li^{+} ions are replaced by Nb^{5+} ions in the 6% of Li sites, forming the Nb antisite defect (Nb_{Li}). Then, in order to compensate the charges, vacancies at Nb sites (V_{Nb}) are created [24].
ii. *Li-site vacancy model.*- The Nb ions occupy the Li sites (Nb_{Li}) and the charge neutrality is compensated by Li vacancies (V_{Li}). According to X-ray diffraction (XRD) measurements, it has been found that Nb atoms occupy only 1% of Li sites [16]. This later model is more favorable energetically and is generally accepted. However, the degree of antisite defects depends also on conditions of preparation of crystals [24, p. 13].

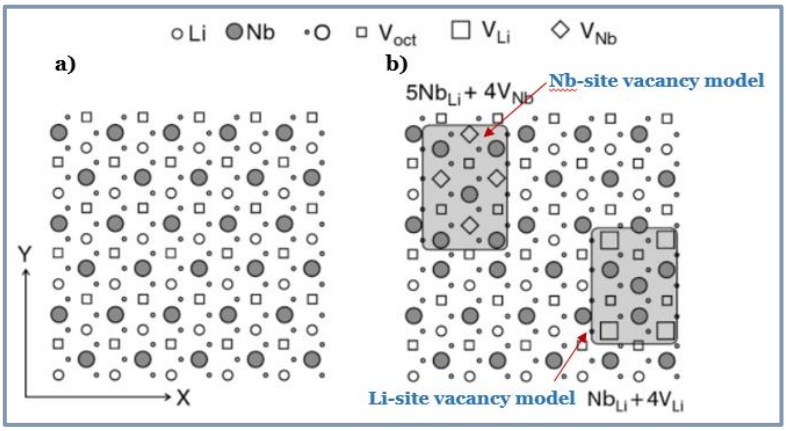

Fig. 1.6 Intrinsic defects in LN crystals in an ideal structure (a). Intrinsic defects according to the Li or Nb vacancy model (b) [24].

1.3.1.2 Influence of Li non-stoichiometry on structural properties

Li non-stoichiometry strongly affects the structural properties of LN and LT (for example, the lattice parameters and the Curie temperature. The lattice parameters vary with Li_2O concentration. The *a*- and *c*- lattice parameters of LN decrease by 0.004 Å and 0.014 Å when Li_2O concentration is increased from 47 to 49.8 mol%, respectively [16]. The *a*-lattice parameter is less sensitive than the *c*-parameter to the deviation from the stoichiometry in LN. Barns et al.[25] have reported similar variation of *a*-and *c*- lattice parameters as a function of stoichiometry for of LT single crystals.

The Curie temperature, T_c, of LN and LT is highly sensitive to the Li-non stoichiometry and increases linearly when defect concentration is decreased [26], [27] (see Table 1.1). Therefore, measurement of T_c is frequently used as an indirect method for the estimation of Li concentration in the LT and LN crystals by using the following relationships:

$$For\ LT:\ T_c\,(°C) = -1054.2 + 34.682\,(\%Li_2O) \qquad Eq.\ 1.5$$

$$For\ LN:\ T_c\,(°C) = -746.73 + 39.06\,(\%Li_2O) \qquad Eq.\ 1.6$$

1.3.1.2.1 Thermal expansion, conductivity and diffusivity

Another important structural property for LT and LN materials is thermal expansion. The thermal expansion coefficient along polar axis and perpendicularly to it is different due to its anisotropy. The expansion parallel to c-axis changes its sign from positive to negative around 600°C. The *a*-lattice parameter, normalized with respect to its value at room temperature increases with temperature for the congruent and near of stoichiometric LN and LT crystals (Fig. 1.7 a). Thus, the thermal expansion along *a*-crystallographic axis (or X-axis) depends a little of the Li-non stoichiometry of crystals [28], [29]. The temperature dependence of *c*-lattice parameter for LN crystals shows a maximum where there is a change of sign from positive to negative around 600 °C in crystals with 48.5 mol% of Li_2O. This change occurs at slightly higher temperatures for SLN (Fig. 1.7 b). This region corresponds to zero thermal expansion along *c*-crystallographic axis. In the case of LT crystals the maximum is found at room temperature (Fig. 1.7 c) [29]. The values of the coefficients of thermal expansion are shown in the Table 1.1. On the second hand, the Li-non stoichiometry affects other properties such as the thermal diffusivity and conductivity. The thermal conductivity in SLN and SLT crystals is almost twice larger than in CLN and CLT crystals, respectively [30] (see Table 1.1). It could be due to phonons that are scattered by the lattice defects in congruent crystals, thus decreasing the thermal conductivity. The thermal diffusivity of stoichiometric crystals is slightly larger than that of the congruent ones, due to the effect of lattice defects as well. The diminution of the Li vacancies in stoichiometric crystals facilitates the diffusion process [31].

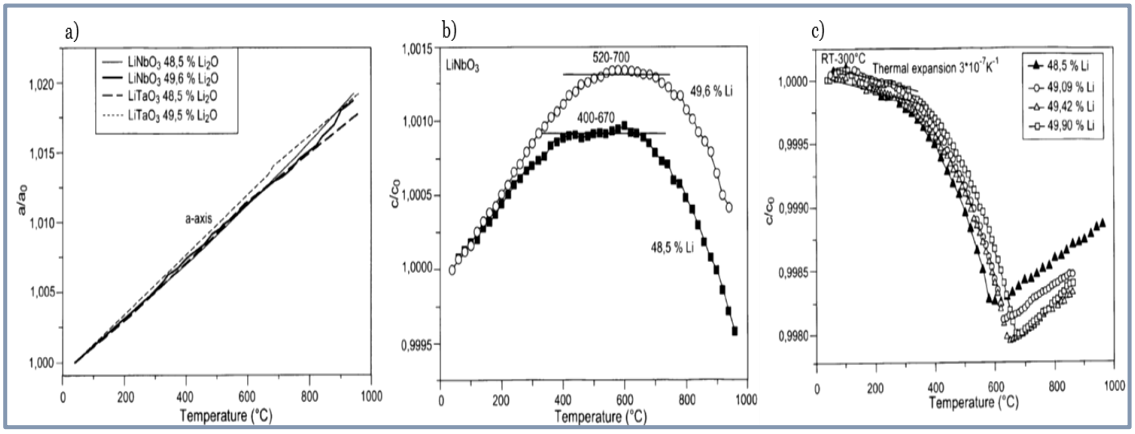

Fig.1.7 Thermal expansion of a-lattice parameter for near of stoichiometric and congruent LN and LT crystals (a). Temperature evolution of c-lattice parameter, normalized with respect its value at room temperature of CLN and NSLN crystals (b). Temperature evolution of c-lattice parameter, normalized with respect its value at room temperature of LT crystals with different Li_2O concentrations (c) [29].

1.3.2 Physical properties

As mentioned above, physical properties of LN and LT depend also on crystal non-stoichiometry. For example, the birefringence, coercive field, acoustic velocity, etc. Congruent crystals have defects such as Li vacancies and Nb anti-sites, which has an important effect on physical properties of material [32], for example, ferroelectric properties, elastic properties and electro acoustical properties. In this section the ferroelectric, elastic and piezoelectric properties and their dependence on Li-non stoichiometry and temperature will be presented.

1.3.2.1 Ferroelectric domain reversal

Ferroelectric domain reversal in LT and LN consists in the application of an electric field of sufficient magnitude to change the direction of the spontaneous polarization. Starting from a single-domain state, the electric field, E_f, has to be applied to reverse the polarization (forward poling). The electric field needed to switch back to the original polarization state (reverse poling), E_r, is different from E_f. The difference between these two fields is called the internal field, -E_{int}- [8]. The E_{int}, can estimated according to:

$$E_{int} = \frac{E_f - E_r}{2} \qquad Eq.\ 1.7$$

The E_{int} tends to realign the polarization direction of the crystal to its original direction [33]. During domain reversal, the Li atom is displaced from one octahedral site to the neighbour vacant oxygen octahedral, accompanied by the simultaneous motion along the *c*-axis of Nb (Ta) atoms, from its acentric location on the opposite side of the octahedron center (see Fig. 1.8) [8]. The direction of motion of these cations defines whether the final polarization is positive or negative [14].

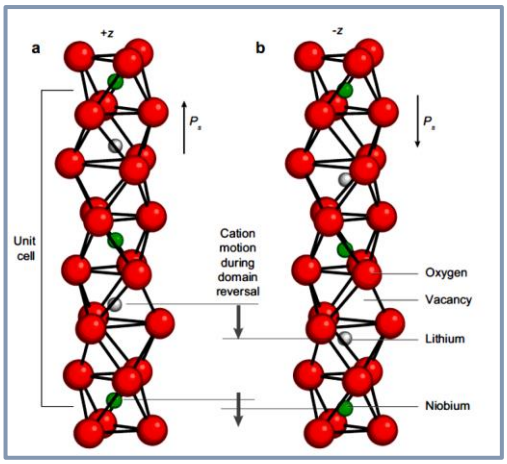

Fig.1.8 Representation of the unit cell of $LiNbO_3$ structure for +Ps and -Ps domains, showing the cation motion during domain reversal [8].

The domain reversal in LT and LN crystals can be explained considering that in congruent crystals the defects are arranged in clusters. These defects have a polarization, P_D, different from the spontaneous polarization of lattice, P_S, in congruent crystals. The Fig. 1.9 illustrates the possible arrangement of the defect clusters at room temperature. In the case of stoichiometric crystals, the unit cell has no defects (Fig. 1.9 a). In congruent crystals, the defect cluster can be in stable or frustrated states:

i) *Stable defect state (Fig. 1.9 b).*- It is obtained when the crystals is cooling down slowly from high temperature. In this way the V_{Li} have enough of time to form stable clusters, whose configuration is kept at room temperature. The defect polarization is parallel to lattice polarization.

ii) *Frustrated defect state (Fig. 1.9 c).*- This state is obtained after domain reversal at room temperature. The Nb or Ta antisite defects (Nb_{Li} or Ta_{Li}) should move to the neighbor octahedral site across the oxygen plane. Simultaneously, the V_{Li}, located around the original defect (Nb_{Li}) should move around the new position of Nb_{Li} in order to get the stable state of the Fig. 1.9 d. However, mobility of Li ions at room temperature is not possible. Thus, the obtained structure is unstable and the defect polarization (P_D) is in opposite direction to P_S of lattice. In order to facilitate the mobility of Li ions, an annealing at T>150°C is required and in this case the frustrated stated becomes stable (Fig. 1.9 d)[8], [34].

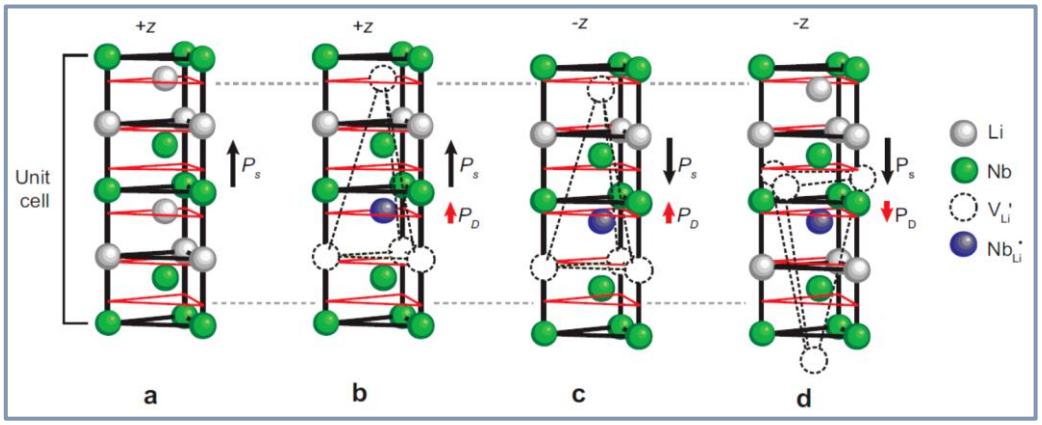

Fig.1.9 Schematic representation of the three possible defect states: stoichiometric crystals without defects (a), stable defect state of congruent crystals in its low-energy configuration (b), frustrated defect state, obtained after polarization reversal at room temperature (c), after annealing at >150°C, the frustrated state becomes stable because of the mobility of Li vacancies (V_{Li}) (d). The planar sheets of oxygen are represented by red triangles [8, p. 459].

The Fig. 1.10 shows the potential energy well for the domain reversal process from $-P_S$ to $+P_S$, taking into account the polarization of defect clusters. Assuming that we have a crystal with initial $-P_S$ polarization and $-P_D$, the $-P_S$ is stabilized by the defect polarization by an amount of potential energy $-\Delta F_V-$ (Fig. 1.10 a). The defects that stabilizes the $-P_S$ polarization has two contributions: one coming from the Nb_{Li} (or Ta_{Li}) antisite defect and the second one from the arrangement of the V_{Li} around the antisite defect. When an electric field is applied in opposite direction, the potential energy (F) of $+P_S$ state decreases, while the energy of $-P_S$ state increases, which results in a reversal of polarization from $-P_S$ to $+P_S$. The $+P_S$ is stabilized by the defect clusters with ΔF_R energy (Fig. 1.10 b) [8], [34]. According to this model, the internal field is proportional to the difference between ΔF_V and ΔF_R) potential energies:

$$E_{int} \approx \frac{N(\Delta F_V - \Delta F_R)}{4P_S}, \qquad \textit{Eq.1.8.}$$

Where N is the density of defect clusters, P_S is the spontaneous polarization, ΔF_V and ΔF_R are the stabilization energies associated to the defect clusters.

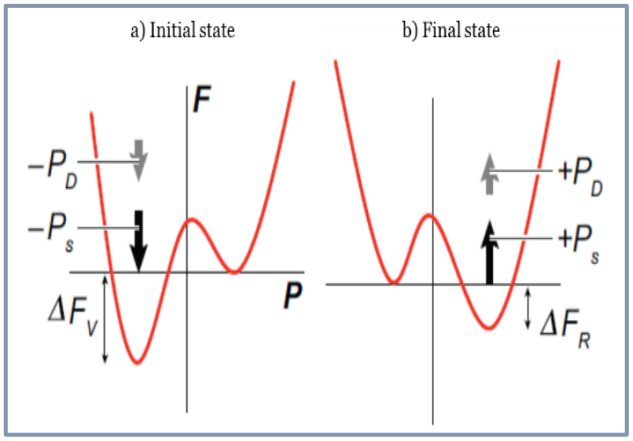

Fig. 1.10 Potential energy diagrams showing the evolution of energy during domain reversal from $-P_s$ to $+P_s$ state in congruent LT or LN crystals [18].

The Li non-stoichiometry has an important effect on ferroelectric properties. For instance, stoichiometric crystals have until 100 times lower coercive field, than the congruent ones (21.1 kV/cm for CLT and 0.161 kV/mm for SLT) [35]. This is an advantageous property of nearly stoichiometric crystals because it allows to perform domains reversal using lower electric field strength [36]. In contrast, the value of spontaneous polarization, P_S, changes little with Li_2O concentration, as is presented in the Table 1.1. On the other hand, a low coercive field may result in spontaneous depolarization, when acoustic devices are driven with high RF

power. The coercive field changes significantly with Li_2O non-stoichiometry in the crystal. It has been reported that the electric field is related to T_c in LN crystals [36]:

$$E_{f\,(kV/mm)} = 335.9(\pm 45.7) - 0.277(\pm 0.039)T_c \qquad \text{Eq. 1.9}$$

$$E_{r\,(kV/mm)} = 249.0(\pm 46.6) - 0.204(\pm 0.040)T_c \qquad \text{Eq. 1.10}$$

Where E_f is the electric field required for the forward poling and E_r is electric field needed for the reverse poling, as defined previously and T_c is given in °C. By using Eqs. 1.5 and 1.6, E_f and E_r can be expressed as a function of Li_2O concentration or X_{Li2O} (in mol%), defined previously:

$$E_{f\,(kV/mm)} = 542.74 - 10.82\,(X_{Li2O}) \qquad \text{Eq. 1.11}$$

$$E_{r\,(kV/mm)} = 401.33 - 7.97\,(X_{Li2O}) \qquad \text{Eq. 1.12}$$

According to the L.Tian PhD thesis [37, p. 33] the electric coercive field in LT crystals depends on the T_c (in °C) and Li_2O (mol%) in crystal, as well. These relationships can be estimated by the following formulas:

$$E_{f\,(kV/mm)} = 105.71 - 0.2153T_c \qquad \text{Eq. 1.13}$$

$$E_{r\,(kV/mm)} = 88.56 - 0.1262T_c \qquad \text{Eq. 1.14}$$

$$E_{f\,(kV/mm)} = 697.02 - 13.935\,(X_{Li2O}) \qquad \text{Eq. 1.15}$$

$$E_{r\,(kV/mm)} = 408.3 - 8.158\,(X_{Li2O}) \qquad \text{Eq. 1.16}$$

The CLT and SLT show important differences in their hysteresis loops, due to the difference in the E_{int} [38]. The SLT has fine hysteresis loop with coercive field values as shown in the Fig. 1.11. The origin of the internal field in crystals depends linearly on the density of defects (according to the Eq. 1.4). Therefore, as the stoichiometric crystal has less defects, its internal field is smaller. Thus, the congruent crystal presents very broad hysteresis loop with high coercive field and slightly higher P_s value.

A summary of the effect of Li-non stoichiometry on physical properties is given in the Table 1.1.

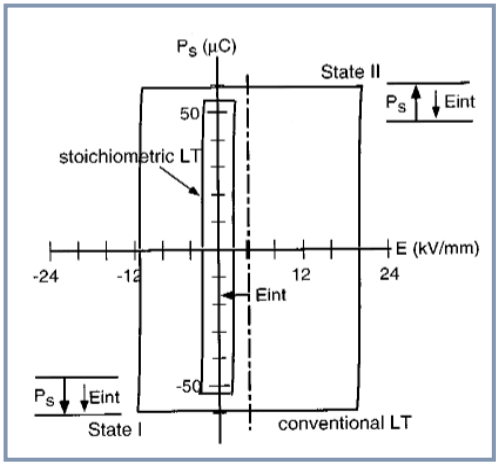

Fig. 1.11 Hysteresis loop of CLT and SLT crystals [38].

Table 1.1 Effect of non-stoichiometry of Li_2O on properties of LT and LN single crystals

	Congruent $LiTaO_3$ (CLT)	***Near-stoichiometric $LiTaO_3$ (NSLT)***	***Stoichiometric $LiTaO_3$ (SLT-VTE)***	***Congruent $LiNbO_3$ (CLN)***	***Near-stoichiometric $LiNbO_3$ (NSLN)***
Li_2O composition (mol%)	48.5 [39]	49.9 [40]	~50 [37]	48.38 [17]	~49.8 [38]
Curie Temperature	628 °C [26]	685±1°C [38]	701±2.5°C [35]	1138°C [18]	1198°C [18]
Coercive field (kV/mm) [8, p. 458]	E_f=21.15 E_r=12.6 E_{int}=4.4	E_f=1.7 E_r=1.5 E_{int}=0.1	E_f=0,139-0.161 E_r=0,123-0.165 E_{int}=0.0065	E_f=21 E_r=16.8 E_{int}=2-3	E_f=4.5 E_r=3.31 E_{int}=0.37
Polarization, Ps ($\mu C/cm^2$)	60±3 [41]	55±3 [42]	55,2±0,5 [36]	75 [43]	80±5 [36]
Thermal expansion coefficient ($x10^{-6}$)	α_c=-0.9 α_a=19.1 [44]			α_c=2.7 α_a=19.2 [44]	α_c=2.8769 α_a=17.1807 [45]
Thermal diffusivity ($x10^{-4}$ m^2/s) [30]	0.0156	0.0288		0.0134	0.0198
Thermal conductivity (W/mK) [30]	4.62	8.78		3.92	5.97

1.3.2.2 Elastic properties of $LiTaO_3$ and $LiNbO_3$

Elasticity is the property that represents the deformation of a material under application of a force and its ability to return to its original state, when the force is removed. The atoms are displaced from their equilibrium positions when a force acts on them. At small deformations, these forces are proportional to the displacement of atoms. It can be expressed by using Hook's Law:

$$F = -ku\,, \qquad Eq.\ 1.17$$

where F is the force acting on an atom, u is the atom displacement and k is an interatomic force constant. When a force or stress σ is applied, the atoms in the crystal will have a displacement, which is defined in terms of *strain* of deformation, S [46].

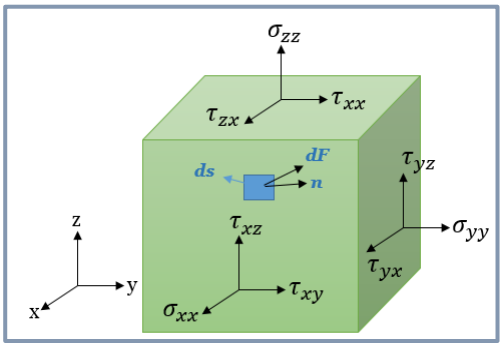

Fig. 1.12 Component of stress acting on a cubic volume of a material.

The stress is the result of internal forces in a material induced by the application of external loadings acting on its surface. Considering an element of surface, *ds*, inside of material, with unit normal vector $\vec{n}$. The surface force acting on ds is defined by $\overrightarrow{dF}$, then the stress is a second order tensor that can be expressed as:

$$\sigma_{ij} = \lim_{ds\to 0}\left(\frac{dF_i}{ds_j}\right) \qquad \textit{Eq. 1.18}$$

The stress σ_{ij} depends on the force orientation with respect to the surface normal on which it is applied. The stress can be applied on three directions, i and on three different surfaces, j, we can write these stresses in the form σ_{ij}. The stress acting perpendicular to surface is defined as compression or *tensile*. The stresses tangent to the surface are the *shear stresses* (see Fig.1.12) The components of normal stresses are σ_{xx}, σ_{yy}, σ_{zz} and the component of shear stresses are τ_{xy}, τ_{xz}, τ_{yx}, τ_{yz}, τ_{zx}, and τ_{zy}. [47, p. 48]. These components constitutes the stress tensor:

$$\sigma = \begin{bmatrix} \sigma_{xx} & \tau_{xy} & \tau_{xz} \\ \tau_{yx} & \sigma_{yy} & \tau_{yz} \\ \tau_{zx} & \tau_{zy} & \sigma_{zz} \end{bmatrix} \qquad \textit{Eq. 1.19}$$

The *strain* is represented by the second order tensor:

$$S_{ij} = \frac{\partial u_i}{\partial x_j}\ , \qquad \textit{Eq. 1.20}$$

where u_i is the extension/compression by unit length of distance resolved along direction $0x_j$. Similarly to stress, the compression or tensile strain has three components (S_{xx}, S_{yy}, S_{zz}) and the shear strain may have six components: S_{xy}, S_{xz}, S_{yx}, S_{yz}, S_{zx} and S_{zy} [47].

Stress and strain are linearly related by elastic constants. By using Einstein's convention of implicit summing over repeated indices, the constitutive relationship can be written as:

$$\sigma_{ij} = C_{ijkl}S_{kl} \qquad \textit{Eq. 1.21}$$

The tensor C_{ijkl} has 81 coefficients called elastic stiffness coefficients of material. However, as σ_{ij}, S_{kl} and C_{ijkl} are symmetric tensors. Thus, the elastic constants are equivalents when the first two or the last two subscripts are interchanged, for example: $C_{ijkl} = C_{jikl}$, $C_{ijkl} = C_{ijlk}$ and $C_{ijkl} = C_{klji}$ [1]. Therefore, C_{ijkl} tensor can be represented by 6x6 matrix with 21 independent values, by using the Voigt notation:

$$\begin{bmatrix} \sigma_1 \\ \sigma_2 \\ \sigma_3 \\ \sigma_4 \\ \sigma_5 \\ \sigma_6 \end{bmatrix} = \begin{bmatrix} C_{11} & C_{22} & C_{31} & C_{41} & C_{51} & C_{61} \\ C_{12} & C_{22} & C_{32} & C_{42} & C_{52} & C_{62} \\ C_{13} & C_{23} & C_{33} & C_{43} & C_{53} & C_{63} \\ C_{14} & C_{24} & C_{34} & C_{44} & C_{54} & C_{64} \\ C_{15} & C_{25} & C_{35} & C_{45} & C_{55} & C_{65} \\ C_{16} & C_{26} & C_{36} & C_{46} & C_{65} & C_{66} \end{bmatrix} \begin{bmatrix} S_1 \\ S_2 \\ S_3 \\ S_4 \\ S_5 \\ S_6 \end{bmatrix} \qquad \textit{Eq. 1.22}$$

On the other hand, LN and LT single crystals belong to the 3m point group. Thus, they have only six independent elastic stiffness constants: C^E_{11}, C^E_{13}, C^E_{14}, C^E_{33}, C^E_{44}, C^E_{66} and $C^E_{12} = (C^E_{11} - 2 * C^E_{66})$, where C^E is the stiffness constant at constant electric field.

LT and LN are piezoelectric, as has been previously showed, for these materials the effect of the electric field on mechanical deformation should be considered, as well. Thus,

according to Eqs. 1.1 and 1.2., the piezoelectric constants, *e*, and the dielectric permittivity, ε, define also the elastic properties of these materials. The LT and LN have four different piezoelectric constants (e_{15}, e_{22}, e_{31} and e_{33}), and two dielectric constants measured at constant strain (ε_{11}^{S} and ε_{33}^{S}) [47].The matrix of elastic constants, piezoelectric coefficient and permittivity of LT and LN are described bellow:

$$C_{ij} = \begin{bmatrix} C_{11} & C_{12} & C_{13} & C_{14} & 0 & 0 \\ C_{21} & C_{11} & C_{13} & -C_{14} & 0 & 0 \\ C_{13} & C_{13} & C_{33} & 0 & 0 & 0 \\ C_{14} & -C_{14} & 0 & C_{44} & 0 & 0 \\ 0 & 0 & 0 & 0 & C_{44} & C_{14} \\ 0 & 0 & 0 & 0 & C_{14} & C_{66} \end{bmatrix} \qquad \textit{Eq. 1.23}$$

$$e_{ij=} \begin{bmatrix} 0 & 0 & 0 & 0 & e_{15} & -e_{22} \\ -e_{22} & e_{22} & 0 & e_{15} & 0 & 0 \\ e_{31} & e_{31} & e_{33} & 0 & 0 & 0 \end{bmatrix} \qquad \textit{Eq. 1.24}$$

$$\varepsilon_{ij} = \begin{bmatrix} \varepsilon_{11} & 0 & 0 \\ 0 & \varepsilon_{11} & 0 \\ 0 & 0 & \varepsilon_{33} \end{bmatrix} \qquad \textit{Eq. 1.25}$$

Several works about measurement of physical constants for LN and LT crystals with congruent composition has been reported. The most of them were done by using ultrasonic microscopy methods [48]–[52]. The most accurate values are summarized in the Table 1.2 and 1.3, respectively. Although LT and LN are isomorphous materials, their piezoelectric, dielectric and elastic properties are quite different.

Table 1.2 Density, elastic, dielectric and piezoelectric constants of CLN [49]

	C_{11}	C_{12}	C_{13}	C_{14}	C_{33}	C_{44}
Elastic constant (x10¹¹ N/m²)	1.9886 ±0.0003	0.5467 ±0.0004	0.6799 ±0.0055	0.0783 ±0.0002	2.3418 ±0.0075	0.5985 ±0.0001
	e_{15}	e_{22}	e_{31}	e_{33}		
Piezoelectric constant (C/m²)	3.655 ±0.022	2.407 ±0.015	0.328 ±0.032	1.894 ±0.054		
	$\varepsilon_{11}^{S}/\varepsilon_0$	$\varepsilon_{33}^{S}/\varepsilon_0$				
Dielectric constant	44.9±0.4	26.7±0.3				
Density (x10³ kg/m³)	4.642±0.2					

Table 1.3 Density, elastic, dielectric and piezoelectric constants of CLT [49]

	C_{11}	C_{12}	C_{13}	C_{14}	C_{33}	C_{44}
Elastic constant (x10¹¹ N/m²)	2.3305 ±0.0004	0.4644 ±0.0006	0.8346 ±0.0067	-0.1075 ±0.0004	2.7522 ±0.0114	0.9562 ±0.0002
	e_{15}	e_{22}	e_{31}	e_{33}		
Piezoelectric constant (C/m²)	2.628 ±0.022	1.831 ±0.015	-0.145 ±0.067	1.849 ±0.118		
	$\varepsilon_{11}^{S}/\varepsilon_0$	$\varepsilon_{33}^{S}/\varepsilon_0$				
Dielectric constant	41.9±0.4	41.8±0.4				
Density (x10³ kg/m3)	7.460±0.4					

1.3.2.3 Dependence of elastic constants on temperature and domain structure

Temperature dependence of C_{ij} for LT and LN was estimated by Smith et al.[52]. It has been found that almost all elastic constants have a negative change with temperature, i.e they decrease with the increase of temperature. However, the behavior of elastic stiffness in ferroelectric and paraelectric phases (single and polydomain states, respectively) is not clear. Later, I. Tomeno et al. [53]–[55] reported the temperature dependence of elastic constants for single-domain and poly-domain crystals of LT and LN. The Fig. 1.13 exhibits the temperature dependence of elastic constants, measured at constant electric field constant polarization, C_{ii}^{E} and C_{ii}^{P}, respectively, for single domain (C_{ij}) and polydomain (C'_{ij}) LT and LN crystals.

In the case of ferroelectric phase of LT, C_{11}^{E} and C_{11}^{P} decrease nonlinearly from 300 K to T_c~880 K. In the paraelectric phase of LT, all elastic constants decrease with the increase of temperature (Fig.1.13 a). The shear elastic constants C_{44}^{E}, C'_{44} C_{66}^{E} and C'_{66} decrease with temperature until about 370-450 K, and then, they increase until T_c (Fig. 1.13 b, d). Longitudinal elastic constants, C_{33}^{P} decreases linearly with temperature. On the other hand, C'_{33} also decreases with temperature but it increases abruptly close to Curie temperature (Fig. 1.13 c) [53]. From these results, it can be observed that the temperature dependences of elastic constants in poly-domain and single domain crystals are similar. However, the temperature change of these constants in poly-domain crystals is less pronounced compared to those of single domain crystals, in the case of C_{44}, and C_{66} elastic constants. According to these results, the values of C_{11}, C_{44}, and C_{66} constants of poly-domain LT crystals are higher than those of the single-domain samples. It agrees well with the results obtained by Takanaga et al. for 36°rotated Y-cut LT crystals (36 RY-LT) [56]. The comparison of a complete set of elastic constants in poly-domain and single-domain 36 RY-LT crystals are given in the Table 1.4. In general, almost all elastic constant of poly-domain samples are slightly larger than elastic constant of single domain crystals, with exception to for C_{12}, C_{13} and C_{14}.

The temperature dependence of elastic constants of LN is presented in Fig. 1.13 e-h, as well. In contrast to C_{11} of LT, the C_{11}^E and C_{11}' of LN decrease linearly with temperature. The behavior of C_{33}^P and C_{33}' are similar to those of LT crystals, it decrease linearly with the temperature. The shear constants of LN, C_{44}^E and C_{66}^E, decreased linearly from room temperature until 450-500 K, but at higher temperatures, their temperature dependence is not linear [53].

Table 1.4 Elastic constants and density of single-domain and poly-domain 36 RY-LT crystals [56]

		Single-domain C_{ij}^E	***Poly-domain*** $C_{ij}^{E'}$	$C_{ij}^{E'} - C_{ij}^{E'}$
Elastic constant ***(x10¹¹ N/m²)***	C_{11}	2,3331	2,37	0,039
	C_{12}	0,464	0,427	-0,037
	C_{13}	0,835	0,835	0
	C_{14}	-0,108	-0,161	-0,053
	C_{33}	2,752	2,761	0,009
	C_{44}	0,953	1,029	0,076
	C_{66}	0,933	0,971	0,038
Density ***(x10³ kg/m³)***	ρ	7,4604	7,4605	0,0001

Temperature dependence of elastic constants of LT:

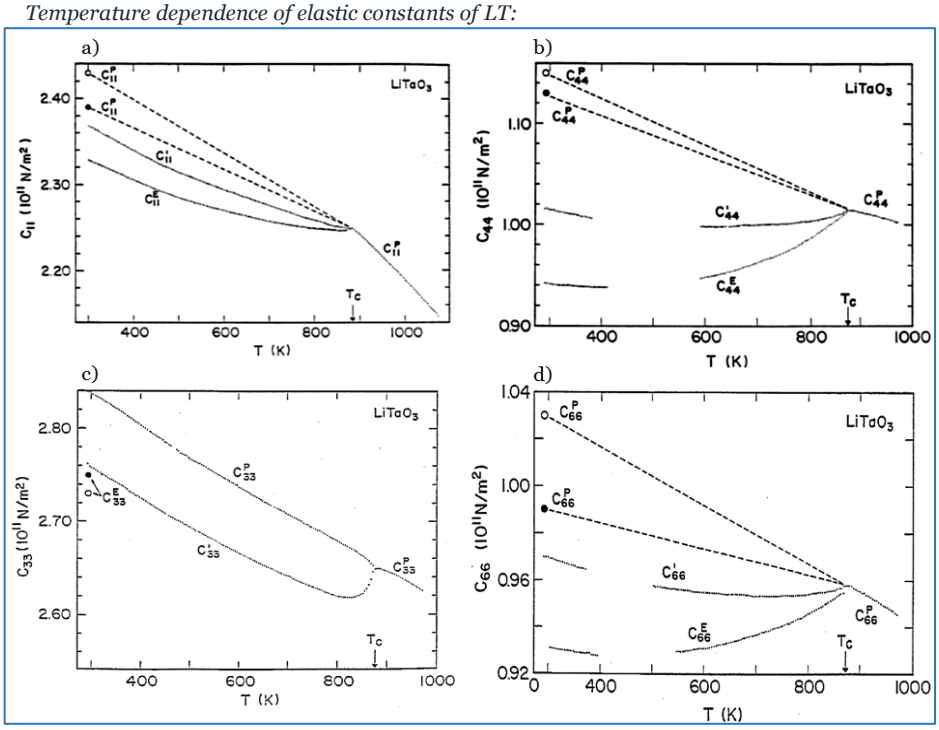

Temperature dependence of elastic constants of LN:

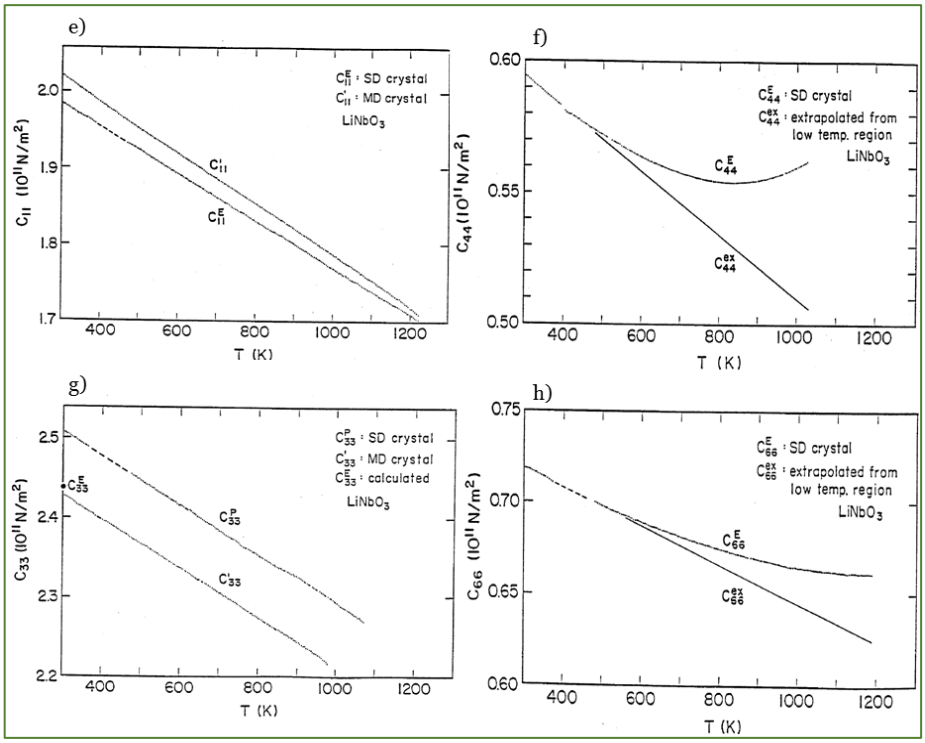

Fig. 1.13 Evolution of elastic constants C_{11}, C_{44}, C_{33} and C_{66} with temperature of CLT and CLN crystals [50]
C^{P}_{ij} : elastic coefficient at constant polarization (i=1,3,4,6);
C'_{ij} : elastic constant of polydomain crystals;
C^{E}_{ij} :elastic coefficient of single domain crystals;
C^{ex}_{ij} : elastic coefficient extrapoled from low temperature region;

The open and closed circles are values of elastic constants taken from results reported by Warner [46] and Yamada [47], respectively.

1.3.2.4 Effect of Li_2O non-stoichiometry on elastic properties of $LiTaO_3$ and $LiNbO_3$

The elastic constants, acoustic velocities and density of LN and LT crystals were measured by Ultrasonic Microscopy for several cuts of crystals with different Li_2O concentrations, close to the congruent composition (from 48.28 to 48.66 mol% of Li_2O [57]. In both materials, the density decreases linearly with the Li_2O content [58]. The elastic constants of LT and LN increase with the increase of Li_2O concentration, with exception to the C_{44} of LN, which decreases when Li_2O concentration diminishes [52]. The values of these constants corresponding to different Li_2O non-stoichiometry in LN and LT are given in Tables A1.1 and A1.2 (Annexe A.1).

Another approach was used by Bernabé et al.[59] to estimate the effect of Li_2O non-stoichiometry on the elastic constants of LN. They have studied five crystals with different Li_2O concentrations, by means of Brillouin scattering Spectroscopy. The compositions close to the stoichiometric one were studied. It was found that sound velocity decreases slightly with the Li_2O content, showing a minimum value for the crystals whose deviation from stoichiometry is 0.05. Further increase in Li deficiency results in the increase of acoustic velocity as illustrated in the Fig. 1.14.

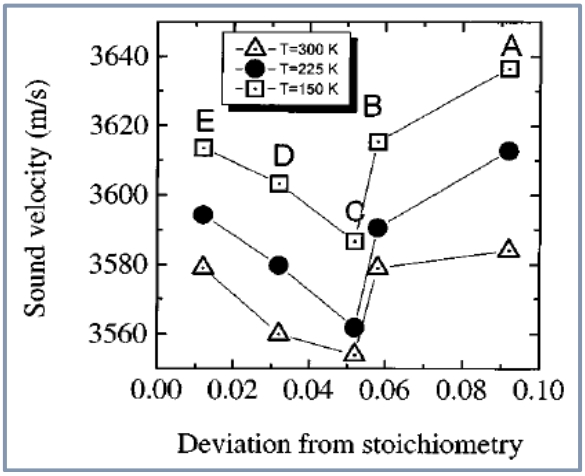

Fig. 1.14 Sound velocity as a function of a deviation from stoichiometry in LN. The E sample contained Li_2O concentration closest to the stoichiometric one [59].

In summary, it has been shown that the composition of LT and LN single crystal has a very important effect on their structural and physical properties. In some cases, the stoichiometric crystal may have advantages over the congruent ones. Stoichiometric crystals exhibit less defects than the congruent crystals, which improves the resistance of material to photorefractive damage [59]–[61]. The potential applications of SLT and SLN crystal in optics have increased the interest in production of such crystals. The fabrication of stoichiometric crystals will be discussed in the Chapter 2. On the other hand, initially produced CLT and CLN single crystals exhibit low acoustic losses and high *piezoelectric coupling coefficients*. For this reason, they are widely used for the fabrication of acoustic wave devices, such as filters band pass for cell phones. Nowadays 70 % of Radio Frequency (RF) SAW filters are fabricated from LT and LN single crystals. We will present the properties of SAW and BAW devices in the next section.

1.4 Bulk and Surface Acoustic Wave devices

1.4.1 Acoustic waves in solids

Acoustic waves can be sorted in two types, according to the type of their propagation: bulk and surface. However, there are another types of waves, which have a combination of characteristics of surface and bulk waves; such are the cases of the pseudo SAW and of plate waves (Lamb waves). The devices take their name depending on the type of wave used for its operation: Surface Acoustic Wave (SAW) or Bulk Acoustic Wave (BAW) devices.

1.4.1.1 Bulk Acoustic Waves (BAW)

The BAW is a wave that propagates in a confined medium, for example in a piezoelectric plate. Bulk acoustic waves can be longitudinal or transverse (shear). In longitudinal waves the displacement of the particles is parallel to the propagation of the wave (Fig. 1.15 a). In isotropic materials, this type of wave has usually velocities of 6000 m/s. The displacement of particles in transverse waves is perpendicular to the direction of propagation (Fig. 1.15 b). The velocity of these waves is often near 3000 m/s [62, p. 2]. Fig. 1.15 b shows a

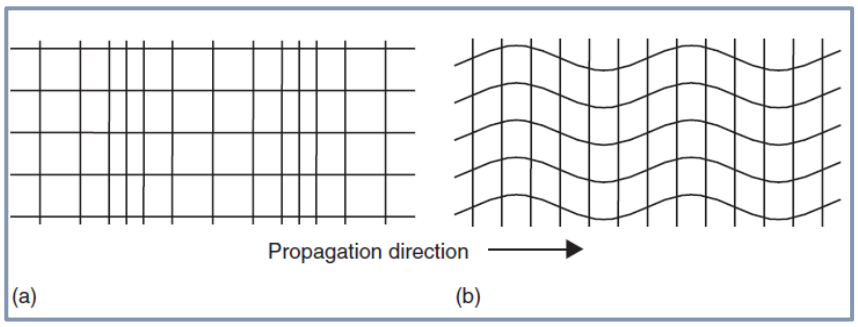

Fig. 1.15 Representation of the longitudinal (a) and transverse (b) modes of a bulk acoustic wave [62].

representation of longitudinal and shear BAW, respectively.

1.4.1.2 Surface Acoustic Waves

The waves propagating on the surface of a material are called Surface Acoustic Waves (SAW). There are different surface acoustic waves, for example, the Rayleigh waves, the Gulyaev-Bleustein waves and the Love waves. But in practice, Rayleigh waves are the most ones used in SAW devices [63]. Rayleigh waves have two components: a component with displacement parallel to the SAW propagation axis, while the other is perpendicular to the surface. For this reason the displacement of the particles is elliptic [63, p. 11], which is represented in Fig. 1.16.

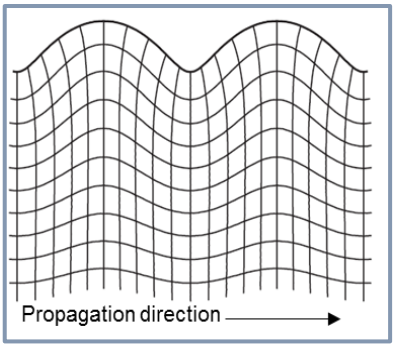

Fig. 1.16 Representation of the strain of a medium in which a Rayleigh wave is propagating [77].

1.4.1.3 Leaky surface acoustic waves

The Leaky surface Acoustic Wave (LSAW) propagates mainly on the surface of materials but has also some components propagating inside the substrate. The LSAW has been reported for the first time in 1967 [64]. In general, these waves present some interesting characteristics: low attenuation, high velocity and higher piezoelectric coupling than that of the SAW [62, p. 342].

Acoustic waves in several cuts of LT and LN present this kind of propagation. For example, the 36°rotated Y-X axis propagating (36 RY-X LT), 42 RY-X LT and 64 RY-X LN. These cuts of LN and LT are frequently used in mobile communication systems due to the large electromechanical coupling coefficient of LSAW, which is a required characteristic for the fabrication of SAW filters with large bandwidth [65].

1.4.1.4 Propagation of waves in $LiTaO_3$ and $LiNbO_3$ crystals

The displacement of waves in elastic media can be described by the following equation [66]:

$$\sigma_{ij,i} = \rho \ddot{u}_j, \qquad \textit{Eq. 1.26}$$

where ρ is the density and $\ddot{u}_i$is the displacement tensor. In piezoelectric materials, the velocity of acoustic waves is smaller than the velocity of electromagnetic waves, typically by a factor 10^5. Therefore, the electric field can be neglected in the constitutive equations (Eq. 1.1 and 1.2). Thus, one the of Maxwell's equation is reduced to $\vec{\nabla} \times \vec{E} = \vec{0}$ and the electric field is the negative gradient of the potential ($\vec{E} = -\overrightarrow{grad}\,\varphi_{,i}$).

Moreover, piezoelectric materials are essentially insulators[1], then $D_i = 0$ in Eq. 1.1. Then by substituting the Eq. 1.26 in Eqs. 1.1 and 1.2, we obtain the following relationships:

$$C_{ijkl}u_{k,li} + e_{kji}\varphi_{ki} = \rho \ddot{u}_j, \qquad \textit{Eq. 1.27}$$

$$e_{klj}u_{i,jk} - \varepsilon_{ij}\varphi_{ij} = 0. \qquad \textit{Eq. 1.28}$$

A solution of the Eqs. 1.27 and 1.28 must be defined in terms potential $\varphi(x_j, t)$ and the displacement vector $u_k(x_{j,}t)$. It can be easily shown that plane waves of well-defined velocity and polarization can propagate in arbitrary directions of piezoelectric solids:

$$u_k(x_{j,}t) = U_k exp\left(i\frac{n_j x_j}{V} - \omega t\right), \qquad \textit{Eq. 1.29}$$

$$\varphi(x_j, t) = \Phi exp\left(i\frac{n_j x_j}{V} - \omega t\right), \qquad \textit{Eq. 1.30}$$

where u_k is the displacement along the direction of propagation defined by the n_j vector (normal to the front wave), V is the phase velocity, ω is the angular velocity, t is the time and k,j=1, 2, 3. Then, V, $\boldsymbol{U}$ and Φ are fixed by $\boldsymbol{n}$ throughout a classical process which we summarize below.

If Eqs. 1.29 and 1.30 are substituted in the Eqs. 1.27 and 1.28, a system of linear equations is obtained:

$$(C_{ijkl}n_j n_k - \rho V^2 \delta_{ij})U_k + e_{ijk}n_j n_i \Phi = 0 \qquad \textit{Eq. 1.31}$$

$$e_{ijk}n_j n_k U_k - \varepsilon_{jk}n_j n_k \Phi = 0 \qquad \textit{Eq. 1.32}$$

Eqs. 1.31 and 1.32 can be written as well as follows:

$$(\Gamma_{il} - \rho V^2 \delta_{ij})U_k + \gamma_i \Phi = 0, \qquad \textit{Eq. 1.33}$$

$$\gamma_i U_k - \varepsilon^S \Phi = 0, \qquad \textit{Eq. 1.34}$$

[1] *Piezoelectric materials can be also semi-conductors, such is the case of GaAs, GaN, ZnO, InN, ...), widely investigated for the development of acoustoelectronic devices.*

where $\Gamma_{il} = C_{ijkl} n_j n_k$, $\gamma_i = e_{ijk} n_j n_k$, $\varepsilon^S = \varepsilon_{jk} n_j n_k$

Eliminating the Φ, Eqs. 1.33 and 1.34 become:

$$\left(\Gamma_{il} + \frac{\gamma_i \gamma_l}{\varepsilon^S} - \rho V^2 \delta_{ij}\right) U_k = 0, \; i=1,2,3, \qquad \textit{Eq. 1.35}$$

which is called the Christoffel equation. The solution of this system can be found by equating its determinant to zero:

$$\Delta = \begin{vmatrix} \bar{\Gamma}_{11} - \rho V^2 & \bar{\Gamma}_{12} & \bar{\Gamma}_{13} \\ \bar{\Gamma}_{21} & \bar{\Gamma}_{22} - \rho V^2 & \bar{\Gamma}_{23} \\ \bar{\Gamma}_{31} & \bar{\Gamma}_{32} & \bar{\Gamma}_{33} - \rho V^2 \end{vmatrix} = 0, \qquad \textit{Eq. 1.36}$$

where $\bar{\Gamma}_{il} = \Gamma_{il} + \frac{\gamma_i \gamma_l}{\varepsilon^S}$. The Eq. 1.35 enables to obtain the three velocities and the polarization of the waves propagating along the direction defined by the n_j vector. Thus, the velocities and the polarizations of waves are defined by the eigenvalues, ρV^2, and eigenvectors, U_k, of the Christoffel tensor $\bar{\Gamma}_{il}$. Thus, three plane waves can be propagating in the same direction with different velocities: one quasi-longitudinal and two quasi-transverse.

The piezoelectricity modifies the propagation velocity of waves due to a modification of the stiffness coefficients. In this case, the Christoffel tensor writes as:

$$\bar{\Gamma}_{il} = \bar{C}_{ijkl} n_j n_k, \qquad \textit{Eq. 1.37}$$

$$\bar{C}_{ijkl} = C_{ijkl} + \frac{(e_{pij} n_p)(e_{qkl} n_q)}{\varepsilon^S_{jk} n_j n_k}, \qquad \textit{Eq. 1.38}$$

where $\bar{C}_{ijkl}$ is called the stiffened constants and depends on the propagation direction. The convention of implicit sum over repeated (dummy) indexes is extensively used in these calculations.

In the case of LT and LN crystals, belonging to the 3m point group, the elements of Christoffel's tensor can be described as [1]:

$$\begin{aligned}
\bar{\Gamma}_{11} &= \bar{C}_{11} n_1^2 + \bar{C}_{66} n_2^2 + \bar{C}_{44} n_3^2 + 2\bar{C}_{14} n_2 n_3 \\
\bar{\Gamma}_{12} &= (\bar{C}_{12} + \bar{C}_{66}) n_1 n_2 + 2\bar{C}_{14} n_1 n_3 \\
\bar{\Gamma}_{13} &= 2\bar{C}_{14} n_1 n_2 + (\bar{C}_{13} + \bar{C}_{44}) n_1 n_3 \\
\bar{\Gamma}_{22} &= \bar{C}_{11} n_2^2 + \bar{C}_{66} n_1^2 + \bar{C}_{44} n_3^2 - 2\bar{C}_{14} n_2 n_3 \\
\bar{\Gamma}_{23} &= \bar{C}_{14} (n_1^2 - n_2^2) + (\bar{C}_{13} + \bar{C}_{44}) n_2 n_3 \\
\bar{\Gamma}_{33} &= \bar{C}_{44} (n_1^2 + n_2^2) + \bar{C}_{33} n_3^2
\end{aligned} \qquad \textit{Eq. 1.39}$$

When the wave propagates along the X-axis ($n_1=1$, $n_2=n_3=0$), Christoffel's tensor is:

$$[\bar{\Gamma}] = \begin{bmatrix} C_{11} & 0 & 0 \\ 0 & C_{66} & C_{14} \\ 0 & C_{14} & C_{44} \end{bmatrix} \qquad \textit{Eq. 1.40}$$

Thus, from this system the velocities of one longitudinal wave, V_{Xl}, and two transverse waves (V_{Xs} and V_{Zs}) can be estimated as following:

$$\rho V_{Xl}^2 = C_{11} \qquad \textit{Eq. 1.41}$$

$$2\rho V_{Xs}^2 = C_{66} + C_{44} + \sqrt{(C_{66} - C_{44})^2 + 4C_{14}^2} \quad \textit{Eq. 1.42}$$

$$2\rho V_{Zs}^2 = C_{66} + C_{44} - \sqrt{(C_{66} - C_{44})^2 + 4C_{14}^2} \quad \textit{Eq. 1.43}$$

In the case of the waves propagating along the Y-axis (n_2=1, n_1=n_3=0), we have a transverse wave propagating with the velocity V_{Ys}, a quasi-longitudinal wave propagating with the velocity V_{Yql} and a quasi-tranversal wave of velocity V_{Yqs}:

$$[\bar{\Gamma}] = \begin{bmatrix} C_{66} & 0 & 0 \\ 0 & C_{11} + \frac{e_{22}^2}{\varepsilon_{22}} & C_{24} + \frac{e_{22}e_{24}}{\varepsilon_{22}} \\ 0 & C_{24} + \frac{e_{22}e_{24}}{\varepsilon_{22}} & C_{44} + \frac{e_{24}^2}{\varepsilon_{22}} \end{bmatrix} \quad \textit{Eq. 1.44}$$

$$\rho V_{Ys}^2 = C_{66} \quad \textit{Eq. 1.45}$$

$$2\rho V_{Yql}^2 = \bar{C}_{11} + \bar{C}_{44} + \sqrt{(\bar{C}_{11} - \bar{C}_{44})^2 + 4\bar{C}_{24}^2} \quad \textit{Eq. 1.46}$$

$$2\rho V_{YqS}^2 = \bar{C}_{11} + \bar{C}_{44} - \sqrt{(\bar{C}_{11} - \bar{C}_{44})^2 + 4\bar{C}_{24}^2} \quad \textit{Eq. 1.47}$$

Finally, in the case of waves propagating along the Z-axis (n_3=1, n_1=n_2=0), we have a longitudinal wave with velocity V_{Zl} and one quasi-transversal wave propagating with V_{Zs} velocity:

$$[\bar{\Gamma}] = \begin{bmatrix} C_{44} & 0 & 0 \\ 0 & C_{44} & 0 \\ 0 & 0 & C_{33} + \frac{e_{33}^2}{\varepsilon_{33}} \end{bmatrix} \quad \textit{Eq. 1.48}$$

$$\rho V_{Zs}^2 = C_{44} \quad \textit{Eq. 1.49}$$

$$\rho V_{Zl}^2 = C_{33}^E + \frac{e_{33}^2}{\varepsilon_{33}^S} \quad \textit{Eq. 1.50}$$

Thus, by using Eqs. 1.41-1.50, the elastic constants of LT and LN crystals can be estimated from the measurements of the velocities of bulk acoustic waves, propagating along of different crystallographic directions. The detailed methodology used for estimating the elastic properties will be given in the Chapter 4

1.4.2 Principles of BAW and SAW devices

1.4.2.1 BAW devices

The basic structure of a BAW resonator consists of a piezoelectric material coated by two metal electrodes (Fig. 1.17). When an electric field is applied, the piezoelectric substrate deforms due to the *reverse piezoelectric effect* and a wave is generated. When the propagating wave encounters the end of the volume, it is reflected. The *resonance* phenomenon appears when the reflected waves overlap with the incident waves, generating a constructive interference. This occurs when the thickness of substrate *(h)* is proportional to an integer multiple *(n)* of a half wavelength (λ). Considering $f=V/\lambda$ and $h=n\,\lambda/2$, where V is the wave velocity, the resonance frequency, f, of a BAW resonator is defined by the following equation [67, p. 2]:

$$f = \frac{nV}{2h} \quad \textit{Eq. 1.51}$$

The configuration of electrodes defines the type of excitation in resonator. The Fig. 1.17 presents a *thickness field excited* (TFE) resonator. The electric field is applied across the plate thickness and the wave propagates in the same direction. This resonator allows the excitation of thickness-extension and/or thickness-shear modes [68], [69], depending on the non-zero terms of the matrix of piezoelectric constants.

A second type of configuration is *lateral field excitation* (LFE). In this case, there are two electrodes on the surface of the plate [70] (see Fig.1.17 b). In the case of crystals belonging the point group 3m (e.g. LT and LN) and rotated around X-axis, this configuration enables the excitation of shear waves. The shear waves cannot be excited by applying an electric field across the thickness of the plate.

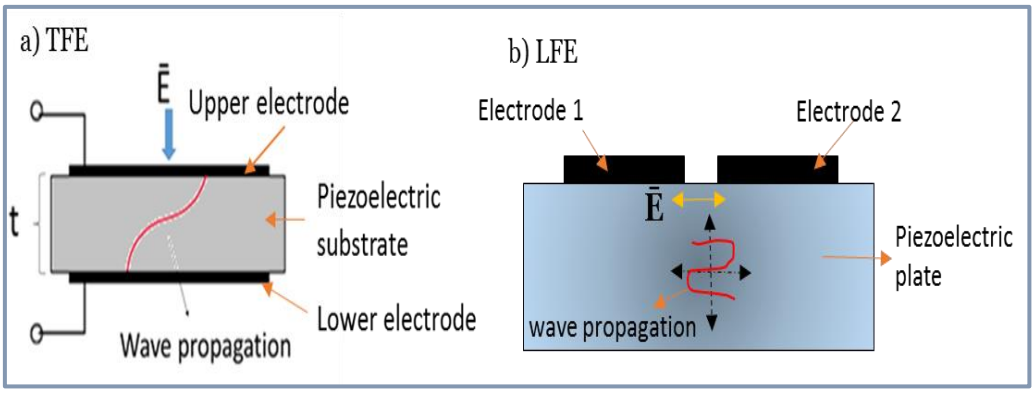

Fig.1.17 Schematic representation of thickness field excitation (TFE) (a) and lateral field excitation (LFE) (b).two types of excitation modes in BAW resonators, showing the displacement of electric potential and the propagation of waves.

1.4.2.2 SAW devices

The first devices using surface acoustic waves were introduced in 1965 with the discovery of Interdigitated Transducer (IDT) [71]. This device consists in several metal electrodes periodically spaced, which are connected to two larger electrodes (bus-bars). An example of a SAW device is a delay line, which is composed of two metallic transducers (IDTs) placed on the surface of a piezoelectric substrate. These components convert the electrical energy to mechanical and vice versa. A voltage is applied across two electrodes of the IDT (input), thus, an electric field is produced. It generates compression and expansion regions on the piezoelectric substrate, resulting in a SAW that propagates along the surface of the substrate (Fig. 1.18 b). Then, the second transducer receives this wave with a delay, and turns the mechanical energy back to an electrical signal [63, p. 20]. An absorber can be applied in order to eliminate undesirable reflections from the end of the substrate [72, p. 10] (Fig. 1.18 a).

In the IDT, the "pitch" -p- is the mechanical period of the structure, namely the distance between two electrodes, without taking into account their polarization. The wavelength -λ- is the period of the electric excitation (see Fig. 1.18 b). Thus, the wavelength can be defined as:

$$\lambda = 2p \qquad \textit{Eq. 1.52}$$

The number of electrodes in an IDT, which is related to the number of periods -N_p- affects the bandwidth of the transducer. The larger is N_p, the narrower is the bandwidth- Δf- [62, p. 15]:

$$N_p = \frac{f_c}{\Delta f}, \qquad \textit{Eq. 1.53}$$

where f_c is the central frequency .

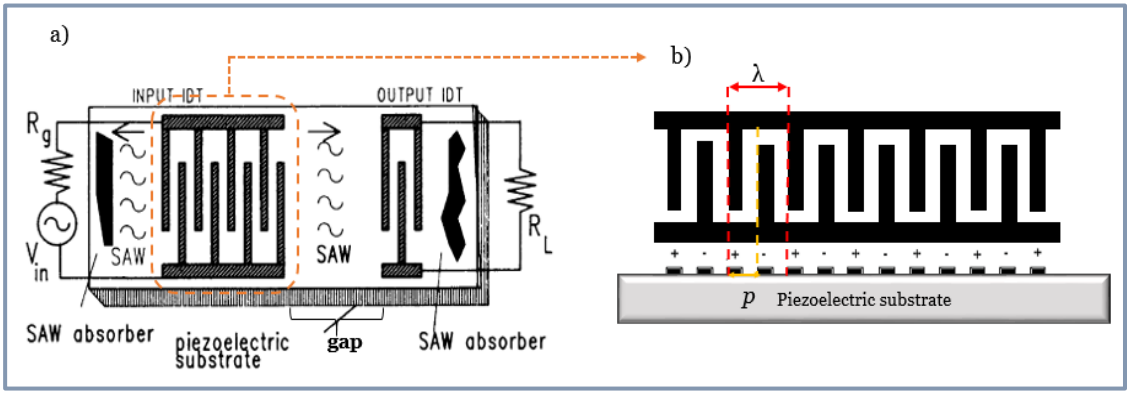

Fig. 1.18 Schematic representation of a basic SAW delay line (a). The propagation of SAW with a wavelength λ and period p. [72].

1.4.3 Properties of BAW and SAW propagation

The propagation properties of BAW and SAW are mainly defined by the following parameters: the wave velocity, the electromechanical coupling coefficient of the piezoelectric substrate (K^2), the Temperature Coefficient of Frequency and the quality factor [72]. In the case of SAW devices, the insertion losses and the bandwidth are important parameters for the design of devices, as well. These concepts will be explained below.

- ***Acoustic Wave velocity (V)***: Is a property related to the operational frequency of the device, *f*, and to the wavelength, λ.

$$f = \frac{V}{\lambda} \qquad \textit{Eq. 1.54}$$

- ***Electromechanical coupling factor (K^2):*** This coefficient defines the efficiency of piezoelectric substrate to transform the electrical into mechanical energy or vice versa [72, p. 19]. It mainly depends on the material piezoelectric properties, its cut or orientation and on the type of propagating wave. It is a very important parameter for the design of SAW and BAW bandpass filters because their bandwidth is defined by K^2.
- ***Quality factor (Q)***: The quality factor represents the losses of a resonant circuit and it is defined as the average ratio of the stored energy to the power dissipated over one period of operation [73].
- ***Temperature Coefficient of frequency (TCF):*** This parameter defines the thermal stability of frequency. The TCF depends on material properties of the piezoelectric substrate: elastic, piezoelectric and permittivity constants [74]. The changes of these parameters with temperature generate a variation of the propagation characteristics. Thus the TCF can by expressed by the following equation [75]:

$$TCF = \frac{1}{f_0}\frac{df}{dT} = \frac{1}{V}\frac{dV}{dT} - \alpha_1, \qquad \textit{Eq. 1.55}$$

where df/dT represents temperature dependence of frequency, f_o corresponds to the frequency at 25 °C, dV/dT is the temperature dependence of wave velocity and α_1 is the thermal expansion coefficient along SAW propagation. Since the wave velocity is

related to elastic constants of materials C_{ijkl}, the variation of these parameters with temperature may be expressed by Taylor series as:

$$C_{ijkl}(T) = C_{ijkl}(T_0)[1 + \frac{dC_{ijkl}(T)}{dT}(T - T_0) + \frac{1}{2}\frac{d^2C_{ijkl}(T)}{dT^2}(T - T_0)^2 + \cdots] \qquad Eq.\ 1.56$$

Eq. 1.56 can expressed as:

$$C_{ijkl}(T) = C_{ijkl}(T_0)[1 + \beta_1(T - T_0) + \beta_2(T - T_0)^2 + \cdots], \qquad Eq.1.57$$

$$\beta_1 = \frac{1}{C_{ijkl}}\frac{dC_{ijkl}}{dT} \text{ and } \beta_2 = \frac{1}{2\,C_{ijkl}}\frac{d^2C_{ijkl}}{dT^2}, \qquad Eq.\ 1.58$$

where β_1 and β_2 are the the first and second order temperature coefficients of elastic constants C_{ijkl}. This equation enables to calculate the temperature characteristics of material in a certain range of temperature, T_0 being the temperature of reference (T=25°C). The TCF is expressed in parts per million per degree Celsius (ppm/°C).

- ***Bandwidth (BW):*** Is the distance between the upper and lower frequencies in a continuous set of frequencies at a determined transmission level [72, p. 5], [76].

$$BW\% = \frac{\Delta f}{f_c} \times 100 \qquad Eq.\ 1.59$$

- ***Insertion loss (IL)*:** This parameter defines the attenuation of the wave during its propagation. It is the ratio of the signal power of a test configuration with no device installed to the signal power with the device installed. This ratio is generally described in terms of dB and can be expressed as [72, p. 5]:

$$IL = 10log_{10}\frac{(power\ at\ load\ with\ no\ device\ present)}{(power\ at\ load\ with\ device\ inserted)}\ dB \qquad Eq.\ 1.60$$

It depends principally on the characteristics of the devices (including piezoelectric material and electrodes) the frequency and the temperature of operation.

1.4.4 Piezoelectric materials used in BAW and SAW devices

It should be noted that the wave parameters are affected by the anisotropy of materials. The convention for axes and cuts of single crystals used in acoustic wave devices is defined by the norm IEEE 1978. It is assumed that the crystal piece is a rectangular plate of three dimensions: length (l), width (w) and thickness (t). The notation used for a piezoelectric plate in the framework of this norm is:

(YX lwt) Φ/θ/ψ

The convention starts from a simple, specific orientation of the plate in the crystallographic frame and defines how rotations have to be applied in sequence to reach the final, effective orientation of the plate. Thus, the first letter indicates the initial direction of the plate thickness. The second letter defines the initial direction of the length of the plate, or the propagation direction on the surface in case of SAW. *l* stands for length, *w* for width and *t* for thickness. At this stage, each dimension of the plate is clearly associated to an axis (X, Y or Z) of the crystallographic frame and then the third letter represents the axis of the first rotation (here *Φ*), the fourth and fifth letters indicates the axis of the second and the third rotations (here *θ* and ψ), respectively. The order of the symbols Φ/θ/ψ indicating the angles

of each rotation is arbitrary, as long as it matches the order of the use of the symbols *lwt* to unambiguously define the orientation of the plate [4]. It is worth remarking that although all orientations can be well-defined within this convention, the way it can be used to define a given orientation is not unique.

For example, the orientation of a GT cut plate of quartz with respect the crystallographic axes is defined as described in the Fig. 1.19.

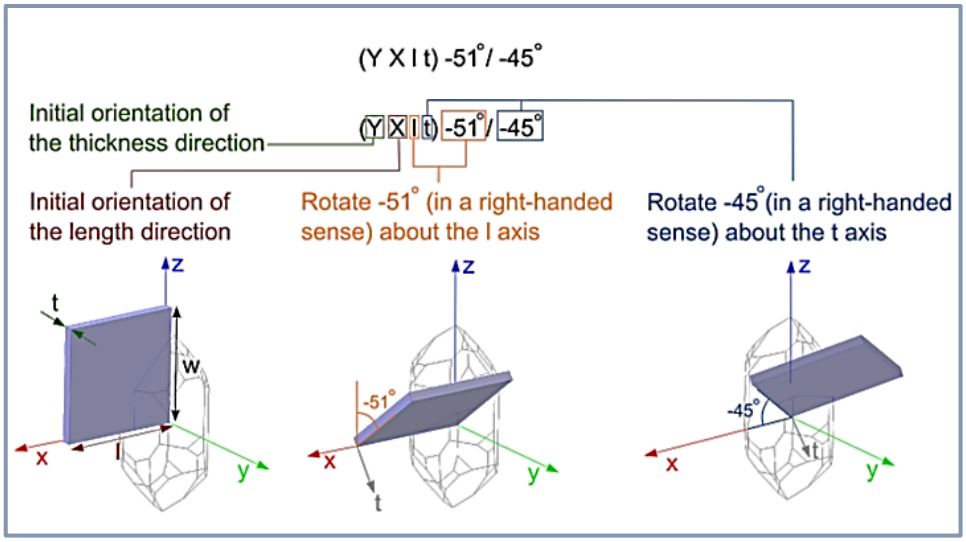

Fig.1.19 Example of the convention used for the crystal orientation according to the IEEE 1978 standard [77]

In the case of LT and LN crystals, the X, Y, Z-axis are defined according to an orthogonal reference system where Z is parallel to the crystallographic *c*-axis and X is parallel to the crystallographic *a*-axis, which is taken perpendicular to the mirror plane of the 3m point group. Hence, YXl/64 indicates that the crystal cut is 64° rotated around X-axis after starting from the YX-cut and the wave propagates along the X-axis. In this work we will use the common notation 64 RY-X LT to indicate the crystal cut and the axis of wave propagation.

Table 1.5 Propagation characteristics of single crystals used in BAW and SAW devices: V, K^2 and TCF.

Material	***Crystal cut-SAW axis***	***V (m/s)***	***K^2 (%)***	***TCF (ppm/°C)***	***Reference***
Quartz	ST-X	3158	0.11	0	[79]
$LiNbO_3$	Y-Z	3488	4.5	-94	[79]
	64RY-X LN	4478	11.3	-81	[79]
	128 RY-LN	3979	5.4	-75	[108]
$LiTaO_3$	36 RY-LT	4112	6.0	-32	[109]
	42 RY-LT	4022	7.6	-40	[110]
	112 RY-LT	3300	0.70	-18	[77]
GaAs	<001> (110)	<2841	<0.06	+49	[79]
$La_3Ga_5SiO_{14}$	Euler angles (0, 138.5°, 26.3°	2743	0.34	1	[111]

Piezoelectric substrates for BAW and SAW devices are usually single crystals, e.g. quartz, langasite ($La_3Ga_5SiO_{14}$), LN or LT. However, structures based on piezoelectric thin films (for example AlN and ZnO), deposited on single crystals, such as sapphire or silicon, are used as piezoelectric substrate, as well [107]. Usually the thickness of thin film is expressed in terms of the wavelength (h/λ). Several examples of piezoelectric single crystals and thin films used in SAW devices, respectively and their propagation properties are given in Tables 1.5 and 1.6, respectively. Since material properties affect strongly the performance of acoustic devices, the choice of the material depends on the target application.

Table 1.6 Propagation characteristics of thin film/substrate structure used in SAW devices: V, K^2 and TCF

Thin film	***Structure***	***V (m/s)***	***K^2 (%)***	***TCF (ppm/°C)***
ZnO	ZnO/glass	2600	1.9	-25 [112]
LN	LN/diamond	11900	9.0	-25 [112]
LT	LT/diamond	10600	3.6	-18 [112]
AlN	AlN/sapphire	5675	0.2	-40[107]

1.4.5 Characterization of BAW and SAW resonators

Typically, the electrical characterization of resonators consists in admittance or impedance measurements. The impedance can be defined as:

$$Z=R+jX, \qquad Eq.\ 1.61$$

where Z is the impedance, R is the resistance, j is the imaginary unit and X is the reactance. The admittance, Y, is the inverse of impedance and it has also real and imaginary parts:

$$Y=G+jB, \qquad Eq.\ 1.62$$

where Y is the admittance, G is the conductance, j is the imaginary unit and B is the susceptance. An example of imaginary and real parts of admittance simulated for a BAW resonator is given in the Fig. 1.20 a). The measurement of the admittance and impedance in a BAW resonator allows to find out the values of the resonance frequency, f_r, or series frequency, f_s, (f_r ~f_s) and anti-resonance, f_a, or parallel frequency, f_p, (f_a~f_p). The series frequency corresponds to the maximum of the conductance (G) and the parallel frequency is the frequency at which the resistance (R) has a maximum value (Fig. 1.20 b).

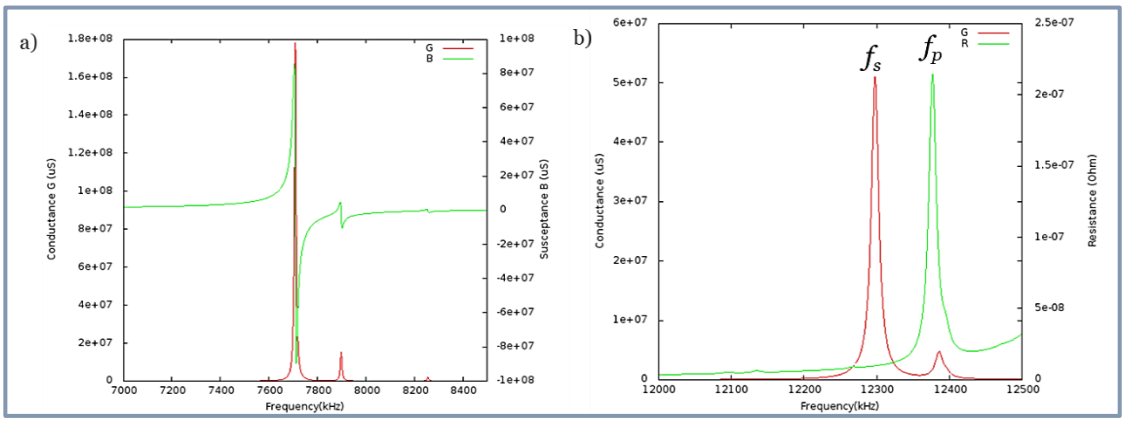

Fig. 1.20 Real and imaginary parts of admittance of a BAW resonator (a). The series frequency (f_s) and the parallel frequency (f_p) obtained from the conductance (G) and the resistance (R) (b).

The main parameters defining the efficiency of resonators are the coupling factor and the quality factor. The difference between series and parallel frequencies depends on the piezoelectric coupling coefficient of material (defined in the Eq. 1.3) and the resonator geometry. Thus, the *effective coupling factor*, K_{eff}^2, can be obtained from f_s and f_p by using the following equation:

$$K_{eff}^2 = 1 - \left(\frac{f_s}{f_p}\right)^2, \qquad \textit{Eq. 1.63}$$

This equation is valid in the case of materials with small electromechanical coupling and small resistance. It is widely used, for instance in the case of filter devices [4, p. 44]. In the case of the measurement of thickness extension mode of plates, the electromechanical coupling factor K^2 can be determined from the following equation [4, p. 49]:

$$K^2 = \frac{\pi}{2}\frac{f_s}{f_p} tan \frac{\pi}{2}\frac{f_p - f_s}{f_p} \qquad \textit{Eq. 1.64}$$

The quality factor of a resonator, Q, can be estimated from the bandwidth of conductance at -3 dB. It can be expressed by:

$$Q = \frac{f_c}{\Delta f}, \qquad \textit{Eq. 1.65}$$

where f_c is the resonator center frequency and $\Delta f = f_2 - f_1$ is the bandwidth at $G = \frac{G_{max}}{\sqrt{2}}$ (Fig. 1.21).

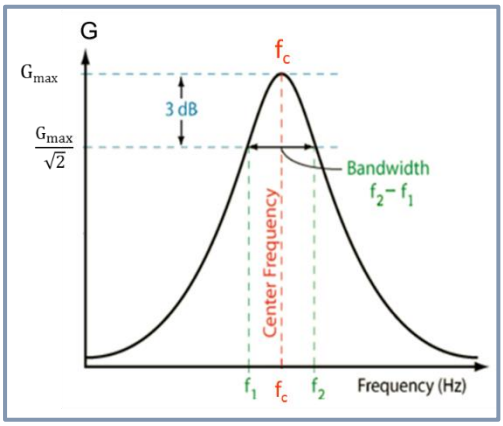

Fig.1.21 Estimation of the quality factor [73].

The equivalent circuit of a piezoelectric resonator is known as the Butterworth-Van Dyke (BVD) model. The Fig. 1.22 a represents the circuit of a BAW resonator in TFE configuration.

The motional resistance, R_1, the motional capacitance, C_1, and the motional inductance, L_1 constitute a resonant circuit that represents the mechanical resonance (motional behavior) [78]. The values of R_1, C_1, L_1 and static capacitance, C_0, can be obtained from the impedance measurement [67]:

$$Z(\omega) = \frac{1}{jC_0\omega}\left(1 - \frac{K^2 \tan X}{X}\right), \qquad \textit{Eq. 1.66}$$

where $X = n\left(\frac{\pi}{2}\right)\left(\frac{f_r}{f_a}\right)$, n is the harmonic order and $\omega = 2\pi f$

From this equivalent circuit we can get three frequencies:

- The antiresonance frequency, corresponding to Z(ω)=∞;
- The resonance frequency of series branch $\omega_s = 1/\sqrt{L_1 C_1}$;
- The series resonance frequency, when Z(ω)=0

On the other hand, the same circuit can be expressed in terms of admittance as:

$$Y(\omega) = \frac{1}{R_1 + j(L_1\omega - 1/C_1\omega)} + jC_0\omega \qquad \textit{Eq. 1.67}$$

The parameters of the equivalent circuit, can be obtained from the admittance or impedance circle [79]. The Fig. 1.22 b shows the admittance circle diagram. The circle is centered on the real axis on the conductance axis G, and its diameter is the reciprocal of the resonance resistance R_1 in the equivalent circuit:

$$R_1 = 1/G_{max} \qquad \textit{Eq. 1.68}$$

The f_s is attained at the intersection of the circle with the real axis, G, at maximum of conductance ($G_{max.}$). The f^- and f^+ represent the maximum and the minimum of conductance, respectively. The values of theses frequencies can be used to estimate the motional parameters C_1, L_1 and the motional quality factor, Q_m, according to the following equations:

$$C_1 = \frac{1}{2\pi R_1}\left(\frac{f^+ - f^-}{f^+ f^-}\right) \qquad \textit{Eq. 1.69}$$

$$L_1 = \frac{R_1}{2\pi}\left(\frac{1}{f^+ - f^-}\right) \qquad \textit{Eq. 1.70}$$

$$Q_m = \frac{2\pi f_s L_1}{R_1} \qquad \textit{Eq. 1.71}$$

Besides, the static capacity,C_0, can be estimated from the susceptance at frequencies 100 times lower than the resonance frequency:

$$Y(\omega) \approx \sim j\omega C_0 \qquad \textit{Eq. 1.72}$$

Finally, the electromechanical coupling factor can be estimated from:

$$K^2 = C_1/C_0, \qquad \textit{Eq. 1.73}$$

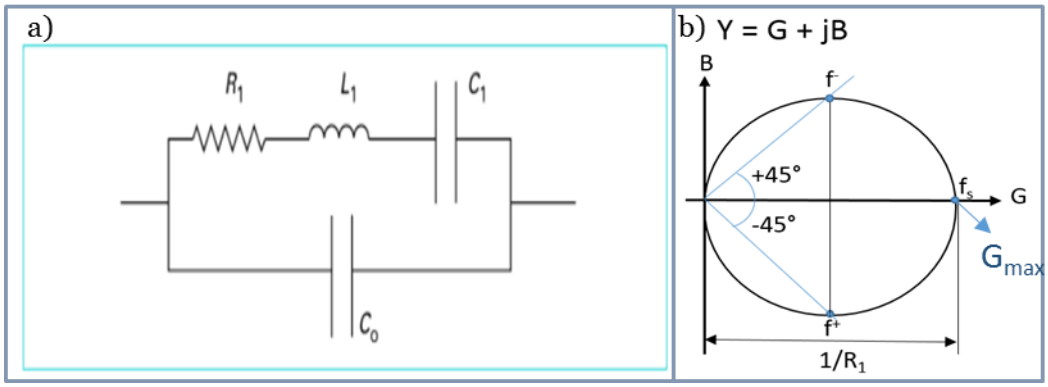

Fig. 1.22 Electrical equivalent circuit Butterworth-Van Dyke of a BAW resonator. Where R_1 is the resistance, C_0 is the static capacitance, C_1 is the motional capacitance and L_1 is the motional inductance [63] (a). Example of the admittance circle diagram (b).

In the case of RF systems it is usual to express the electrical response in terms of the scattering matrix S_{ij} (i,j=1,2). Whereas the propagation of electrical waves creates voltage variations along a transmission line, the power carried by the waves remains constant and

can easily be measured. S parameters measurements take advantage of this fact to characterize the device under test (DUT), getting rid of the influence of the transmission lines (coaxial cables) connecting the elements of the experimental setup. Measurements involve the use of a matched load that does not reflect electrical waves. Then S_{21} represents the transmission coefficient of electrical waves across the DUT, from a source connected to its port 1 to the matched load connected to its port 2. S_{21} is the transmission coefficient the other way around. S_{11} and S_{22} are the reflection coefficients from either port, respectively [62, p. 17]. The modulus of *transfer function* $|S_{12}|$ or $|S_{21}|$ can be defined as:

$$|S_{ij}| = \sqrt{\left[Re|S_{ij}|\right]^2 + [Im|S_{ij}|]^2} \qquad \textit{Eq. 1.74}$$

This function defines the amplitude of the transmitted signal and it can be expressed in terms of decibels, as well:

$$|S_{ij}|\ (dB) = 20log_{10}|S_{ij}| \qquad \textit{Eq. 1.75}$$

The *reflection coefficient*, S_{ij} (where i=j), is defined as the ratio between the amplitude of incident and reflected waves.

The filters can be characterized electrically to extract the mixed-matrix parameters by means of admittance and impedance measurements. Considering the propagation of wave within a periodic grating of electrodes, it is sensitive to the surface conditions. A part of the energy is reflected at the edges of electrodes. When the reflections are in the Bragg condition, the wave is completely reflected and then "stopped" by the electrodes. It occurs at specific frequencies called stop band [76]. The parameters of the mixed-matrix can be estimated from the start and the end of the stop band. The measurement of the resonance frequencies at the start of the stop band (f_{SB}) and at the end of the stop band (f_{EB}) and their associated admittances (Y_{SB}, Y_{EB}) (Fig. 1.25) allows the estimation of the main characteristics of the wave propagation, such as [76]:

- The phase velocity (V);

$$V = (f_{SB} + f_{EB})p \qquad \textit{Eq. 1.76}$$

- The effective conduction coefficient per electrode H;

$$H = -j\frac{Y_{EB}-Y_{SB}}{tan\Delta} \qquad \textit{Eq. 1.77}$$

- The reflection coefficient on a unit obstacle $|\Delta|$;

$$|\Delta| = \pi\frac{f_{EB}-f_{SB}}{f_{EB}+f_{SB}} \qquad \textit{Eq. 1.78}$$

- The mode directivity, γ, which represents the amplitude ratio of the admittance at start and end of the stop-band;

$$\cos(2\gamma) = \frac{Y_{EB}+Y_{SB}}{Y_{EB}-Y_{SB}} \qquad \textit{Eq. 1.79}$$

The single port resonators that compose the filter structure can be individually analyzed by admittance measurements, as well. The conductance and resistance of resonators allow the estimation of f_s and f_p and the electromechanical coupling by using the Eq. 1.63. The quality factor can be estimated from the conductance by using the Eq. 1.65.

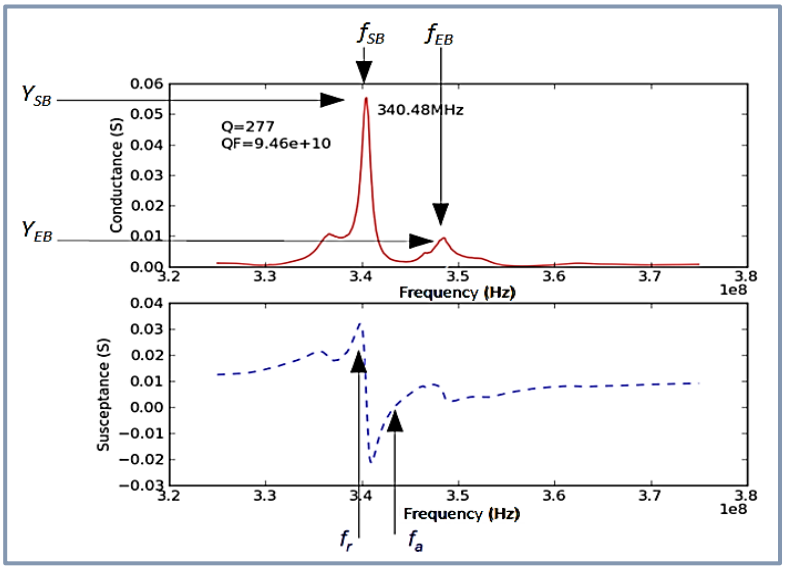

Fig. 1.23 Extraction of parameters from admittance measurement of a SAW single-port resonator, where f_{SB} and f_{EB} are the resonance frequencies at the start and the end of the stop band, respectively, Y_{SB} and Y_{EB} are their corresponding admittances. The identification of resonance and anti-resonance frequencies f_r and f_a in susceptance are represented, as well [76].

1.4.6 BAW and SAW devices configurations

1.4.6.1 Types of BAW devices

The first BAW resonators based on quartz worked at frequency range from 10 KHz to 1 MHz. As the resonant frequency depends on the thickness of the plate, it constitutes a limitation for the design of devices working at higher frequencies [80]. In order to get higher frequencies (100-200 MHz), it is necessary to use thinner plates, which can be obtained by mechanical lapping and ion beam etching of single crystal wafers [81]. The resonators able to work at very high frequencies (VHF, from 30-300 MHz) [82] and at ultra high frequencies (UHF, from 300 MHz ~2.5 GHz)[83] can be obtained by using piezoelectric thin films, such as Cadmium Sulfide (CdS), Aluminium Nitride (AlN), and Zinc Oxide (ZnO), deposited on thick wafers of silicon or sapphire[84]–[86]. There are several different configurations of BAW operating at high frequencies: the Thin Film Acoustic Bulk Acoustic Resonators **(*FBAR*)**, the Solidly Mounted Resonators **(*SMR*)** and the High Overtone Bulk Acoustic Resonator **(*HBAR*)**.

An example of a ***FBAR*** resonator consists in a thin piezoelectric film (e.g. AlN or ZnO) deposited on a thicker substrate having an air cavity, which enables the acoustic insulation (Fig. 1.24 a) [87]. The metallic electrodes are deposited on the piezoelectric thin film, in which a BAW propagates. The advantage of this kind of structures is their ability to operate at higher frequencies than SAW devices (>2.5 GHz). But the main drawback in comparison to SAW technologies is the complexity of the technology because the fabrication of FBAR requires different masks. Other problematic is the brittleness of the piezoelectric film and the higher packaging cost than SAW devices.

In the case of ***SMR***, the structure consists in a high resistive substrate (e.g. Si) and low and high impedance, alternately deposited on the substrate (Fig. 1.24 b) [88]. The layers with different wave velocities, ¼ of wavelength in thickness, generate a reflectance of the BAW whose performance is close to that of a free surface. This technology allows the operation at frequencies from 2 to 8 GHz. Moreover, this kind of resonators has several advantages regarding the FBAR, for example, the fabrication of SMR can be done by using standard procedures used in microelectronics. However, the quality factor and the electromechanical coupling factor of SMR is more challenging because SMR has a reduced acoustic insulation in comparison with FBAR.

Finally, the ***HBAR*** is constituted from a transducer (formed by a piezoelectric thin film and electrodes), which is placed on a thicker substrate with a high acoustic quality factor (Fig. 1.24 c). Acoustic waves are generates by the piezoelectric transducer and they propagate along the whole structure. The substrate acts as a resonant cavity accumulating the most of acoustic energy. This kind of resonator operate at frequencies between 1.5-8 GHz and present very high values of quality factor [89].

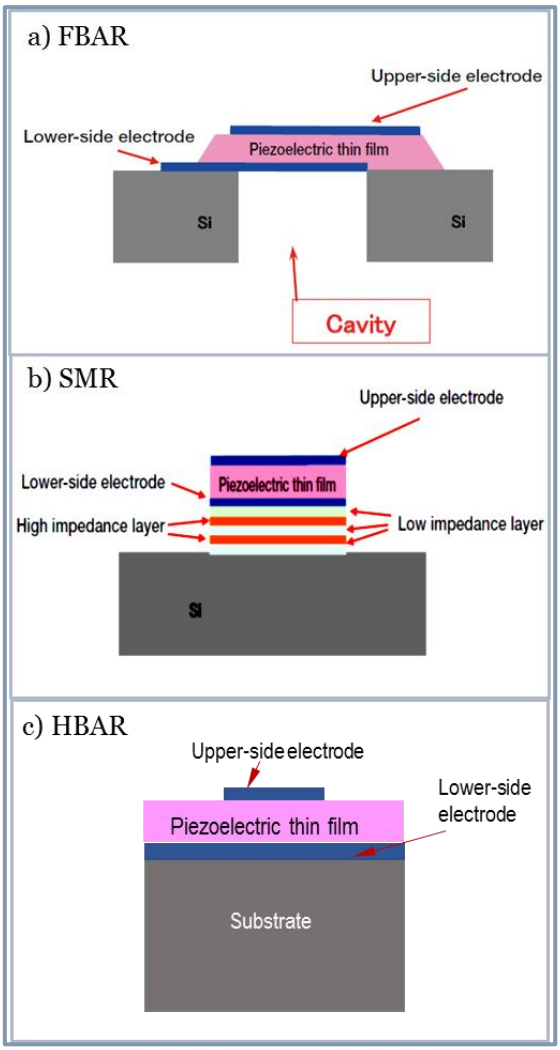

Fig. 1.24 Different type of BAW resonators based on thin films: Thin Film Bulk Acoustic Resonator, FBAR, (a), Solidly Mounted Resonators, SMR, (b) and the High Overtone Bulk Acoustic Resonator, HBAR, (c).

1.4.6.2 SAW device configurations

There is a wide variety of SAW devices: delay lines, resonators, oscillators and filters. In this work we have focused mainly on resonators and filters. The ***SAW resonators*** can be classified in two groups: one port and two ports resonators. The *one-port resonator* is constituted of an IDT and grating reflectors (Fig. 1.25). The reflectors consist of short metal electrodes, which are placed perpendicularly to the SAW propagation direction. Their function is to reflect the SAW coming from both sides of the IDT. The reflection is constructive when the periodicity is equal to a half of the wavelength, and then the resonance appears [62, p. 26]. The *two ports resonator* has two IDTs placed between the grating reflectors, the separation between the gratings can be selected in order to have a resonance at a determined frequency (Fig. 1.25) [72, p. 221]. This configuration can be used as a narrow-band filter. The performance of SAW resonators depends on several parameters such as the disposition of the electrodes and the spacing between the gratings and the IDTs, the

number of IDTs, the thickness of the electrodes and their resistivity, the properties of the piezoelectric substrate (K^2 and static capacitance C_0) and finally the operational frequency [72, p.228].

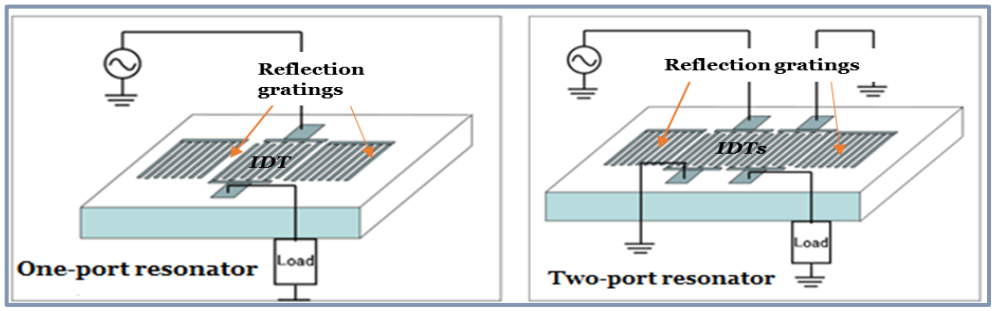

Fig.1.25 Schematic representation of the structure of one-port and two- port SAW resonators [65].

Filters are devices that allow to select a signal from a desired channel, and to reject the other signals without altering the transmitted information. There is a wide variety of ***SAW filters***. In this work we were interested mainly in filters used in telecommunications. An example is the ***Interdigitated Interdigital Transducer (IIDT)*** filter, which is formed by a series of IDTs connecting the electrical input and output of each IDT alternatively. The Fig. 1.26 illustrates the structure of the IDTs of this kind of filters. If the ports are correctly matching, the insertion losses are small in these filters. However, the variations in the matching between the elements could affect the response [90]. To overcome these problems, other types of filters such as *Double Mode SAW filter* or the *ladder-type filters* with structures of connected resonators are used.

The ***Double Mode SAW filter (DMS)*** consists of three IDTs symmetrically placed between two reflectors (see Fig. 1.26 c). This arrangement allows the use of two resonant modes coupled in the longitudinal direction. Hence, the 1st order mode and the 3rd order mode are coupled and form a wide bandwidth [91].

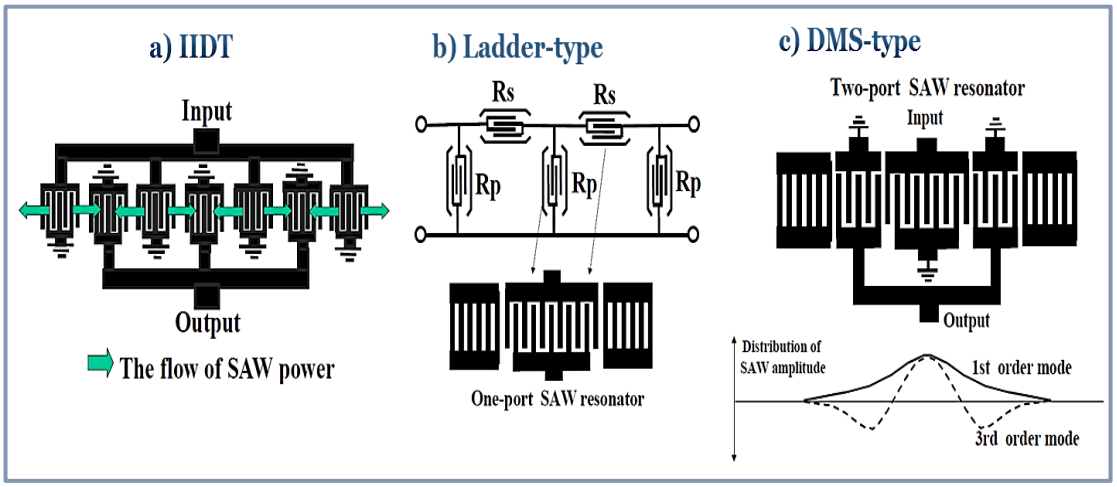

Fig. 1.26 Different types of SAW filters: interdigitated interdigital transducer (IIDT) (a), ladder-type (b) and double mode SAW filter (DMS-type) (c) [91]

The ***ladder-type SAW filter*** is also known as ***impedance element filter (IEF)***. This kind of filter is widely used in mobile phone handsets. Its center frequency is typically around of 1~2 GHz, it can get insertion losses lower than 2 dB. Moreover, the possibility to handle power of 2W is necessary for its operation [92]. These filters are structured from several one-port resonators connected in parallel (R_p) and in series (R_s), as it is shown in the Fig. 1.26 b. The resonance frequency of the series resonator, R_s (f_{rs}), coincides with the anti-resonance frequency of the parallel resonator, R_p (f_{ap}) in the center of the pass-band filter, in order to maximize the transmission level (Fig. 1.27).

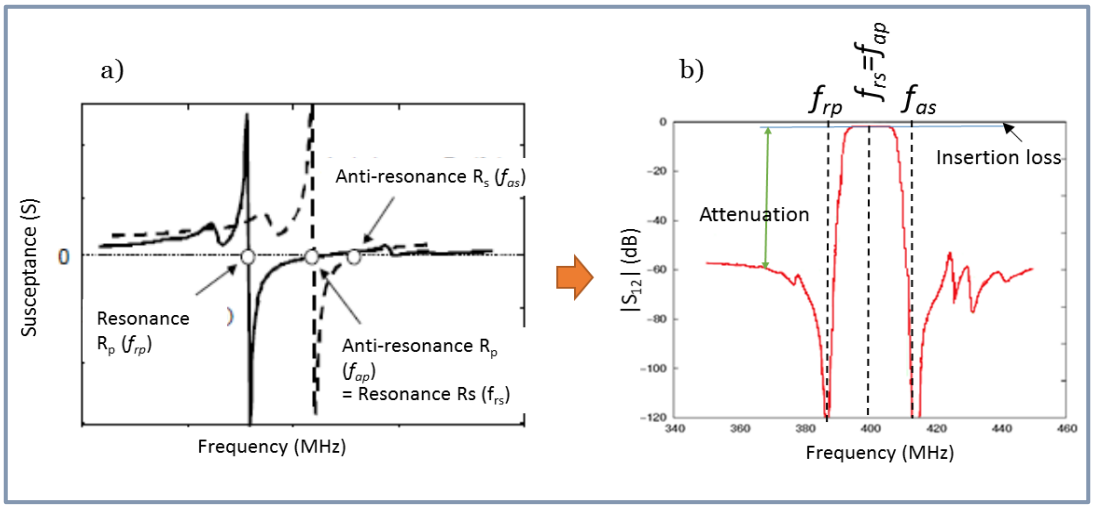

Fig. 1.27 Impedance elements of ladder-type SAW filter, composed of a series resonator (R_s) and parallel resonator (R_p). The resonance frequency of the series resonator, R_s (f_{rs}) is matched to the anti-resonance frequency of the parallel resonator, R_p (f_{ap}) (a). The transfer function S_{12} of the filter showing the resonance, anti-resonance frequencies, attenuation and insertion loss (b).

The performance of the three types of filters is compared in the Table 1.7. The ladder-type filters present the lowest insertion losses, the wide bandwidth and a good power durability. At present, this structure is the most widely used in the RF filters.

Table 1.7 Propagation characteristics of thin film/substrate structure used in SAW devices: V, K^2 and TCF

Thin film	***Structure***	***V (m/s)***	***K^2 (%)***	***TCF (ppm/°C)***
ZnO	ZnO/glass	2600	1.9	-25 [112]
LN	LN/diamond	11900	9.0	-25 [112]
LT	LT/diamond	10600	3.6	-18 [112]
AlN	AlN/sapphire	5675	0.2	-40[107]

1.4.6.3 Requirements for SAW filters performance

Due to the increased usage of radio-frequency spectra, it is necessary to improve the performance of SAW devices. In the case of band-pass filters, it is necessary to get very selective RF-filters. The principal parameters defining the performance of SAW filters are listed below:

- ***Center frequency, f_c.-*** Is the central frequency between the upper and lower cutoff frequencies at a determined level of transmission, typically from -1 dB to -3 dB [This parameter defines the operational frequency of filters [72].

- ***Attenuation level.-*** It defines the out-of band rejection. It should be as large as possible to increase the selectivity of filter [65].
- ***Transition band (Bt).-*** It is defined as the range of frequencies representing the transmission between the band pass at a level of -3 dB and the stop band at -40 dB) [72].
- ***Return loss (RL).-*** It is the loss of power (in decibels) in the reflected signal with respect to the reflected one. The filter should have a small reflection coefficient in the band-pass, thus a high RL (typically from 12 to 15 dB)[72].
- ***Insertion loss (IL).-*** Ideally, the insertion loss should be zero but in practice, there are always some losses coming from the structure of devices, e.g. the losses in reflection and the resistivity of electrodes. In the case of RF filters, it should be small (1-2 dB)[93].
- ***K².-*** The piezoelectric material must have high K^2 because it allows the design of filters with wide bandwidths. For this reason, the Y rotated cuts of LT and LN crystals with K^2~0.7-11.3% are used (see Table 1.6).
- ***TCF.-*** This coefficient should be as close as possible to zero, in order to limit the changes in frequency with temperature during SAW filters operation.
- ***Power durability.-*** It is a property required for devices working at high power density and high frequency [94]. It can be defined by the time to failure (T_F), or in other words, by the life time of the devices. The T_F can be determined by cycling a power (P) and observing the response of filters. The power is applied until the observation of the increase of insertion losses [95]. The T_F can be estimated according to the following equation:

$$T_F = Ae^{\frac{E_a}{kT_d}}P^{\beta} \qquad Eq.\ 1.80$$

Where T_F is the time to fail, E_a is the activation energy, k is the Boltzmann constant ($1.38X10^{-23}$ J/K), T_d is the temperature of the device, P is the input power (mW), A and β are design and material specific constants.

1.4.7 Applications of SAW and BAW devices

SAW devices are widely used in automotive, telecommunications and information systems, as well as in medical, consumer and military industries [96]:

- ***Automotive systems:*** Tire-pressure monitoring, car alarms, keyless entry and car navigation systems.
- ***Information & telecommunications systems*:** filters for TV and mobile telephones, tablet, GPS, duplexers for cellular radio, radars.
- ***Industrial applications**:* ultrasound imaging, patient care monitoring, advanced monitoring infrastructures, fire alarms, radio modules.
- ***Consumer applications***: garage open-door, wireless audio, remote control.

The advantage of the BAW resonators using thin films over resonators based on single crystals is their ability to operate at frequencies above 1.5 GHz. This market of BAW devices became economically important [97]. BAW devices are used mainly in RF filters working at frequencies higher than 2.5 GHz. They are used for fabrication of filters and duplexers, which can be found in space and military applications, in radar and communications systems and

in 3G and 4G smartphones [98]. SAW and BAW technologies are complementary in some range of frequencies (around 2 GHz) [97]. However, when higher frequencies are required, the BAW devices are the best suited (see Fig. 1.29)

Fig. 1.28 Examples of applications of SAW devices [119]

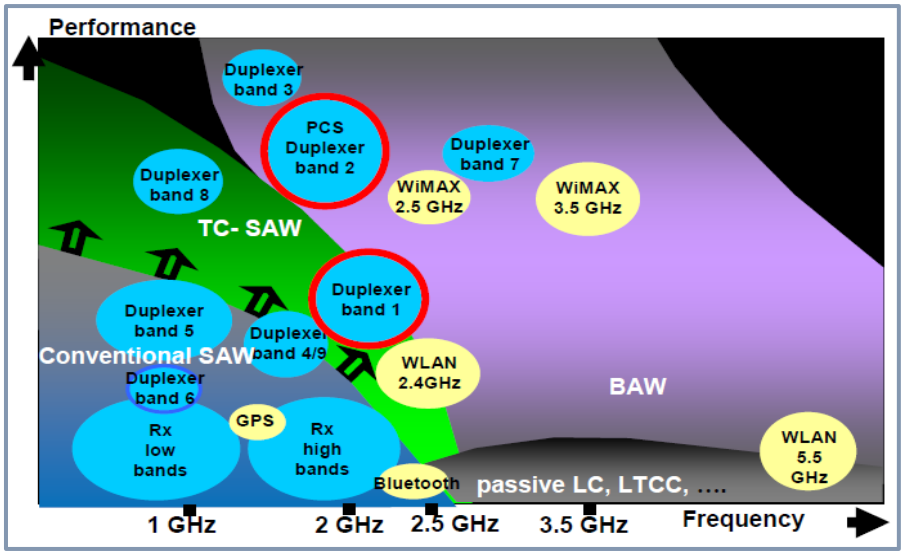

Fig. 1.29 Distribution of frequencies for commercial applications of SAW, temperature compensated SAW (TC-SAW) and BAW devices [97]

1.4.8 Limitations and challenges of SAW devices

The range of frequencies of SAW filters used in mobile phones is from 800 MHz to 2.5 GHz. Nowadays a big part of filters production is based on SAW technology, because its production cost is low and because it allows to embed several filters into one chip. However, SAW filters have some limitations concerning the operational frequency. At frequencies >2 GHz it is more difficult to have an adequate selectivity [99]. On the other hand, there is a technological limitation for the production of filters operating at higher frequencies. Although it has been achieved the fabrication of devices allowing their operation in the 10 GHz range, at this frequency it is necessary to use very fine IDTs (width of ~0.1 μm) [100], which cannot be achieved by using conventional methods of deep UV lithography. This limits

their industrial production. The power durability of SAW devices is limited by the degradation of the electrodes after some time of usage. In the case of devices based on LN and LT crystals, the main problematic is the failure at high power density due to the ferroelectric domain reversal at high power and the diffusion of Li. As it is an important requirement for optimum operation of SAW devices, the problematic and the methods to improve it will be discussed in the next section.

Another limitation of SAW devices is their temperature sensitivity. The piezoelectric substrates mostly used in SAW filters are LT and LN because these materials have a high electromechanical coupling factor (7.6 % for 42 RY-X LT and 5.4% for 128 RY-X LN). However, these materials have an important TCF (-40 and -75 ppm/°C, respectively) as is indicated in the Table 1.6. It means that the response of a SAW filter changes its frequency when the temperature is modified. It constitutes a problem because in some cases the frequency bands for transmission and reception are separated from each other by only 20 MHz, as for example the pass-bands used in Personal Communication Services (PCS) in USA [62]. Thus, systems having low frequency shift with temperature, are desired to ensure the proper functioning of filters. Therefore, different temperature compensation techniques were developed, as will be later presented.

1.4.8.1 Improvement of power handling capability

The power durability defines the life time of SAW devices, which is determined by the optimum operation of all components. It has been reported that one of the problems is the degradation of Al electrodes, which is due to the migration of Al atoms. The Fig.1.30 illustrates the surface and the cross section of deteriorated Al IDTs. The possible solutions to resolve this problem has been investigated. The most common used approach is the change of the composition of the electrode. For example, to dope Al with 2 mol% of Cu [101]. Another solution is the usage of multilayers of metals or their alloys: Al-Cu/Cu/Al-Cu or Al/Mg/Al. Using this technique, the power durability of devices has been ameliorated by 250 times as compared to a device having electrodes of Al-Cu single layers [102]. These improvements allow the correct operation of SAW filters at 1.5-2 GHz.

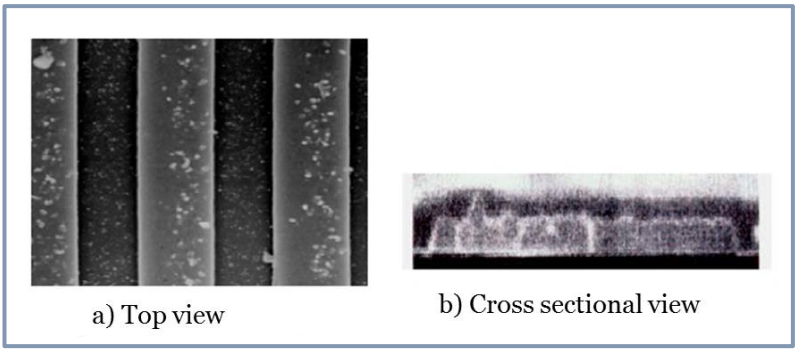

Fig. 1.30 SEM images of surface and cross section of a deteriorated IDT [101]

Other methods are based on the modification of the piezoelectric substrate, by using compound structures including materials with different properties such as thermal conductivity and diffusivity, for example, the application of the bonded LT/sapphire structure. The power handling capability decreases when a high temperature is concentrated in a small volume. Thus, a high capability of heat dissipation is required to improve the power durability. It is known that the sapphire has a higher thermal conductivity than LT.

Thus, it is a good candidate to increase the stability of devices based on LT operating at high power density. It has been shown that mini-duplexers based on the structure LT/sapphire has a longer lifetime under a power of 1W [103].

1.4.8.2 Methods for temperature compensation

Different methods to reduce the TCF of LT and LN have been reported in the literature. They can be principally sorted in three methods: i) deposition of compensation layers, ii) wafer bonding and iii) inversion layer at the surface of the substrate.

1.4.8.2.1 Deposition of compensation layers

This technique has been widely investigated [104]–[111]. The idea is to join two materials having TCF with opposite signs in order to obtain a global TCF close to zero. A layer of SiO_2 (having a positive TCF) is usually deposited on SAW device based on LT or LN as piezoelectric substrate, whose TCF is negative. This technique was first reported by T.Parker [104]. The obtained results showed that the TCF might be improved for Y-Z LT and Y-Z LN single crystals when a layer of SiO_2 is deposited on the IDTs. A TCF of -1.8 pm/°C was obtained by increasing the thickness of the SiO_2 layer (6 μm) and K^2~1.4 %. However, spurious levels were also found while the coupling factor decreases with the thickness of layer. Although the SiO_2 was widely used for the temperature compensation, this material is non-piezoelectric, thus it reduces the K^2. Later, the investigations on the substrates used for filters and duplexers (36 RY-X LT, 42 RY-X LT and 128 RY-X LN) were carried out [107], [111]. For a device formed by SiO_2/Al/36 RY-X LT, an important improvement of the TCF of -15 ppm/°C and an acceptable value of K^2 were found (4-6%).

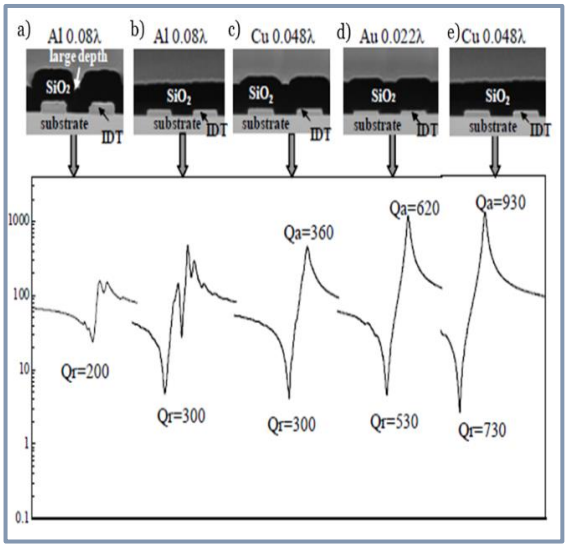

Fig. 1.31 Effect of application of SiO_2 layers and different type of electrodes on the performance of SAW resonators (frequency responses and quality factor) [112]

However, the SiO_2 film causes a deterioration in impedance response, the quality factor diminishes and important insertion losses were found (>30dB) [107]. An example of a device obtained after deposition of a layer of SiO_2 having a thickness of 0.2λ is shown in the Fig. 1.31 a. As can be observed, the frequency characteristics of these devices are degraded due to the presence of convex portions of SiO_2 deposited over the IDTs, which increases the insertion losses. To overcome this problem, an alternative is the flattening of the SiO_2 layer (Fig.1.31 e). By using this technique the TCF of -5 to -10 ppm/°C was obtained [107]. K^2 and insertion losses were improved but the reflection coefficient was reduced by ten times (0.18 to 0.025). Moreover, the K^2 obtained is not high enough for duplexer applications [112]. In order to obtain a device with high reflection coefficient and K^2, a structure having grooved electrodes has been proposed (see Fig. 1.32). This structure offered a TCF of -3 ppm/°C and good frequency characteristics [108]. The temperature compensation of LN crystals has been investigated by using these techniques, as well. The use of the convex SiO_2 layer deposited on the gap positions of the

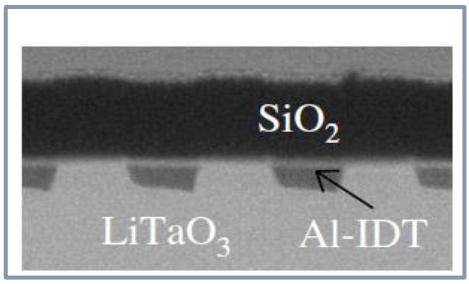

Fig.1.32 Structure of SAW device having the electrodes grooved in the piezoelectric plate [108]

electrodes allows to attain TCF=-10 ppm/°C [111]. Further investigations have been carried out in order to achieve devices with low TCF and without deterioration of other properties. Hence, a SAW duplexer using 39°Y-X LT as a piezoelectric substrate and a compensation layer of SiO_2 has been successfully performed. This device presents all needed characteristics: TCF=-17 ppm/°C and insertion losses<3.0 dB and K^2=5.8 %[113]. However, a method that simplifies the industrial production should be investigated.

On the other hand, piezoelectric thin films of AlN deposited on LN are also used for temperature compensation [131]. Thin films of AlN can be deposited by Chemical Vapor Deposition (CVD) or by sputtering method. The thin film modifies the propagation properties of the SAW based on LN substrate. It has been reported an improvement of the TCF (from -80 to -56 ppm/°C), when a thin film of AlN with thickness of h/λ=0.11 has been deposited [114]. The velocity of the wave has been increased, but the insertion losses were higher.

1.4.8.2.2 Wafer bonding technique.

Another approach used for the temperature compensation is the wafer bonding technique. It consists in a combination of two materials with different thermal properties in the same structure. At least one of the used materials has to be piezoelectric. An example of this type of structure is provided in Fig. 1.33. In such structure, the SAW propagates on the piezoelectric substrate, which may be of LT or LN, which is bonded to a base substrate. The function of the base substrate is to limit the thermal expansion of LT or LN. It must have small coefficient of thermal expansion (CTE) [113]. When the thermal expansion of the piezoelectric substrate is reduced the TCF is also modified. The materials frequently used as a base substrate are glass (fused quartz), silicon (Si), sapphire (Al_2O_3) [114]–[116], and spinel ($MgAl_2O_4$) [117]. The properties of these materials are presented in Table 1.8.

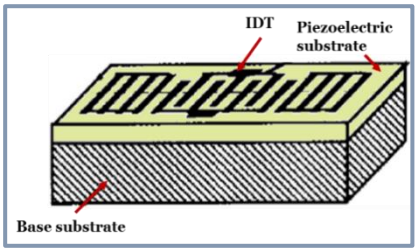

Fig.1.33 Example of a SAW device wafer bonded

Table 1.8 Properties of materials used as a base substrate and properties of LT and LN single crystals. The CTE of LT and LT single crystals is the value in the propagation direction of the wave.

Material	***Cut/propagation direction***	***CTE (ppm/°C)***	***Young's modulus (GPa)***	***Thermal conductivity (W/m/K)***
***Glass* [115]**	-	4.5	66	1
Sapphire [116]	-	5	470	42
Silicon [116]	-	3	160	160
Spinel [117]	-	5.9	280	16.9
LT [116]	36 RY/X-axis	16.1	230	2
LN	Z /X-axis	19.2 [44]	202 [118]	4.18 [118]

The results obtained for temperature compensation of SAW devices based on LN and LT using wafer bonding technique are summarized in Table 1.9. According to these results, the TCF is improved by bonding two materials having different CTE. In the case of LT or LN/glass structure a reduction of the TCF has been obtained keeping almost the same value of electromechanical coupling factor.

It has been shown that the TCF can be further improved when the thickness of the piezoelectric layer decreases. However, this structure has some limitations concerning the thickness of the structure. For example, the thickness of LT piezoelectric layer must be thin because the Young's modulus of the glass is smaller than LT or LN. If a thicker layer of LT is used the glass may exhibit difficulty to resist the thermal stresses, resulting in a bending of the wafer [119]. But the problem is that a thin layer of LT produces spurious responses resulting from bulk waves that reflect at the interface between the two wafers [116]. The structure formed by LT/Si shows an improvement of TCF when the size of the piezoelectric layer is 30µm. In order to have further improvement, it is necessary to thin down the LT layer but it is not possible because below this value the device produce a spurious response [120]. Alternatively, the thickness of the base substrate may be increased to 500µm. Unfortunately, this thickness is not compatible with the size requirements in mobile phone market [112]. Finally, the structure based on LT/sapphire offers an improved TCF without deterioration of other characteristic of SAW propagation. However, the cost of sapphire is elevated compared to the other materials used as substrate and sapphire is extremely hard material, which makes the dicing into discrete devices very challenging.

Table 1.9 Properties of temperature compensated SAW devices by wafer bonding technique

Structure	***Thickness***	***TCF (ppm/°C)***	***K^2 (%)***	***Advantages***	***Drawbacks***
36 RY-X LT	-	-35	6,5	Improvement of TCF without deterioration of K^2, low cost of material	Large total thickness
36 RY-X LT/glass [116]	100µm/300µm	-26			
36 RY-X LT/glass [119]	30µm/500µm	-6	5,8		
64 RY-X LN	-	-80			
64 RY-X LN/glass [121]	0,5λ/300µm	-15			
42 RY-X LT	-	-40		Improvement of TCF	Large total thickness and spurious response
42 RY-X LT/Si [120]	30µm (10λ)/100µm	-31			
	30µm/300µm	-24			
	30µm/500µm	-12			
LT/sapphire [122]	10µm/300µm	-20		Improvement of TCF	Price and hardness of sapphire wafers
	30µm/300µm	-20			
	40µm/300µm	-22			

1.4.8.3.3 Inversion layer for Temperature Compensation

A third method investigated for temperature compensation of SAW devices consists in the use of a layer with reversed direction of polarization [123], [124]. It can be fabricated by the proton exchange of 36 RY-X LT crystals, by using a solution of benzoic acid, followed by a heat treatment at 590°C for 3h. The inverted layer has a polarization with opposite sign to the non-inverted part. Then, the domain boundary acts as an electric-field short circuit that decreases the TCF. When the inversion layer has a thickness of 0.7 µm, the TCF was reduced

to -15 ppm/°C but the K^2 was decreased as well, from 5 to 3.9% [123]. Another proposal was made using a SAW device based on a substrate having regions with different polarization states. The SAW device consists in several resonators forming a ladder-type filter, where at least one of the resonators has a region with opposite polarization to the rest of the matrix. In this case, the TCF was improved by 3-10 ppm/°C [125]. However, the drawback of this technique is the difficulty to control the thickness of the inversion layer, which is not suitable for a regular production.

In summary, we have shown in this last section the methods to improve the power handling and TCF in SAW devices. The most of the techniques used to enhance the stability at high power densities are based in the modification of the composition of electrodes. However, there is no much information about the modification of properties of the substrate itself. On the second hand, the improvement of TCF has been achieved by using the deposition of SiO_2 layers on devices. TCF values as low as -5 or -10 ppm/°C were obtained by using this technique. However, in the most of cases other properties of SAW, especially the coupling factor and the insertion losses, were deteriorated. Moreover, in practice this technique introduce a problem of the control of the deposited SiO_2 thickness [94].

Otherwise, it has been shown that the wafer bonding method allows the improvement of TCF keeping almost the same propagation characteristics of SAW. However, the main drawback of this kind of structure is that the piezoelectric layer and the base substrate have different CTE. Therefore, when the whole structure is submitted to a change in temperature, the piezoelectric layer tends to expand or contract more rapidly than the support substrate, causing deformations and the cracking of the structure. Finally, although the inversion layer method used for temperature compensation shows a reduction of TCF, the coupling coefficient is reduced and the effect on the other characteristics of SAW propagation is not known. Moreover, the control of the thickness of the inversion layer is challenging. All methods presented for temperature compensation have advantages and drawbacks. Thus, innovative methods allowing to ameliorate the stability at high power densities and/or to reduce the TCF, without introduction of additional and numerous technological steps, are demanded by SAW industry.

1.5 Context and objectives of the thesis

As described above, the properties of LT and LN, including the elastic properties, strongly depend on the Li-non stoichiometry. The TCF depends mainly on the temperature dependence of wave velocity and on thermal expansion (according to the Eq. 1.55). It has been shown that thermal expansion along X-axis does not change with Li-non stoichiometry. Moreover, the wave velocity depends on elastic constants as well. Thus, the change in elastic constants by modifying the Li-

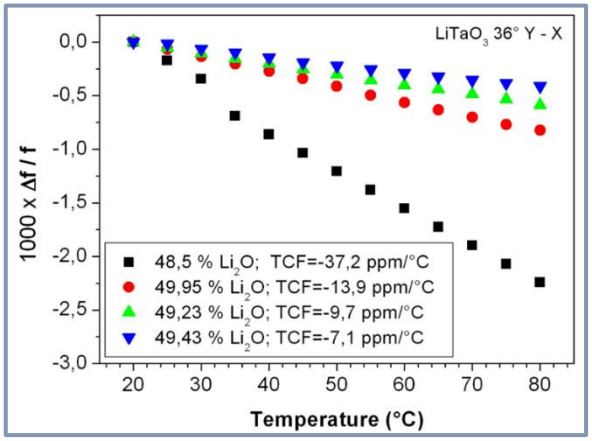

Fig. 1.34 Temperature evolution of frequency of L-SAW on 36 RY-X LT crystals with different Li_2O concentration [29]

composition of LT and LN crystals is expected, which could affect the value of TCF. Recently, it has been shown that the Li-non stoichiometry may have an effect on the TCF of SAW delay line devices based on LT crystals [126]. The composition of 36 RY-X LT was modified by using the Vapor Transport Equilibration (VTE) method. It has been found that the TCF was reduced from -37.2 ppm/°C, for CLT to -7.1 ppm/°C for VTE treated NSLT (49.43 mol % of Li_2O) (Fig. 1.34). However, as the VTE is a high temperature treatment carried out above T_c, the heated LT single crystals were polydomain, which could affect the TCF and the K^2. Thus, it is necessary to decouple the effects of the domains and the Li-non stoichiometry on the properties of SAW devices.

On the second hand, the modification of Li non-stoichiometry induces a shift in Curie temperature and changes in properties that depend on temperature. In the case of congruent crystals, the C_{44} elastic stiffness increases with the increasing of temperature. If we approximate the temperature evolution of C_{44} of congruent crystals to that of sub-congruent and stoichiometric crystals, by taking into account the value of T_c, we obtain a behavior described in the Fig. 1.35. The variation of C_{44} with temperature could be more pronounced in the case of sub-congruent crystals, which could decrease the absolute value of TCF. While more negative values of TCF are expected in the case of stoichiometric samples.

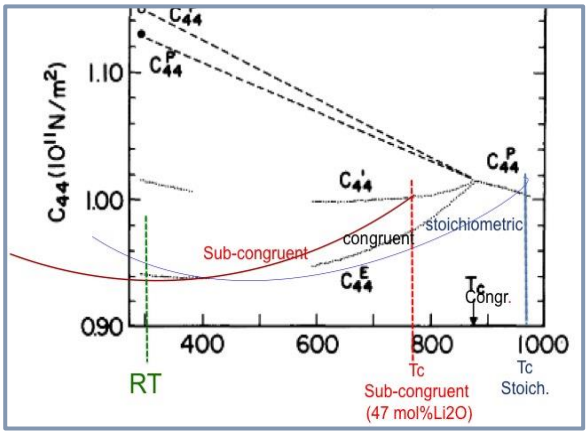

Fig. 1.35 Temperature evolution of C_{44} of CLT crystals and results expected in the case of sub congruent and stoichiometric LT crystals. Modified from Ref. [53].

The aim of this thesis is to investigate the effect of Li-non stoichiometry and ferroelectric domain state on the acoustical performance of acoustic devices based on LT and LN crystals. In the case of LT crystals, it is expected to improve the TCF and the K^2. Furthermore, power handling capability of LN has to be ameliorated. For this purpose, in this work, we will focus in these tasks:

- Optimization of the process for crystal preparation (VTE) and its technological transfer to 4 inches wafers;
- Development of a method by uniform electric field poling of VTE treated crystals with different orientations (42 RY LT, Z-cut LT) and having different Li_2O concentrations (congruent, stoichiometric and sub-congruent).
- In order to determine the effect of Li-non stoichiometry on properties of acoustic devices, BAW and SAW devices, based VTE treated crystals of LT and LN with different Li_2O concentration, will be fabricated and characterized.

1.6 References

[1] Dieulesaint, E and D Royer, *Ondes élastiques dans les solides. Tome 1: Propagation libre et guidée*, vol. 1. Paris: Elsevier Masson, 1999.
[2] G. H. Haertling, "Ferroelectric Ceramics: History and Technology," *J. Am. Ceram. Soc.*, vol. 82, no. 4, pp. 797–818, 1999.
[3] M. Brissaud, *Matériaux piézoélectriques: caractérisation, modélisation et vibration*. PPUR presses polytechniques, 2007.
[4] "IEEE Standard on Piezoelectricity," *ANSIIEEE Std 176-1987*, p. 0_1-, 1988.
[5] A. Palshikar and N. N. Sharma, "Review on Piezoelectric Materials as Thin Films with their Applications," *Mater. Sci. Res. India*, vol. 12, no. 1, Mar. 2015.
[6] I. Turner, "Piezoelectric Materials and Applications," *Materials Classroom.University of Liverpool*. [Online]. Available: http://classroom.materials.ac.uk/casePiez.php.
[7] C. Malgrange, C. Ricolleau, and M. Schlenker, *Symmetry and Physical Properties of Crystals*. Springer, 2014.
[8] V. Gopalan, V. Dierolf, and D. A. Scrymgeour, "Defect–Domain Wall Interactions in Trigonal Ferroelectrics," *Annu. Rev. Mater. Res.*, vol. 37, no. 1, pp. 449–489, 2007.
[9] F. Endres and P. Steinmann, "Molecular static simulations of ferroelectric material hysteresis behaviour," *Proceedings in Applied Mathematics and Mechanics*, pp. 409–410, 2014.
[10] R. J. . Tilley, *Understanding Solids : The Science of Materials*. West Sussex, England: John Wiley & Sons, 2004.
[11] D. Dragan, "Hysteresis in Piezoelectric and Ferroelectric Materials," in *The Science of Hysteresis*, vol. 3, I.Mayergryz and G.Bertotti(Eds;); Elsevier, 2005.
[12] S. C. Abrahams, W. C. Hamilton, and J. M. Reddy, "Ferroelectric lithium niobate. 4. Single crystal neutron diffraction study at 24°C," *J. Phys. Chem. Solids*, vol. 27, no. 6–7, pp. 1013–1018, Jun. 1966.
[13] S. C. Abrahams and J. L. Bernstein, "Ferroelectric lithium tantalate—1. single crystal X-ray diffraction study at 24°C," *J. Phys. Chem. Solids*, vol. 28, no. 9, pp. 1685–1692, Sep. 1967.
[14] M. Marangoni and R. Ramponi, "Nonlinear Optical Waveguides in Stoichiometric Lithium Tantalate," in *Ferroelectric Crystals for Photonic Applications*, D. P. Ferraro, D. S. Grilli, and D. P. D. Natale, Eds. Springer Berlin Heidelberg, 2009, pp. 79–99.
[15] R. S. Weis and T. K. Gaylord, "Lithium niobate: Summary of physical properties and crystal structure," *Appl. Phys. A*, vol. 37, no. 4, pp. 191–203, Aug. 1985.
[16] N. Iyi, K. Kitamura, F. Izumi, J. K. Yamamoto, T. Hayashi, H. Asano, and S. Kimura, "Comparative study of defect structures in lithium niobate with different compositions," *J. Solid State Chem.*, vol. 101, no. 2, pp. 340–352, Dec. 1992.
[17] P. F. Bordui, R. G. Norwood, C. D. Bird, and G. D. Calvert, "Compositional uniformity in growth and poling of large-diameter lithium niobate crystals," *J. Cryst. Growth*, vol. 113, no. 1–2, pp. 61–68, Aug. 1991.
[18] J. R. Carruthers, G. E. Peterson, M. Grasso, and P. M. Bridenbaugh, "Nonstoichiometry and Crystal Growth of Lithium Niobate," *J. Appl. Phys.*, vol. 42, no. 5, pp. 1846–1851, Apr. 1971.
[19] A. A. Ballman, "Growth of Piezoelectric and Ferroelectric Materials by the CzochraIski Technique," *J. Am. Ceram. Soc.*, vol. 48, no. 2, pp. 112–113, Feb. 1965.
[20] K. Nassau and M. E. Lines, "Stacking-Fault Model for Stoichiometry Deviations in LiNbO3 and LiTaO3 and the Effect on the Curie Temperature," *J. Appl. Phys.*, vol. 41, no. 2, pp. 533–537, Feb. 1970.
[21] S. Miyazawa, "Ferroelectric domain inversion in Ti-diffused LiNbO3 optical waveguide," *J. Appl. Phys.*, vol. 50, no. 7, pp. 4599–4603, Jul. 1979.
[22] S. C. Abrahams and P. Marsh, "Defect structure dependence on composition in lithium niobate," *Acta Crystallogr. Sect. B*, vol. 42, no. 1, pp. 61–68, Feb. 1986.
[23] A. P. Wilkinson, A. K. Cheetham, and R. H. Jarman, "The defect structure of congruently melting lithium niobate," *J. Appl. Phys.*, vol. 74, no. 5, pp. 3080–3083, Sep. 1993.
[24] T. Volk and M. Wöhlecke, *Lithium Niobate: Defects, Photorefraction and Ferroelectric Switching*. Springer Science & Business Media, 2008.
[25] R. L. Barns and J. R. Carruthers, "Lithium tantalate single crystal stoichiometry," *J. Appl. Crystallogr.*, vol. 3, no. 5, pp. 395–399, Oct. 1970.

[26]P. F. Bordui, R. G. Norwood, C. D. Bird, and J. T. Carella, "Stoichiometry issues in single-crystal lithium tantalate," *J. Appl. Phys.*, vol. 78, no. 7, pp. 4647–4650, Oct. 1995.
[27]P. F. Bordui, R. G. Norwood, D. H. Jundt, and M. M. Fejer, "Preparation and characterization of off-congruent lithium niobate crystals," *J. Appl. Phys.*, vol. 71, no. 2, pp. 875–879, Jan. 1992.
[28]P. K. Gallagher, H. M. O'Bryan, and C. D. Brandle, "Application of thermal analysis to study the crystal growth, defect structure and thermal expansion of LiNbO3," *Thermochim. Acta*, vol. 133, pp. 1–10, Oct. 1988.
[29]Bartasyte A. and El Mazria O., "Acoustic wave device comprising a lithium niobate and/or lithium tantalate material with an optimised, low-tcf composition, and method for manufacturing said material."
[30]K. Kitamura, S. Takekawa, M. Nakamura, S. Kurimura, and O. Louchev, "Defect density dependence of thermal conductivity and temperature control of quasi-phase matching devices," in *Quantum Electronics and Laser Science Conference, 2005. QELS '05*, 2005, vol. 2, p. 900–903 Vol. 2.
[31] D. P. B. Iii and P. F. Bordui, "Defect-based description of lithium diffusion into lithium niobate," *J. Appl. Phys.*, vol. 76, no. 6, pp. 3422–3428, Sep. 1994.
[32]D. P. Birnie, "Model for the Ferroelectric Transition in Nonstoichiometric Lithium Niobate and Lithium Tantalate," *J. Am. Ceram. Soc.*, vol. 74, no. 5, pp. 988–993, May 1991.
[33]V. Gopalan and M. C. Gupta, "Origin of internal field and visualization of 180° domains in congruent LiTaO3 crystals," *J. Appl. Phys.*, vol. 80, no. 11, pp. 6099–6106, Dec. 1996.
[34]S. Kim, V. Gopalan, K. Kitamura, and Y. Furukawa, "Domain reversal and nonstoichiometry in lithium tantalate," *J. Appl. Phys.*, vol. 90, no. 6, pp. 2949–2963, Sep. 2001.
[35]L. Tian, V. Gopalan, and L. Galambos, "Domain reversal in stoichiometric LiTaO3 prepared by vapor transport equilibration," *Appl. Phys. Lett.*, vol. 85, no. 19, pp. 4445–4447, Nov. 2004.
[36]V. Gopalan, T. E. Mitchell, Y. Furukawa, and K. Kitamura, "The role of nonstoichiometry in 180° domain switching of LiNbO3 crystals," *Appl. Phys. Lett.*, vol. 72, no. 16, pp. 1981–1983, Apr. 1998.
[37]L. Tian, "Nanoscale probing and photonic applications of ferroelectric domain walls," Ph.D.Thesis, Pennsylvania State University, Pennsylvania State, 2006.
[38]K. Kitamura, Y. Furukawa, K. Niwa, V. Gopalan, and T. E. Mitchell, "Crystal growth and low coercive field 180° domain switching characteristics of stoichiometric LiTaO3," *Appl. Phys. Lett.*, vol. 73, no. 21, pp. 3073–3075, Nov. 1998.
[39]I. G. Kim, S. Takekawa, Y. Furukawa, M. Lee, and K. Kitamura, "Growth of LixTa1–xO3 single crystals and their optical properties," *J. Cryst. Growth*, vol. 229, no. 1–4, pp. 243–247, Jul. 2001.
[40] Y. Furukawa, K. Kitamura, E. Suzuki, and K. Niwa, "Stoichiometric LiTaO3 single crystal growth by double crucible Czochralski method using automatic powder supply system," *J. Cryst. Growth*, vol. 197, no. 4, pp. 889–895, Mar. 1999.
[41]V. Gopalan and M. C. Gupta, "Observation of internal field in LiTaO3 single crystals: Its origin and time-temperature dependence," *Appl. Phys. Lett.*, vol. 68, no. 7, pp. 888–890, Feb. 1996.
[42]S. Kim, V. Gopalan, and B. Steiner, "Direct x-ray synchrotron imaging of strains at 180° domain walls in congruent LiNbO3 and LiTaO3 crystals," *Appl. Phys. Lett.*, vol. 77, no. 13, pp. 2051–2053, Sep. 2000.
[43]S. Kim, V. Gopalan, and A. Gruverman, "Coercive fields in ferroelectrics: A case study in lithium niobate and lithium tantalate," *Appl. Phys. Lett.*, vol. 80, no. 15, pp. 2740–2742, Apr. 2002.
[44]A. Bartasyte, V. Plausinaitiene, A. Abrutis, T. Murauskas, P. Boulet, S. Margueron, J. Gleize, S. Robert, V. Kubilius, and Z. Saltyte, "Residual stresses and clamped thermal expansion in LiNbO3 and LiTaO3 thin films," *Appl. Phys. Lett.*, vol. 101, no. 12, p. 122902, Sep. 2012.
[45]S. Yao, J. Wang, H. Liu, X. Hu, H. Zhang, X. Cheng, and Z. Ling, "Growth, optical and thermal properties of near-stoichiometric LiNbO3 single crystal," *J. Alloys Compd.*, vol. 455, no. 1–2, pp. 501–505, May 2008.

[46]Tsymbal E.Y, “Introduction to Solid State Physics. Physics 927.” University of Nebraska-Lincoln, 2015.
[47]M. Sadd, *Elasticity : Theory, Applications, and Numerics*, 2nd ed. Oxford, UK: Elsevier Science, 2009.
[48]R. T. Smith, “Elastic, piezoelectric, and dielectric properties of Lithium Tantalate,” *Appl. Phys. Lett.*, vol. 11, no. 5, pp. 146–148, Sep. 1967.
[49]A. W. Warner, M. Onoe, and G. A. Coquin, “Determination of Elastic and Piezoelectric Constants for Crystals in Class (3m),” *J. Acoust. Soc. Am.*, vol. 42, no. 6, pp. 1223–1231, Dec. 1967.
[50]T. Yamada, N. Niizeki, and H. Toyoda, “Piezoelectric and Elastic Properties of Lithium Niobate Single Crystals,” *Jpn. J. Appl. Phys.*, vol. 6, no. 2, p. 151, Feb. 1967.
[51] G. Kovacs, M. Anhorn, H. E. Engan, G. Visintini, and C. C. W. Ruppel, “Improved material constants for LiNbO3 and LiTaO3,” in *Ultrasonics Symposium, 1990. Proceedings., IEEE 1990*, 1990, pp. 435–438 vols.1.
[52]J. -i. Kushibiki, I. Takanaga, M. Arakawa, and T. Sannomiya, “Accurate measurements of the acoustical physical constants of LiNbO/sub 3/ and LiTaO/sub 3/ single crystals,” *IEEE Trans. Ultrason. Ferroelectr. Freq. Control*, vol. 46, no. 5, pp. 1315–1323, Sep. 1999.
[53]I. Tomeno and S. Matsumura, “Elastic and Dielectric Properties of LiNbO3,” *J. Phys. Soc. Jpn.*, vol. 56, no. 1, pp. 163–177, Jan. 1987.
[54]I. Tomeno and S. Matsumura, “High Temperature Elastic Anomalies in LiTaO3 and LiNbO3,” *Jpn. J. Appl. Phys.*, vol. 24, no. S2, p. 679, Jan. 1985.
[55]I. Tomeno and H. Hirano, “Anomalous Temperature Behavior of the Elastic Constant C11 in LiTaO3,” *J. Phys. Soc. Jpn.*, vol. 50, no. 6, pp. 1809–1810, Jun. 1981.
[56]I. Takanaga and J. Kushibiki, “Elastic constants of multidomain LiTaO3 crystal,” *J. Appl. Phys.*, vol. 86, no. 6, pp. 3342–3346, Sep. 1999.
[57]J. Kushibiki, I. Takanaga, S. Komatsuzaki, and T. Ujiie, “Chemical composition dependences of the acoustical physical constants of LiNbO3 and LiTaO3 single crystals,” *J. Appl. Phys.*, vol. 91, no. 10, pp. 6341–6349, May 2002.
[58]J. Kushibiki, Y. Ohashi, and J. Hirohashi, “Ultrasonic microspectroscopy of congruent LiNbO3 crystals,” *J. Appl. Phys.*, vol. 98, no. 12, p. 123507, Dec. 2005.
[59]Y. Furukawa, K. Kitamura, S. Takekawa, A. Miyamoto, M. Terao, and N. Suda, “Photorefraction in LiNbO3 as a function of [Li]/[Nb] and MgO concentrations,” *Appl. Phys. Lett.*, vol. 77, no. 16, pp. 2494–2496, Oct. 2000.
[60] Y. Furukawa, K. Kitamura, A. Alexandrovski, R. K. Route, M. M. Fejer, and G. Foulon, “Green-induced infrared absorption in MgO doped LiNbO3,” *Appl. Phys. Lett.*, vol. 78, no. 14, pp. 1970–1972, Apr. 2001.
[61]M. Z. M. Jazbinšek, “Reduced space-charge fields in near-stoichiometric LiTaO3 for blue, violet, and near-ultraviolet light beams,” *Appl. Phys. B*, vol. 75, no. 8, pp. 891–894, 2002.
[62]D. Morgan, *Surface Acoustic Wave Filters: With Applications to Electronic Communications and Signal Processing*. Academic Press, 2010.
[63]C. K. Campbell, *Surface Acoustic Wave Devices for Mobile and Wireless Communications*, 1 edition. San Diego: Academic Press, 1989.
[64]H. Engan, K. A. Ingebrigtsen, and A. Tonning, “Elastic Surface Waves in α-quartz: Observation of leaky surface waves,” *Appl. Phys. Lett.*, vol. 10, no. 11, pp. 311–313, Jun. 1967.
[65]Taiyo Yuden Co., “Working Priciples and Applications of SAW/FBAR Devices,” *https://www.yuden.co.jp/productdata/navigator/en/004/E-SP2_101013.pdf*
[66]Abo-el-nour, “Calculation of Bulk Acoustic Wave Propagation Velocities in Trigonal Piezoelectric Smart Materials,” *Appl. Math. Inf. Sci.*, vol. 8, no. 4, pp. 1625–1632, Jul. 2014.
[67]J.-P. Aubry, “Composants piezo-electriques,” in *Techniques de l’ingénieur Matériaux pour l’électronique et dispositifs associés*, vol. TIB271DUO, Ed. Techniques Ingénieur, 1998, p. E 2205.
[68]A. Ballato, E. R. Hatch, M. Mizan, and T. J. Lukaszek, “Lateral Field Equivalent Networks and Piezocoupling Factors of Quartz Plates Driven in Simple Thickness Modes,” *IEEE Trans. Ultrason. Ferroelectr. Freq. Control*, vol. 33, no. 4, pp. 385–393, Jul. 1986.

[69] A. Khan and A. Ballato, "Piezoelectric coupling factor calculations for plates of langatate driven in simple thickness modes by lateral-field-excitation," *IEEE Trans. Ultrason. Ferroelectr. Freq. Control*, vol. 49, no. 7, pp. 922–928, Jul. 2002.
[70] D. F. McCann, J. M. McGann, J. M. Parks, D. J. Frankel, M. P. da Cunha, and J. F. Vetelino, "A lateral-field-excited LiTaO3 high-frequency bulk acoustic wave sensor," *IEEE Trans. Ultrason. Ferroelectr. Freq. Control*, vol. 56, no. 4, pp. 779–787, Apr. 2009.
[71] R. M. White and F. W. Voltmer, "Direct piezoelectric coupling to surface elastic waves", *Appl. Phys. Lett.*, vol. 7, no. 12, pp. 314–316, Dec. 1965.
[72] C. Campbell, *Surface acoustic wave devices and their signal processing applications*. Academic Press, 1989.
[73] "Q factor vs bandwidth in octaves band filter -3 dB pass." [Online]. Available: http://www.sengpielaudio.com/calculator-bandwidth.htm.
[74] M. Y. Dvoesherstov, S. G. Petrov, V. I. Cherednik, and A. P. Chirimanov, "The temperature coefficients of delay of surface acoustic waves in LGS and LGN crystals in a wide temperature range," *Tech. Phys.*, vol. 46, no. 3, pp. 346–347, Mar. 2001.
[75] G. Zhang and W. SHI, "Temperature Characteristics of Surface Acoustic Waves Propagating on La3Ga5SiO4 Substrates," *J. Mater. Sci. Technol.*, p. 63, 2004.
[76] S. Ballandras and W.Steichen, "Composants acoustiques utilisés pour le filtrage Modèles et outils de simulation," *Techniques de l'ingénieur Matériaux pour l'électronique et dispositifs associés*, p. E 2 001-1-32, 10-Nov-2010.
[77] "Piezoelectric Materials: Understanding the Standards," *COMSOL Blog*.
[78] E. Dieulesaint and D. Royer, *Ondes Elastiques dans les solides. Tome 2: Génération, interaction acousto-optique, applications.*, vol. 2. Paris: Elsevier Masson.
[79] H. S. J. -P. Rivera, "Piezoelectric measurements of Ni-I boracite by the techniques of admittance circle motional capacitance," *Ferroelectrics*, vol. 42, pp. 35–46, 1982.
[80] D. M. Pozar, *Microwave Engineering*, 4th Edition. Hoboken, NJ: John Wiley & Sons, 2011.
[81] G. J. Coussot, "Bulk Wave Resonator for the 100-300 MHz Frequency Range," in *1974 Ultrasonics Symposium*, 1974, pp. 590–591.
[82] "IEEE Standard Letter Designations for Radar-Frequency Bands," *IEEE Std 521-2002 Revis. IEEE Std 521-1984*, p. 0_1-3, 2003.
[83] "UHF Band Table." [Online]. Available: http://life.itu.int/radioclub/rr/uhfband.htm.
[84] N. F. Foster, "Ultra-high frequency cadmium-sulphide transducers," *IEEE Trans. Sonics Ultrason.*, vol. 11, no. 2, pp. 63–67, Nov. 1964.
[85] K. M. Lakin and J. S. Wang, "UHF Composite Bulk Wave Resonators," in *1980 Ultrasonics Symposium*, 1980, pp. 834–837.
[86] T. W. Grudkowski, J. F. Black, T. M. Reeder, D. E. Cullen, and R. A. Wagner, "Fundamental Mode VHF/UHF Bulk Acoustic Wave Resonators and Filters on Silicon," in *1980 Ultrasonics Symposium*, 1980, pp. 829–833.
[87] K. M. Lakin, "Thin film resonators and filters," in *1999 IEEE Ultrasonics Symposium, 1999. Proceedings*, 1999, vol. 2, pp. 895–906 vols.2.
[88] K. M. Lakin, G. R. Kline, and K. T. McCarron, "Development of miniature filters for wireless applications," *IEEE Trans. Microw. Theory Tech.*, vol. 43, no. 12, pp. 2933–2939, Dec. 1995.
[89] G. R. Kline, K. M. Lakin, and K. T. McCarron, "Overmoded high Q resonators for microwave oscillators," in *Frequency Control Symposium, 1993. 47th., Proceedings of the 1993 IEEE International*, 1993, pp. 718–721.
[90] C. C. W. Ruppel, W. Ruile, G. Scholl, K. C. Wagner, and O. Manner, "Review of models for low-loss filter design and applications," in *, 1994 IEEE Ultrasonics Symposium, 1994. Proceedings*, 1994, vol. 1, pp. 313–324 vols.1.
[91] Y. Satoh, O. Ikata, T. Miyashita, and H. Ohmori, "RF SAW Filters," in *International Symposium on Acoustic Wave Devices for Future Mobile Communication Systems*, 2001, pp. 125–132.
[92] O. Ikata, T. Miyashita, T. Matsuda, T. Nishihara, and Y. Satoh, "Development of low-loss band-pass filters using SAW resonators for portable telephones," in *Ultrasonics Symposium, 1992. Proceedings., IEEE 1992*, 1992, pp. 111–115 vols.1.

[93]W. Steichen and Ballandras Sylvain, “Composants acoustiques utilisés pour le Filtrage-Revue des différentes technologies,” in *Techniques de l’ingénieur Matériaux pour l’électronique et dispositifs associés*, vol. TIB271DUO, Ed. Techniques Ingénieur, 2008.
[94]Y. Satoh, T. Nishihara, O. Ikata, M. Ueda, and H. Ohomori, “SAW duplexer metallizations for high power durability,” in *, 1998 IEEE Ultrasonics Symposium, 1998. Proceedings*, 1998, vol. 1, pp. 17–26 vols.1.
[95]R. Takayama, H. Nakanishi, and K. Hashimoto, “Impact of composition and structure of Al alloy electrodes to power durability of SAW devices,” in *Ultrasonics Symposium (IUS), 2014 IEEE International*, 2014, pp. 886–892.
[96]“Application Guides | TDK Product Center.” [Online]. Available: http://product.tdk.com/en/applicationguide/index.html.
[97]S. Mahon and !robert Aigner, “Bulk Acoustic Wave Devices-Why, How, and Where They are Going,” presented at the CS MANTECH Conference, Austin, Texas, USA, 2007, pp. 15–18.
[98]“TriQuint - Reach Further, Reach Faster™ - BAW.” [Online]. Available: http://www.triquint.com/about-us/innovation/baw.
[99]W. Phil and N. Layus, “Selecting Filters for Challenging Mobile Applications Worldwide | 2013-11-15 | Microwave Journal,” *Microwave Journal*, Nov-2013. [Online]. Available: http://www.microwavejournal.com/articles/21040-selecting-filters-for-challenging-mobile-applications-worldwide.
[100] K. Yamanouchi, “Generation, propagation, and attenuation of 10 GHz-range SAW in LiNbO3,” in *, 1998 IEEE Ultrasonics Symposium, 1998. Proceedings*, 1998, vol. 1, pp. 57–62 vols.1.
[101] J. I. Latham, W. R. Shreve, N. J. Tolar, and P. B. Ghate, “Improved metallization for surface acoustic wave devices,” *Thin Solid Films*, vol. 64, no. 1, pp. 9–15, Nov. 1979.
[102] R. Takayama, H. Nakanishi, and K. Hashimoto, “Impact of composition and structure of Al alloy electrodes to power durability of SAW devices,” in *Ultrasonics Symposium (IUS), 2014 IEEE International*, 2014, pp. 886–892.
[103] J. Tsutsumi, S. Inoue, Y. Iwamoto, M. Miura, T. Matsuda, Y. Satoh, T. Nishizawa, U. M. Ueda, and O. Ikata, “A miniaturized 3 times; 3-mm SAW antenna duplexer for the US-PCS band with temperature-compensated LiTaO3/sapphire substrate,” in *2004 IEEE Ultrasonics Symposium*, 2004, vol. 2, p. 954–958 Vol.2.
[104] T. E. Parker, M. B. Schulz, and H. Wichansky, “Temperature Stable Materials for SAW Devices,” in *29th Annual Symposium on Frequency Control. 1975*, 1975, pp. 143–149.
[105] T. E. Parker and H. Wichansky, “Material Parameters of the Temperature-Stable Si02/ YZ LiTaO3 Structure,” in *1975 Ultrasonics Symposium*, 1975, pp. 503–507.
[106] F. S. Hickernell, “The SAW properties of sputtered SiO2 on X-112 deg;Y LiTaO3,” in *Frequency Control Symposium and Exhibition, 2000. Proceedings of the 2000 IEEE/EIA International*, 2000, pp. 218–222.
[107] M. Kadota, T. Nakao, N. Taniguchi, E. Takata, M. Mimura, K. Nishiyama, T. Hada, and T. Komura, “SAW substrate for Duplexer with Excellent Temperature Characteristics and Large Reflection Coefficient realized by using Flattened SiO2 Film and Thick Heavy Metal Film,” in *Microwave Symposium Digest, 2006. IEEE MTT-S International*, 2006, pp. 382–385.
[108] T. K. Michio Kadota, “SiO2/Grooved Al Electrode/LiTaO3 and Edge-Reflection Surface Acoustic Wave Structures Having Large Reflection Coefficient, Large Coupling Factor, and Excellent Temperature Characteristic Even If Al Electrodes Are Used,” *Jpn. J. Appl. Phys.*, vol. 45, pp. 4647–4650, 2006.
[109] K. Yamanouch, “High coupling and zero TCF SH-SAW and SH-Boundary SAW using electrodes/Rotated Y-X LiTaO3 and SiO2/electrodes/Rotated Y-X LiTaO3,” in *Ultrasonics Symposium (IUS), 2013 IEEE International*, 2013, pp. 1061–1064.
[110] M. Kadota, T. Nakao, N. Taniguchi, E. Takata, M. Mimura, K. Nishiyama, T. Hada, and T. Komura, “SAW substrate, with coupling factor and excellent temperature stability suitable for duplexer of PCS in US,” in *2004 IEEE Ultrasonics Symposium*, 2004, vol. 3, p. 1970–1975 Vol.3.
[111] Y. Nakai, T. Nakao, K. Nishiyama, and M. Kadota, “Surface acoustic wave duplexer composed of SiO2 film with convex and concave on Cu-electrodes/LiNbO3 structure,” in *IEEE Ultrasonics Symposium, 2008. IUS 2008*, 2008, pp. 1580–1583.

[112] K.-Y. Hashimoto, M. Kadota, T. Nakao, M. Ueda, M. Miura, H. Nakamura, H. Nakanishi, and K. Suzuki, "Recent development of temperature compensated SAW Devices," in *Ultrasonics Symposium (IUS), 2011 IEEE International*, 2011, pp. 79–86.
[113] G. Kovacs, W. Ruile, M. Jakob, U. Rosler, E. Maier, U. Knauer, and H. Zoul, "A SAW duplexer with superior temperature characteristics for US-PCS," in *2004 IEEE Ultrasonics Symposium*, 2004, vol. 2, p. 974–977 Vol.2.
[114] K. S. Kao, C. C. Cheng, Y. C. Chen, and C. H. Chen, "The dispersion properties of surface acoustic wave devices on AlN/LiNbO3 film/substrate structure," *Appl. Surf. Sci.*, vol. 230, no. 1–4, pp. 334–339, May 2004.
[115] K. Onishi, A. Namba, H. Sato, T. Ogura, S. Seki, Y. Taguchi, Y. Tomita, O. Kawasaki, and K. Eda, "A novel temperature compensation method for SAW devices using direct bonding techniques," in *, 1997 IEEE Ultrasonics Symposium, 1997. Proceedings*, 1997, vol. 1, pp. 227–230 vols.1.
[116] M. Miura, T. Matsuda, Y. Satoh, M. Ueda, O. Ikata, Y. Ebata, and H. Takagi, "Temperature compensated LiTaO3/sapphire bonded SAW substrate with low loss and high coupling factor suitable for US-PCS application," in *2004 IEEE Ultrasonics Symposium*, 2004, vol. 2, p. 1322–1325 Vol.2.
[117] K. Geshi, K. Teraoka, S. Kinoshita, M. Nakayama, Y. Imagawa, S. Nakayama, K. Hashimoto, S. Tanaka, K. Totsu, and H. Takagi, "Wafer bonding of polycrystalline spinel with LiNbO3/LiTaO3 for temperature compensation of RF surface acoustic wave devices," in *Ultrasonics Symposium (IUS), 2012 IEEE International*, 2012, pp. 2726–2729.
[118] "Lithium Niobate - Boston Piezo-Optics Inc." [Online]. Available: http://bostonpiezooptics.com/lithium-niobate.
[119] K. Bhattacharjee and Z. Sergei, "Piezoelectric substrate for a saw device," US7408286 B1, 05-Aug-2008.
[120] Y. Hori, H. Kobayashi, K. Tohyama, Y. Iwasaki, and K. Suzuki, "A hybrid substrate for a temperature-compensated surface acoustic wave filter," in *Ultrasonics Symposium (IUS), 2009 IEEE International*, 2009, pp. 2631–2634.
[121] K. Eda, K. Onishi, H. Sato, Y. Taguchi, and M. Tomita, "Direct bonding of piezoelectric materials and its applications," in *2000 IEEE Ultrasonics Symposium*, 2000, vol. 1, pp. 299–309 vols.1.
[122] M. Miura, T. Matsuda, M. Ueda, Y. Satoh, O. Ikata, Y. Ebata, and H. Takagi, "Temperature compensated LiTaO3/sapphire saw substrate for high power applications," in *2005 IEEE Ultrasonics Symposium*, 2005, vol. 1, pp. 573–576.
[123] K. Nakamura and A. Tourlog, "Effect of a ferroelectric inversion layer on the temperature characteristics of SH-Type surface acoustic waves on 36/spl deg/ Y-X LiTaO/sub 3/ substrates," *IEEE Trans. Ultrason. Ferroelectr. Freq. Control*, vol. 41, no. 6, pp. 872–875, Nov. 1994.
[124] A. Tourlog and K. Nakamura, "Influence of proton-exchange conditions on ferroelectric domain inversion caused in LiTaO3 crystals," in *, Proceedings of the Ninth IEEE International Symposium on Applications of Ferroelectrics, 1994.ISAF '94*, 1994, pp. 222–225.
[125] M. Miura, M. Imai, T. Matsuda, M. Ueda, and O. Ikata, "Surface acoustic wave device having a polarization inverted region," US6903630 B2, 07-Jun-2005.
[126] A. Bartasyte, O. Elmazria, M. Gonzalez, L. Bouvot, E. Blampain, and P. Boulet, "Reduction of temperature coefficient of frequency in LiTaO3 single crystals for surface acoustic wave applications," in *Applications of Ferroelectrics held jointly with 2012 European Conference on the Applications of Polar Dielectrics and 2012 International Symp Piezoresponse Force Microscopy and Nanoscale Phenomena in Polar Materials (ISAF/ECAPD/PFM), 2012 Intl Symp*, 2012, pp. 1–3.

Chapter 2

Controlled modification of Li concentration within $LiTaO_3$ & $LiNbO_3$ single crystals

2.1 Introduction

It has been mentionned previously that many physical and structural properties of LT and LN single crystals depend on Li non-stoichiometry. Even though these crystals are commercialised mainly with a congruent composition, many works have been carried out in order to produce crystals with other compositions, principally stoichiometric, due to its advantages with respect to the congruent one, as has been previously shown. The *Czochralski method (CZ)* is widely used for production of congruent crystals (CLN and CLT)[1]. In this method, the crystal is grown from a melt, the crystal and melt are rotated in opposite directions to aid homogeneity of the melt and to prevent thermal gradients at the crystal-melt interface. After growth, the boule is cooled down, keeping the same crystalline structure as used seed [2]. The Fig. 2.1-a shows the apparatus used for the growth of crystals by Czochralski method with application of an electric field.

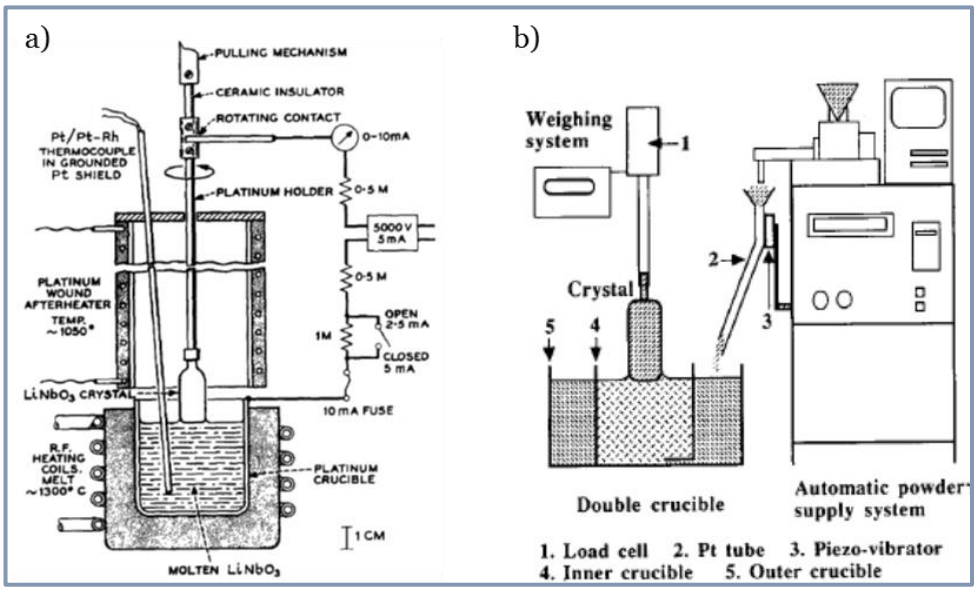

Fig. 2.1 Apparatus for growth of LN crystals: Czochralski (a) and double crucible Czochralski methods [2], [6]

Although its known that is difficult to produce non-congruent crystals by the CZ method, due to segregation problems during the growth, some works have been published about the fabrication of Nearly Stoichiometric crystals of LT (NSLT) and LN (NSLN) by this

method [3]–[5]. NSLT and NSLN crystals were grown by using starting melts of 58 and 60.8 mol% Li_2O. The concentration in the crystal obtained by using these melts were 49.75 and 49.97 %mol Li_2O, respectively [3]. An advantage of this technique is the possibility to produce crystals with different concentration, in function of the composition of the melt. However, this method has various drawbacks. For example, thermal gradients, usually present in the system growth, generate problems of twining, cracking and inclusions in the crystal. Moreover, during the growth process there is a volatilization of Li_2O from the melt surface, yielding compositional gradients along of the volume of crystal [4]. For this reason, only small crystals can be produced: 30-50 mm of diameter and 15-60 mm of length.

In order to find alternative methods that allow the production of non-congruent crystals of high quality, several techniques have been developped. One of the most used techniques for production of NSLN and NSLT crystals is the *double-crucible Czochralski method (DCCZ)* [6]. The crystal is pulled from a melt growth Li-rich (58-60%mol of Li_2O) contained in the inner crucible, surrounded by an external crucible containing a stoichiometric melt. Stoichiometric powder is automatically supplied to the external crucible, which continuously feeds the first crucible (Fig. 2.1-b). In this way, the melt in the inner crucible keeps its stoichiometric composition and has a constant surface level. This technique Oovercomes the problem of composition homogeneity, present in the CZ method. By using DCCZ technique, the Li_2O content in crystals was 49.6-49.9 %mol, obtained with melt of 58 and 60 mol% of Li_2O, respectively. Similarly, NSLT crystals were produced from a melt of 58-59 %mol of Li_2O and crystals with composition of 49.77 and 49.92 were obtained [7]. However, by this method it is possible to produce only NSLT and NSLN crystals, but not completely stoichiometric ones. Most recently, the method was improved to produce crystals of 100 mm of diameter and 125 mm of length. Homogenous, free of crack and twins crystals were obtained by using a correct control of temperature and the material flow rates [8]. However, the size of crystals is limited to 100 mm of diameter and 125 mm of length.

Another technique is the *top-seeded solution growth (TSSG)* with *K_2O quasi-flux* ; in this technique SLN crystals are grown by a method similar to Czochralski, but a K_2O flux is added in a different molar ratio K_2O/LN (0.09-0.21) into the an starting melt of Li/Nb=1 ratio [9], [10]. An advantage of this method, compared to the DCCZ, is that the composition of crystals is closer to stoichiometric (~50%mol of Li_2O) [11][12]. However, in some systems growth the main problem is the formation of twins, cracks and inclusions due to thermal gradients [13].

Another method used is *Vapor Transport Equilibration (VTE)*. The VTE treatment is an after growth treatment, realized at high temperature (usually ≥1100°C), which is used to produce crystals with a desired Li_2O content from the commercially available, congruent crystals (CLT or CLN) [14], [15]. The main advantage of this method is the possibility to prepare crystals with different stoichiometry, from sub-congruent (sub CLN, <48.38 mol% or sub CLT, <48.5 mol%) to stoichiometric composition (50%mol) [16], [17]. It was reported that crystals of SLN, prepared by VTE, have a closer to stoichiometric composition than crystals obtained by DCCZ method. According to high resolution X-ray diffraction characterization, SLN VTE treated crystals have better structural quality than crystals prepared by DDCZ and TSSG techniques [18]. However, this method requires long times to complete the diffusion process. For this reason, only thin crystals can be treated, the

thickness of plates is usually <1mm and up to 3mm [19]. Another problem is the production of poly-domain crystals because VTE treatment takes place at temperatures higher than T_c of LT crystals, thus it is necessary to perform the domain reversal after growth. Moreover, after treatment, thin wafers (thickness of 250 µm) and diameter of 4 inches, show an important deformation of its shape (bowing).

Each method has advantages and drawbacks, summarized in the Table 2.1. For example, the main drawback of CZ and TSSG is the problem of cracking and twinning due to thermal gradients present in the system growth, and compositional inhomogeneity. DCCZ produces crystals of high quality but requires a very precise control of parameters during the growth and it is only possible to obtain nearly stoichiometric crystals. VTE may provide stoichiometric, homogenous, free of crack, and twins crystals. However it is appropriated only for wafer thickness <3mm, but the wafers suffer deformation during the treatment.

In this work, we used the VTE technique because, compared to the other methods, it is relatively easy to control the parameters required to produce crystals. Furthermore, VTE treatment provides homogenous and uncracked crystals and various crystals with different stoichiometry can be prepared simultaneously. For this reason, we will focus on this method. Its principles and a literature review will be presented in the next section.

Table 2. 1 Summary of features of several methods used for preparation of stoichiometric crystals of LT and LN (SLT and SLN)

Technique	Li_2O (mol%)	Advantage	Drawback
CZ **[3]–[5]**	49.75-49.97	Production of crystals with different concentration in function of melt composition.	Difficulty to produce stoichiometric crystals with homogenous composition and with high quality. Problems of cracking , twining and inclusions
DCCZ **[6]–[8]**	49.6-49.9	Crystal homogenous and control of stoichiometry. Temperature gradients smaller than those in CZ method.	Requires a precise control of temperature and material feed rates. Production of not fully stoichiometric crystals. The crystal size is limited to 100 mm of diameter and 125 mm of length
TSSG with K_2O quasi-flux **[10], [11], [20]**	50	Crystals with stoichiometric composition	Problem to control the concentration in crystal precisely. Incorporation of K cations to the crystal Mechanical twins, cracks and inclusions.
VTE **[14]–[17]**	50	Obtaining of homogenous crystals with controlled Li-content, free of cracks and twins.	Only appropriated for thin samples, thickness up to 3 mm. Poly-domain crystals after VTE, a re-poling is required. Warping or bowing of wafers.

2.1.1 Vapour Transport Equilibration method

In VTE treatment, congruent crystals are placed in proximity of equilibration powders of specific composition. The Fig. 2.2 shows an example of experimental set up used in VTE [21]. The treated crystal is held by a platinum (Pt) wire, in order to avoid the contact with the equilibration powder, contained in a crucible. Then the crucible is sealed by using a lid. Powders are formed by pre-reacting mixtures of Li_2CO_3 and Nb_2O_5 or Ta_2O_5. The weight of

equilibration powders exceeds considerably that of the crystal. The crucible is heated at high temperature, usually below the melting point of crystals, during a determined time. During the treatment, the composition of crystal is modified due to an exchange of Li_2O between crystal and powder by vapor transport. The exchange takes place until the chemical potential of crystal reaches that of the powder, namely when the equilibrium is reached [15], [16].

In order to obtain LN or LT crystals with different Li_2O concentration, the composition of equilibration powders used for VTE processing have to be adapted. Li_2O concentration is defined by the mole fraction of Li_2O, X_{Li2O}, according to the following equation:

$$X_{Li_2O}(mol\%) = \left[100 - X_{Nb(Ta)_2O_5}\right] \qquad \textit{Eq. 2. 1}$$

Different types of equilibration powder can be used:

a) Single phase powder: ($Li_{1-x}Nb(Ta)_{1+x}O_{3+2x}$), where $46.5 \leq X_{Li2O} \leq 50$ mol%
b) Li-rich powders, composed of two phases: [$LiNb(Ta)O_3$ + $Li_3Nb(Ta)O_4$], where $75 > X_{Li2O} > 50$ mol %
c) Li-poor powder, composed of two phases [$Li_{0.93}Nb(Ta)_{1.07}O_{3.14}$ +$LiNb(Ta)_3O_8$], where $25 < X_{Li2O} < 46.5$ mol %

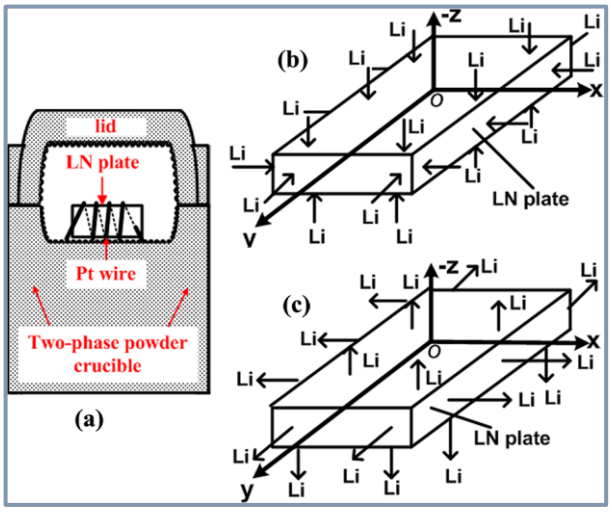

Fig. 2.2 Schematic representation of experimental set-up used for VTE process (a); representation of Li diffusion in Li-rich (b) and Li-poor (c)VTE [21]

In the case of single phase powder and Li-rich powders, during the heating of the system at high temperature, the $LiNb(Ta)O_3$ and $Li_3Nb(Ta)O_4$ phases deliver Li_2O vapor to the crystal, respectively. The Li diffuses into crystal and consequently, the concentration of Li_2O is increased (Fig. 2.2-b). The Li-rich powders provides an infinite source of Li_2O [21]. As explained in the Chapter 1, according to the Li vacancy model, the CLN or CLT crystals have Li deficiency. The VTE process is based on a process of diffusion of Li ions and subsequent migration of Nb^{+5} or Ta^{+5} ions. The Li ions diffuse into the crystal and the Li vacancies are filled. Thus, the number of vacancy defects is reduced in stoichiometric crystals, and consequently the structural and physical properties are changed. In the case of Li-poor powder (25 mol%$< X_{Li2O} <$46.5 mol%), the Li_2O out-diffuses from the crystal to the powders (Fig. 2.2-c) at elevated temperature, which results in a loss of Li_2O content in the crystal. In both cases, the diffusion process self-terminates when thermodynamic equilibrium is reached between powders and crystals. Thus, at this stage, the mass transport of Li_2O is stopped and formation of a secondary phases in crystals ($Li_3Nb(Ta)O_4$ or $LiNb(Ta)_3O_8$) is not expected.

In order to obtain homogenous crystals with defined concentration, the temperature and duration of VTE should be adjusted [14]. Moreover, the concentration of equilibration powders, crystallographic cut and thickness of treated crystal have an important influence on

the concentration and homogeneity of crystals. For this reason, the investigations were performed on the control of these parameters, as will be discussed in next sections.

2.1.1.1 Duration of VTE treatment

The VTE is a dynamic process, the composition of crystals varies with duration of treatment. Bordui et al. [16] treated Z-cut LN crystals with thickness of 0.5-2 mm. In order to obtain SLN crystals and sub-CLN with Li_2O concentrations near of the boundary phase (50 mol% and 46.5 mol%), they used equilibration powders with 65 mol% of Li_2O and 40 mol% of Li_2O for the lithium-rich and the lithium-poor two-phase mixtures, respectively, The processing temperature was 1100°C and the duration was adapted to the crystal thickness. In the case of crystals with thickness of 0.5 mm, it was found that the required times to produce stoichiometric and subcongruent crystals are 60 h and 400 h, respectively.

The effect of VTE duration on the composition of treated X-cut, Y-cut and Z-cut LN crystals with thickness of 1 mm was reported [22]. Crystals were treated at 1100°C with equilibration powder with 70 and 30 mol% of Li_2O. The used treatment times were tested from 0.5 to 250 h and it was found that samples processed in Li-rich equilibration powders for a short time (0.5-9h) exhibit severe cracking and structural disorder. Thus, in order improve the structural quality of crystals, at least 150h are required. Later, it has been demonstrated that in the case of Li-rich VTE, the Li_2O content ($\%Li_2O$) on surface of treated X-cut LN and Z-cut LN single crystals increase with VTE duration (t) as a square root function (Eqs. 2.2 and 2.3). This relationship depends on the crystal cut [23].

$$\%Li_2O = 0.28t^{0.56} \quad For\ X\text{-}cut\ LN \qquad Eq.\ 2.2$$

$$\%Li_2O = 0.35t^{0.53} \quad For\ Z\text{-}cut\ LN \qquad Eq.\ 2.\ 3$$

It was found that VTE treatment of 20 h and 16 h yields stoichiometric X-cut and Z-cut LN crystals. However, the concentration on the surface was indirectly determined by birefringence methods. Later, the concentration on cross section of Z-cut LN crystals treated in similar conditions during 12 h has shown is the existence of a concentration gradient within the crystal (Fig. 2.3-a) [21], therefore, VTE treatments realized during short times provides crystals with inhomogeneous distribution of Li_2O within the crystals.

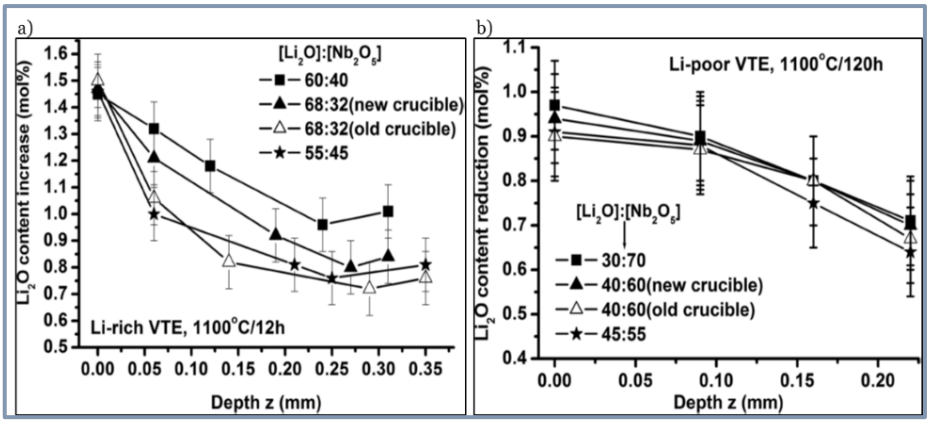

Fig. 2. 3 Depth profile of Z-cut LN crystals with thickness of 0.5mm after VTE treatment: at 1100°C for 12h, using Li-rich powders (a); treated at 1100°C, for 120h, using Li-poor powders (b) [21]

Concerning the Li-poor VTE, the Li_2O content decreases with the increase of VTE duration, and a minimum of 323-400 h are needed to reach the Li-poor phase boundary

(46.5 mol%) at 1100°C [24]. Furthermore, it was observed that the distribution of Li_2O within the crystals treated for 120 h was not homogenous (Fig. 2.3-b).

On the other hand, investigations in VTE treatments of Z-cut LT crystals, showed that higher Li_2O concentration in the crystals can be achieved by treating for a long time at the same temperature (1200°C) and using the same composition of equilibration powders (X_{Li2O}=50 mol%). The average concentration in surface, estimated from the T_c of NSLT crystals increases slightly from 49.06 mol% to 49.11 mol% as the VTE duration was increased from 146 to 213 h [25]. Thus, a complete study about the effect of time in the concentration and homogeneity of LT crystals is lacking. To summarize, although the effect of the VTE duration on crystal composition was studied in literature, usually only average or surface Li_2O concentration were given and it remains unclear if the treated crystals were homogenous or presented gradients.

2.1.1.2 VTE treatment temperature

The VTE temperature dependence of the average Li_2O concentration of treated crystal was investigated for X-cut LN and Z-cut LN crystals [26]. VTE was carried out for 7 h at different temperatures by using Li-rich powders (X_{Li2O}=68 mol %). It was found that the Li_2O concentration increases with temperature, according to the Arrhenius law:

$$\overline{\Delta Li_2O} = \Delta C_0 exp\left(-\frac{E_a}{kT}\right), \qquad \textit{Eq. 2. 4}$$

where $\overline{\Delta Li_2O}$ is the increment of Li_2O concentration within the crystal with respect to the initial congruent composition, ΔC_0 is the Li_2O content alteration constant, E_a is the activation energy, T is temperature and k is the Boltzmann constant. It was found that X-cut LN plates exhibited a larger ΔC_0 and Li diffusion needed a higher activation energy than that of the Z-cut LN crystal. After VTE treatment at 1130°C, the average Li_2O concentration on surface of NSLN crystal was 49.71±0.1 mol % and 49.73±0.1 mol %, for X-cut and Z-cut LN, respectively. In the case of Li-poor VTE, the Li_2O concentration in crystals decreases with increase of VTE temperature. Moreover, the values of E_a is higher in sub CLN than in SLN crystals, being 2.2±0.2 eV and 0.53±0.03 eV, respectively [27]. It explains also the fact that the Li-poor VTE process requires longer times than Li-rich VTE.

2.1.1.3 Composition of equilibration powders

The effect of the composition of equilibration powders, the volume of crucible occupied by equilibration powders and the possibility to use the powders were investigated in literature, as well. Z-cut LN crystals were treated by using Li-rich powders (X_{Li2O}=68, 60 and 55 mol %). It has been reported that in the case of Li-rich VTE, the Li_2O concentration on surface of crystal increases with the increased Li_2O content in powders. Treated crystal composition also depends on the volume occupied by the powders in the crucible. Thereby, the fuller crucible yields crystals with higher Li_2O content [21]. Moreover, it has been demonstrated that the powders used several times produce less Li concentrated crystals. Furthermore, VTE treatment for 120h, by using Li-poor powders with various concentrations (30, 40 and 45 mol %), provides crystals with similar lithium content. Thus, in this case, these three factors have less effect on the Li content of crystals. The out-diffusion of the Li_2O is related to the time and temperature parameters. As was discussed above, the Li_2O out-diffusion from congruent crystals is a much longer process than in-diffusion.

The diffusivity depends on Li content. Hence, it has been shown that the diffusivity of lithium in LN increase from $3x10^{-9}$ cm^2/s to $50x10^{-9}$ cm^2/s, for congruent (CLN) and nearly stoichiometric crystals (NSLN), respectively [28]. Similarly, in the case of sub-CLN crystals, the diffusivity drops by one order of magnitude as the Li_2O content diminishes by 1 mol% [29]. This can be explained by the ambipolar (Li^+ and Nb^{5+}) diffusion model. It proposes that diffusion process involves the motion of point defects (vacancies and/or interstitials). It was observed that the interdiffusion coefficient increases as the amount of vacancies diminishes [30]. Thus, the decreased Li non-stoichiometry in the crystals reduces the amount of Li vacancies. Thus, larger lithium diffusivity (faster diffusion) in stoichiometric samples is expected. It explains why longer duration is required for VTE of sub-congruent crystals.

2.1.1.4 Effect of thickness and crystallographic orientation

The thickness and crystallographic cut affects the distribution of the Li concentration in the crystal, as well. VTE treated Z- cut LN crystals with different thicknesses (1.3-3.1 mm) were studied [19]. It was found that the homogenous composition can be achieved faster in thinner samples. Concerning the effect of crystal orientation, it has been reported that Z-cut LN crystals have slightly higher diffusivity than X-cut LN crystals [23], [29]. The anisotropy of Li_2O diffusion was demonstrated by modeling of VTE treatments as well [31]. The Fig. 2.4 shows the concentration depth profiles obtained by simulation of VTE process with different for Z-cut and X-cut LN crystals with different thicknesses. It can be observed that in all cases short treatments produce crystals with a gradient of concentration. Moreover, the time required to obtain homogeneous crystals is longer for the X-cut LN crystals, because it has lower diffusivity. Besides, the higher thickness of crystal requires longer time for Li diffusion to the crystal depth. It was estimated a roughly quadratic relationship between the thickness and the time necessary to obtain homogenous stoichiometric concentration.

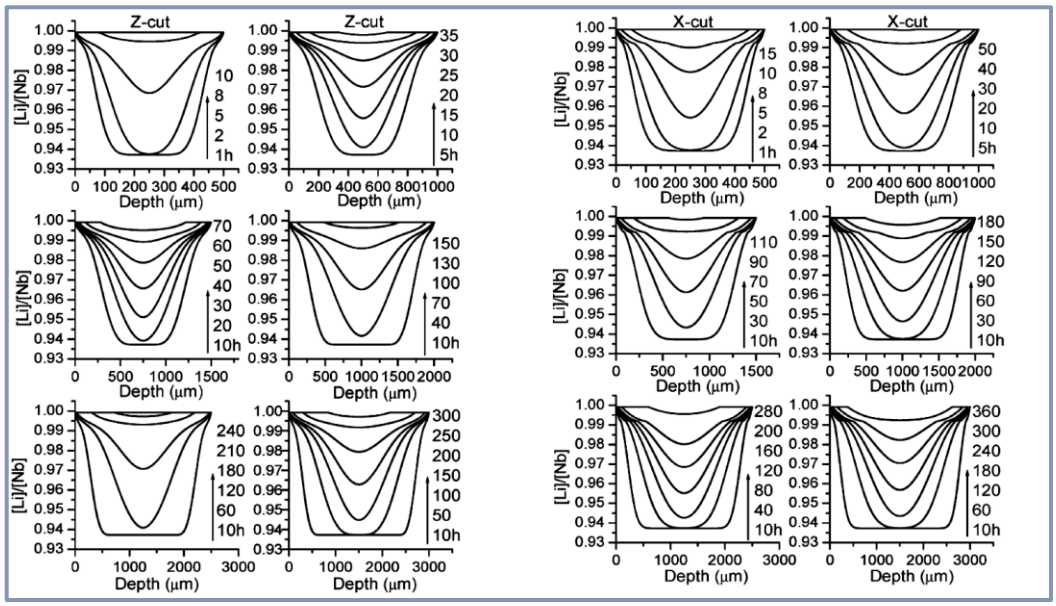

Fig. 2.4 Simulated depth profiles of Li concentration in Z and X-cut LN crystals with thicknesses from 0.5 to 3 mm, treated for different VTE durations [30]

In summary, the parameters involved in VTE treatment of LN have been widely explored. It has been demonstrated that the temperature, time and composition of equilibration powders are the parameters that have a major influence on the composition of

treated crystals. The duration of VTE has to be adapted according to the thickness, composition of equilibration powders and the crystal cut. In general, thicker crystals and sub-congruent composition need longer treatment times. Besides, diffusion process is anisotropic and the Li diffusivity increases with Li_2O concentration in crystals.

However, the most of the literature reports concerns VTE treatment of LN crystals. In the case of LT crystals, knowledge about VTE conditions is not exhaustive. Even though LN and LT are similar materials, the same VTE conditions cannot be applied. For example, the LT crystals can be treated at higher temperatures because its melting point is much higher than that of LN crystals. Furthermore a wider experimental investigation about the homogeneity of crystals, treated by VTE is needed. For this reason, in this work we focused on the optimization of VTE parameters for LT crystals. For this purpose, different series of experiments were done, which will be detailed in the section 2.2.

2.2 Experimental techniques

2.2.1 Synthesis of equilibration powders

The first step to perform the VTE treatment consists in the preparation of equilibration powders. Single phase ($LiTaO_3$) and two-phase powders [$Li_{0.93}Ta_{1.07}O_{3.14}$ + $LiTa_3O_8$ (Li-poor powders)] or $LiTaO_3$ + Li_3TaO_4 (Li-rich powders)] were prepared using Li_2CO_3 (99.9% of purity) and Ta_2O_5 (99.9% of purity) as starting chemicals, which were supplied by Alfa Aesar. The Li_2CO_3 was dried for 24h at 250°C in order to eliminate the moisture. Powders with different mole fraction of Li_2O (X_{Li2O}) were prepared: Li-poor powders (X_{Li2O} = 25 and 40 mol%), Li-rich powders (X_{Li2O} = 51, 52, 53, 54 and 60 mol%) and single phase powders (X_{Li2O} =50 mol%). Powders of Li_2CO_3 and Ta_2O_5 were mixed and milled in acetone during 24h by using a rotator shaker Heidolph. After that, the powders were pelletized by using a desktop powder presser model YLJ-24T, provided by MTI Co. Then, the pellets were sintered for 70h at 1000°C. The solid phase reactions involved in this sintering step are:

- ***For Li-poor two-phase powders with 40 mol% of Li_2O:***

$$0.4\ Li_2CO_3 + 0.6\ Ta_2O_5 => 0.4\ CO_2\uparrow + 0.7\ Li_{0.93}Ta_{1.07}O_{3.14} + 0.15\ LiTa_3O_8 \qquad \text{Eq. 2.5}$$

- ***For Li single-phase powders with 50 mol% of Li_2O:***

$$0.5\ Li_2CO_3 + 0.5\ Ta_2O_5 => 0.5\ CO_2\uparrow + LiTaO_3 \qquad \text{Eq. 2.6}$$

- ***For Li-rich two-phase powder with 60 mol% of Li_2O:***

$$0.6\ Li_2CO_3 + 0.4\ Ta_2O_5 => 0.6\ CO_2\uparrow + 0.6\ LiTaO_3 + 0.2\ Li_3TaO_4 \qquad \text{Eq. 2.7}$$

2.2.2 Experimental set up for VTE processing

After preparation of powders, single crystals were treated in a Li-rich/Li-poor atmosphere created by the equilibration powder. For this purpose, the crystals are placed on a small crucible of Al_2O_3, located in proximity of equilibration powders, which are contained in an external crucible. Then, the external crucible is sealed by a lid and the whole set up is

heated in a furnace. By this way, the equilibration powder are close to crystals and at high temperatures, an exchange of Li_2O vapor takes place between them. Our used experimental setup is shown in Fig. 2.5. The diameters (ø) of the crucibles were adapted to the size of the wafers (see Table 2.2). The ratio between the quantity of equilibration powder and the volume of crucible was 0.3. For optimization of parameters of VTE, commercial X, Y and Z-CLT crystals (48.5%mol Li_2O) with optical and SAW grade surface (supplied by MTI Corporation) were used. The details will be explained in the section 2.3.2.

Moreover, different series of VTE treatments were done on 128 RY-CLN crystals and 42 RY-CLT (48.34 and 48.5%mol Li_2O, respectively). Undoped and Fe doped SAW grade wafers, were supplied by Yamaju Ceramics and Crystal Technology Inc. Wafers with different dimensions and thicknesses were treated by VTE: samples of 25x30 mm², 50x50 mm² (wafers of 1/4") and wafers of 4" with thickness of 250, 350 and 500 µm.

Table 1 Table 2. 2 Geometrical parameters of crucibles used for VTE treatments of wafers with different sizes

Size of wafer	**Diameter of internal crucible (ø in mm)**	**Diameter of external crucible (ø in mm)**
25x30 mm²	10	30
50x50 mm²	15	60
ø=100 mm	15	150

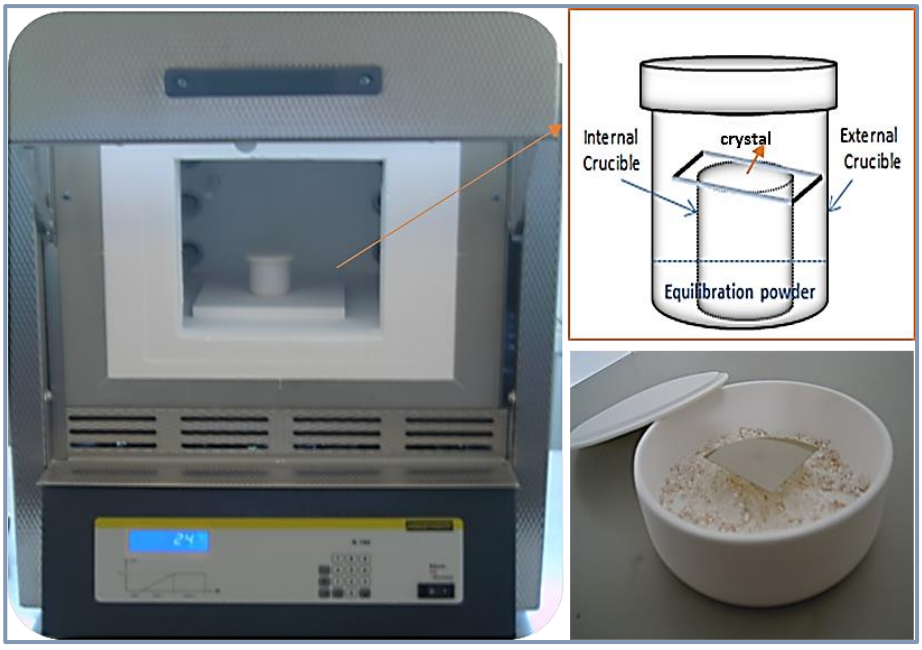

Fig. 2.5 Experimental set-up used for VTE treatments: schematic representation of the arrangement of double crucible- crystal and a photo of the double crucible used for VTE treatments of wafers of 50x50 mm² and ø=100 mm.

The preparation of equilibration powders, the series of VTE treatments for optimization of parameters, and the VTE treatments of 128 RY-CLN crystals were achieved by using a Nabertherm furnace, model LT3/13, with inner dimensions of 160x140x100 mm.

The VTE treatments of 42RY-CLT crystals and the VTE upscaling were done in a ROHDE furnace with inner dimensions of 400x400x400 mm. In the first furnace, cooling rate cannot be controlled and thus, natural cooling was used (exponential decay of temperature). It took around 20 h to cool down from 1250°C to room temperature. The cooling rates in RHODE furnace were controlled by thermoregulator. However, in the temperature range of 200 °C to room temperature, the cooling rates higher than 27 °C/h were not possible due to high quality thermoisolation of furnace.

2.2.3 Methods for evaluation of Li_2O concentration in LT and LN crystals

Lithium is a very light element. Thus, its concentration cannot be very precisely estimated by using direct methods. Most of the indirect methods used for measuring the Li concentration, within the limits of LN and LT single phase existence, are based on the linear dependence of structural or physical properties on Li concentration. The most frequently used methods are: measurement of UV absorption edge (with a typical accuracy in Li_2O concentration of 0.05 mol% [32]), birefringence (0.1 mol%) [32],[33], Curie temperature (0.1 mol%) [16] measurement of lattice parameters by X-Ray Diffraction (XRD) (0.4 mol%) [35], [36] and Raman modes damping (0.05 mol%) [34], [37], [38].

The T_c of LN and LT crystals increase linearly with Li_2O concentration [6], [16], [39]. The values of T_c of CLN crystals measured by different groups are quite different, for example, 1150°C and 1138°C, [16] and [6] respectively. T_c measurement is a very accurate method, but the value of the estimated Li_2O concentration depends on the used standards for calibration of Li_2O concentration and temperature. These discrepancies can be explained by the fact that the T_c of LN is very close to its melting point and thus, T_c is estimated by extrapolation of the data. These difficulties do not exist for LT, which has much lower T_c (~600 °C).

In this work, we have used Raman Spectroscopy and XRD to evaluate the concentration of Li_2O in crystals and powders, for this reason, we will present in details these two methods.

2.2.3.1 Raman spectroscopy

Raman spectroscopy uses scattered light to obtain information about the structure, structural characteristics of materials such as perturbations of lattice vibration, symmetry, defects, strain or lattice disorder. Thus, it is a versatile technique for the quantitative and qualitative analysis of materials.

When a source of monochromatic light is in contact with matter, two types of light scattering occur: elastic and inelastic. In the first case, the wavelength or photon frequency is the same as the incident light (*Rayleigh scattering*). In the case of inelastic scattering, a shift in the wavelength and the photon frequency are

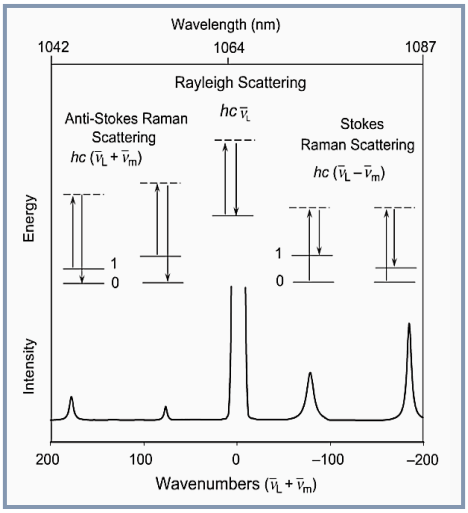

Fig. 2.6 Schematic representation of Raman effect: elastic scattering (Rayleigh) and inelastic scattering (Raman Stokes and Anti-Stokes) [39].

produced [40]. Raman Spectroscopy is based on the inelastic light scattering, phenomenon known as *Raman effect*. In Raman scattering, two kinds of phenomena can occur:

i. *Stokes scattering* occurs when the light interact with the matter and part of the energy of photon, with frequency ν_L, is transferred to excite the atoms in matter. Thus, the frequency of scattered light is reduced to ν_L-ν_m.
ii. *Anti-Stokes scattering* occurs when a molecule that is initially in the excited vibrational state, absorbs a photon with frequency ν_L. Then, molecule returns to the basic vibrational state, and transfers a part of its energy to the photons, which results in increase of frequency of scattered light (ν_L+ ν_m.) [41, pp. 14–16].

Fig. 2.6 illustrates the Rayleigh and Raman scattering process. The lines whose frequencies have been modified in the Raman effect constitutes the Raman spectra. It has been shown that the Raman linewidths are sensitive to non-stoichiometry variations in LN and LT crystals [38], [42]. There is a linear dependence of the damping parameters, full width at half maximum (FWHM), of Raman modes, on the Li_2O concentration. Thus, it is a useful and non-destructive technique to estimate Li_2O concentration in LN and LT crystals and powders.

2.2.3.2 X-Ray Diffraction

XRD is a convenient technique for determining the structural properties of materials. It provides information about crystallographic structure and phase composition of the studied material.

In a diffraction experiment, an incident X-ray beam with wavelength λ is directed to the material at an angle θ. Constructive or destructive interferences occur when scattered waves are emitted by atoms of different types and positions. The atoms are orderly distributed inside a crystal. They form a series of parallel planes separated from one another by a distance d, which varies according to the symmetry of the material. According to Bragg's law, diffraction takes place only when the distance travelled by the rays reflected from successive plans ($2d\ sin\theta$) is equal to a whole number, n, of wavelength, λ:

$$2dsin\theta=n\lambda. \qquad Eq.\ 2.8$$

The Bragg's condition for X-ray diffraction is represented in the Fig. 2.7 [43, pp. 2–4]. A diffraction pattern from a material typically contains many distinct reflections, each corresponding to a different interplanar spacing, d. The positions of reflections are the first information provided by a diffraction pattern, but it is also useful to identify the phases in a sample and for estimation of lattice parameters.

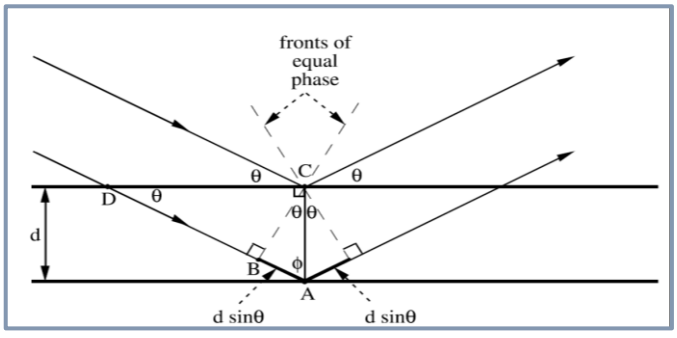

Fig. 2.7 Schematic representation of X-ray diffraction from atomic planes [42].

2.2.4 Estimation of Li_2O concentration in crystals and in equilibration powders

2.2.4.1 Estimation of Li_2O content in equilibration powders by Raman spectroscopy

The local Li_2O concentration in crystals was mapped by means of Raman spectroscopy, with a lateral resolution of 2 µm and depth focus of 7 µm. Measurements were done by S. Margueron at Laboratoire Matériaux Optiques, Photonique et Systèmes (LMOPS), at Institut de Chimie Physique et Matériaux, Université de Lorraine (Metz, France) and at School of Engineering and Applied Science (SEAS), Harvard University. Characterization by Raman spectroscopy were done by using Jobin-Yvon/Horiba LabRam HR spectrometers. The measurements were performed in a micro-Raman mode, in a backscattering geometry. Ar^+ ion laser with wavelength of 514 nm was used as a source of light. The Raman spectra were measured in $X(YZ)\bar{X}, Z(XY)\bar{Z}$ and $Y(ZX)\bar{Y}$ configurations, and were fitted with damped oscillator function by using the Igor Pro software and a procedure "Unifit" (written by I. Gregora, Academic of Sciences of Czech Republic). The frequencies of optic modes were assigned according to frequencies reported in Ref. [44]. Li_2O concentration in single crystals was estimated on surface and on cross section of treated crystals. In order to check the homogeneity of Li content within the crystals, the cross sections of crystals were diced and polished by using an automatic dicing saw DISCO DAD 320. The Raman spectra were collected across the cross section in steps of 1-5 µm. The Fig. 2.8-a illustrates the scans done on the cross section and on the surface of crystals. $X(ZY)\bar{X}$ Raman spectra of stoichiometric, congruent and sub-congruent LT crystal are compared in the Fig. 2.8-b. The identification of LN and LT modes, reported in in Ref. [44], [45] were used in this work. Only E (TO) modes of LN and LT are observed in this polarization configuration. The damping of Raman modes of stoichiometric samples are smaller than the congruent ones.

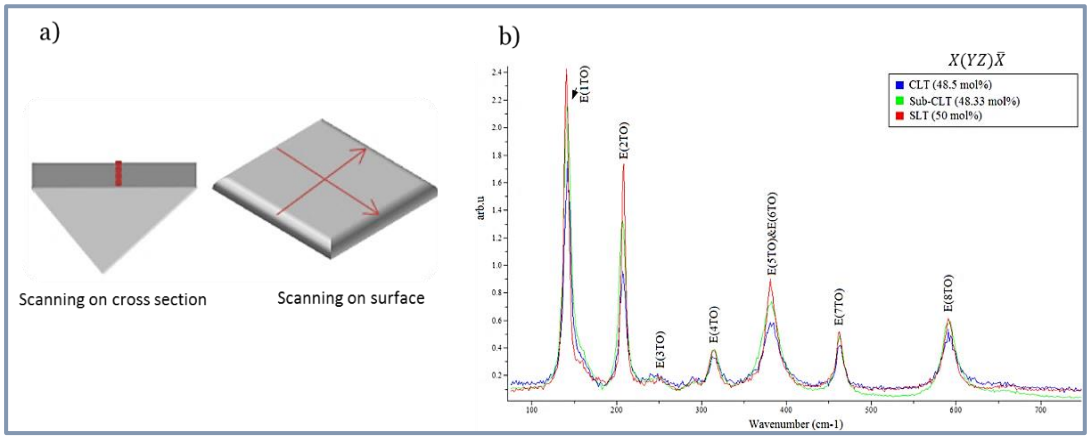

Fig. 2.8 Illustration of composition mapping done by Raman on the cross section and the surface of crystals (a). Raman spectra of $LiTaO_3$ crystals with different non-stoichiometries, measured in $X(ZY)\bar{X}$ polarization configuration (b).

Li_2O concentration on the cross section of LT and LN crystals was estimated from damping parameters, FWHM, of E (1TO) and E (7TO) modes in Raman spectra, collected in crossed polarization configuration. The relationships between the damping and Li concentration was assumed to be linear. These relationships were found for E (1TO) and E (7TO) modes from the damping of these modes in congruent and stoichiometric X, Y, 42 RY and Z-cut LT and 128 RY-LN crystals:

$$X\text{-cut and Y-cut: } \%Li_2O=54.505-0.4918[FWHM_{E(7TO)}], \quad \text{Eq. 2. 9}$$

$$42RY\text{-}LT: \%Li_2O= 52.566-0.503[FWHM_{E(1TO)}], \quad \text{Eq. 2. 10}$$

$$Z\text{-cut: } \%Li_2O=54.247-0.5906[FWHM_{E(1TO)}], \quad \text{Eq. 2. 11}$$

$$128RY\text{-}LN: \%Li_2O=53.73-0.4675[FWHM_{E(1TO)}]. \quad \text{Eq. 2. 12}$$

The polarization configurations used were $Z(XY)\bar{Z}$, for X-cut LT crystals, $X(YZ)\bar{X}$ for Y-cut LT crystals and $Y(ZX)\bar{Y}$ for Z-cut LT crystals. The precision in Li_2O concentration was from ±0.06 to ±0.15 mol % of Li_2O, depending on the optics used for Raman measurements. Lower precision was obtained for the $Z(XY)\bar{Z}$ spectra as compared to $X(YZ)\bar{X}$ and $Y(ZX)\bar{Y}$ spectra.

The Li_2O concentration on the surface of LT crystals was estimated with:

$$X \text{ and Y-cut LT: } \%Li_2O= 53.785-0.4732\ [FWHM_{E(1TO)}], \quad \text{Eq. 2.13}$$

$$Z\text{-cut LT: } \%Li_2O= 54.247-0.5906\ [FWHM_{E(7TO)}]. \quad \text{Eq. 2.14}$$

Li content in single phase equilibration powders ($Li_{1-x}Ta_{1+x}O_{3+2x}$), was estimated from damping parameters (FWHM) of the mode A_1(4TO) in unpolarized Raman spectra. Similarly to crystals, in order to estimate lithium concentration in powders, a linear relationship was found from the A_1(4TO) mode dampings of LT powders with different stoichiometry:

$$\%Li_2O=55.156-0.4108[FWHM_{A1(4TO)}]. \quad \text{Eq. 2. 15}$$

According to the phase diagram of Li_2O-Ta_2O_5 system, at X_{Li2O}<46.5 mol% and X_{Li2O}>50 mol%, the composition of the $Li_{1-x}Ta_{1+x}O_{3+2x}$ phase is constant and the excess or deficiency of Li_2O is compensated by the formation of a secondary phase, $LiTa_3O_8$ or Li_3TaO_4, respectively. Thus, in the two-phase region, the damping of Raman modes of LN and LT phase is constant. The modes corresponding to the secondary phases are present in the Raman spectra. Thus, the proportion of each phase in powders could be determined from the comparison of the Raman intensities of two coexisting phases. However, the two phases are not homogeneously distributed in the powders, and Raman spectroscopy is a local method. Thus, in order to estimate phase composition by means of Raman spectroscopy, Raman mapping and time-consuming data treatment have to be done. For this reason, we used Raman spectroscopy only for estimation of Li_2O in single phase equilibration powders and the two phase powders were analyzed by XRD in order to estimate the phase composition.

2.2.4.2 Phase compositional analysis by X-Ray Diffraction

XRD measurements were done by using a Bruker D8 Advance diffractometer (Cu Kα1, λ=1.5418Å). The θ/2θ scan measurement was carried on by a linear detector in *Bragg-Brentano* geometry. The incident X-rays are diffracted on the sample and converges on the detector. The apparatus used for this measurement is shown in Fig. 2.9. In θ-2θ configuration, the sample is fixed in the horizontal position and the X-ray tube and the detector move symmetrically with an angle θ and 2 θ with respect to the normal of the sample surface. The XRD measurements were performed at UTINAM Institute (University of Franche-Comté) and at the Institut Jean Lamour (University of Lorraine).

In order to identify the phases present in powders from the XRD pattern, the measured diffraction patterns were compared to a known pattern from a standard sample, taken from a crystallographic database. In this work, we have used the crystallographic data from *Pearson's Crystal Data* database [46]. The crystallographic information files (CIF) of the Li_3TaO_4, $LiTa_3O_8$ and $LiTaO_3$ phases [47]–[49] used in this work are given in the Annex A.2.1.

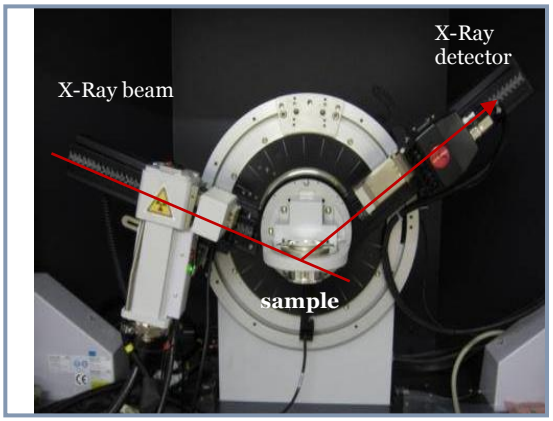

Fig. 2.9 Bruker D8 Advance diffractometer in the Bragg-Brentano configuration

Single phase and two phase equilibration powders were analyzed. The ***c*** and ***a*** lattice parameters of LT and the percentage of each phase ($Li_{1-x}Ta_{1+x}O_{3+2x}$, Li_3TaO_4 or $LiTa_3O_8$) present in powders were estimated by using a Rietveld structure refinement under the Fullprof interface. The scripts needed for the structure refinement of each compound are given in the Annex A 2.2. In this method, a diffraction pattern is simulated from a crystallographic data of phase and then, the parameters of the model are adjusted until good matching between the simulated and measured diffraction pattern are reached. According to our measurements, in the case of single phase powders ($Li_{1-x}Ta_{1+x}O_{3+2x}$) with $46.5 \leq X_{Li2O} \leq 50$ mol%, a linear dependence between the *a*- and *c*-lattice parameters and lithium concentration in powders was found (see Fig. 2.10-a):

$$c = 13.882 - 0.0021 X_{Li2O} \qquad \text{Eq. 2.16}$$

$$a = 5.236 - 0.0017 X_{Li2O} \qquad \text{Eq. 2. 17}$$

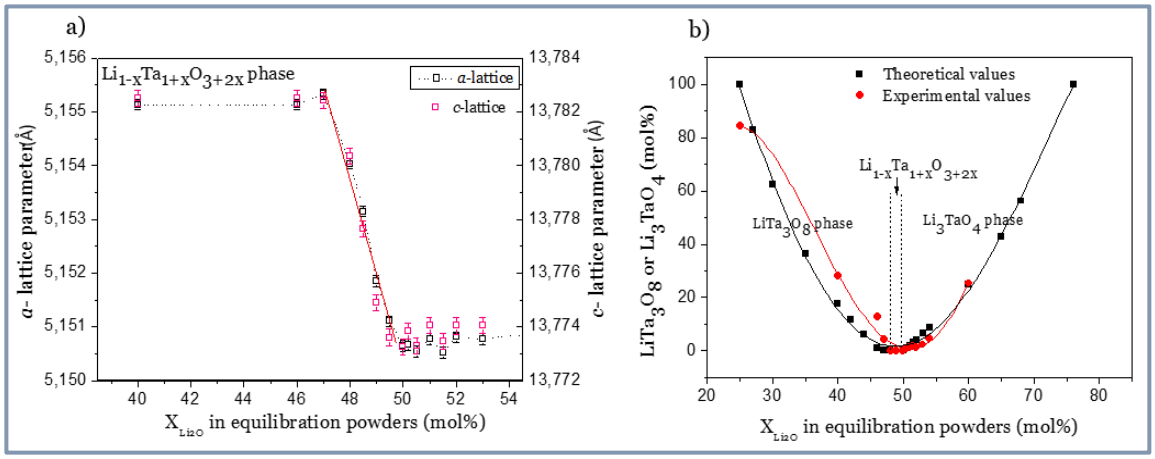

Fig. 2.10 The a- and c-lattice parameters of Li $Li_{1-x}Ta_{1+x}O_{3+2x}$ phase as a function of Li_2O concentration in equilibration powders (a). Comparison of calculated and experimental content of secondary phase in equilibration powders (b).

In the case of two-phase equilibration powders, the *a*-and *c*-lattice parameters of the phase $Li_{1-x}Ta_{1+x}O_{3+2x}$ remains constant with the increase of Li_2O concentration in powder. Therefore, we used another method to estimate the Li_2O concentration in two-phase equilibration powders. First, the molar percentages of each secondary phase in Li-poor and Li-rich two-phase powders, were theoretically estimated, according to the following reactions:

Li-poor (X_{Li2O}<46.5 mol %): $A\ Li_2O + B\ Ta_2O_5 \Rightarrow C\ Li_{1-x}Ta_{1+x}O_{3+2x} + D\ LiTa_3O_8$ *Eq. 2. 18*

Li-rich (X_{Li2O}>50 mol %): $F\ Li_2O + G\ Ta_2O_5 \Rightarrow H\ LiTaO_3 + I\ Li_3TaO_4$ *Eq. 2. 19*

The amount of Li_3TaO_4 or $LiTa_3O_8$ phase was plotted as a function of the Li_2O molar ratio in equilibration powders. Then, series of powders with different Li_2O content were prepared and analyzed by means of XRD. The quantity of secondary phase in each powder was estimated by the Rietveld structural refinement, as explained above. The experimental calibration curve was estimated thereafter. A comparison of calculated and experimentally measured values of the quantity of secondary phase is presented on Fig. 2.10-b. In powder prepared with X_{Li2O}<46.5 mol%, the molar ratio of the $LiTa_3O_8$ phase increases with decreasing of Li_2O amount, whereas, the quantity of Li_3TaO_4 phase increases with the increase of the Li_2O content. There is a good agreement between experimental and theoretical data. From the deviation of experimental concentration, we have estimated the precision of this compositional analysis to be ±5 mol%. The theoretical calibration curve, shown in Fig.2.10-b, was used to evaluate the content of Li_2O in two phase powders.

The Li_2O concentrations in synthesized equilibration powders, estimated by means of XRD and Raman spectroscopy are summarized in Table 2.3. It should be noted that the Li_2O concentration in two-phase powders was estimated only by means of XRD method and the X_{Li2O} in single-phase powders was estimated from lattice parameters of $Li_{1-x}Ta_{1+x}O_{3+2x}$ phase. A good agreement is observed between results obtained by two methods. However, Raman Spectroscopy is a more accurate method than XRD for estimation of Li_2O percentage in single-phase powders.

Table 2. 3 Li_2O content (mol%) in equilibration powders, estimated by XRD and Raman Spectroscopy

X_{Li2O} prepared in powders (mol %)	X_{Li2O} calc. from XRD (mol %)	X_{Li2O} calc. from Raman (±0.05 mol %)
40	33.2±5	-
47	47.3±0.2	47.17
49	49.1 ±0.2	49.20
49.5	49.9 ±0.2	49.81
50	50.1±0.2	49.93
51	50.2±5	-
52	50.3±5	-
54	52.2±5	-
60	60±5	-

2.2.5 Other characterization techniques

2.2.5.1 Determination of flatness of wafers

The flatness of wafers, before and after annealing of VTE treatments, was determined by using three methods: gage check probe, film stress measurement system, and interferometer.

1. *Gage check probe*.- For this purpose, a Gage check probe HEIDENHAIN was used. First, the probe was calibrated. Then, the wafer was positioned on a flat surface and the thickness was measured in various points on the front and the back surface of wafer. The Fig. 2.11-a illustrates the placement of measured points on a 4" wafer.

Then, the difference between the maximum and minimum values of height was calculated (Δh) and we will call it "bow height" hereafter. By this method, an approximate profile can be depicted as is shown in Fig. 2.11b. The Δh_3 indicates the bow height in the center of wafer. In flat wafers, the bow height is close to zero (2±2 µm). The thickness of wafer was measured on both sides of wafer (h_3^+ and h_3^-). This allowed to estimate the sign of the bowing:

$$\Delta h_3 = h_3^+ - h_3^- \qquad \textit{Eq. 2. 20}$$

The Δh_3 is positive when the shape of wafer is convex and it is negative when the shape of wafer is concave (see Fig. 2.11-c).

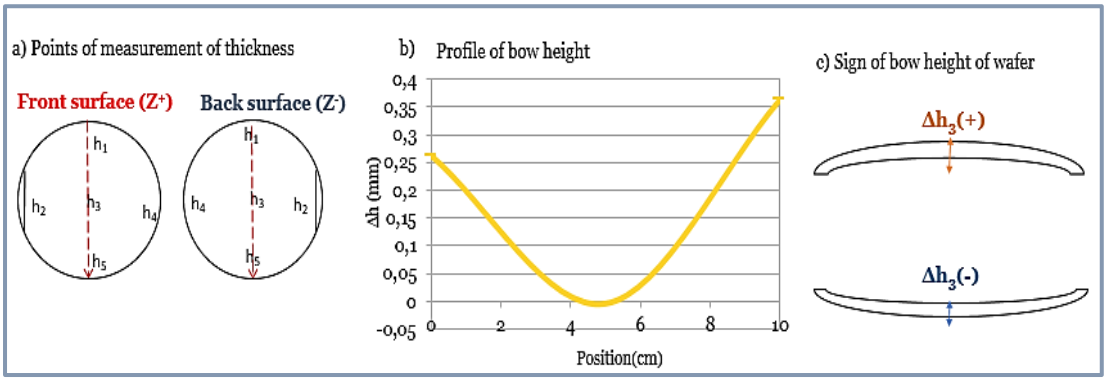

Fig. 2. 11 Schematic representation of the placements of different points on the Z+ and Z- side of wafers for the measurement of bow height with a gage probe (a). Profile of bow height of a 4-inch wafer of 42 RY- CLT single crystal, after annealing at 1250°C for 48h (b). Definition of sign of bowing (c).

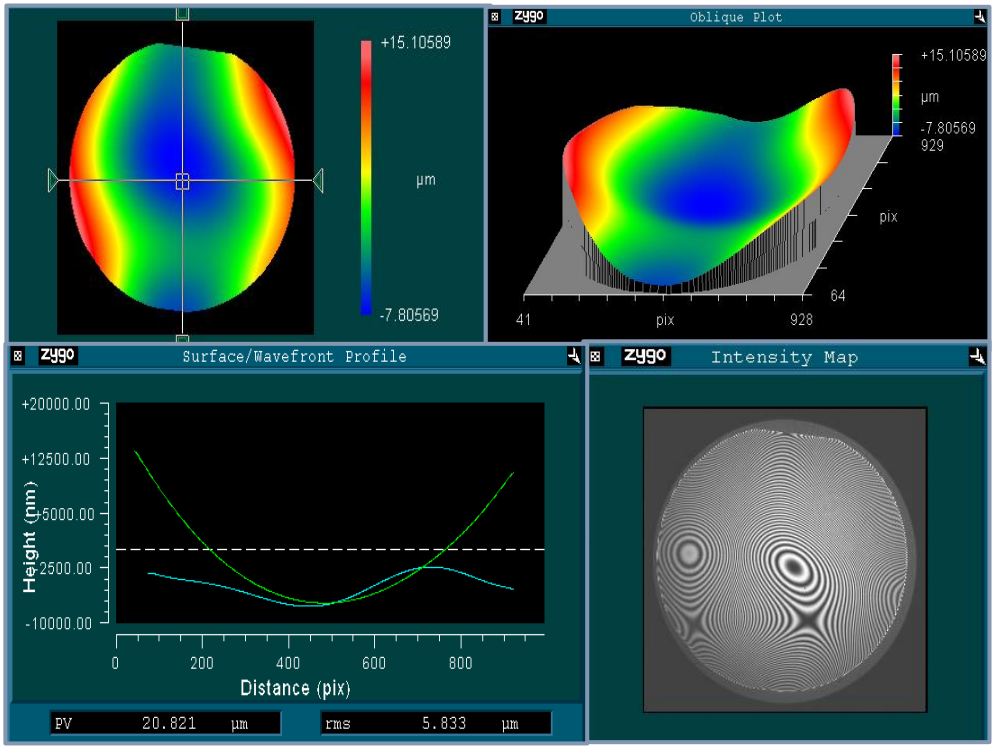

Fig. 2. 12 Images obtained after surface scanning by laser interferometer ZYGO on a 4 inches wafer of 42 RY-CLT: the map (a) and the oblique plot (b) of scanned wafer's surface; profile indicating the Peak to Valley distance (c); interference fringes on surface created by a laser beam (d)

2. *Estimation of surface flatness with a laser interferometer ZYGO*. In this method a laser is used to produce interference fringes. A test plate is put on a reference plate, then a shift in the position of fringes is produced due to wafer deformation, which is

used to determine the flatness of the surface of the test plate. Thus, it is possible to know the flatness value, PV, defined as the distance between the highest peak (P) and the lowest valley (V) of the surface [50]. The Fig. 2.12 gives an example an example of the image of scanned surface of untreated 42RY-CLT crystal with thickness of 250 µm. The surface profile shows the peak–to–valley distance, which indicates a bow height of 19±2 µm of untreated wafers.

3. *Measurement of bow height with a film stress measurement system (FSM 500TC).* The Film Stress Measurement system, provided by Frontier Semiconductor Inc. (FSM), consists of a quartz-lined chamber, receiving the wafer while a laser beam scans its surface. Then the light is reflected at an angle related to the radius of curvature [51]. The bow height value of the wafer, was estimated according to the following relationship:

$$\Delta h_{3FSM} = \frac{(d/2)^2}{2R}, \qquad \textit{Eq. 2.21}$$

where Δh_{3FSM} is the bow height, d is the wafer diameter and R is radius of curvature.

Untreated 42RY-CLT wafer with diameter of 4" and with thickness of 250 µm was measured by FSM. The bowing height obtained was 17 µm±1 was obtained (Fig. 2.13).

The advantage of the interferometry and FSM methods is that we can obtain information on flatness taking into account the whole surface of the wafer. However, it is not possible to measure wafers having a significant bow height (>70 µm for the interferometer ZYGO and > 200 µm for FSM system). Besides, the interferometer ZYGO is not adapted to the measurements of transparent materials. Thus, it was not possible to measure the two-side polished samples. The check probe was used for highly deformed wafers and it was not limited by the bow height value.

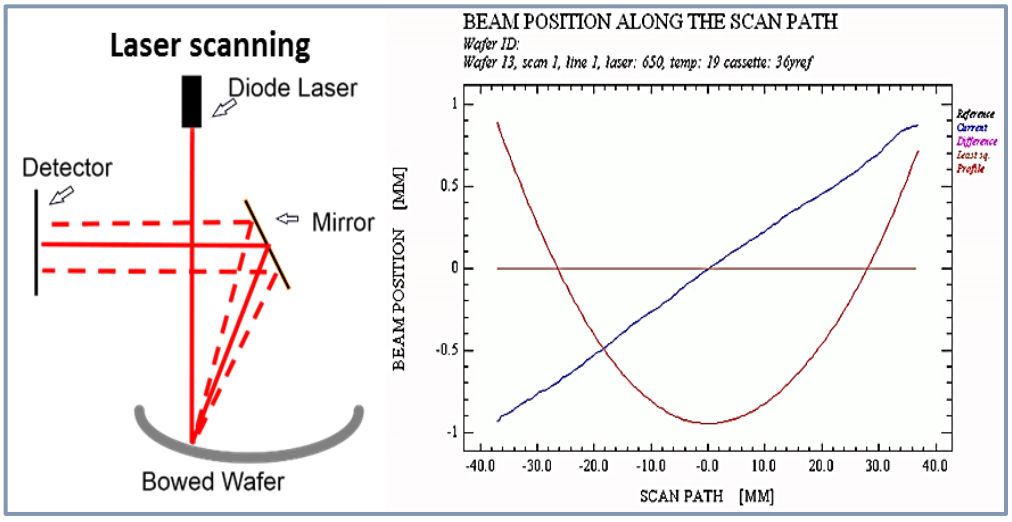

Fig. 2.13 Principle of bow height measurement: a laser is directed to the sample and then, it's reflected at an angle corresponding to the radius curvature of wafer (a) [38]. Example of a profile obtained after the measurement of a 4 inches wafer of 42 RY-CLT (b).

2.2.5.2 Characterization and polishing of crystals surfaces

After VTE treatments, the morphology and surface of crystals were characterized by using the Leica DM8000 and INM20 optical microscopes. The cross polarized light was used to investigate the birefringence of crystals. On the other hand, the cross section of samples

after VTE treatment were examined by using optical microscopy, as well. Some samples were cleaned and polished, after VTE treatment, in order improve the quality of the surface. The mechanical polishing was done by using a polishing machine "SOMOS", which was composed of a disc recovered by felt. The wafer was held on a metal support by a vacuum. Then, the sample was rotated against the polishing disc with a controlled speed. A suspension of colloidal silica with grain size of 50 nm was used as abrasive.

The atomic force microscopy (AFM) method was used to investigate the roughness of our samples. The roughness average (Ra) and root mean square (RMS) were measured in several points on the surface by using an AFM Veeco in contact mode.

2.3 VTE treatment of LT and LN crystals

2.3.1 Lithium oxide volatility during VTE process.

Li_2O partial pressure is a key parameter of VTE defining the Li_2O concentration in treated crystal and its homogeneity. Therefore, we have studied the volatility and loss of Li_2O as a function of composition of equilibration powders and treatment temperature. The Li_2O losses in powders with different lithium concentration, during VTE treatments carried out at 1250 °C and 1300 °C for 24 h were measured by means of Raman spectroscopy and XRD (for details see sections 2.2.4.2 and 2.2.4.3). The results are summarized in Fig. 2.14. It was observed that the Li_2O losses are more important for Li-rich two–phases powders ($LiTaO_3$+Li_3TaO_4). In the powders with X_{Li2O}>50 mol%, Li_3TaO_4 phase decomposes first to $LiTaO_3$ and Li_2O. Thus, the Li_2O loss decreases linearly with the decreased quantity of Li_3TaO_4 in equilibration powders. In the case of $Li_{1-x}Ta_{1+x}O_{3+2x}$ powders, Li_2O loss decreases fast with the increase of Li deficiency [52]. The volatility of lithium oxide is 9 times higher at 1300°C, comparing to that of 1250°C because the Li_2O out-diffuses and evaporates faster by increasing the temperature. The loss of Li_2O induces the change of composition of equilibration powders as a function of treatment time.

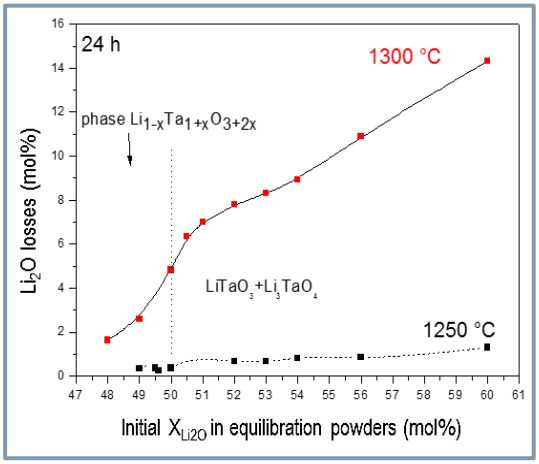

Fig. 2.14 Evolution of Li_2O losses as a function of Li_2O concentration in equilibration powders at 1300°C and 1250°C [52],

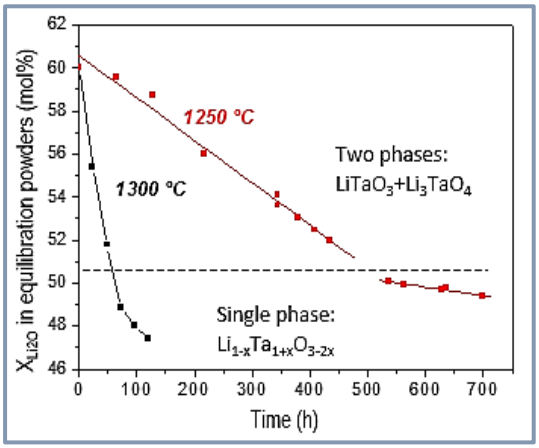

Fig. 2.15 Effect of VTE duration and temperature on Li_2O content in equilibration powders [52].

The change of Li_2O content in equilibration powders as a function of VTE duration was also estimated (Fig. 2.15). For this purpose, the equilibration powders were treated several times at the same conditions. The starting composition of studied

equilibration powders was 60 mol % of Li_2O. The Li_2O content in powders decreases linearly with treatment time. The rate of Li_2O loss at 1300°C is 0.1716 mol %/h whereas at 1250°C it is 0.019 mol %/h. Moreover, the loss rate decreases significantly in the single phase powders.

The Li_2O concentration changes much faster in the $LiTaO_3$-Li_3TaO_4 mixture than in single phase powders. This indicates that Li_3TaO_4 phase losses 4 times faster Li_2O than the phase $Li_{1-x}Ta_{1+x}O_{3+2x}$. The vapor concentration of Li_2O is a critical parameter defining the composition of equilibrated crystals. The losses rate of Li_2O at 1300°C is much faster than at 1250°C. Therefore, the crystals treated with Li-rich powders at higher temperatures will contain higher Li_2O concentration. However, the faster changing concentration of Li_2O vapor (induced by change of powder composition) makes difficult a precise control of crystal composition and homogeneity. For this reason, in this work we preferred to use temperatures lower than 1300°C.

2.3.2 Optimization of VTE parameters for $LiTaO_3$ single crystals

We investigated the effect of VTE temperature, duration and composition of equilibration powders on Li_2O concentration and its homogeneity in treated X, Y and Z-cut $LiTaO_3$ crystals . The details about the performed VTE treatments will be given in following sections.

2.3.2.1 Effect of VTE Temperature and composition of equilibration powders in crystal concentration.

The effect of temperature was investigated in X, Y and Z-CLT crystals with size 5x20 mm^2 and thickness 500 µm, treated by using equilibration powder with X_{Li2O}= 40, 50 and 60 mol% at different temperatures (1150°C, 1200°C, 1250°C and 1300°C) for 10 h. These treatments were done by using a Nabertherm furnace, model LT3/13, with inner dimensions of 160×140×100 mm. Employed heating and cooling rates were 122.5°C/h and ~60 °C/h, respectively. The VTE duration was chosen at 10h because this short duration is not sufficient to homogenize the composition and a concentration gradient in crystals is expected. Thus, it allows the investigation of the effects of temperature and of powder composition on the Li diffusion. The Table 2.4 summarizes the conditions used in these experiments.

Table 2. 4 Conditions of VTE treatments of X, Y and Z-cut LT crystals with thickness of 500 µm, realized during 10 h, in order to investigate the effect of temperature and concentration of equilibration powders.

Li_2O in powders: 40 mol%				
Temperature (°C)	1150	1200	1250	1300
Li_2O in powders: 50 mol%				
Temperature (°C)	1150	1200	1250	1300
Li_2O in powders: 60 mol%				
Temperature (°C)	1150	1200	1250	1300

The Li_2O content in crystals was measured in cross sections of the crystals by Raman spectroscopy. The depth profiles of Li_2O concentration in X, Y and Z-cut LT crystals, obtained at different VTE temperatures, using several compositions of equilibration powders, are given in the Fig. 2.16. The distribution of Li_2O concentration in treated crystals

is highly dependent on VTE temperature. The crystals treated at 1150-1250 °C using powders with X_{Li2O}≥50 mol% present a gradient of concentration. The Li_2O content has a maximum value on the crystal surface and then it diminishes in the depth of the crystal. The gradient is reduced with the increase of temperature. At treatment temperature of 1300 °C, the distribution of Li content becomes more homogenous in the crystals treated with X_{Li2O}≥50 mol% because the volatility and diffusion of Li are much faster at this temperature [26], [29]. It can be observed that the diffusion of Li^+ is anisotropic, diffusion is faster along Z-axis as compared to X and Y-axis of LT. Similar results were found for Z and X-axis of LN crystals [31]. The diffusivity along X- and Y-axis looks similar at 1150-1250°C. The difference might be attributed to the precision of measurements and the calibration used for estimation of Li_2O concentration in different cuts. The diffusion can be expressed as a second rank tensor:

$$D = \begin{pmatrix} D_1 & 0 & 0 \\ 0 & D_2 & 0 \\ 0 & 0 & D_3 \end{pmatrix} \qquad \textit{Eq. 2.22}$$

Since LN and LT are trigonal crystals, $D_1=D_2\neq D_3$, where D_1, D_2 and D_3 are the diffusivities along the X, Y and Z axis in an orthogonal reference system, respectively [53, p. 34]. Therefore, one expects the same diffusivity in X and Y crystals and a different one along Z-axis.

In the case of X- and Y-cut LT crystals treated for 10 h at 1150°C and 1200°C, using equilibration powders with 60 mol% of Li_2O, the Li concentration in the crystal diminishes with the depth. The composition is stoichiometric on the surface and around 48.00-48.5 mol% in the middle of the crystal (Fig. 2.16 a-c). It is important to note that in the case of X- and Y-cut LT crystals, concentration gradient induces high thermal stresses, which affect the Raman mode damping as well. Therefore, the errors in estimated Li_2O concentration is much higher in the crystals with higher concentration gradients. In the case of Z-cut LT crystals, the gradient of concentration is smaller as compared to X and Y-cut LT crystals, treated at the same conditions.

The increase of VTE temperature reduces the gradients and at 1300 °C the Z-cut LT crystals become homogenous during a 10 h treatment. This can be explained by faster Li^+ in-diffusion at higher VTE temperatures. Thus, at lower VTE temperatures, it takes longer time to reach a homogenous composition. On the other hand, X, Y and Z-cut LT crystals treated by using powders with 50 mol% of Li_2O during 10h at 1150°C-1250°C, produces crystals with Li concentration of 49.25-50 mol% on the surface. However, in the middle depth of the crystal the composition is close to the congruent one, as can be seen in Fig. 2.16 d-f. At 1300 °C, the X, Y and Z-cut LT crystals have a homogenous concentration across the depth, close to the congruent one, 48.71, 48.54 and 48.66 mol%, respectively. At this temperature, the volatility/ diffusion of Li_2O is very fast. Thus, powders with 50 mol% of Li_2O loose quickly Li_2O. The amount of Li_2O in diffused in crystal is small and the composition of crystals is similar to the congruent one.

The crystals treated for 10 h using equilibration powders with 40 mol% of Li_2O lost a small amount of Li_2O during the treatment and presented compositions close to the congruent one. The average Li_2O concentration ($\overline{Li_2O}$) in the crystals treated at 1150 °C-1300 °C ranged from 48.28-48.5 mol% (see Table 2.5). The gradient of concentration was smaller in sub-congruent crystals than those in crystals treated by using powders with 50 and 60

mol% (Fig. 2.16-g, h, i). The out-diffusion of Li^+ in crystals with congruent and sub-congruent compositions is a long process. According to P.F. Bordui *et al.*[17] the duration of VTE treatment of LN crystals performed at 1100 °C in Li-poor atmosphere was around 400 h. Thus, the time used here is probably not sufficient to produce important losses in Li_2O concentration of crystals.

We estimated the difference of concentration between the surface of crystal and the middle depth, called ΔC_{Li2O} hereafter, using the following equation:

$$\Delta C_{Li2O} = C_s - C_m \qquad \textit{Eq. 2. 23}$$

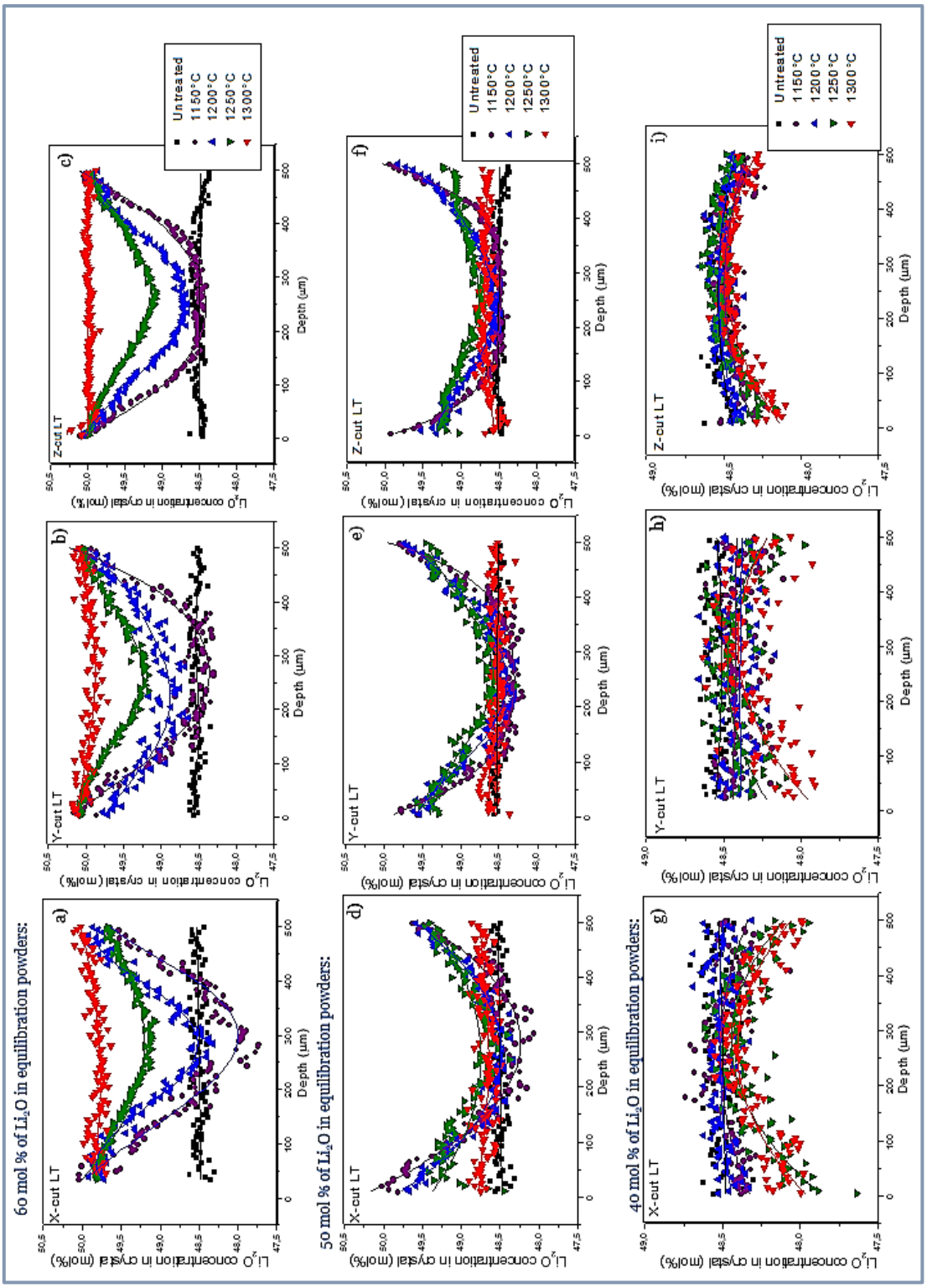

Fig. 2. 16 Effect of temperature on the depth profile of Li_2O concentration measured on cross section of X, Y and Z-cut crystals LT crystals, treated for 10h using equilibration powders with X_{Li2O}=40, 50 and 60 mol%.

Where C_s and C_m are the Li_2O concentration on surface and in the middle depth of crystals, respectively. The values of ($\overline{Li_2O}$) and ΔC_{Li2O} in the cross section and the average Li_2O concentration measured on surface ($\overline{C_s}$) of crystals treated at 1150-1300 °C using different equilibration powders are summarized in the Table 2.5

Table 2. 5 Average Li_2O concentration, $\overline{Li_2O}$, difference in Li_2O concentration on the surface and middle depth of crystals, ΔC_{Li2O}, and Li2O concentration on crystal surface, $\overline{C_s}$, of X, Y and Z-cut LT crystals treated by VTE for 10h at different temperatures and compositions of Li_2O in equilibration powders.

T	X_{Li2O} in powders (mol %)								
(°C)	40	50	60	40	50	60	40	50	60
	$\overline{Li_2O}$ in crystals (mol%)			ΔC_{Li2O} (mol %)			($\overline{C_s}$) (mol %)		
X-cut: $\overline{Li_2O}$ 0.15 (mol%)							($\overline{C_s}$)±0.05 (mol%)		
1150	48.44	48.78	48.96	0.18	1.76	1.94	48.50	49.62	49.87
1200	48.5	48.91	49.26	0.07	1.26	1.26	48.61	49.26	49.79
1250	48.48	48.97	49.85	0.42	0.6	0.45	48.24	49.10	49.89
1300	48.39	48.71	49.99	0.54	0.11	0.09	48.16	48.55	49.93
Y-cut: $\overline{Li_2O}$ ±0.11 (mol%)							($\overline{C_s}$)±0.05 (mol%)		
1150	48.38	48.70	49.01	0.02	1.57	1.64	48.51	49.43	49.88
1200	48.43	48.88	49.23	0.06	1.15	0.86	48.52	49.34	49.92
1250	48.37	48.96	49.69	0.25	0.81	0.68	48.33	49.05	49.93
1300	48.28	48.54	49.98	0.43	0.1	0.12	48.10	48.42	50.00
Z-cut: $\overline{Li_2O}$ ±0.06 (mol%)							($\overline{C_s}$)±0.14 (mol%)		
1150	48.44	48.78	48.96	0.18	1.49	1.59	48.37	49.66	49.88
1200	48.50	48.91	49.26	0.12	0.77	1.27	48.40	49.49	49.88
1250	48.48	48.97	49.86	0.28	0.39	0.34	47.85	49.20	49.83
1300	48.39	48.66	49.99	0.34	0.14	0.01	47.90	48.39	49.92

In the crystals treated using powders with 60 mol% of Li_2O, the $\overline{Li_2O}$ content, measured on cross section and surface, increases with temperature. It occurs because the amount of evaporated Li_2O from equilibration powders increases with temperature. Thus, the increased average Li content in crystals treated at higher VTE temperatures is expected. However, in the case of crystals treated by using powders with X_{Li2O}= 50 mol%, the $\overline{Li_2O}$ within the crystal increases with the increase of VTE temperature from 1150°C to 1250°C, but it diminishes at 1300°C. The $\overline{C_s}$ diminishes with the increase of temperature because the loss of Li_2O concentration in equilibration powders increases with temperature. Therefore, the continuous excess of Li_2O is not assured by powders with 50 mol% of Li_2O. In the case of crystals treated with equilibration powders with X_{Li2O}=40 mol%, the $\overline{Li_2O}$ measured on their cross section and surface diminishes with the increase of treatment temperature, as expected (see Table 2.5).

In the case of the Li_2O measured on the surface($\overline{C_s}$), crystals treated using powders with X_{Li2O}= 60 and 50 mol% present higher values than the $\overline{Li_2O}$ measured on their cross section. The Li^+ in/ out-diffusion during VTE starts on the surface of crystals and the crystals treated at 1150°C-1300 °C for 10 h presented a concentration gradient, as it was shown above. Thus, one expected different values of Li_2O concentration measured on cross section and on surface .

The absolute value of ΔC_{Li2O} highly depends on VTE temperature and on Li_2O concentration in powders. It was found that in the case of Li-rich and intermediate Li concentration of equilibration powders (60 and 50 mol% of Li_2O, respectively) the ΔC_{Li2O} diminishes with the increase of temperature (Fig. 2.17), because Li in-diffusion is faster at high temperatures and therefore crystals become more homogenous. In the case of Li-poor equilibration powders with 40 mol% of Li_2O, gradients increases with the increase of treatment temperature because at higher temperatures, the crystal can loss higher amount of

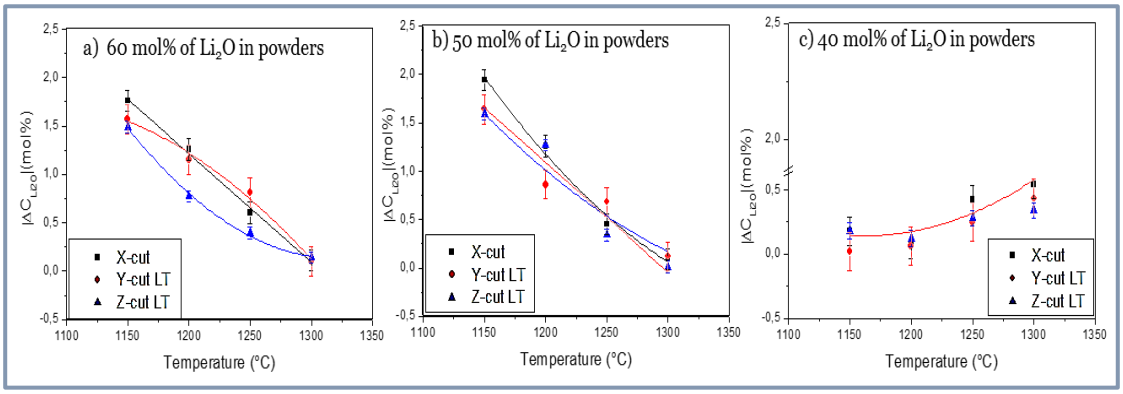

Fig. 2. 17 Temperature dependence of absolute value of concentration difference between the surface and middle depth of crystals ($|\Delta C_{Li2O}|$) in X, Y and Z-cut LT crystals. VTE treatment was done for 10 h using 60, 50 and 40 mol% of Li_2O in equilibration powders.

Li_2O.

On the other hand, it has been reported that the change in lithium concentration in LN crystals follows the Arrhenius Law (Eq. 2.4) [26]. Thus, the E_a can be estimated by plotting $\overline{\Delta Li_2O}$ versus temperature. Where $\overline{\Delta Li_2O}$ is the increase of Li_2O concentration with respect to its initial content (48.5 mol%) in the crystal. The Fig. 2.18 shows the temperature dependence of $\overline{\Delta Li_2O}$ in the case of X-cut LT crystals, treated using powders with 60 mol% of Li_2O during 10h. After a linear fitting, the following equations were found, which allows the estimation of activation energy for each crystallographic cut

$$ln(\overline{\Delta Li_2O}) = 1.91 - 2432.3\,(1/T) \quad \textit{for X-cut LT,} \qquad \textit{Eq. 2. 24}$$

$$ln(\overline{\Delta Li_2O}) = 1.15 - 1190.6\,(1/T) \quad \textit{for Y-cut LT,} \qquad \textit{Eq. 2.25}$$

$$ln(\overline{\Delta Li_2O}) = 1.25 - 1358\,(1/T) \quad \textit{for Z-cut LT.} \qquad \textit{Eq. 2.26}$$

The values of E_a estimated experimentally for X, Y and Z-cut LT crystals, treated using equilibration powders with 60 and 40 mol% of Li_2O are given in the Table 2.6. For comparison, the values of E_a of X and Y-cut LN crystals, reported in literature are indicated as well. Although the values cannot be directly compared because LT and LN are two different materials, it can be seen that the values have the same order of magnitude.

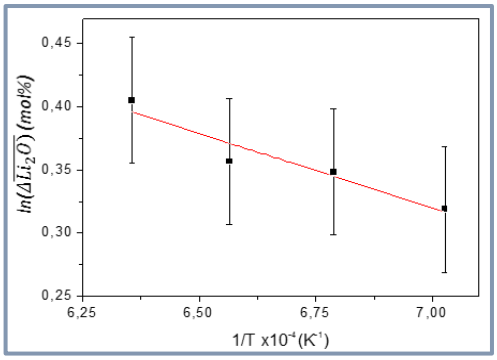

Fig. 2. 18 Change in average Li_2O concentration in crystal, relative to the initial value (ΔC_s) as a function of 1/T for X-cut LT crystals.

In the case of crystals treated with Li-rich powders, we found similar values for X and Y-cut

crystals, whereas a slightly smaller E_a was found for Z-cut LT crystals. In the case of Li-poor, the E_a of Z-cut LT crystals is larger than that of X and Y-cut LT crystals, which agrees with results reported in literature. Moreover, the values of E_a of crystals, treated with Li-rich equilibration powders is much smaller than the crystals treated with Li-poor equilibration powders. For this reason, the Li^+ diffusion in crystals treated with this kind of powders is very long.

Table 2. 6 Experimental values of activation energy (E_a exp.) for X, Y, and Z-cuts of LT crystals and reported ones in literature for X and Z-cut LN crystals, after VTE treatment using Li-rich and Li-poor equilibration powders.

Cut	E_a , exp (eV)		E_a, (eV) for LN crystals	
	Li-rich (60 mol%)	Li-poor (40 mol%)	Li-rich (68 mol%)	Li-poor (40 mol%)
X	0.21±0.10	2.26±0.10	--	--
Y	0.27±0.09	2.6±0.09	0.76±0,05 [26]	2.20±0.20 [27]
Z	0.11±0.05	3.20±0.05	0.53±0,03 [26]	2.80±0.20 [27]

On the other hand, the diffusivity in each cut of LT and its dependence on temperature and composition were estimated according to the following model, assuming that:

1. The Li diffusion in crystals follows the second Fick's law:
$$\frac{\partial C}{\partial t}(x,t) = \frac{\partial}{\partial x}\left(D_c \frac{\partial C}{\partial x}\right), \qquad \textit{Eq. 2. 27}$$
where C is the concentration in the crystal, which is dependent on depth position, x, in crystal, t-time and D_c is the concentration dependent Li-diffusion coefficient.
2. The concentration in the surface, C_s, is constant after a given time (for t>0, $C=C_s$ at x=0)
3. Before the diffusion, crystals have initially congruent concentration, C_0 (for t=0, $C=C_0$ at $0 \le x \le \infty$);
4. The position x on the surface is zero and it increases with distance in the depth of crystal;
5. Before the diffusion of Li_2O the time is zero (t=0).

The following equation can be solved by applying these boundary conditions:

$$\frac{C_x - C_0}{C_s - C_0} = 1 - erf\left(\frac{x}{2\sqrt{D_c t}}\right), \qquad \textit{Eq. 2. 28}$$

where C_x is Li_2O concentration at a given position after a time t. The $erf\left(\frac{x}{2\sqrt{D_c t}}\right)$ is the Gaussian error function defined by $\mathrm{erf}(z) = 2/\pi \int_0^z e^{-y^2} dy$. The values of erf(z) were taken from the Table 6.1, Ref. [54, p. 133], given in the Annex A.2.3. If C_x, C_0 and C_s are known at a given time t, the value of the coefficient of diffusion of self-diffusion D_c can be estimated from Eq. 2.25. The D_c was estimated for different cuts of LT treated at different temperatures during 10h. The Fig. 2.19-a shows the temperature dependence of the diffusion coefficient of X-, Y- and Z-cut LT crystals treated using Li-rich equilibration powders for 10h. We observe that the rate of diffusion of Li ions increases exponentially with temperature, according to Arrhenius Law. Thus, the concentration gradients diminish with the increase of temperature, which explains the previously shown results. At 1300°C, the diffusivity of Li_2O in Z-cut is almost nine times faster than that of the Y-cut and 3 times higher than that of X-cut LT

crystals. It was 2.29×10^{-12} m²/s, 1.67×10^{-12} m²/s and 9.9×10^{-12} m²/s, for X-, Y- and Z-cut LT crystals, respectively. Therefore, the concentration in Z-cut LT crystals is homogenous after VTE treatment at 1300 °C for 10 h, whereas there is still a small gradient of concentration in X- and Y-cuts. The values of diffusivity of LN and LT can be compared with respect to the *Tamman temperature (T_m),* which is defined as the temperature when the diffusion becomes significant and it is around 40% of melting point of materials [55, p. 120]. The diffusivity of Z-cut NSLN crystal was reported to be ($D=5x10^{-12}$ m/s²)[28] and it is ($9.9x10^{-12}$ m²/s) in the case of LT crystals. The VTE process of LN is done very close to the melting point (0.93 T_{fusion}), while the LT is treated around 400°C below its fusion temperature. Thus, diffusivity is expected to be lower from this point of view. However, the diffusion E_a is lower in stoichiometric LT than that in LN and E_a is defined by internal structure (bond lengths, etc.)

The effect of lithium concentration in equilibration powders on Li^+ diffusivity was estimated as well. The Fig. 2.19-b shows the Li-diffusivity as a function of X_{Li2O} in powders along X, Y and Z crystallographic axis, for crystals treated at 1300°C during 10h. It can be observed that Li-diffusivity increases with Li_2O content in powders, which agrees with results reported in literature [29], [31], [56]. The increase of Li_2O concentration in equilibration powders produces more Li_2O vapor and more Li^+ ions will available to fill the vacancies in LT crystals. Thus, the diminution of the vacancies facilitates the diffusion process, according to the ambipolar (Li^+ and Nb^{5+}) diffusion model [30]. Moreover the Li^+ diffusivity along the X, Y and Z crystallographic directions is similar in crystals treated using powders with X_{Li2O}= 40 and 50 mol%. However, it is almost nine times faster in Z-cut than in X and Y-cut when the Li_2O in equilibration powders is 60 mol%.

From these experiments, it can be deduced that the VTE process depends strongly on VTE temperature but also on the Li_2O content in the equilibration powders. Moreover, the diffusion is faster along Z-axis in LT crystals. In our experiments we fixed temperature to 1250°C because it yields crystals with smaller gradient of concentration, compared to that obtained by using temperatures of 1150°C and 1200°C. Besides, at 1250°C, the volatility of Li_2O vapor is smaller than that at 1300°C. Thus, it is easier to achieve homogenous crystals with a desired composition.

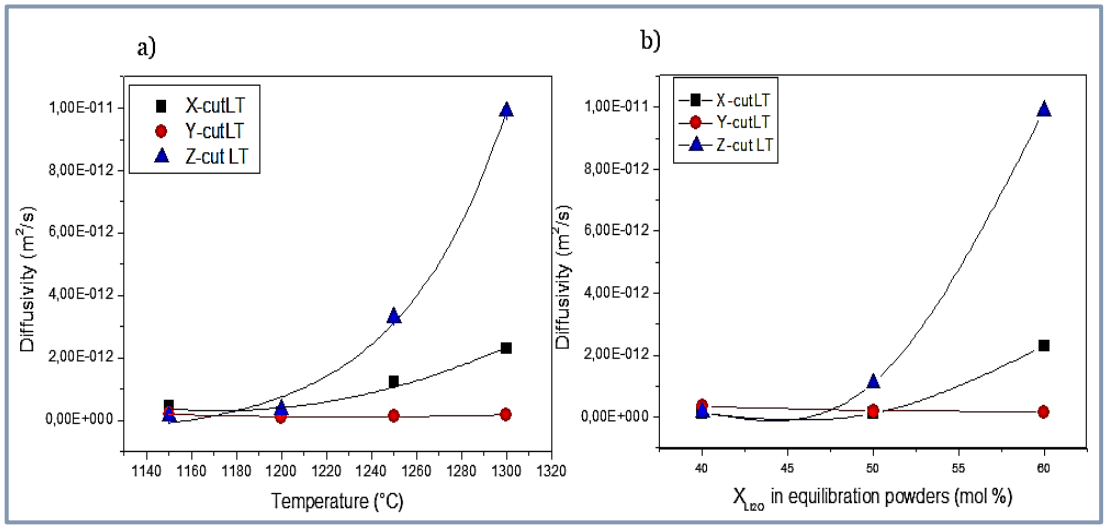

Fig. 2. 19 Li diffusivity along X, Y and Z directions: temperature dependence of VTE treated LT crystals using equilibration powders with X_{Li2O}= 60 mol% for 10h (a), Li concentration dependence for VTE carried out at 1300°C for 10h (b).

2.3.2.2 Optimization of VTE treatment time for fabrication of homogenous crystals

VTE treatments with durations of 5, 10, 24, 48 to 64 h using the powder with 60 mol% of Li_2O were carried out at 1250°C (Table 2.7). The Li content was measured on the cross section of these treated X, Y, Z-cut LT crystals. The $\overline{Li_2O}$ and ΔC_{Li2O} of these crystals, are summarized in the Table 2.8. The profile of Li_2O concentration is illustrated in the Fig. 2.20.

In the case of crystals treated for a short time (5-10h) the Li_2O concentration is stoichiometric on the crystal surface and it decreases with the increase of depth. It can be seen as well that the gradient of concentration in Z-cut LT is less important than in other crystal cuts due to the faster diffusion along this direction. It should be noted that, at short treatment times (5h), the gradient of concentration is the most important and the concentration in the middle depth of X- and Y-cut LT crystals is close to congruent one. Moreover, ΔC_{Li2O} diminishes exponentially with the increase of VTE duration (Fig.2.21) because the Li^+ has more time to reach the depth of the crystal. Experimental results show that for X -, Y-cut and Z-cut LT crystals, the VTE time of >24 hours is necessary to obtain homogeneous crystals. This time will be called *homogenization time (t_{hom})* hereinafter. VTE duration longer than t_{hom} may provide homogenous crystals if the powders are able to provide continuous and constant Li_2O vapor concentration. Z. Wang *et al.* found that shorter VTE times can produce LN crystals closer to stoichiometric composition [23] but the results about homogeneity of crystals and the powder concentration after VTE treatment were not reported.

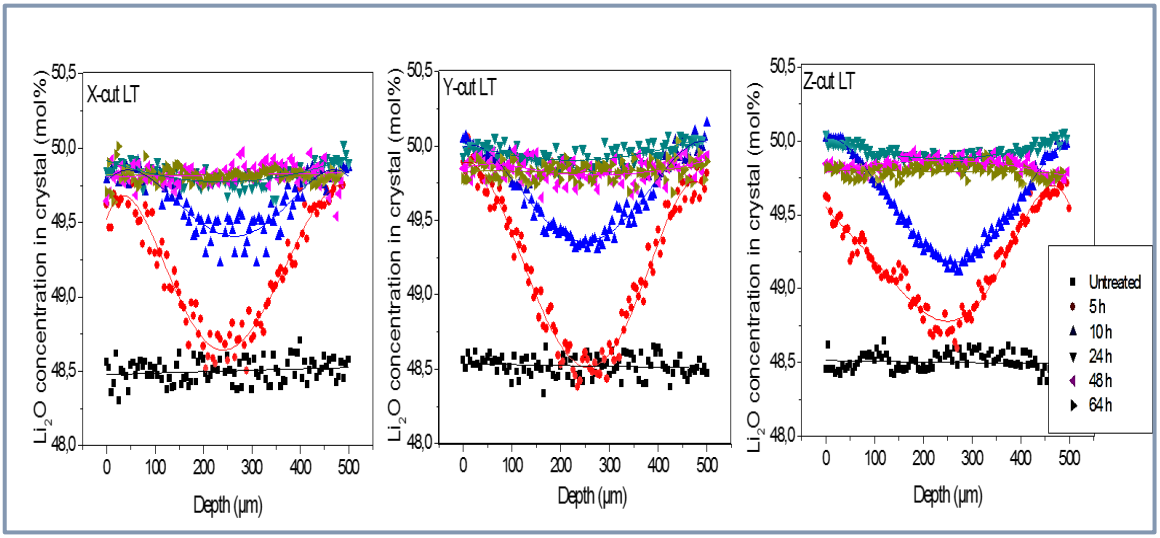

Fig. 2.20 Depth profiles of X-, Y- and Z-cut LT crystals treated for different durations at 1250°C using powders with 60 mol% of Li_2O.

Table 2. 7 Conditions of VTE treatments used to investigate the effect of treatment duration on Li_2O concentration in X, Y and Z-cut LT crystals with 500 µm of thickness.

T=1250°C, Li_2O in equilibration powders: 60 mol%					
t (h)	5	10	24	48	64

Table 2. 8 Average Li_2O concentration ($\overline{Li_2O}$) and ΔC_{Li2O} measured on cross section and average Li_2O concentration measured on surface ($\bar{C}_s$) of X, Y and Z-cut LT crystals treated by VTE at 1250°C, by using equilibration powders with 60 mol% of Li_2O.

Crystal cut	time (h)	$\overline{Li_2O}$ in crystal (mol %)	ΔC_{Li2O} (mol %)	$\bar{C}_s$ (mol %)
		X-cut: $\overline{Li_2O}$ ±0.15 (mol%)		
X-cut LT	5	49.19	0.96	49.56
	10	49.65	0.38	49.89
	24	49.84	0.16	49.96
	48	49.82	0.04	49.75
	64	49.82	0.06	49.60
		Y-cut: $\overline{Li_2O}$ ±0.10 (mol%)		
Y-cut LT	5	49.19	1.42	49.54
	10	49.69	0.65	49.92
	24	49.95	0.15	50
	48	49.84	0.05	-
	64	49.83	0.02	49.68
		Z-cut: $\overline{Li_2O}$ ±0.06 (mol%)		
Z-cut LT	5	49.19	0.93	49.55
	10	49.54	0.86	49.91
	24	49.93	0.11	49.99
	48	49.84	0.04	49.77
	64	49.79	0.02	49.60

The evolution of the average Li_2O concentration ($\overline{Li_2O}$) within the crystal as a function of VTE duration at 1250°C, using equilibration powders of 60 mol% of Li_2O is illustrated in Fig. 2.22 a. It can be observed that $\overline{Li_2O}$ follows a quadratic dependence on time. The relationship obtained experimentally for X, Y and Z-cut LT crystal is:

$$\overline{Li_2O}\ (mol\%) = 49.16 + 0.042t - 5.33x10^{-4}\ t^2 \qquad Eq.\ 2.\ 29$$

By using this expression, the average concentration in the crystals can be approximatively estimated if the duration of VTE is known. It should be noted that the X-, Y- and Z-cut LT crystals have the same dependence in the limits of error. Moreover, the average Li_2O content on cross section and on surface of treated crystals increase with VTE duration. Crystals treated for 24 h presented a stoichiometric composition, then it slightly decreases for longer treatments (Fig. 2.22). This can be explained by the amount of Li+ in-diffused in crystals due to the difference in chemical potential between equilibration powders and crystals. After a determined time, when the chemical potential reaches the equilibrium, the Li+ in diffusion self terminates. If the annealing at high temperature is prolonged, the powders are not able to saturate Li_2O concentration in atmosphere for long treatment durations. Then Li out-diffusion can take place. For this reason, the Li_2O concentration in crystals treated during 48 and 64 h is slightly smaller than that of obtained

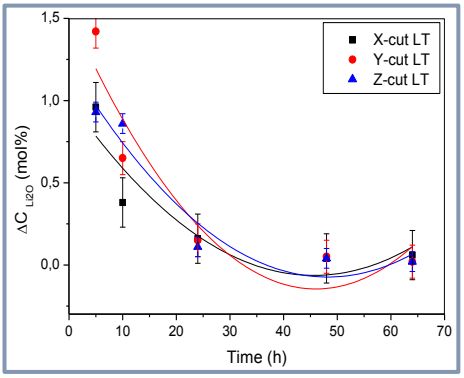

Fig. 2. 21 Effect of VTE duration time on ΔC_{Li2O} for X, Y and Z-cut LT crystals, treated at 1250°C with Li-rich powders (60 mol% of Li_2O).

for 24 h of VTE duration (see Table 2.8). However, the VTE treated crystals for 48 h and 64 h were more homogenous. It indicates that a time between 24 and 48 h could provide more stoichiometric and homogenous crystals.

From these experiments, it was found that the treatment duration of >24 h at 1250°C is well adapted to obtain in a controlled way, crystals with homogenous distribution of Li_2O in all volume of the crystal with thickness of 0.5 mm. In the case of crystals treated for 48 h and 64 h using equilibration powders with 60 mol % of Li_2O, the Li content in crystals was nearly stoichiometric. It should be noted that at temperatures lower than 1250°C, longer treatment times are needed to obtain homogenous crystals. P.F. Bordui et al. [17] have reported that the VTE treatment of LN realized at 1100°C using Li-rich powders requires between 100 and 200h, in order to obtain stoichiometric crystals and 300-400 h are required at 1050°C.

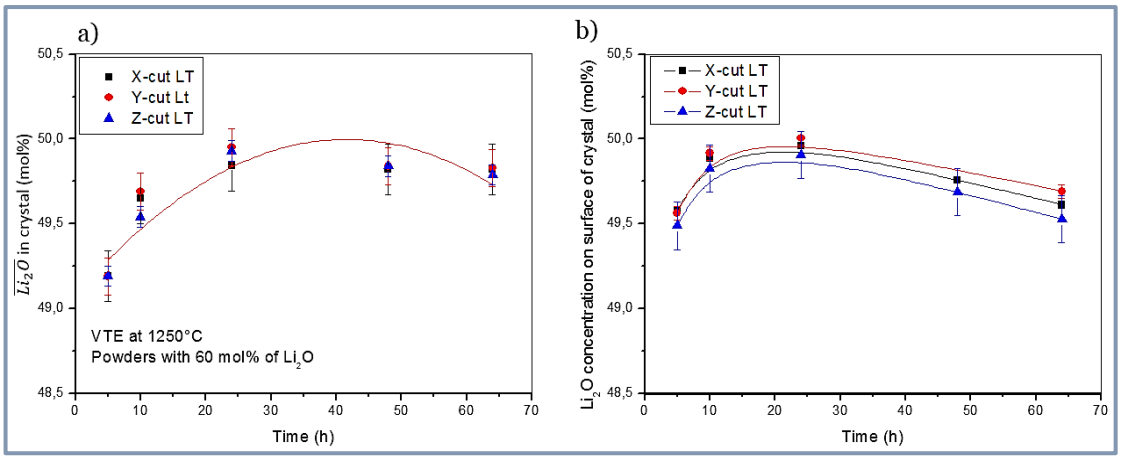

Fig. 2.22 Dependence of average Li_2O concentration measured on cross section (a) and on surface (b) of X-, Y- and Z-cut LT treated crystals on VTE durations. VTE was done at 1250°C by using powders with 60 mol% of Li_2O.

2.3.2.3 Relationship between Li_2O concentration in equilibration powders and treated crystals.

Z, Y and 42 RY-LT crystals were treated using equilibration powders with X_{Li2O} of 40-60 mol% at 1250°C for 64 h. The dependence of Li_2O concentration in VTE treated crystals on the composition of equilibration powders is given in Fig. 2.23.

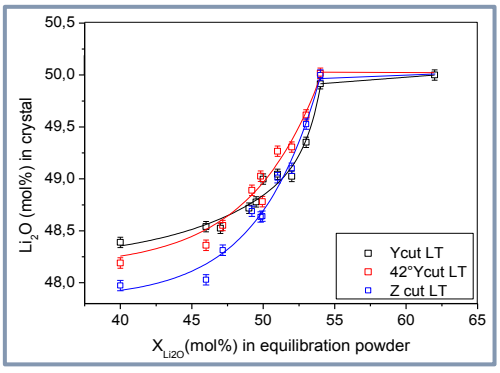

Fig. 2. 23 Variation of lithium concentration in crystal as a function of the Li content in equilibration powders. The crystals were treated

Lithium concentration in crystals increases nonlinearly with increasing Li_2O content in powders. Crystals treated with Li-poor powder, X_{Li2O}=40 mol %, have Li_2O content slightly lower than untreated crystal, between 47.98 and 48.40 mol%. In this case,

equilibration powders act as an infinite sink of Li_2O and the Li ions within the crystal out-diffuse to the surface at elevated temperatures and the Li_2O evaporates [19]. Crystals treated with powders containing >50 mol % Li_2O have a higher concentration (48.6-50 mol%) than congruent crystals. Equilibration powders with different Li_2O concentrations can be used in order to obtain crystals with desired homogenous concentration from sub-congruent to stoichiometric composition. Moreover, when equilibration powders with $X_{Li2O} \geq 54$ mol % are used, stoichiometric crystals were obtained. In this case, when the atmosphere is saturated by vapor of Li_2O, the Li_2O content on crystal surface is saturated as well. It reaches the highest value which can be accommodated by the single phase $LiTaO_3$ (50 mol %). Thus, Li_2O concentration is hold stoichiometric even if powders with higher Li_2O concentration (i.e. 60 mol %) are used. Lithium concentration in treated crystals depends also on the crystallographic cut because the diffusion velocity changes with crystallographic axis, as described above. The curve shown in the Fig. 2.23 was fitted by using an exponential function. Therefore, the expected content of Li_2O in the treated crystals (% Li_2O) can be estimated from the concentration of Li_2O in the equilibration powders (X_{Li2O}) by using the following equations:

$$\%Li_2O = 48.40 + 8.82x10^{-8}e^{X_{Li_2O}/3.25} \quad \textit{for Y-cut LT;} \qquad \textit{Eq. 2. 30}$$

$$\%Li_2O = 48.01 + 7.69x10^{-5}e^{X_{Li_2O}/5.32} \quad \textit{for 42RY-LT;} \qquad \textit{Eq. 2. 31}$$

$$\%Li_2O = 47.84 + 8.81x10^{-6}e^{X_{Li_2O}/4.35} \quad \textit{for Z-cut LT;} \qquad \textit{Eq. 2. 32}$$

In summary, it has been shown that Li_2O content in powders allows to control the Li_2O concentration in crystal. The parameters of VTE required to provide homogeneous crystals were temperature of 1250°C and duration >24h. We will use a duration of 48 h in VTE treatments of 42 RY-LT in order to obtain completely homogeneous crystals.

2.3.2.4 Twinning and surface quality of VTE treated crystals

The surface and cross section of previously presented crystals treated by VTE were observed by using optical microscope. In the case of VTE realized at the same temperature but by using powder with different Li content, it was found that the concentration of Li_2O in powders has a high impact on the surface quality of treated crystals. The images of the surfaces of Y-cut LT crystals treated at 1200°C during 10h are given as an example in Fig. 2.24.

The surface of X-, Y- and Z-cut LT crystals treated using equilibration powders with 40 mol% of Li_2O seems to be very rough. The surface defects arranged in lines were observed in X-, Y- and Z-cut crystals treated by equilibration powders with 60 mol% of Li_2O. The

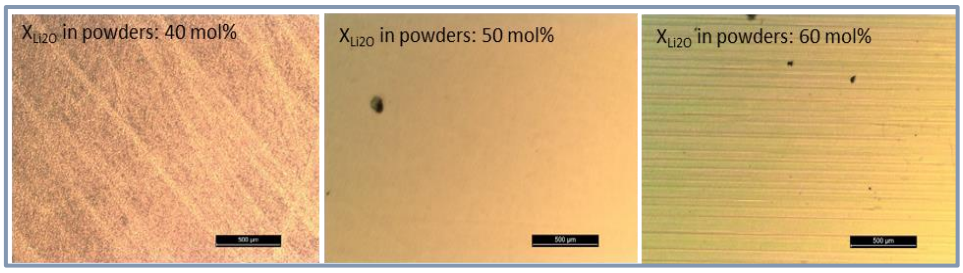

Fig. 2. 24 Optical images of surfaces of Y-cut LT crystals VTE treated at 1200°C for 10h, using equilibration powders with 40, 50 and 60 mol% of Li_2O.

surface of LT crystals treated using powders with 50 %mol of Li_2O was smooth.

In the case of the crystals treated using powders with 60 mol% of Li_2O, at different temperatures for 10 h, the presented defects, arranged in lines, were twins (Fig. 2.25 a-d). The twins were observed on the cross sections of these crystals, as well (Fig. 2.25 d-g). The twins were not observed in crystals treated using powders with 40 mol% of Li_2O. These crystals presented much lower concentration gradients. It is known that short duration of VTE (0.5-9h) yields twinned crystals. High concentration gradients generate the strain due to the lattice mismatch during cooling down [22], [57]. This strain is relaxed by the formation of twins and cracks.

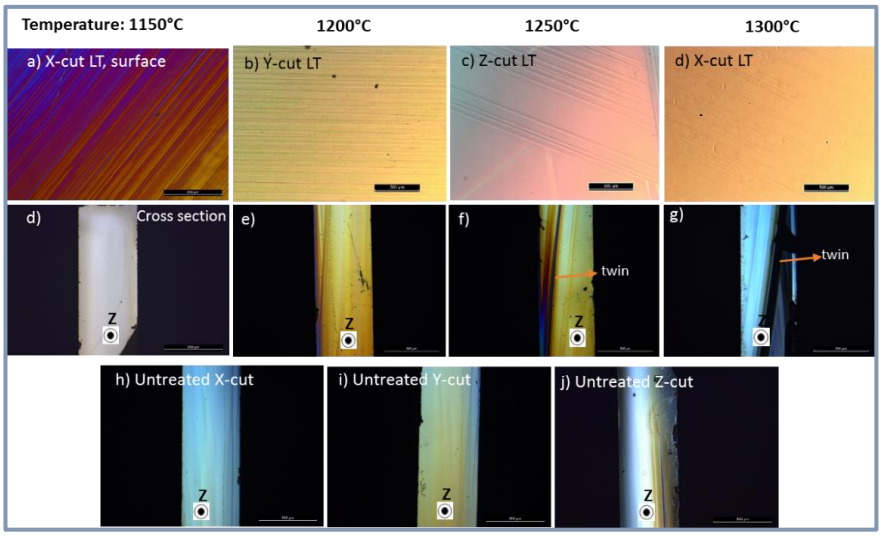

Fig. 2. 25 Optical images of surfaces (a-d) and cross sections (d-g) of X, Y and Z-cut LT crystals, VTE treated using equilibration powders with 60 mol% of Li_2O for 10 h at different temperatures.

Concerning the duration dependence series, the surface and the cross section of crystals treated for 5, 10, 24, 48 and 64 h was observed, as well (Fig. 2.26). It was found that all X-, Y- and Z-cut LT crystals were twinned, independently of the VTE duration. It seems that concentration gradient is not the only reason of the twinning of treated crystals. Homogenous nearly stoichiometric X-, Y- and Z-cut LT crystals treated at 1250°C for 48h

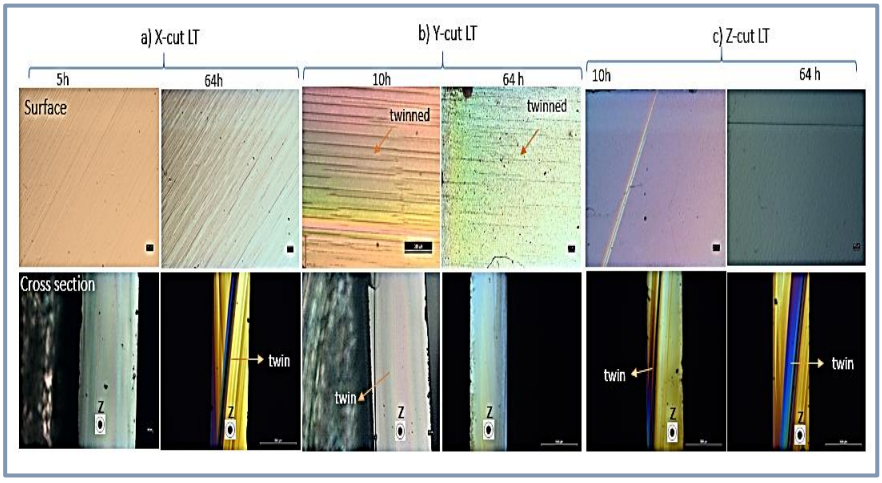

Fig. 2.26 Optical images of surfaces and cross sections of X-, Y- and Z-cut LT crystals, treated by VTE using equilibration powders with 60 mol% of Li_2O at 1250°c, for 5, 10 and 64h.

and 64h were twinned, as well. However, crystals with sub-congruent or close to congruent composition were not twinned, even if the small gradient of concentration were present. It should be noted that these experiments were realized in the Naberthem furnace whose cooling down rate cannot be controlled. The natural cooling rate after VTE treatment was too fast, especially at high temperature, it took around 20 h to cool down from 1250°C to RT. It is known that rapid cooling down rates generate mechanical twinning in LN and LT crystals [8], [22]. Thus, by reducing the cooling down rate, it is expected to have crystals of better quality. For this reason a furnace allowing to reduce the cooling down rate was used in further VTE treatment of LT crystals.

2.3.3 VTE treatment of 42 RY-LT crystals

Iron doped and undoped 42RY-LT crystals with thickness of 250 and 350 µm were processed by VTE. Several treatments were done in order to obtain crystals with sub-congruent (<48.5 mol%), stoichiometric (50 mol%) and intermediate (49.5 mol%) compositions. Equilibration powders with 60 mol% of Li_2O were re-used after treatments at 1250 °C, which provided NSLT crystals (~49.87 mol%) (see Table 2.9). These crystals were treated by using the optimized parameters presented previously *i. e.* temperature of 1250 °C and duration of 48 h. By using these conditions, it is expected to obtain homogeneous crystals. In order to check the composition homogeneity of the VTE treated crystals, scans were done on the cross section and surface of crystals by using Raman spectroscopy. The Table 2.9 shows the $\overline{Li_2O}$ concentration on surface and cross section of 42 RY-LT crystals treated by VTE. There are also some crystals that were only annealed at 750°C and 1250°C without the use of equilibration powders in crucible. The most of treatments were performed at 1250°C for 48h, but other conditions were investigated, as well. For example, the samples A3_LT40 and LT4_LT60 were VTE treated using two different temperatures of dwelling: the first step was done at 1300°C (T_1) for 24h (t_1), followed by a second step at 1100°C for 10h (T_2 and t_2).

The distributions of Li_2O concentration on the surface of 42 RY-LT crystals with thickness of 250 µm, treated with different equilibration powders are presented in the Fig. 2.27. It should be noted that all VTE processed samples have a homogenous distribution of Li_2O concentration on surface, independently of the concentration in equilibration powder (Fig. 2.27-a), with exception to the locations where the crystal was in contact with the

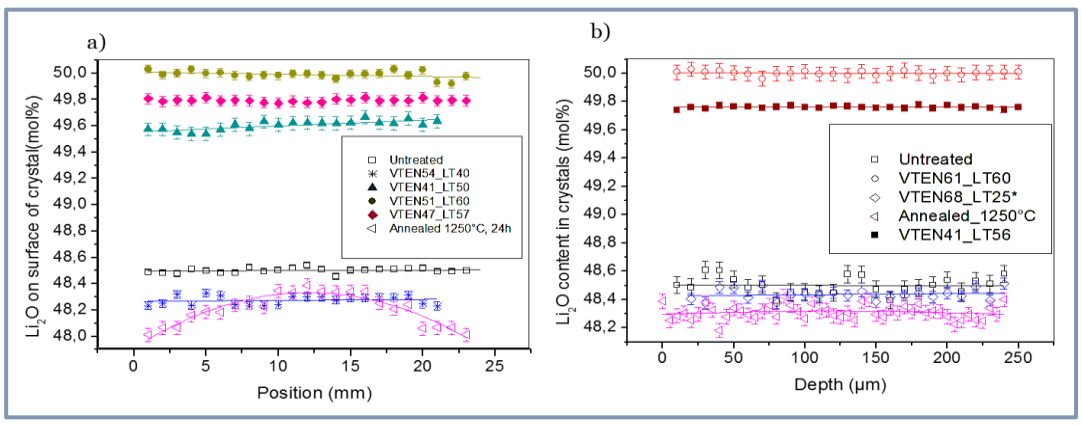

Fig. 2.27 Distribution of Li_2O concentration on surface (a) and in cross section (b) of 42 RY-LT crystals with thickness of 250µm, after VTE at 1250°C for 48 h.

crucible. The inhomogeneity due to contact with crucible can be clearly seen in the sample that was only annealed at 1250°C for 24 h without equilibration powders. The Li_2O content in treated crystal increased with the Li_2O concentration of equilibration powders, as expected. The homogeneity in the depth of treated 42 RY-LT crystals was studied by measuring Raman spectra on the cross section of crystals. The scans were performed by 10 µm steps. The crystals were homogenous independently of their composition and the treatment atmosphere (Li-rich or Li-poor) (Fig. 2.27-b).

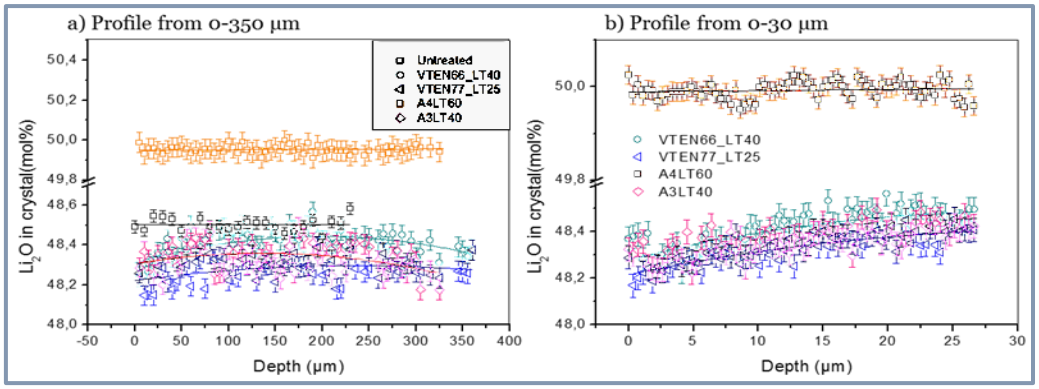

Fig. 2.28 Li_2O content on cross section of 42 RY-LT crystals with thickness of 350µm. Samples were VTE processed at 1250°c for 48h: measurements done across all the thickness of crystals (a) measurements done up to the depth of 30 µm (b). VTE conditions of these crystals can be found in the Table 2.9.

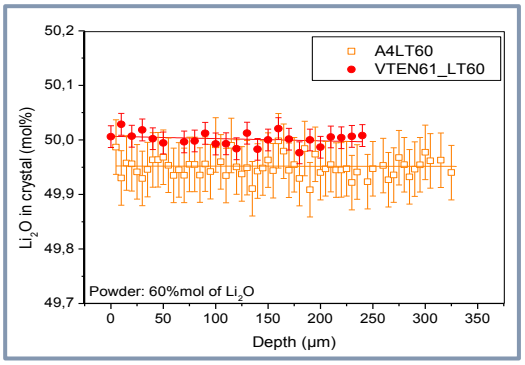

Fig. 2.29 Homogeneity in Li_2O concentration of 42 RY-NSLT crystals with thickness of 250 and 350 µm.

In the case of crystals with thickness of 350 µm, the concentration inside the crystals was characterized by studying the cross section, as well. The scanning was done with steps of 5 µm across all the thickness of the crystal. Moreover, measurements with steps of 0.5 µm from the surface to the depth of 30 µm were done in order to verify more precisely the gradients and inhomogeneity of concentration. The depth profiles of Li_2O concentration in treated 42 RY-LT crystals with thickness of 350 µm by using different Li-poor and Li-rich powders are presented in the Fig. 2.28. The sub-congruent samples (VTEN77_LT25, VTEN66_LT40 and A3_LT40) showed a small gradient of concentration close to the surface the surface. The gradient can be better seen in the case of more precise measurements (Fig. 2.28-b). Crystal with sub-congruent composition (A3_LT40), treated in two temperature steps (1300 and 1100°C) was compared to crystals treated at 1250°C for 48h (VTEN77_LT25 VTEN66_LT40). The crystals had similar $\overline{Li_2O}$ (48.20-48.38 mol%) and ΔC_{Li2O} (0.10 -0.15 mol%, see Table 2.9). Thus, no significant differences in composition were found when crystals were treated in one or in two temperature steps. Furthermore, the

crystals with Li_2O concentration higher than congruent one (>48.5 mol%) were homogenous in Li_2O concentration, independently of their thickness. The Fig. 2.29 presents as example the depth profile of concentration in the 42 RY-NSLT crystals (A4_LT60 and VTEN61_LT60 samples), with thickness of 350 and 250 µm, respectively

Table 2.9 VTE treatment conditions and Li_2O concentration measured on the cross section and surface treated 42RY-LT crystals.

Sample name	***T (°C)***	***t (h)***	***Substrate***	***Thickness (µm)***	***Li_2O in powders (mol %)***	***$\overline{Li_2O}$ on surface (mol %)***	***$\overline{Li_2O}$ in c. section (mol %)***	***ΔC_{Li2O} (mol %)***
42RY-CLT(untreated)	-	-	42 RY-LT	250	-	48.50	48.50	0.0
Annealed 750°C	750	10	42 RY-LT	250	-	48.45	48.43	0.0
A3	750	48	42 RY-LT	350	-	48.45		
Ann_1250_10	1250	10		250	-	48.39		
Annealed 1250°C	1250	24	42 RY-LT	250	-	48.20	48.31	0.00
VTEN41_LT54	1250	48	42 RY-LT	250	54	49.62		0.0
VTEN41_LT56	1250	48	42 RY-LT	250	56	49.75	49.76	0.0
VTEN42_LT55	1250	48	42 RY-LT	250	55	49.79		
VTEN43_LT62	1250	48	42 RY-LT	250	60 (used 48 h)	49.71		
VTEN56_LT60	1250	48	42 RY-LT	250	60 (used 144h)	49.69		
VTEN56_LT40	1250	48	42 RY-LT	250	40 (used 192h)	48.67		
VTEN58_LT60	1250	48	42 RY-LT:Fe	250	60	49.97	49.93	0.0
VTEN59_LT60	1250	48	42 RY-LT:Fe	250	60 (used 48h)	50.05		
VTEN60_LT60	1250	48	42 RY-LT:Fe	250	60 (used 192h)	49.87		
VTEN61_LT60	1300	48	42 RY-LT:Fe	250	60 (used 48h)	49.95	49.95	0.0
VTEN61_LT40	1300	48	42 RY-LT:Fe	250	40 (used 240h)	47.32		
VTEN62_LT40	1250	48	42 RY-LT:Fe	250	40 (used 192h)	48.99		
VTEN62_LT60	1250	48	42 RY-LT:Fe	250	60 (used 96h)	49.95		
VTEN66_LT40	1250	48	42 RY-LT:Fe	350	40	48.48	48.38	0.10
VTEN70_LT52	1250	48	42 RY-LT:Fe	350	60 (used 48h)	49.90		
VTEN71_LT60	1250	48	42 RY-LT:Fe	350	60 (used 48h)	49.90		
VTEN72_LT25	1250	48	42 RY-LT:Fe	350	25 (used 48h)	48.52		
VTEN74_LT60	1250	48	42 RY-LT:Fe	350	60 (used 192h)	49.59		
VTEN75_LT50	1250	48	42 RY-LT:Fe	350	50(used 48h)	49.21		
VTEN76_LT50	1250	48	42 RY-LT:Fe	350	50(used 96h)	48.49		
VTEN77_LT25	1250	48	42 RY-LT:Fe	350	25 (used 96h)	48.10	48.25	0.15
VTEN78_LT50	1250	48	42 RY-LT:Fe	350	50(used 144 h)	48.46		
VTEA2_LT60	1250	48	42 RY-LT	350	60	50.00		
VTEA3_LT40	1st: 1300 2nd:1100	24 24	42 RY-LT	350	40	48.30	48.34	0.15
VTEA5_LT60	1st:1300 2nd:1100	24 24	42 RY-LT	350	60	49.9	49.9	0.00

2.3.3.1 Characterization of 42RY-LT crystals

42 RY-LT crystals were treated in the ROHDE furnace, which allows to control the rate of cooling down. We kept the minimal contact between the crucible and the crystals. The surface of 42 RY- LT crystals were observed by optical microscope after VTE and the roughness of several treated crystals was measured by AFM (Fig. 2.30). The results are summarized in Table 2.10. We found that crystals annealed at high temperatures (1250°C) and VTE–treated crystals had rough surfaces. Rough surfaces of VTE treated samples were reported in Ref. [16]. Annealed crystals had roughness two times higher than untreated samples. VTE treated samples show higher roughness than crystal annealed at 1250°C during 10 h without the use of equilibration powders. The quality of surface of treated crystals was improved by mechanical polishing during 1.5 hours (see Table 2.10 and the Fig. 2.30-b and c). According to these results, annealed and VTE treated crystals had an increased roughness around 1 nm. The crystal quality of surface is considerably improved by mechanical polishing (R_{rms}~0.3 nm). For example the RMS of the VTEN74_LT60 sample was improved from 1.05 nm to 0.27 nm.

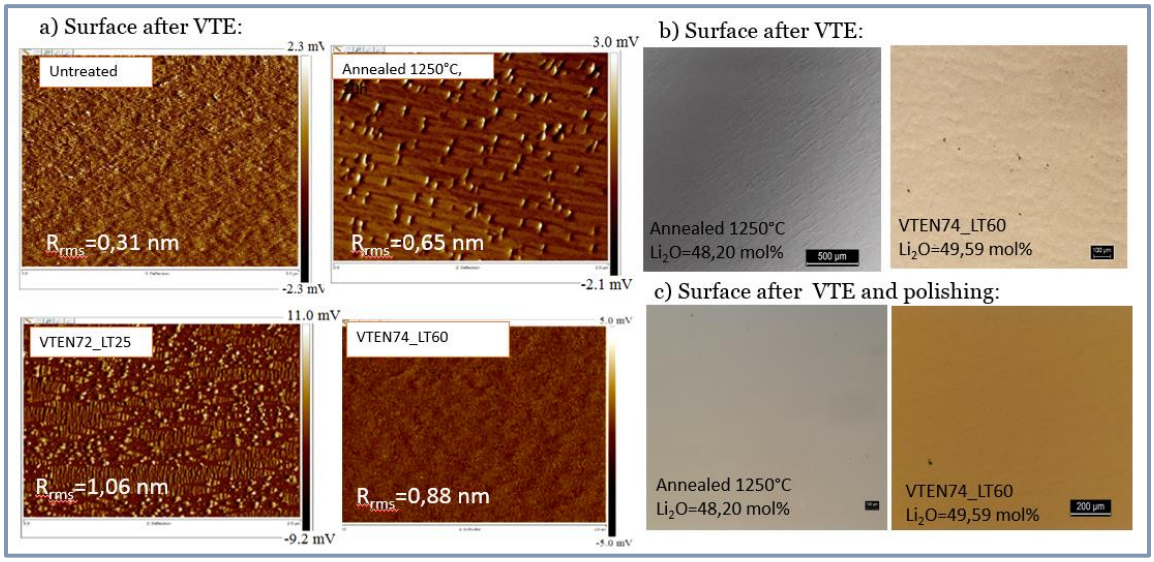

Fig. 2.30 Surface quality of 42RY-LT VTE treated crystals and annealed crystals at 1250°C without the use of equilibration powders: AFM images and roughness (a); optical images of surface after VTE treatment (b); optical images of the same crystals after polishing by 1.5 hours (c).

Table 2. 10 Roughness of 42RY-LT crystals processed y VTE

Sample	***%Li_2O on surface (mol%)***	***R_{rms} (nm±0.07)***	
		After VTE	***After polishing***
42RY-CLT (untreated)	48.5	0.31	-
Annealed 1250°C	48.39	0.65	0.31
VTEN76_LT50	48.49	1.13	0.37
VTEN72_LT25	48.52	1.06	-
VTEN71_LT60	49.9	0.88	0.25
VTEN74_LT60	49.59	1.05	0.27

Fig. 2.31-a and b present the optical images of cross sections of 42RY-NSLT and 42RY-sub CLT crystals (VTEN61_LT60 and VTEN66_LT40, respectively) treated at 1250°C for 48h. The cross sections of crystals treated by using at two different temperatures (see Table 2.9 for A4_LT60 and A3_LT40) are presented in the Fig. 2.31-c and d, respectively. All crystals were free of twins and cracks.

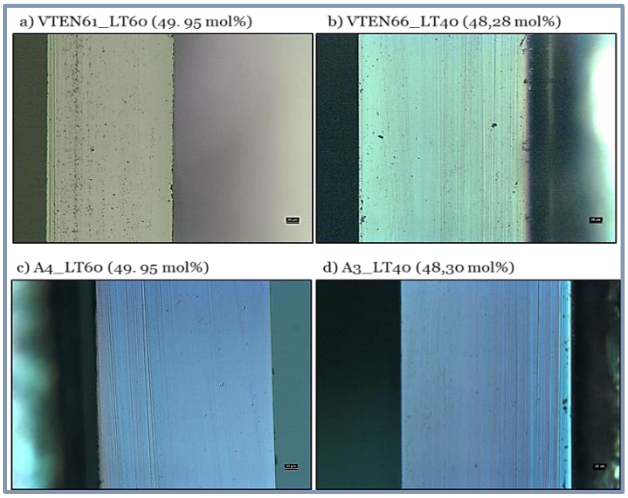

Fig. 2. 31 Optical images of cross section of 42RY-NSLT (a, c) and 42RY-subCLT crystals (b, d) treated by VTE: at 1250°C for 48h (a, b); crystals treated using dwellings at two different temperatures, the first step was done at 1300°C for 24h, followed by a second step at 1100°C for 10h (c, d).

2.3.4 Vapour Transport Equilibration of Lithium Niobate

128 RY-CLN crystals with thickness of 350 µm were treated by VTE using powders with X_{Li2O}=25 and 40 mol% of Li_2O in order to obtain 128 RY sub-CLN crystals. In this case, the treatments were performed at 1050°C and several dwelling times were tested: 5, 10, 25 and 99 h. The concentration of Li_2O within the crystals was estimated by scanning the cross section of the crystals by Raman spectroscopy. The scans were done with steps of 5 µm. Moreover, more precise scans from the surface into the depth of 30µm was done with steps of 0.5 µm. The Li_2O concentration of crystals was estimated from Eq.2.9. The concentration profiles of Li_2O content within the treated crystals are given in the Fig. 2.32. All treated 128 RY-LN crystals exhibited a small gradient of concentration. The average concentration of Li_2O ($\overline{Li_2O}$) of the crystals and the concentration change from the surface to the depth of 30 µm (ΔC_{Li20}) of these LN crystals are summarized in Table 2.11.

Table 2. 11 Effect of VTE duration on the average Li content (measured on cross section) of 128RY-cut LN treated by VTE at 1050°C using equilibration powders with 25 and 40 mol% of Li_2O.

	VTE: powders with 25%mol of Li_2O		**VTE: powders with 40%mol of Li_2O**	
Time (h)	**$\overline{Li_2O}$ (mol%)±0.06**	**ΔC_{Li2O} (mol%)±0.05**	**$\overline{Li_2O}$ (mol%)±0.06**	**ΔC_{Li2O} (mol%)±0.05**
5	48.34	0.12	48.37	0.10
10	48.33	0,14	48.33	0.18
25	48.22	0.13	48.26	0.13
50	48.16	0,21	48.11	0.22
99	47.99	0,41	48.02	0.28

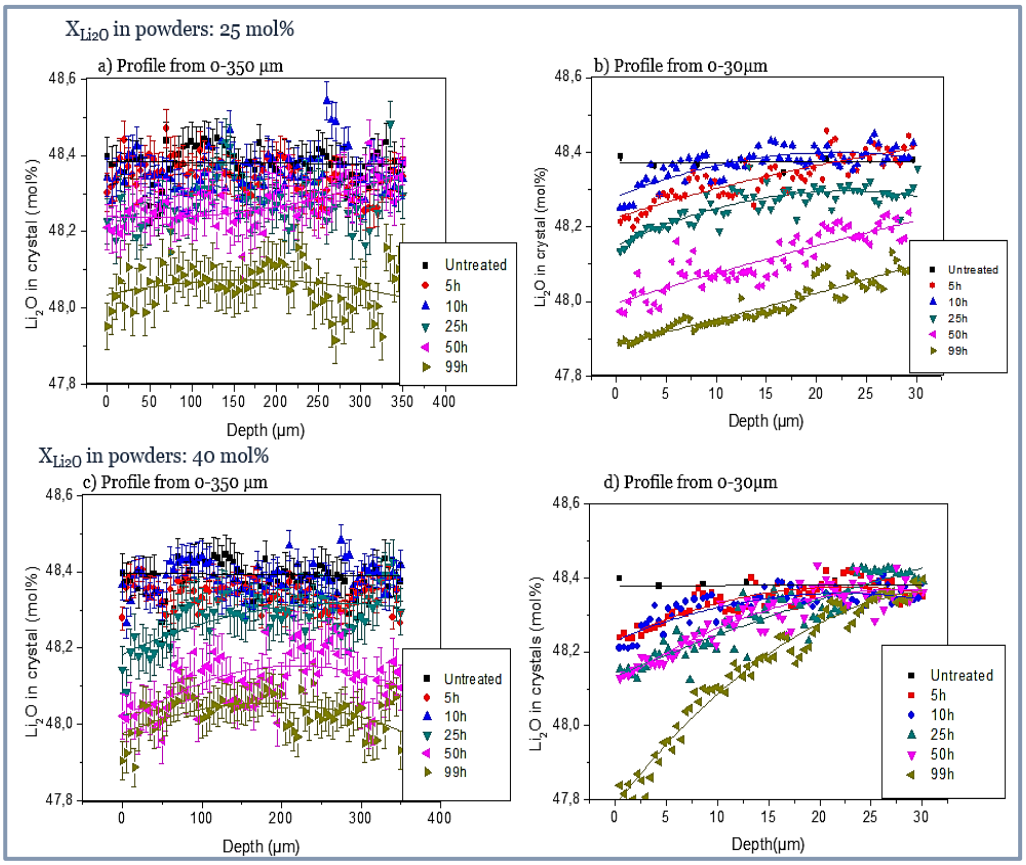

Fig. 2.32 Li_2O concentration, measured on the cross section of treated 128RY-LN crystals as a function of VTE duration: depth profile of samples measured across the thickness of the crystal (a, c); Li_2O distribution in the surface layer of 30 µm of crystal (b, d). The error bars were omitted here in order to facilitate the reading. The VTE treatments were done at 1050°C using powders with 25 and 40 mol% of

The Fig.2.33-a shows the dependence of $\overline{Li_2O}$ on the VTE duration. The Li_2O content decreases with the increase of treatment duration. One observes a quadratic relationship between the Li_2O losses and the duration of VTE. A similar relationship was reported on the time dependence of Li content on the surface of sub-congruent X and Z- cut LN crystals [27]. Moreover, the Li_2O concentration decreases similarly in crystals treated using equilibration powders with 25 and 40 mol% of Li_2O. The ΔC_{Li2O} increases with duration of treatment (Fig. 2.33-b). After 99 h of treatment, the ΔC_{Li2O} is slightly higher in crystals treated using

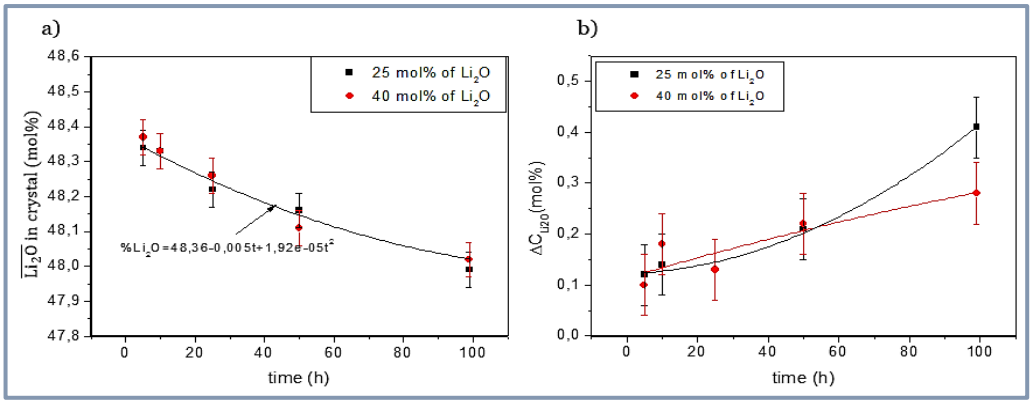

Fig. 2.33 Effect of VTE duration on average Li_2O concentration reduction (a) and on the gradient of concentration (b) in 128RY- LN crystals treated using equilibration powders with 25 and 40%mol of Li_2O at 1050°C.

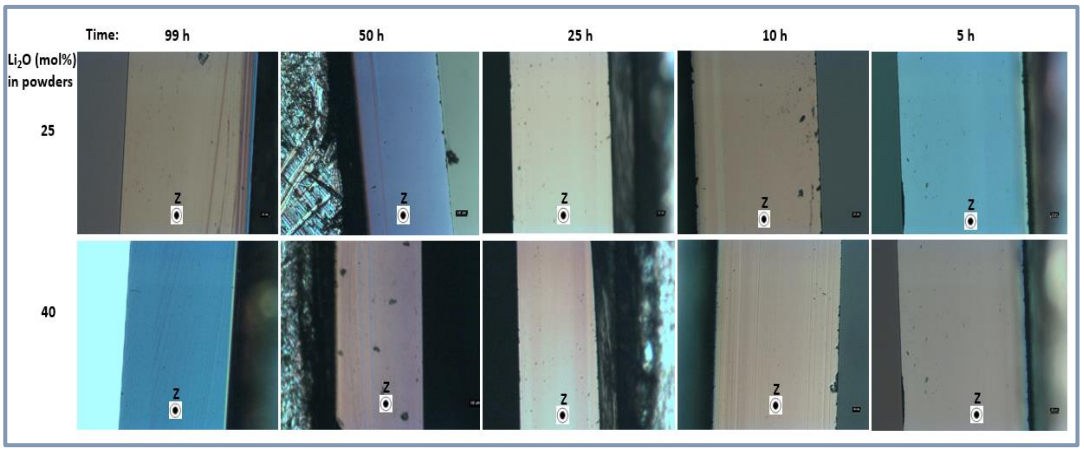

Fig. 2.34 Optical images of cross sections of 128 RY-LN crystals treated by VTE at 1050°C for 5-99 h, using equilibration powders with 25 and 40 mol% of Li_2O.

powders with 25 mol% of Li_2O.

The cross–section of treated 128 RY-LN crystals was observed by optical microscope (Fig. 2.34). Crystals treated using powders with 25 and 40 mol% of Li_2O presented similar surface morphology and were free of cracks and twins as well.

To summarize, the Li ions out-diffuse to the surface of the crystal and it looses Li_2O. By increasing the duration of VTE, the quantity of lost Li is more and more important, which creates a bigger gradient of concentration. Li-poor powders react as an infinite sink of Li_2O. A reduction in Li content of 0.4 mol% in crystals was obtained by VTE treatment for 99 h. It has been reported that longer treatments (400 h) are required in order to obtain LN crystals with concentration close to the Li-deficient boundary (~46.5 mol%)[16], [27]. For the purpose of this work, only a diminution in Li_2O concentration of <1 mol% was required in order to evaluate the effect of Li-deficiency on the performance of acoustic devices.

2.4 Technological transfer to 4 inch wafers

VTE process was optimized by using small samples. The first experiments realized on 4" wafers of 42RY-LT crystals indicated that the annealed/VTE treated crystals exhibit an important deformation (warping). In order to eliminate the warping, several experiments were conducted. The experimental set-ups tested in order to reduce the bowing height of treated wafers are illustrated in Fig. 2.35. The wafers, positioned on Al_2O_3 crucibles with different sizes, were annealed without equilibration powders. The effects of size of wafers and crucible, polarity, surface quality (polished and unpolished),

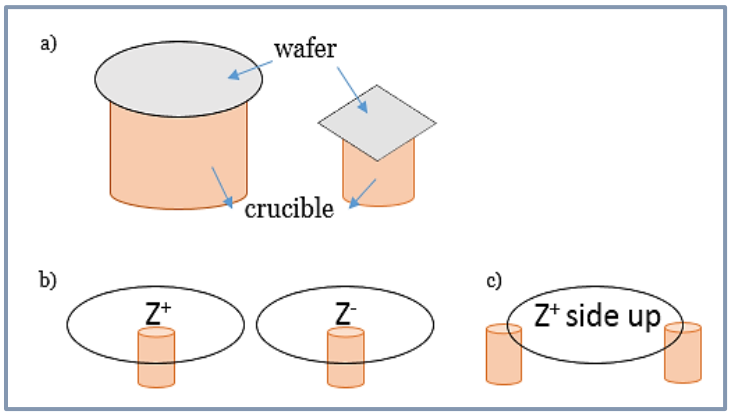

Fig. 2.35 Experimental set-ups used to test the possibility to reduce the bowing of wafers. Effects of wafer/crucible size (a); effect of polarity and surface quality (b); wafer placed on two crucibles (c).

temperature, time and the placement of the wafers and different heating profiles were investigated, as described in details in the following sections. We used SAW grade wafers, which had one-side optically polished and the rough backside (Z^+ and Z^-, respectively). After that, the bow height was measured with the gage check probe, the FSM system and the interferometer ZYGO (methods described in the Section 2.2.5.1).

2.4.1 Effect of wafer/ crucible's size and polarity

In order to determine the effect of the diameter of crucible, the size and polarity/ surface roughness on the bowing, wafers of different sizes were positioned with the Z^+ or Z^- side up, on crucibles with different diameters (Fig. 2.35-a, b). Then, crystals were annealed at 1250°C during 10 h. The Table 2.12 summarizes the results obtained on bowing as a function of size ratio of crucible/crystal and the crystal polarity/surface roughness. The negative and positive signs of Δh_3 indicate that the shape is concave and convex, respectively. We observed a difference between the results obtained by using the three characterization methods. In the case of gage check probe the bow height is measured locally, in the middle of the wafer, whereas the other two methods take into account the curvature of wafer. The industrial lines require the wafers with bow height <40 µm. The bow height in this range was measured in untreated wafers by the FSM system and the interferometer (see Table 2.12). Thus, these values were used as references.

Table 2. 12 Effect of sizes of wafer and crucible on the bowing of 42RY-LT wafer, with thickness of 250 µm, heated at 1250°C for 10h. The bow height values were obtained by several methods, where NM stands for not-measured.

			Measurement of bow height (Δh_3)		
No. experiment	***Diameter of wafer***	***Ø crucible (mm)***	***Gage check probe (±2µm)***	***FSM system (±1 µm)***	***Interferometer ZYGO (±2µm)***
Z^+ (polished) side up:					
Untreated (reference)	4"	-	0	-17	-19
1	4"	60	- 672	NM	NM
2	30mm	20	-5	-21	-17
3	4"	15	-2	-25	-22
Z^- (unpolished) side up:					
4	4"	60	570	NM	NM
5	4"	15	1	23	22

In the experiments 1 and 2, the size of crucible and wafers was chosen in order to keep constant the ratio of crucible /crystals (~2.77). The 4" wafer is 3 times bigger than the small sample but the bow height of 4" wafer is 135 times bigger than the second one, according to measurements done by using the gage check probe. Thus, the effect of the size of wafer is very important. In the experiments 1 and 3, the size of wafer is constant but the size of crucible changes. Thus, by reducing the diameter of crucible from 60 to 15 mm, the value of bow height decreases considerably (300 times). It indicates that due to the smaller contact area between the crucible and the wafer, the possibility for chemical interaction between the two materials at high temperature is reduced, resulting in less warped wafers. Crystals are non-polar at high temperature (1250°C), thus different warping of crystals with polished and rough surfaces in contact with crucible were expected. Comparing the experiments 3 and 5,

where the only difference is the position of wafer (Z+ or Z- side up), it can be seen that the sign of bow height is opposite in the two experiments. This indicates that the wafer deforms to decrease the size of polished surface and to increase the rough one. The lowest value of bow height (Δh_3) was obtained when the diameter of crucible was 15 mm. However these experiments were done during 10 h and as we discussed above, the time required for our VTE treatment is >24 h hours. Therefore, the effect of time was investigated, which is presented in the next section.

2.4.2 Effect of annealing duration

The effect of annealing duration on warping of wafers was studied for 4"wafers of 42RY- LT, annealed at 1250°C. For these experiments, we used a crucible with diameter of 15 mm (using the crucible configuration showed in the Fig. 2.35-b). It was observed that by increasing the time, the concave deformation of wafers positioned on the crucible with the Z^+ side up became more pronounced for longer treatments (see Fig. 2.36-a and b). The wafers heated with Z^- side up presented a convex shape (Fig. 2.36-d). Their deformation increased considerably with duration of annealing, as well (see Fig. 2.36-c). After annealing for 10h, the bowing height was close to the maximum value permitted for targeted applications (≤40 µm). However, the thermal treatment for 48 h induced a bow height of 1051 and 1186 µm (see experiments 10-12 in Table 2.13). Such high value of bow height is not acceptable for practical use of wafers in industrial lines. Furthermore, another support crucible-crystal configuration was tested. It consists in support of the 4" wafer by two crucibles of 15 mm of diameter (as shown in the Fig. 2.35-c.) The effect of the annealing duration on the bowing of crystals placed on the two crucibles is summarized in the Table 2.13 (experiments 13-15). The values of Δh_3 are similar to those obtained by using only one

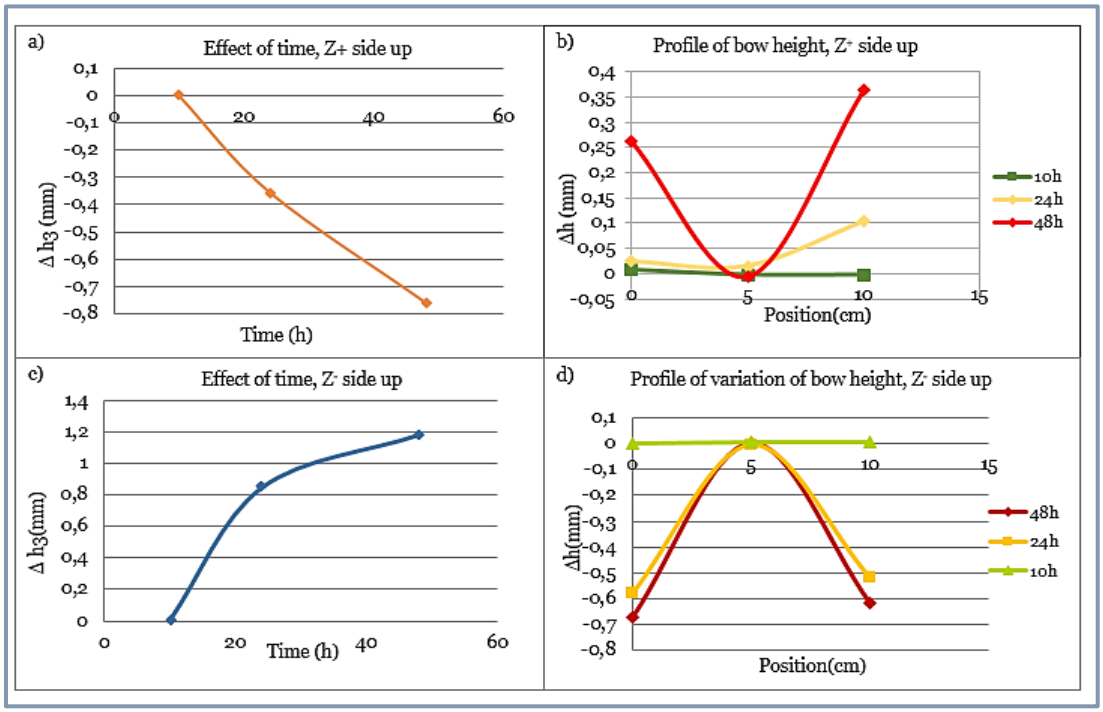

Fig. 2.36 Bow height of 4" 42RY-LT wafers with thickness of 250µm as a function of annealing duration. The annealing was carried out at 1250°C, without equilibration powders.

crucible.

Table 2.13 Effect of temperature and annealing duration on the bow height of wafer with thickness of 250 µm. The bow height values were obtained by several methods, where nm stands for non-measured.

			Measurement of bow height (Δh_3)					
Wafer supported by one crucible:			***Gage check probe (±2µm)***		***FSM (±1 µm)***		***Interferometer ZYGO (±2µm)***	
No. experiment	**Temperature (°C)**	**Time (h)**	***Z^+ side up (µm)***	***Z^- side up (µm)***	***Z^+ side up (µm)***	***Z^- side up (µm)***	***Z^+ side up (µm)***	***Z^- side up (µm)***
Untreated	-	-	0	0	-17	17	-19	19
6	1200	10	-2	12	-24	30	nm	nm
7	1250	10	-2	1	-25	23	-22	22
8	1275	10	530	449	nm	nm	nm	nm
9	1300	10	612	847	nm	nm	nm	nm
10	1250	10	-2	1	-25	23	-22	22
11	1250	24	-518	849	nm	nm	nm	nm
12	1250	48	-1.051	1186	nm	nm	nm	nm
Wafer supported by two crucibles:								
13	1250	10	2		-28		-26	
14	1250	24	-518		nm		nm	
15	1250	48	-1089		nm		nm	

2.4.3 Effect of annealing temperature

The effect of annealing temperature on the crystal deformation was studied, as well. In these experiments, 4" wafers were annealed during 10 h at different temperatures, ranging from 1200 to 1300 °C. For this purpose, we have used the crucible with diameter of 15 mm to support the wafer. The curvature of wafers increases drastically with the increase in temperature (see Fig. 2.37-a, b) and Table 2.13, experiments 6-9). For example, after thermal treatments at 1250 °C and 1300 °C, the Δh_3 was found to be 2 and 612 µm, respectively. The effect of polarity/surface roughness was investigated, as well. In the case of wafers were positioned on the crucible with the side Z^+ up, they presented a concave shape after annealing at 1200 °C and 1250 °C. However, the wafers annealed at 1275 °C-1300 °C presented a convex deformation (see Fig. 2.37-b). In the case of crystals positioned on the crucible with the Z^- side up, no change of sign in the bowing was observed.

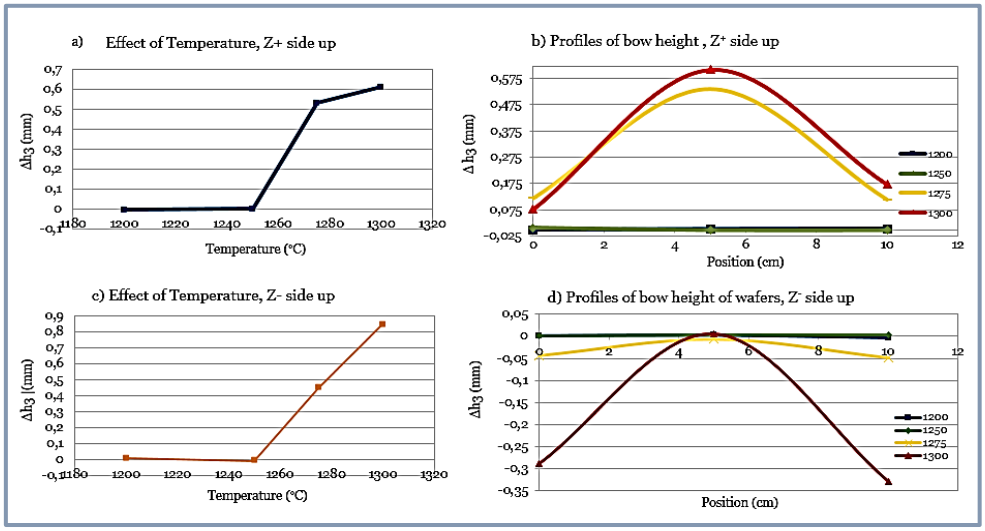

Fig. 2.37 Effect of temperature on the bow of 42RY-LT 4" wafers with 250µm of thickness (a, c) and profiles of bowing height of wafer annealed at different temperatures (b, d).

In order to reduce the warping of wafers, thermal treatments were tested with two dwelling times and temperatures. The crystals were annealed at 1250°C (T_1) during a dwelling time (t_1), then the temperature was increased to 1300 °C (T_2) and kept for a time (t_2). The Fig. 2.38-a shows the thermal ramp used in these experiments including the heating and cooling rates in each step. The values of bow height of wafers annealed at two temperature steps are presented in the Table 2.14. The 16th and 17th experiments were achieved at the same conditions but with wafers with different thickness. It should be noted that thicker wafers were flatter after annealing (smaller Δh_3) comparing to 250 µm thick wafer. For this reason, the next experiments were done by using wafers of 350 µm. It was observed that the duration of annealing had a high impact on the bow height of wafer, as in the case of single step treatments, described above (see Fig. 2.38-b). For example, comparing the 17th and 19th experiments, the increase of duration of annealing treatment at 1250 °C by 12 h results in wafer with Δh_3 increased 33 times. From these experiments, we can conclude that the best conditions of annealing were at 1250 °C during 24 h followed by a heating at 1300 °C for 10 h, which allows to obtain a bow height of 12 µm. Then, these conditions were used to treat several wafers of 42RY-LT by VTE (VTEN66 in Table 2.14). Three crucibles were prepared: i) the first one without powders, used for comparison; ii) two crucibles with equilibration powders with 40 and 60 mol% of Li_2O. After treatment at 1250 °C for 24 h and 1300 °C for 10 h, the wafer annealed without powders, had a smaller bow height (73 µm) compared to the wafers treated with equilibration powders (492 µm). The optimized bow heights were much higher than the permitted value (≤40 µm). It indicates that the vapor

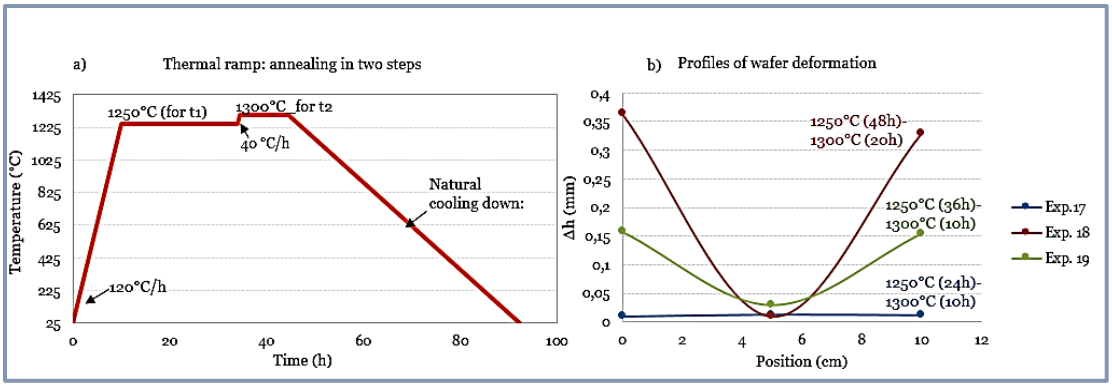

Fig. 2.38 Annealing of 4" wafers in two steps: used heating curve (a), profiles of thickness of wafers after annealing (b).

equilibration process affects also wafer deformation at high temperature.

Table 2.14 Bow height of 4" 42RY-LT wafers treated by two-step thermal process. The two dwelling times and temperatures are given, as well.

No. experiment	***T1 (°C)***	***t1 (h)***	***T2 (°C)***	***t2 (h)***	***Thickness (µm)***	***Measurement of bow height by gage check probe (Δh_3 ±2 µm)***
16	1250	24	1300	10	250	-897
17	1250	24	1300	10	350	-12
18	1250	48	1300	20	350	-81
19	1250	36	1300	10	350	-401
VTEN66 (without powders)	1250	24	1300	10	350	-73
VTEN66_LT40	1250	24	1300	10	350	492
VTEN66_LT60	1250	24	1300	10	350	467

In summary, wafers annealed at high temperature (1250 °C) for 10 hours, using a crucible of 60 mm diameter as support, were drastically deformed. We have demonstrated that by reducing the diameter of the support crucible, the bowing of wafer was reduced by 300 times, which allowed to obtain a wafer flatness close to the required value. However, for VTE treatments at 1250 °C, the duration longer than 24 h is needed to obtain compositionally homogenous crystals. But after annealing for 24 h, the bow height of wafers increased drastically to 518 µm. On the other hand it was observed that the sign of bow height changed from negative to positive when wafers were heated at temperatures higher than 1250 °C. Then, we considered the two-step thermal treatments with two dwelling times and temperatures in order to compensate the sign of curvature. Moreover, it was observed that the flatness of wafers is improved by using thicker samples (350 µm). Wafers with thickness of 350 µm, annealed at 1250 °C for 24 h and 1300 °C for 10 h, showed an acceptable bow height (12 µm). Thus, these conditions were used to realize VTE treatments with equilibration powders of 40 and 60 mol% of Li_2O. We expected to obtain wafers with a value of bow height close to the specified value but we obtained strongly warped wafers. More experiments are required in order to reduce the bowing of crystals. For example, by changing the crystal position from horizontal to vertical one or by using thicker crystals (of 0.5 mm or 1 mm). However, due to the limited time of the project, it was not possible to continue these tasks. Thus, we have used small samples (1/4 of a 4" 42 RY-LT wafers) for the fabrication of acoustic devices.

On the second hand, some VTE treatments on 128 RY-LN crystals were achieved in order to measure the warping of LN wafers. For this purpose, 4" wafers with thickness of 350 µm were VTE treated by using equilibration powders with 40 mol% of Li_2O at 1050°C for 5 and 99 h. In this case, the wafers were positioned on a platinum crucible instead of Al_2O_3 crucible. Then, the bow height was measured by using the FSM method. The Table 2.15 shows the values of bowing height obtained after VTE treatment.

Table 2.15 Bow height of 4" 128 RY-LT wafers with thickness of 350 µm, treated by VTE, using equilibration powders with 40 mol% of Li_2O at 1050 °C for different durations.

Sample	***VTE duration (h)***	***Measurement of bow height by using FSM (±1 µm)***
128 RY_LN untreated	-	-21
B3_LN40_5 h	5	-23
B13_LN40_99 h	99	-63

The bow height of VTE treated wafer for 5 h is very similar to that of the untreated sample, as expected. Longer VTE treatment provided a more warped wafer. However, the bow height of 128 RY-LN crystals is smaller by one order of magnitude compared to that of 42 RY-LT crystals (treated at 1250 °C). Thus, the temperature used in VTE treatment affects strongly the warping of wafers, as discussed above.

Finally, although the bow height obtained for 128 RY-LN wafers is almost two times higher than the required one in production lines, these samples can be used for test of acoustical properties such as the stability at high power densities.

2.5 Conclusions

In this chapter, we used the VTE method to produce LT and LN crystals with different Li_2O non-stoichiometry. In comparison with other techniques, VTE allows the preparation of LT and LN crystals with varied composition, from sub-congruent to stoichiometric, and it is relatively easy to control the parameters involved in this process. Although there are many publications about the VTE process carried out in LN crystals, it is not the case for LT crystals. For this reason, in this work, the effect of parameters of VTE process (duration, temperature, powder composition and different crystal cuts) on Li_2O non-stoichiometry of treated LT samples were investigated. From our experiments, we have determined the empirical equations that allow to quantify the dependence on duration, temperature and Li_2O concentration in powders on Li_2O content in treated crystals. It is useful to know the optimal conditions to obtain crystals with a desired concentration. On the other hand, the estimation of lithium concentration and evaluation of homogeneity of crystals was done by means of Raman spectroscopy with a rather good accuracy (0.05-0.15 mol%, depending on the crystal cut). The analysis by X-Rays diffraction was used to quantify the secondary phases (Li_3TaO_4 and $LiTa_3O_8$) in equilibration powders.

Our experimental results indicated that lithium concentration in crystals increases with X_{Li2O} in equilibration powders. Powders with $X_{Li2O} \geq 54$ mol% provide stoichiometric crystals as Li-rich equilibration powders act as an "infinite" source of Li_2O. Crystals with intermediate Li_2O concentrations (between stoichiometric and congruent) were obtained by using equilibration powders with X_{Li2O} ranging from 51 to 53%mol of Li_2O. The Li-poor equilibration powders serve as an "infinite" sink of Li_2O that can be used as long as desired, inasmuch the crystal can supply very small amount of Li_2O.

Furthermore, it was found that VTE duration and temperature are very important parameters in control of the Li_2O content and homogeneity of crystals. The duration required to produce homogenous crystals (t_{hom}) was >24 h for X-, Y- and Z-cut LT at 1250 °C. VTE treatments, carried out at 1250 °C for 48 h of crystals with ≤ 500 μm of thickness, provide homogenous crystals. Temperatures lower than 1250 °C require longer treatments. The VTE treatments of 42RY-LT performed at 1250 °C for 48 h, with slow cooling down rate provided crack-free crystals with homogenous composition. Although the surface of crystals after VTE had increased roughness, it was improved by polishing. The diffusion rate depends on temperature of VTE process. The Li-diffusivity, estimated experimentally, increases with temperature and with Li_2O concentration in powders. Furthermore, Li_2O diffusion shows anisotropy and is slightly faster along Z-axis than in the basal plane, which agrees well with information reported on LN in literature.

In the case of 128 RY-cut LN crystal, the VTE treatments were done in order to obtain sub-congruent crystals. The surface concentrations obtained were slightly smaller than the congruent, 47.93 and 47.91 mol% of Li_2O, in crystals treated for 99 h and by using equilibration powders of 25 and 40 mol%, respectively. These crystals presented a small gradient of concentration, which increased with duration of VTE. Longer times (~400 h) are required to obtain completely homogenous LN crystals and with Li_2O concentrations close to Li-poor boundary of single phase.

Finally, several experiments were conducted to investigate the upscaling of VTE process from small samples to 4”of 42 RY-LT wafers. It was found that the annealing in two steps including two dwelling times at different temperatures (1250 °C for 24 and 1300 °C for 10 h) provided a bow height >76 μm (2 times higher than the required). Such high value of bow height of wafers makes impossible their use in the industrial process lines. More experiments are required in order to reduce the bow height of wafers during treatment at high temperatures. For this reason, we have used small samples to prepare and characterize the BAW and SAW devices (presented in 4th Chapter). In the case of 4” 128 RY-LN wafers, the warping of VTE treated crystals at 1050 °C for 99 h was smaller than that of 42 RY-LT wafers by one order of magnitude. The 128 RY-LN wafers with sub-congruent composition can be used for fabrication of acoustic devices. However, we did the upscaling of VTE of 128 RY-LN wafers at the end of my thesis and it was not possible to accomplish this final task.

2.6 References

[1] A. A. Ballman, "Growth of Piezoelectric and Ferroelectric Materials by the CzochraIski Technique," *J. Am. Ceram. Soc.*, vol. 48, no. 2, pp. 112–113, Feb. 1965.
[2] K. Nassau, H. J. Levinstein, and G. M. Loiacono, "Ferroelectric lithium niobate. 1. Growth, domain structure, dislocations and etching," *J. Phys. Chem. Solids*, vol. 27, no. 6–7, pp. 983–988, Jun. 1966.
[3] D. P. Shumov, J. Rottenberg, and S. Samuelson, "Growth of 3-inch diameter near-stoichiometric LiTaO3 by conventional Czochralski technique," *J. Cryst. Growth*, vol. 287, no. 2, pp. 296–299, Jan. 2006.
[4] L. Gao, J. Y. Wang, H. Liu, X. B. Hu, S. H. Yao, J. B. Wu, X. Y. Qin, and R. I. Boughton, "Inhomogeneity of composition in near-stoichiometric LiNbO3 single crystal grown from Li rich melt," *Cryst. Res. Technol.*, vol. 41, no. 4, pp. 332–336, Apr. 2006.
[5] S. Yao, J. Wang, H. Liu, X. Hu, H. Zhang, X. Cheng, and Z. Ling, "Growth, optical and thermal properties of near-stoichiometric LiNbO3 single crystal," *J. Alloys Compd.*, vol. 455, no. 1–2, pp. 501–505, May 2008.
[6] K. Kitamura, J. K. Yamamoto, N. Iyi, S. Kirnura, and T. Hayashi, "Stoichiometric LiNbO3 single crystal growth by double crucible Czochralski method using automatic powder supply system," *J. Cryst. Growth*, vol. 116, no. 3–4, pp. 327–332, Feb. 1992.
[7] Y. Furukawa, K. Kitamura, E. Suzuki, and K. Niwa, "Stoichiometric LiTaO3 single crystal growth by double crucible Czochralski method using automatic powder supply system," *J. Cryst. Growth*, vol. 197, no. 4, pp. 889–895, Mar. 1999.
[8] S. Kumaragurubaran, S. Takekawa, M. Nakamura, and K. Kitamura, "Growth of 4-in diameter near-stoichiometric lithium tantalate single crystals," *J. Cryst. Growth*, vol. 285, no. 1–2, pp. 88–95, Nov. 2005.
[9] K. Polgár, Á. Péter, and I. Földvári, "Crystal growth and stoichiometry of LiNbO3 prepared by the flux method," *Opt. Mater.*, vol. 19, no. 1, pp. 7–11, Feb. 2002.
[10] K. Polgár, Á. Péter, L. Kovács, G. Corradi, and Z. Szaller, "Growth of stoichiometric LiNbO3 single crystals by top seeded solution growth method," *J. Cryst. Growth*, vol. 177, no. 3–4, pp. 211–216, Jun. 1997.
[11] G. I. Malovichko, V. G. Grachev, E. P. Kokanyan, O. F. Schirmer, K. Betzler, B. Gather, F. Jermann, S. Klauer, U. Schlarb, and M. Wöhlecke, "Characterization of stoichiometric LiNbO3 grown from melts containing K2O," *Appl. Phys. A*, vol. 56, no. 2, pp. 103–108, 1993.
[12] K. Polgár, Á. Péter, I. Földvári, and Z. Szaller, "Structural defects in flux-grown stoichiometric LiNbO3 single crystals," *J. Cryst. Growth*, vol. 218, no. 2–4, pp. 327–333, Sep. 2000.
[13] S. Solanki, T.-C. Chong, and X. Xu, "Flux growth and morphology study of stoichiometric lithium niobate crystals," *J. Cryst. Growth*, vol. 250, no. 1–2, pp. 134–138, Mar. 2003.
[14] Y. S. Luh, M. M. Fejer, R. L. Byer, and R. S. Feigelson, "Stoichiometric LiNbO3 single-crystal fibers for nonlinear optical applications," *J. Cryst. Growth*, vol. 85, no. 1–2, pp. 264–269, Nov. 1987.
[15] R. L. Holman, P. J. Cressman, and J. F. Revelli, "Chemical control of optical damage in lithium niobate," *Appl. Phys. Lett.*, vol. 32, no. 5, pp. 280–283, Mar. 1978.
[16] P. F. Bordui, R. G. Norwood, D. H. Jundt, and M. M. Fejer, "Preparation and characterization of off-congruent lithium niobate crystals," *J. Appl. Phys.*, vol. 71, no. 2, pp. 875–879, Jan. 1992.
[17] P. F. Bordui, R. G. Norwood, C. D. Bird, and J. T. Carella, "Stoichiometry issues in single-crystal lithium tantalate," *J. Appl. Phys.*, vol. 78, no. 7, pp. 4647–4650, Oct. 1995.
[18] R. Bhatt, I. Bhaumik, S. Ganesamoorthy, A. K. Karnal, P. K. Gupta, M. K. Swami, H. S. Patel, A. K. Sinha, and A. Upadhyay, "Study of structural defects and crystalline perfection of near stoichiometric LiNbO3 crystals grown from flux and prepared by VTE technique," *J. Mol. Struct.*, vol. 1075, pp. 377–383, Oct. 2014.
[19] X. Liang, X. Xuewu, C. Tow-Chong, Y. Shaoning, Y. Fengliang, and T. Y. Soon, "Lithium in-diffusion treatment of thick LiNbO3 crystals by the vapor transport equilibration method," *J. Cryst. Growth*, vol. 260, no. 1–2, pp. 143–147, Jan. 2004.

[20] G. I. Malovichko, V. G. Grachev, L. P. Yurchenko, V. Y. Proshko, E. P. Kokanyan, and V. T. Gabrielyan, "Improvement of LiNbO3 Microstructure by Crystal Growth with Potassium," *Phys. Status Solidi A*, vol. 133, no. 1, pp. K29–K32, Sep. 1992.
[21] D.-L. Zhang, B. Chen, D.-Y. Yu, and E. Y.-B. Pun, "Influence of Factors on Growth of Off-Congruent LiNbO3 Single-Crystal by Li-Rich/Li-Poor Chemical Vapor Transport Equilibration," *Cryst. Growth Des.*, vol. 13, no. 4, pp. 1793–1798, Apr. 2013.
[22] N. Cheng, W. Hua, X. Feng, and H. Ta, "Modification of lithium niobate crystals using vapour phase transport equilibration technique," *Mater. Sci. Eng. B*, vol. 33, no. 2–3, pp. 91–95, Sep. 1995.
[23] Z. Wang, P.-R. Hua, B. Chen, D.-Y. Yu, E. Y.-B. Pun, and D.-L. Zhang, "Li-Rich/Li-Poor Vapor Transport Equilibration Time Dependence of Surface Composition of Congruent LiNbO3 Crystal," *J. Am. Ceram. Soc.*, vol. 95, no. 5, pp. 1661–1664, May 2012.
[24] P.-R. Hua, D.-L. Zhang, Y.-M. Cui, Y.-F. Wang, and E. Y.-B. Pun, "Off-Congruent LiNbO3 Crystals Prepared by Li-Poor Vapor Transport Equilibration for Integrated Optics," *Cryst. Growth Des.*, vol. 8, no. 7, pp. 2125–2129, Jul. 2008.
[25] M. Palatnikov, O. Shcherbina, V. Sandler, N. Sidorov, and K. Bormanis, "Effects of VTE Treatment on Composition of Lithium Tantalate Single Crystals," *Ferroelectrics*, vol. 417, no. 1, pp. 46–52, Jan. 2011.
[26] D.-L. Zhang, Z. Wang, P.-R. Hua, and E. Y.-B. Pun, "Li-Rich Vapor Transport Equilibration Temperature Dependence of Surface Composition of Initially Congruent LiNbO3 Crystal," *J. Am. Ceram. Soc.*, vol. 95, no. 9, pp. 2798–2800, Sep. 2012.
[27] D.-L. Zhang, B. Chen, P.-R. Hua, and E. Y.-B. Pun, "Influence of Postgrowth Li-Poor Vapor-Transport Equilibration on the Surface Li2O Content of a Congruent LiNbO3 Crystal," *Inorg. Chem.*, vol. 51, no. 17, pp. 9552–9556, Sep. 2012.
[28] D. H. Jundt, M. M. Fejer, R. G. Norwood, and P. F. Bordui, "Composition dependence of lithium diffusivity in lithium niobate at high temperature," *J. Appl. Phys.*, vol. 72, no. 8, pp. 3468–3473, Oct. 1992.
[29] B. Chen, P.-R. Hua, D.-L. Zhang, and E. Y.-B. Pun, "Stoichiometry Dependence of Li+ Diffusivity in LiNbO3 Crystal in Off-Congruent, Li-Deficient Regime," *J. Am. Ceram. Soc.*, vol. 95, no. 3, pp. 1018–1022, Mar. 2012.
[30] D. P. B. Iii and P. F. Bordui, "Defect-based description of lithium diffusion into lithium niobate," *J. Appl. Phys.*, vol. 76, no. 6, pp. 3422–3428, Sep. 1994.
[31] D.-L. Zhang, W.-J. Zhang, Y.-R. Zhuang, and E. Y. B. Pun, "Dynamic Simulation of Vapor Transport Equilibration in Congruent LiNbO3 Crystal," *Cryst. Growth Des.*, vol. 7, no. 8, pp. 1541–1546, Aug. 2007.
[32] C. Bäumer, C. David, A. Tunyagi, K. Betzler, H. Hesse, E. Krätzig, and M. Wöhlecke, "Composition dependence of the ultraviolet absorption edge in lithium tantalate," *J. Appl. Phys.*, vol. 93, no. 5, pp. 3102–3104, Mar. 2003.
[33] C. Bäumer, D. Berben, K. Buse, H. Hesse, and J. Imbrock, "Determination of the composition of lithium tantalate crystals by zero-birefringence measurements," *Appl. Phys. Lett.*, vol. 82, no. 14, pp. 2248–2250, Apr. 2003.
[34] U. Schlarb, S. Klauer, M. Wesselmann, K. Betzler, and M. Wöhlecke, "Determination of the Li/Nb ratio in lithium niobate by means of birefringence and Raman measurements," *Appl. Phys. A*, vol. 56, no. 4, pp. 311–315, Apr. 1993.
[35] N. Iyi, K. Kitamura, F. Izumi, J. K. Yamamoto, T. Hayashi, H. Asano, and S. Kimura, "Comparative study of defect structures in lithium niobate with different compositions," *J. Solid State Chem.*, vol. 101, no. 2, pp. 340–352, Dec. 1992.
[36] R. L. Barns and J. R. Carruthers, "Lithium tantalate single crystal stoichiometry," *J. Appl. Crystallogr.*, vol. 3, no. 5, pp. 395–399, Oct. 1970.
[37] F. Abdi, M. Aillerie, P. Bourson, M. D. Fontana, and K. Polgar, "Electro-optic properties in pure LiNbO3 crystals from the congruent to the stoichiometric composition," *J. Appl. Phys.*, vol. 84, no. 4, pp. 2251–2254, Aug. 1998.
[38] S. M. Kostritskii, M. Aillerie, P. Bourson, and D. Kip, "Raman spectroscopy study of compositional inhomogeneity in lithium tantalate crystals," *Appl. Phys. B*, vol. 95, no. 1, pp. 125–130, Mar. 2009.
[39] J. G. Bergman, A. Ashkin, A. A. Ballman, J. M. Dziedzic, H. J. Levinstein, and R. G. Smith, "Curie Temperature, birefringence, and phase matching temperature variations in LiNbO3 as a function of melt stoichiometry," *Appl. Phys. Lett.*, vol. 12, no. 3, pp. 92–94, Feb. 1968.

[40] R. S. Das and Y. K. Agrawal, "Raman spectroscopy: Recent advancements, techniques and applications," *Vib. Spectrosc.*, vol. 57, no. 2, pp. 163–176, Nov. 2011.
[41] P. Larkin, *Infrared and Raman Spectroscopy; Principles and Spectral Interpretation*. Elsevier, 2011.
[42] A. Ridah, P. Bourson, M. D. Fontana, and G. Malovichko, "The composition dependence of the Raman spectrum and new assignment of the phonons in," *J. Phys. Condens. Matter*, vol. 9, no. 44, p. 9687, Nov. 1997.
[43] B. Fultz and J. Howe, *Transmission Electron Microscopy and Diffractometry of Materials*. Berlin, Heidelberg: Springer Berlin Heidelberg, 2013.
[44] S. Margueron, A. Bartasyte, A. M. Glazer, E. Simon, J. Hlinka, I. Gregora, and J. Gleize, "Resolved E-symmetry zone-centre phonons in LiTaO3 and LiNbO3," *J. Appl. Phys.*, vol. 111, no. 10, p. 104105, May 2012.
[45] L. Shi, Y. Kong, W. Yan, J. Sun, S. Chen, L. Zhang, W. Zhang, H. Liu, X. Li, X. Xie, D. Zhao, L. Sun, Z. Wang, J. Xu, and G. Zhang, "Determination of the composition of lithium tantalate by means of Raman and OH− absorption measurements," *Mater. Chem. Phys.*, vol. 95, no. 2–3, pp. 229–234, Feb. 2006.
[46] "Pearson's Crystal Data." [Online]. Available: http://www.crystalimpact.de/pcd/Default.htm.
[47] R. Hsu, E. N. Maslen, D. Du Boulay, and N. Ishizawa, "Synchrotron X-ray Studies of LiNbO3 and LiTaO3," *Acta Crystallogr. Sect. B*, vol. 53, no. 3, pp. 420–428, Jun. 1997.
[48] D. du Boulay, A. Sakaguchi, K. Suda, and N. Ishizawa, "Reinvestigation of β-Li_3TaO_4," *Acta Crystallogr. Sect. E Struct. Rep. Online*, vol. 59, no. 5, pp. i80–i82, May 2003.
[49] B. M. Gatehouse, T. Negas, and R. S. Roth, "The crystal structure of M-LiTa3O8 and its relationship to the mineral wodginite," *J. Solid State Chem.*, vol. 18, no. 1, pp. 1–7, May 1976.
[50] "Typical Interferometer Setups." [Online]. Available: http://www.zygo.com/?/met/interferometers/setups/. [Accessed: 03-Jan-2016].
[51] "Frontier Semiconductor." [Online]. Available: http://frontiersemi.com/fsm7/Technology.php?type.
[52] Gonzalez M., "Procédé pour le contrôle du TCF dans des dispositifs à ondes élastiques de surface à base de LiTaO3," Institut National Polytechnique de Lorraine, Vandodoeuvre-lès-Nancy, France, Rapport stage Master 2, Jul. 2011.
[53] H. Mehrer, *Diffusion in Solids*, vol. 155. .
[54] W. D. Callister and D. G. Rethwisch, *Fundamentals of Materials Science and Engineering: An Integrated Approach*. John Wiley & Sons, 2012.
[55] C. Koch, I. Ovid'ko, S. Seal, and S. Veprek, *Structural Nanocrystalline Materials: Fundamentals and Applications*. Cambridge University Press, 2007.
[56] D. H. Jundt, M. M. Fejer, R. G. Norwood, and P. F. Bordui, "Composition dependence of lithium diffusivity in lithium niobate at high temperature," *J. Appl. Phys.*, vol. 72, no. 8, pp. 3468–3473, Oct. 1992.
[57] J. Yang, J. Sun, J. Xu, Q. Li, J. Shang, L. Zhang, S. Liu, and C. Huang, "Twin defects in thick stoichiometric lithium tantalate crystals prepared by a vapor transport equilibration method," *J. Cryst. Growth*, vol. 433, pp. 31–35, Jan. 2016.

Chapter 3

Domain reversal in lithium tantalate

3.1 Introduction

As described in the previous chapter, we observed that the crystals treated by VTE were in poly-domain state. In order to get the crystals with uniform polarization, electrical poling of equilibrated crystals was done. In this chapter we will overview the literature on the principles, the mechanisms and the kinetics of domain reversal in LT crystals. The mechanisms of domain reversal in congruent, stoichiometric and doped crystals will be compared. Afterwards, the experimental techniques used in this work for poling and visualization of domains will be detailed. Finally, the procedures, optimized and used in this work, for electrical poling of doped/undoped Z- and 42 RY-LT wafers with different Li stoichiometry, will be discussed.

3.1.1 Electric field poling

LT and LN are ferroelectric materials and thus, their spontaneous polarization can be reversed. One of the techniques used to obtain single-domain LN crystals is the application of an electric field along the polar axis during the crystal growth *(in-situ* electric field poling*)* [1]–[3]. The most common poling technique used in industry of ferroelectric single-crystals is the ex-situ electrical poling of grown poly-domain crystals. In this case, the electric field applied has to be higher than the electric coercive field, E_c, of crystal (defined in section 1.1.2, Chapter 1). The crystals with applied electrodes are heated above T_c and then, the electric field is applied during the cooling from $T>T_c$ to room temperature (RT). In general, when crystal is passing through the T_c or is at temperatures close to the T_c, its coercive field is small and thus, the small electric fields (0.2-5 V/cm) are sufficient to orient domains uniformly [2]. Domain reversal at temperatures considerably below the T_c (250°C or 350°C) and at RT were reported, as well [4], [5]. It has been achieved by the application of high electric fields (>21.2 kV/mm for LT) [6] and (> 21 kV/mm for LN [7]) in single pulses of short duration (few milliseconds) [8].

Initially, the electrical poling at RT was limited to thin crystals because of the dielectric breakdown of the air at high electric fields. Later, to overcome this limitation the liquid electrodes of LiCl solution were applied which permitted to apply electric fields as high as 25kV/mm [9]–[11]. Since then, electric field poling at RT has been widely investigated especially for the fabrication of periodically poled structures in LN and LT [12]–[16], which are used in electro-optics devices. Electrical poling technique does not impose any limitations on the crystal diameter. However, the strength of the electrical applied field is

limited by the dielectric breakdown of the poling media (air, LiCl solution, oil, etc.), which restrains the thickness of the poled crystals with high coercive fields.

3.1.2 Kinetics of domain reversal by electric field poling

The mechanism of domain reversal was already described in Chapter 1. In order to define the duration and the intensity of the electric field applied during the poling it is important to understand the kinetics of domain reversal. The kinetics of domain reversal in LN and LT was described by several research groups [12], [17], [18]. According to these works, it consists principally of six stages, which are detailed in G.Miller's PhD thesis [12]:

1. **Domain nucleation (Fig. 3.1 a):** in the first stage, each domain has a nucleation site, which is a point where the domain starts its formation. Nucleation sites are located generally on electrode edges, but also nucleation starts at the places where defects occur on the surface. The quantity of nucleation sites depends on the intrinsic defects of the crystal, the temperature and the electric field [18].
2. **Tip propagation (Fig. 3.1 b):** the second stage corresponds to the propagation of the domain tip from the nucleation site to the other side of crystal, along the polar axis.
3. **Tip termination (Fig. 3.1 c):** after propagation, the domains grow to form parallel walls. This stage is very short in a time scale (less than 1 μs).
4. **Rapid coalescence (Fig. 3.1 d):** during this stage the domains of proximity merge to form a larger domain.
5. **Propagation of domain walls (Fig. 3.1 e): t**his stage corresponds to the propagation of domains in the plane perpendicular to the polar axis.
6. **Stabilization of the new domains (Fig. 3.1 f):** the new domains have a time-dependent coercive field [19]. Therefore, if the electric field is applied during a shorter time than the time needed for the decay of the negative coercive field (called stabilization time, t_{stab}), the new domains will return to their initial state (back-switching). Thus, to stabilize the orientation of polarization and to avoid the back switching process, the pulses of electric field with longer duration than t_{stab} must be

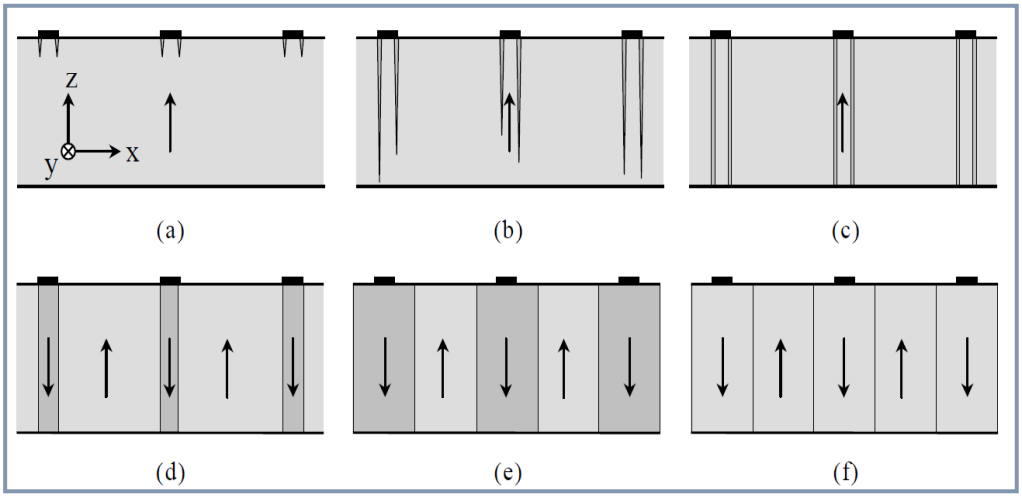

Fig. 3. 1 Stages of domain kinetics during electric field periodic poling [12]: domain nucleation (a), tip propagation (b), tip termination (c), rapid coalescence under the electrodes (d), propagation of the domain walls (e), stabilization of the new domains (f).

applied.

During the reversal of polarization, there is a transfer of charges to compensate the reversal, which causes a transient current. The delivered charges, Q, can be estimated by integrating the current, I_{pol}, over the time, t:

$$Q = \int I_{pol} dt = 2P_s A \qquad \textit{Eq. 3.1}$$

where P_s is the spontaneous polarization and A is the area of the domain-reversed region [11].

3.1.3 Effect of Li nonstoichiometry on mechanism and dynamics of domain reversal

As mentioned in the Chapter 1 (section 1.2.2.1), stoichiometric LN and LT crystals have very low E_c compared to the congruent ones. The E_c of SLT is two orders of magnitude smaller than the E_c of CLT. Besides, other properties associated to the domain reversal, such as the internal field (see Chapter 1, Table 1.1) and the stabilization time (Table 3.1), depend on the crystal stoichiometry, as well. The stoichiometric LT crystals present very short stabilization times and low internal fields. Moreover, the lattice defects may act as pinning sites to the movement of domain walls [20]. Therefore, the propagation/growth of domains in stoichiometric LT crystals is made easier, as well.

Table 3. 1 Stabilization time of newly created domains in LT crystals with different Li_2O non-stoichiometries

	CLT	***NSLT***	***SLT-VTE***
Li_2O composition (mol%)	48.5 [21]	49.9 [22]	~50 [23]
t_{stab} (ms)[24]	~1700	700	< 1

The internal structure and non-stoichiometry of the crystals are also reflected in the form of the transient current generated during poling. According to L. Tian [25], the transient currents in SLT and NSLT samples are presented as “spikes” (Fig. 3.2-a and b, respectively), whereas the current in CLT is more continuous (Fig. 3.2-c). This can be explained by the difference in the velocity of domain propagation in these crystals. The velocity of domain propagation depends on the presence intrinsic defects and on the strength of the electric field [25]. It has been reported that the application of weak electric fields (70 V/mm) in stoichiometric samples produces a transient current in form of “spikes” but if the electric field is increased (500 V/mm), the time-dependence of the current becomes smoother [21], [25], [26] (like the current profile shown in the Fig. 3.2-b). At high fields the domain walls move continuously whereas at low fields a “jump” movement is presented (i.e., domains move very fast initially, then they don’t move, move again and so on), which results in several thin current peaks as a function of time [21] (Fig. 3.2-a). Another difference between CLT and SLT is the domain morphology. Domains in CLT crystals have a triangular shape, whereas the domains in SLT have a hexagonal shape [27]. The domains in CLN and SLN have the same hexagonal shape [28].

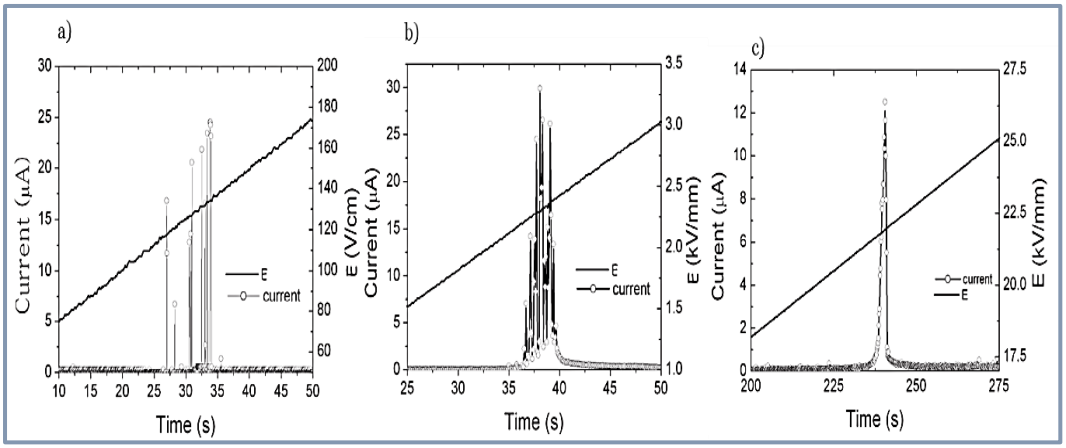

Fig. 3. 2 Transient current as a function of time observed during domain reversal in SLT (a), NSLT (b), and CLT (c) [25].

3.1.4 Effect of doping on domain reversal

The MgO–doped LN (LN:MgO) crystals is a material widely used for optical applications because, unlike the undoped CLN, it is resistant to photo-refractive damage. These crystals are widely used for the fabrication of the periodically poled structures [29], [30]. For MgO:LN (5% doped) the E_c is 4.45 kV/mm and the transient current occurs as spikes, similarly to the case of NSLT. The dynamics of the domain growth during the electric field poling in LN:MgO is slightly different from that in the CLT and CLN. The time required for complete domain reversal, or poling time (t_{pol}) is considerably longer, for MgO:LN is around 100 s [29] whereas for CLN is around 30 ms [31, p. 48].

Iron doped congruent LN (CLN:Fe) crystals are highly studied for the photorefractive applications due to their high diffractive efficiencies, high density data storage and long lasting dark storage [32]. Congruent LT crystals slightly doped with iron (CLT:Fe) are used for fabrication of SAW devices, because iron doping improves flexural strength of the crystals and thus, it ensures a better yield (less chipping and cracking in slicing) during the production process [33]. In LT:Fe or LN:Fe the iron ions occupy the sites of lithium vacancies [34]. The presence of iron ions in the crystal structure affects its physical and structural properties. For example, the a- and c-lattice parameters decrease by ~0.02 Å when 610 ppm of iron ions are added to the structure [35]. The Fe^{3+} ions in the structure help to introduce the space-charge field (which is proportional to the concentration of Fe^{3+} ions), used for the fabrication of holograms [36]. When an electric field with strength close to the coercive field, is applied, the space-charge pattern might be transformed to the ferroelectric domain pattern. This process is used for the electrical fixing of holograms (Fig. 3.3) [36]. In early work on photorefractive effect in CLN:Fe, it has been reported that the CLN:Fe can be

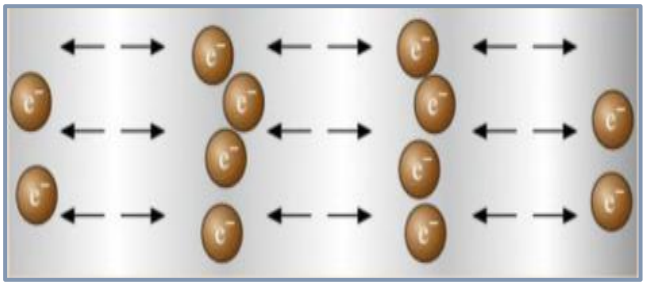

Fig. 3. 3 Schematical representation of electrical fixing in iron doped LN or LT [36]. The arrows indicate the direction of polarization in the created domains.

partially poled at electric fields weaker than the coercive electric field, but stronger than an electric field threshold (E_{thr}). This latter is defined as the electric field required to produce partial reversal of domains and its value is ~10 kV/mm at RT for CLN:Fe. In this case, the reversal of domains occurs like jumps, this phenomenon is called Barkhausen effect, which consists in short displacements of the charges due to domain reversal. In CLN:Fe the E_{thr} decreases gradually with temperature until 100°C and then, it falls abruptly. In contrast, in undoped crystals, the value of E_{thr} is much higher and it does not decrease above 100°C [37]. However, the effect of Fe doping on the kinetics of domain reversal has not been reported.

3.2 Experimental techniques

3.2.1 Experimental setup used for electrical poling

In this work, electrical poling at RT of VTE treated and untreated LT single crystals was done using similar electrical poling procedure to those reported in literature [9], [10], [14]–[16]. Our used electrical poling cell (shown in the Fig. 3.5) and the electrical circuit were developed by Jérome Hauden and Emilie Courjon, and were already described in details [38]. The schematic representation of the experimental set-up used for poling at RT is shown in Fig. 3.4. The external circuit consists of a high voltage power amplifier (HVA), TREK model 20/20B. It amplifies the voltage by a factor of 2000, which is connected to a signal generator (HP 33120A), which amplifies the voltage by a factor of 2. A function of voltage versus time (electric pulse) is designed by using a computer that transmits this function to the signal generator. The HVA is directly connected to the crystal to be poled by using a poling cell. The poling cell consists of two plates made from Plexiglas, which squeeze the sample between two O-rings (Fig. 3.5-a). The fixtures in the Plexiglas are filled up with a

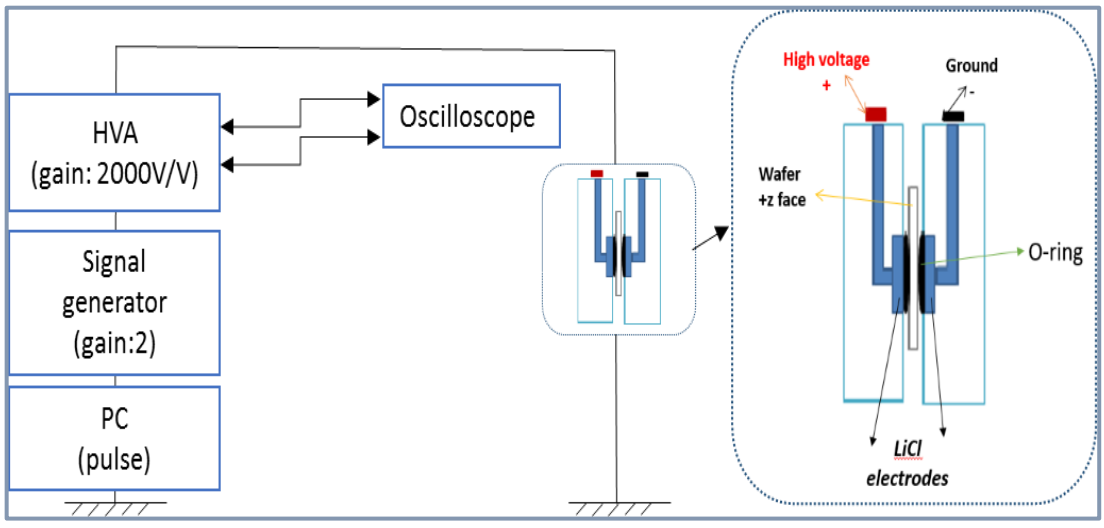

Fig. 3. 4 Schematic representation of external circuit and cell used for electric field poling.

saturated solution of LiCl in order to form electrolytic contact (Fig. 3.4).

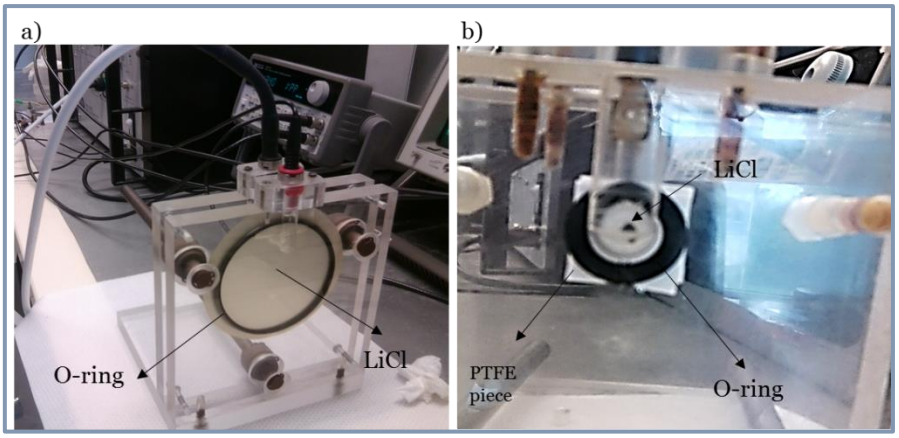

Fig. 3. 5 Poling cell used in this work for crystals with diameters of 15-100 mm (a) and 10 mm (b).

The two liquid electrodes are isolated by O-rings. LiCl solution was prepared by adding gradually 250 g of LiCl to 200 ml of deionized water. The filling-up step must be done carefully to avoid the formation of air bubbles, which can cause a dielectric breakdown when high voltages are applied. This experimental setup was adapted for 4" wafers and for crystals larger than 15x15 mm², because the diameter of the hole used to fill-up the poling cell with LiCl is 11 mm (Fig. 3.5-a). The poling cell for 10x10 mm² specimens had to be modified by inserting a small square piece (15x15 mm²) of PTFE with a hole of 5 mm in the middle (Fig. 3.5-b).

The electric field is applied in a single pulse across the sample thickness. Both current and voltage waveforms were visualized on the oscilloscope LeCroy Waverunner 610Zi, connected to the amplifier. These signals provide information about the dynamics of domain reversal. The amplifier operates in saturation regime and the maximal current that can be reached is 22.4 mA. Typical voltage and current evolutions as a function of time during our poling process of 42 RY-CLT crystals with thickness of 250 µm are shown in Fig. 3.6. We observe that a peak of saturated current appears when the polarization reversal takes place. The drop of current value close to zero indicates the self-termination of the domain reversal process [14]. The charges produced during the domain reversal were estimated by integrating the area of the current peak and by using Eq. 3.1. The several single pulses were applied at the same voltage or slightly higher voltages until the complete disappearance of the transient current peak(s). When the theoretically calculated charges were similar to experimental charges, it was considered that the poling of the crystal was completed.

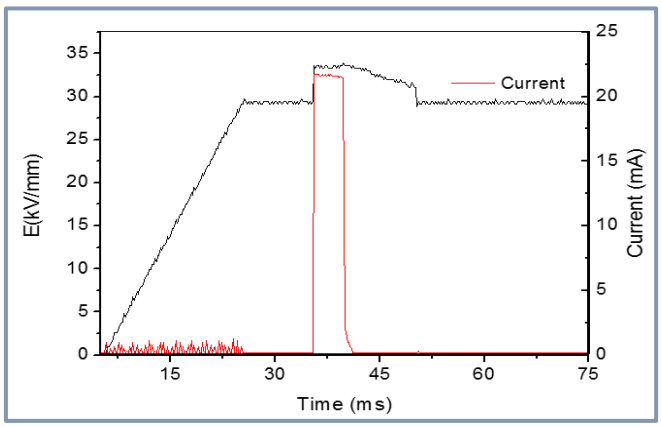

Fig. 3. 6 Applied electric field and transient current as a function of time measured by the oscilloscope during the domain reversal of 42 RY CLT wafer with thickness of 250 µm.

3.2.2 Settings of electrical pulse

The electric field poling was realized by applying one or several single pulses of electric field. The time and the magnitude of voltage were adapted to the coercive field, E_c, and the kinetics of domain reversal in crystals. The initial parameters of electrical pulses were based on the previous developments on domain reversal by applied electric field in Z-cut CLN and CLT at the Institute FEMTO-ST [39], [38, pp. 52–54], [31, pp. 48–50] and on literature reports [15]–[17], [21]. As described in the PhD thesis of F. Bassignot, the electric pulse consists mainly of 4 stages [31]:

1st Stage (Δt1): The applied electric field (E, in kV/mm) is gradually increased during the time, Δt1, to 85% of the expected coercive field (E/E_c=0.85). The goal of this phase is the preparation of the material to the nucleation stage and keeping away from an electric breakdown due to the large variations in voltage.

2nd Stage (Δt2): The domain reversal takes place during this stage. The applied electric field is increased to a value higher than the E_c expected ($E>E_c$) and is maintained during time, Δt_2. Δt_2 depends on the size of poled area (A), it must be longer than the time Δt, needed to transfer the charges (for example, $\Delta t_2 \sim 2\Delta t$) and must be adapted to the kinetics of domain reversal. The value of Δt can be estimated from following equation

$$\Delta t = 2P_s A / I_{pol} \qquad \textit{Eq. 3.2}$$

I_{pol} is the transient current produced during poling, which is limited to 22.4 mA in our system.

3rd Stage (Δt3): This stage is dedicated to the stabilization of domains. The applied voltage is decreased to the value slightly smaller than E_c (80-90 %) and is kept during a time longer than the stabilization time (**Δt3**>t_{stab}) to avoid back switching. The values of t_{stab} used for stabilization of created domains in LT crystals with different Li stoichiometry are given in the Table 3. 1. It can be seen that **Δt3**=~2 s for CLT is necessary. In this work we used **Δt3**=4 s to ensure that the stabilization time is long enough to stabilize all newly created domains.

4th Stage (Δt4): The electric field is gradually decreased to zero during **Δt4.**

These four stages were adapted to our experiments, as well. We have used three different types of voltage pulses with differences in stages 1 and 2 (Fig. 3.7). The 1st stage consist of rising time during which the voltage is increased from 0% to 85 % of E_c value (Fig. 3.7) and the preparation time at constant voltage (85 % of E_c) in the first and second waveforms (Fig. 3.7-a and c). The third waveform does not have the preparation time and was used used for poling of NSLT and SLT crystals with low coercive fields more details will be given in the section 3.3.2.2).

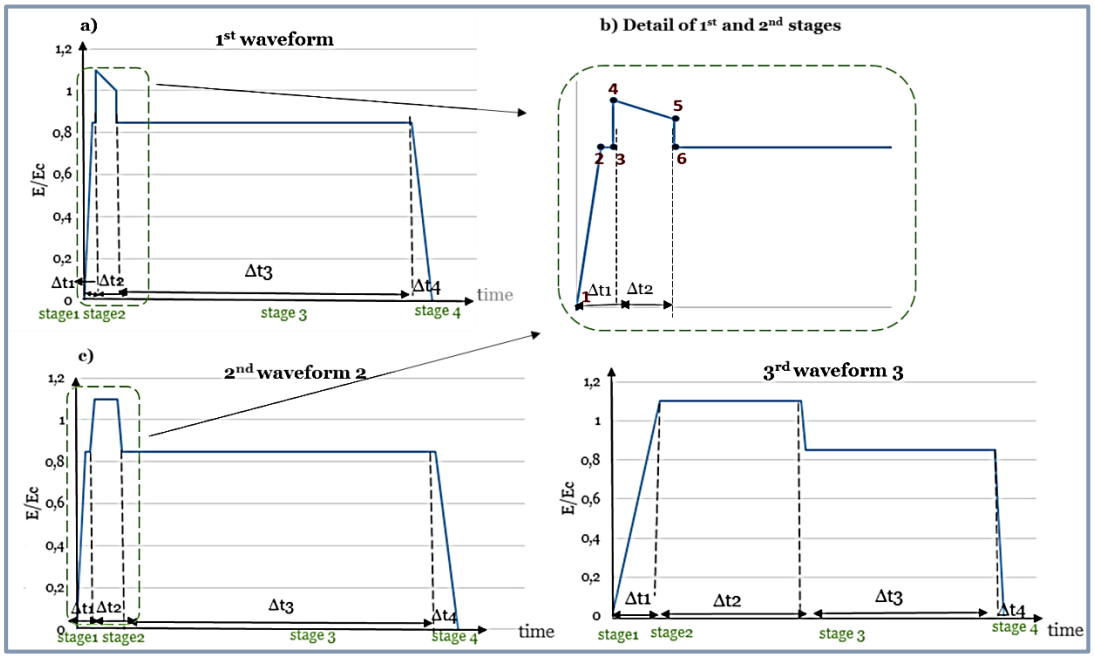

Fig. 3. 7 Different waveforms of voltage pulses used for the domain reversal in LT crystals

In the case of the 1st waveform, the voltage is decreased gradually from $E>E_c$ to E_c during the domain reversal stage (see Fig. 3.7 b, points 4-5 b). Moreover, the time used to increase the electric field from 85 % to $E>E_c$ (points 3-4) and then decrease (points 5-6) is very short (0.1 ms). This abrupt increase of field always generates a small peak of a current of displacement, I_{dpl} [39, p. 110]. The intensity of the displacement current increases with the increase of the step of the applied voltage. This current is produced because the crystal exhibits a capacitance when a voltage is applied across it. The I_{dpl} can be expressed as a function of the capacitance C, the applied voltage V, and the transferred charge Q during a time t:

$$C=Q/V \qquad \textit{Eq. 3.3}$$

$$I_{dpl}(t) = C\frac{dV(t)}{dt} \qquad \textit{Eq. 3.4}$$

In the second waveform (Fig. 3.7 c), the time used to attain E_c and then to reduce the applied field (in the points 3-4 and 5-6) was 10 ms instead of 0.1 ms used in first waveform. Therefore, this abrupt increase/decrease of voltage was replaced by a gradual one. Thus, the I_{dpl} peak was substituted by a series of several less intense current peaks. The usage of the second waveform allows easier identification of weak currents related to the domain reversal process, as it will be explained later.

To summarize, the main parameters that must be known before poling procedure are:

i) The thickness h, of the sample because the magnitude of applied voltage (U_{appl}) depends on it. The value of voltage, supplied by signal generator, required to generate the electric field (in kV/mm) with the strength higher than that of coercive electric field of the crystal, can be found from:

$$U_{appl} = \frac{E_f * h}{4000}, \qquad \textit{Eq. 3.5}$$

where $E_f > E_c$

ii) The value of the spontaneous polarization, P_s;

iii) The area of the electrode, A, to estimate the quantity of theoretical charges Q_{th}, that will be delivered during the complete domain reversal (Eq. 3.1). The area of the electrode is defined by the diameter of the O-ring used to delimit the liquid electrode. The charges, Q_{exp}, delivered during the poling procedure, were calculated by integrating the measured current over the time (Eq. 3.1), by using the Integrate function on *Originlab* software. The quantity of charges generated by the current of displacement were subtracted from the whole charges.

3.2.3 Fabrication of periodically poled structures

Although the fabrication of periodically poled structures is not the objective of this work, we choose to do periodical poling because it is easier to evaluate the effectiveness of the used poling method by visualising the periodic structure of domains. The methodology for the realization of the periodically poled structures was adapted from F. Bassignot PhD thesis [31, p. 105]. Usually, periodically poled structures are realized on the two-side polished wafers. In our case, the wafers were single side polished. For this purpose, we have realized a periodical structure with a period of 600 µm from the patterned photoresist on the Z^+ or Z'^+ (Z'^+ corresponds to the positive projection of the Z^+ axis on the surface) surface of the crystal by using photolithographic techniques. The main steps and conditions of this procedure are summarized in Fig. 3.8. First, the wafer was cleaned with a solution of H_2O_2/H_2SO_4 (1:2) during 2 minutes. Then, it was covered by a coating of 3.2 µm of a positive photoresist Shipley 1828 (S1828). The wafer with the photoresist coating was baked in an oven at 90 °C for 25 min and was left to cool naturally to the RT afterwards. The baked photoresist was exposed through the mask to UV light with energy of 150 mJ/cm² in order to carboxylize it selectively. Finally, the photoresist was developed by dissolving the exposed areas in the developer MF-206A during 60 s.

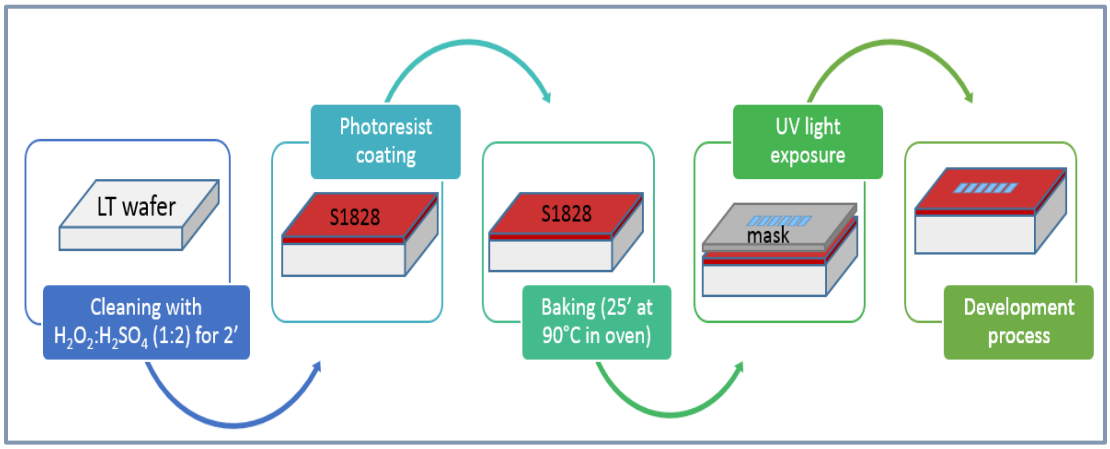

Fig. 3. 8 Process of photolithography for fabrication of the isolated periodically structure

3.2.4 Visualization of ferroelectric domains

The most used technique for revealing the ferroelectric domain structure in LT or LN is a chemical etching with concentrated hydrofluoric acid (48 mol%) or with a mixture of HF and HNO_3. This technique is based on the difference in etching rates of domains with opposite directions of spontaneous polarization. Thereby, Z^- face is etched faster than Z^+ one. There is a difference in the etching rates of Z^- surface of stoichiometric and congruent crystals, (~0.8 nm/min for SLT and ~0.95 nm/min [40]). It was observed that HF etches more rapidly and more homogenously than the HF/HNO_3 mixture [41]. Different temperatures and durations used for etching of LT or LN have been reported in literature and are summarized in the Table 3. 2

Table 3. 2 Parameters of chemical etching used in this work (*) for the revealing of ferroelectric domains in LT and LN crystals in comparison to the parameters used in literature.

Etched material	*Etching agent*	*Temperature*	*Time*	*Etching rate (nm/min)*	*Ref*
CLN	HF/HNO_3 (1:2)	110°C	10 min		[42]
CLT	HF (48%)	20° C	120 min	0.9	[40]
SLT				0.8	
SLT	HF/HNO_3 (1:1)	20°C	120 min	0.35	[40]
CLT				0.39	
CLT and SLT*	HF (48%)	RT	60 and 300 min	0.16	
CLT and SLT*	$HF:HNO_3$ (1:1)	RT	60 and 300 min		

In this work, we have tested several etching recipes to reveal the domain structure in VTE treated and/or electrically re-poled LT, we have tested several etching recipes: (i) 60 or 300 min in concentrated HF and ii) 60 or 300 min in 1:1 mixture of HF and HNO_3. The domain structures were observed by using an optical microscope LEICA INM20 and a Scanning Electron Microscope (SEM) QUANTA 450, working at low vacuum mode.

In order to test the efficiency of domain revealing, the polarization was inverted in the circular zone in the untreated single-domain 42 RY-CLT crystal. Two zones with opposite polarization directions and O-ring mark, revealed after etching with concentrated HF for 5h, can be clearly identified in optical image, given in Fig. 3.9-a. This recipe was suitable for revealing the domain structure in re-poled VTE treated 42 RY-SLT crystals (Fig. 3.9-b), as well. Later we have found out that the duration of 1 h of etching is sufficient to reveal the domains and this duration was used in our further experiments.

The second technique used in this work to reveal the ferroelectric domain structure was mechanical polishing, because there is a difference in hardness of Z^+ and Z^- oriented domains [43]. The removal rate by polishing is one order of magnitude larger than chemical etching. The mechanical polishing for 1.5 h of Z^+ and Z^- surfaces was done by using a polishing machine SOMOS (described in the Chapter 2). A suspension of colloidal silica with grain size of 50 nm was used as an abrasive. The optical images of zones with inverted

polarization direction revealed by mechanical polishing in re-poled untreated 42 RY-CLT crystal is given in Fig. 3.10-a.

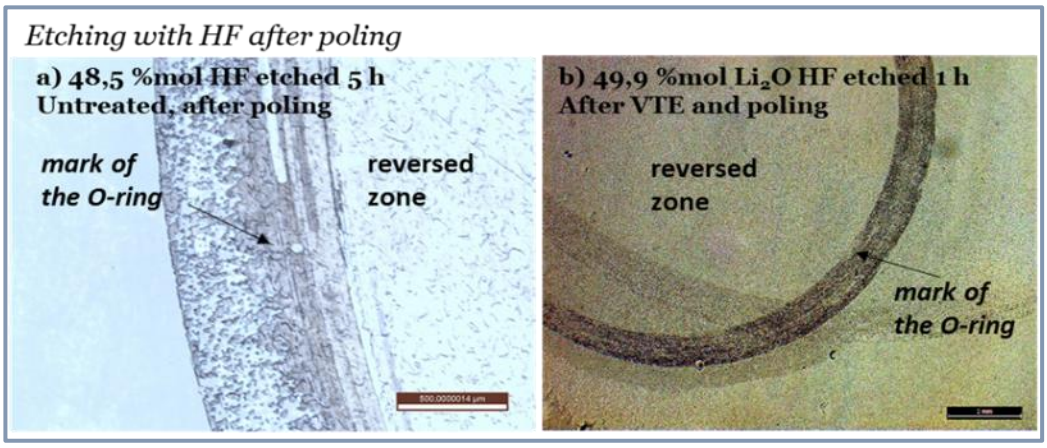

Fig. 3. 9 Optical images of surfaces of re-poled untreated 42 RY- CLT crystal (a) and re-poled VTE treated 42 RY-NSLT (b) etched HF for 5h and 1 h, respectively.

Both techniques, mechanical polishing and the chemical etching, reveal not only the ferroelectric domain structures but also the changes in chemical composition of the crystals. During the VTE treatment, the treated crystals were placed on the alumina crucible. In the contact area between the crucible and the crystal, alumina diffusion into the crystal may take place and the Li_2O in- (out-) diffusion is restrained. Thus, this zone presents different chemical composition and can be clearly identified after mechanical polishing (or chemical etching) as can be seen in Fig. 3.10 b.

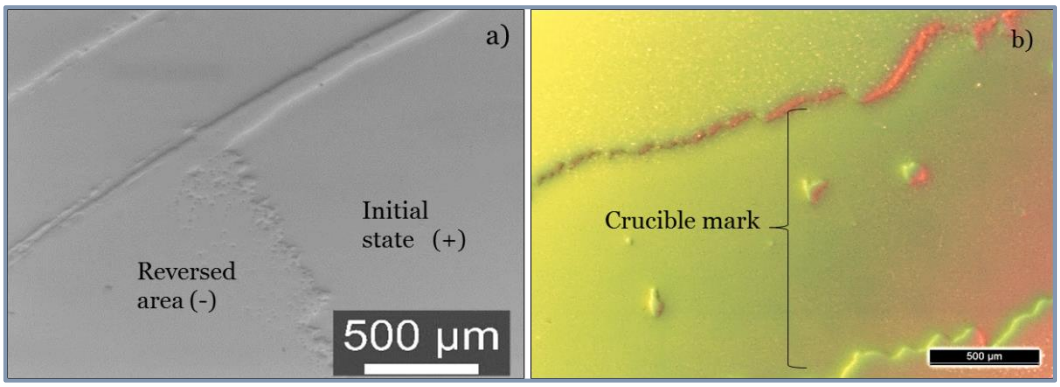

Fig. 3. 10 Optical images of domain structures revealed by mechanical polishing: uniform domain zones with opposite polarization directions in untreated 42 RY-CLT crystal (a), the mark of the alumina crucible on the surface of VTE treated 42 RY-NSLT (b).

The mechanical polishing is a simple technique that allows the visualization of domains after VTE treatment and after electrical poling. However, in most cases, the VTE treated crystals were warped (for more details see previous chapter). This makes polishing of the surface inhomogeneous and in the case of highly warped crystals only some zones are polished. This makes difficult the visualization of domains on the whole crystal surface. In these cases, we preferred the chemical etching. The domain structures inside the crystal were revealed by chemical etching of the cross sections of the crystals.

3.3 Results

3.3.1 Ferroelectric domain structure in VTE treated and annealed samples

To reveal the poly-domain structure of the 42 RY-LT crystals treated by VTE, the etching with concentrated HF during 1 h was done at RT. Usually, we could not find the presence of domains on the surface of the VTE treated crystals after etching during 1 h with HF (Fig. 3.11-a). We tried to apply longer etching times (5h) and to use a mixture HNO_3:HF=1:1. However, we could typically observe only some defects on the surface (Fig. 3.11 b and d), which were found frequently after VTE treatment and could be removed by polishing. Homogeneous single-domain state was normally observed on the surface of a 42

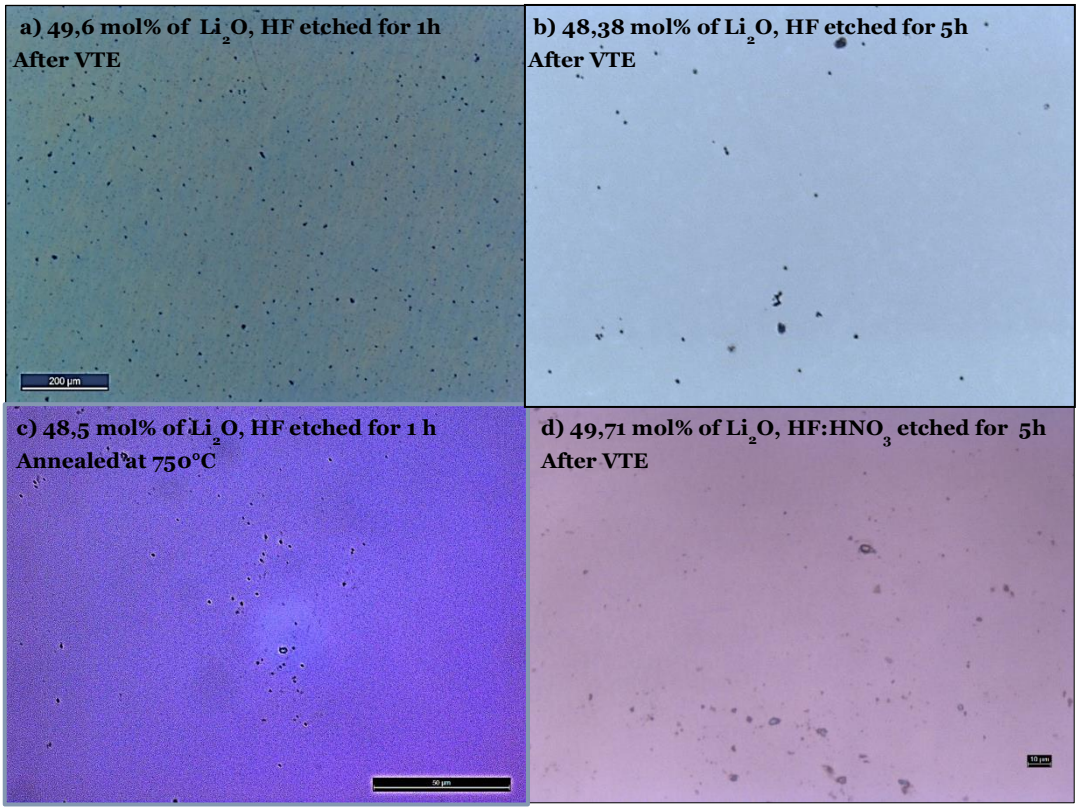

Fig. 3. 11 Optical images of surfaces of 42RY-LT crystals , treated by VTE, after etching with HF (a, b , c) and with HF:HNO_3 (1:1) (d) for different durations.

RY-CLT crystal annealed at 750 °C for 10h ($T>T_c$), Fig. 3.11-c, as well.

The ferroelectric domains with dendritic shape [20] (illustrated in Fig. 3.12) were seldom observed on the surface of our VTE samples. In order to investigate the domain structure inside of crystals, the cross sections of several samples 42 RY-LT crystals, annealed at $T>T_c$ or treated by VTE, were observed after etching with HF for 1 hour. The SEM images of the cross section of the nearly stoichiometric (42 RY-NSLT) and sub-congruent (42 RY-subCLT) crystals, treated by VTE, and congruent (42 RY-CLT) single crystal annealed at 750°C (above T_c), are given in the Fig. 3.13. In the cross section, the samples presented layered poly-domain structure. This explains why it was difficult to observe the domains on the crystal surface after etching or polishing. The borders of the domains inside the crystal were wavy/dendritic.

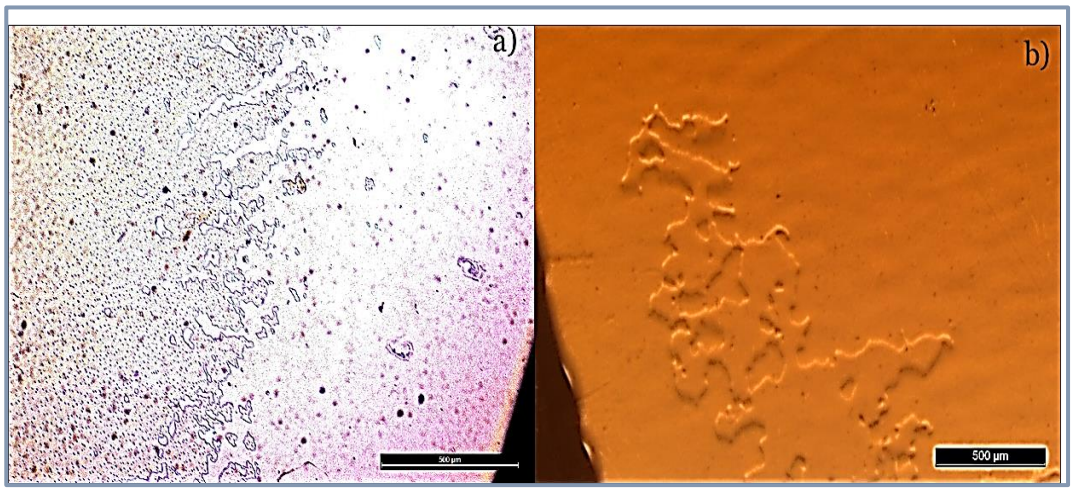

Fig. 3. 12 Optical image of domain structure of VTE treated 42RY-NSLT crystals: surface of a sample with 49.9 mol% of Li_2O, revealed by HF etching for 5h (a) and the surface of a crystal with 49.87 mol% of Li_2O, revealed by polishing for 1.5 h (b).

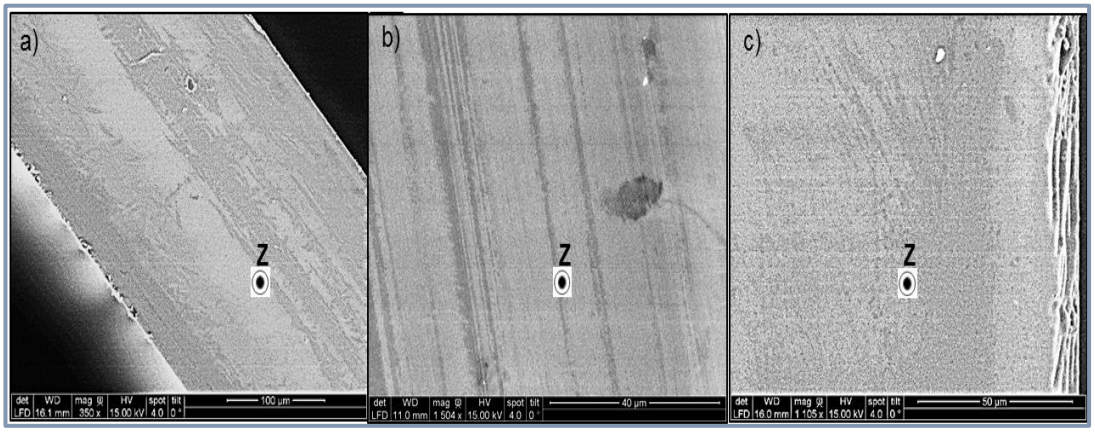

Fig. 3. 13 SEM images of cross sections of 42 RY-LT crystals etched with concentrated HF for 1 h: 42 RY-CLT crystal annealed at 750°C (a), 42 RY-NSLT crystal with 49.8 mol% of Li_2O (b) and 42 RY-subCLT with 48.4 mol% of Li_2O (c) obtained by VTE treatment.

3.3.2 Electric field poling of Z cut $LiTaO_3$ single crystals

To optimize the electrical poling procedure at RT for our VTE treated Z-cut crystals with different Li_2O stoichiometry, congruent (Z-CLT) and (nearly) stoichiometric Z-cut LT crystals (Z-SLT) from different sources were electrically poled. The Li_2O concentration, grade, fabrication methods, and suppliers of these crystals are summarized in Table 3. 3. Commercial crystals were poled uniformly at high temperature and were supplied in single-domain state. Thus, the comparison of poling parameters needed to reverse the polarization in commercial congruent and stoichiometric crystals obtained by different methods was done to evaluate the effects of Li_2O nonstoichiometry and the defects related to the fabrication method of stoichiometric crystals. Then, we have tried to adapt these poling procedures to our VTE treated poly-domain samples. The values of transferred charges and coercive electric field (E_c) were calculated by taking into account the size of the reversed area and nonstoichiometry of these Z-cut LT crystals, respectively (Table 3.4). The estimation of

theoretical charges (Q_{th}) was obtained by using the Eq. 3.1, where the values of P_s=60 μC/cm² and P=55 μC/cm² were used for congruent and stoichiometric samples, respectively. These values will be discussed and will be compared to the experimental ones in the following sections.

Table 3. 3 The Li_2O concentration (estimated by means of Raman spectroscopy), grade, fabrication methods, suppliers and domain state (before our poling procedure) of Z—cut crystals used in our electrical poling experiments. CZ stands for Czochralski technique, TSSG – top seeded solution growth, l –length, w- width, and h-thickness.

Sample name	***Grade***	***Size lxwxh (mm)***	***%Li_2O (±0.05), mol%***	***Fabrication methods***	***Initial domain state***	***Supplier***
Z-CLT	SAW	50x30x0.5	48.50	CZ	single	MTI Corporation
Z-SLT_Deltr	Optical	10x12x0.5	49.95	TSSG	single	Deltronic Crystal Technologies*
Z-SLT_CrTech	Optical	10x12x1	~50.00	CZ & VTE	single	Crystal Technology (TDK Company)*
Z-SLT_VTEN59	SAW	50x30x0.49	49.98	CZ & VTE	poly	MTI crystal treated by VTE in this work **

** The samples were provided by C. Kajiyama, a member of our industrial partner.*

***Sample was treated at 1250 °C for 48h using equilibration powder with 60 mol% of Li_2O (see Chapter 2 for more details).*

Table 3. 4 Comparison of experimentally measured (exp) and theoretical (th) values of transferred charges (Q) and forward electric field (E_f) for stoichiometric and congruent Z-cut LT crystals. The type and area of electrodes are given, as well. PE stands for periodical electrodes, and CE - circular electrode.

Sample (type of electrodes)	***Type of electrodes***	***Electrode area (mm²)***	***Q_{th} (μC)***	***Q_{exp} (μC)***	***$E_{c\,th}$ (kV/mm)***	***E_f (kV/mm)***
Z-CLT	PE	44	53±3	54.8±3	21.0±0.3 [23]	≤ 20.6
Z-SLT_Deltr	CE	20	31.1±6	33.6±6	1.0±0.4*	≤ 1.2
Z-SLT_Deltr	PE	10	15.5±3	15.4±3	1.0±0.4*	≤ 1.2
Z-SLT_CrTech	CE	20	31.1±6	40.4±6	0.16 ±0.06 [23]	≤ 0.12
Z-SLT VTEN59	CE	44	95.2±10	110.8±10	0.5±0.4*	≤ 0.48

**Values estimated from the Eq. 1.11-1.12 (Chapter 1)*

3.3.2.1 Congruent crystals

The coercive field of congruent Z-cut crystals is ~21 kV/mm, thus the minimum voltage that needs to be applied to reverse the ferroelectric domains in 0.5 mm thick crystal is 10.5 kV. In order to reverse the direction of the polarization in untreated and single-domain Z-CLT crystal, with periodic electrodes, a pulse of electric field with the 1st waveform (defined in section 3.2.2 and Fig. 3.7-a), was applied at RT. The voltage was gradually increased from 7.2 kV to 10.32 kV. The voltage of 10.32 kV created an electric field of 20.6 kV/mm which was very close to the reported E_c values [8], [20], [44]. At this tension, the peak of transient current was observed indicating the beginning of the domain reversal (Fig. 3.14)

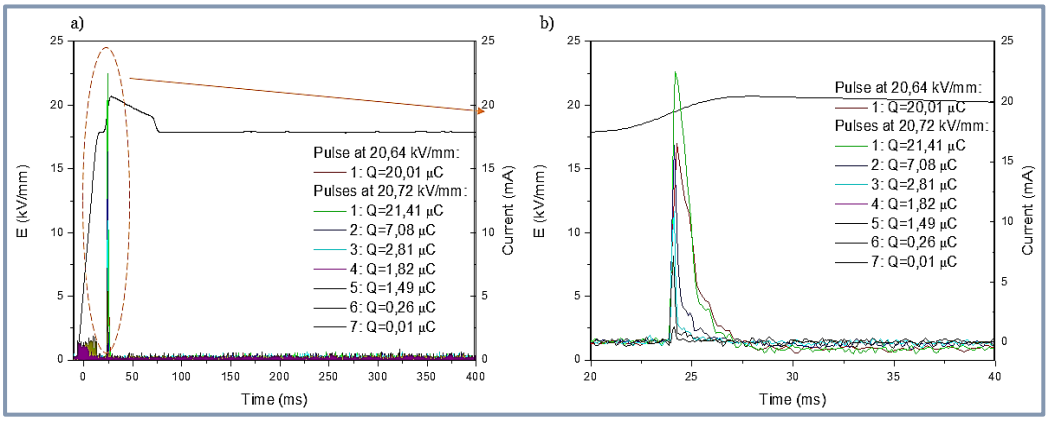

Fig. 3. 14 Current as a function of time observed during the first electric pulse with E_{max}= 20.64 kV/mm and the following seven pulses with E_{max}= 20.72 kV/mm applied to reverse the direction of polarization in Z-CLT single crystal (a), zoom on the current peak (b).

The shape of the current peak was similar to those reported in literature for congruent Z-cut LT crystals [8], [20], [44]. However the quantity of the transferred charges (20.01 µC) were smaller than expected (53 µC). Then, we continued to apply successively seven times the pulses of electric field with E_{fmax}= 20.72 kV/mm until the disappearance of the peak of current, (Fig. 3.14). Negative current was not observed, which indicated that there was no back switching of domains. The sum of delivered charges during all applied pulses was 54.8 µC which was very close to the calculated one (53 µC). Thus, we concluded that the domain reversal was complete. After that we reversed the direction of the electric field and we applied the field of 16.6 kV/mm, which was higher than the E_r reported in literature (12.6 kV/mm) [23]. For backward reversal only one pulse was necessary to pole completely the crystal. E_r might be smaller than our applied electric field during the first pulse. We could estimate that the internal field was equal or higher than 2.06 kV/mm (estimated according to Eq. 1.7, Chapter 1), which was of the same order of magnitude as the values found in literature (4-5kV/mm)[23], [45]. The

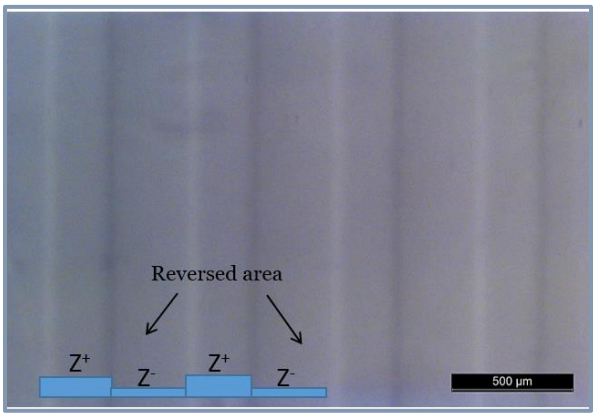

Fig. 3. 15 Periodic domain structure in Z-CLT revealed by polishing the surface.

origin of the internal field comes from the defects such as Li vacancies or Ta anti-sites, present in the congruent crystals [46].

The domain structure on the surface of the periodically poled sample was revealed by polishing during 1 hour (Fig. 3.15). The difference in the height of the Z^+ and Z^- zones is quite visible. The ratio of the widths of Z^+ and Z^- domains was not exactly 1:1. The Z^- domains were slightly wider than the Z^+ domains due to an over-poling – the reversed domains started to expand to the zones not covered by the electrodes, used for poling. Our aim was only to validate the procedure for the domain reversal, thus the optimization of periodical structure with well-defined domain period was not further developed.

3.3.2.2 Nearly stoichiometric crystals

To (re)pole the nearly stoichiometric and stoichiometric crystals, we started always the poling procedure using very low maximum voltages (U_{appl}), between 0.120 and 0.2 kV. Then we gradually increased it in steps of 0.2 kV until the appearance of a peak of the transient current generated during the domain reversal. The values of the voltages (U_{appl}), which initiated the domain reversal in the crystal, were used to estimate approximately the forward electric field of the crystal by using Eq. 3.5. In the case of single-domain (nearly) stoichiometric crystals (Z-SLT_Deltr and Z-SLT_CrTech), only two pulses were needed to pole completely the crystals. The poling current observed during the domain reversal in each crystal is shown in the Fig. 3.16. One observes that the transient current in SLT crystals (Fig.3.16-a and b) reaches the limit at around 3 mA, while it was limited to 22.5 mA in the case of congruent crystals due to the limits of our experimental set-up. In the case of stoichiometric crystals, the current peaks presented a spiky shape similar to those reported in literature on poling of (nearly) stoichiometric LT crystals [26], [47], while the single current peak appeared during domain reversal in congruent crystals. The poly-peak nature of the transient current was especially well seen during the poling of Z-SLT_Deltr (PE) where the quantity of delivered charges were twice smaller and thus the current did not reach the limit of 3 mA (Fig. 3.1 6 c).

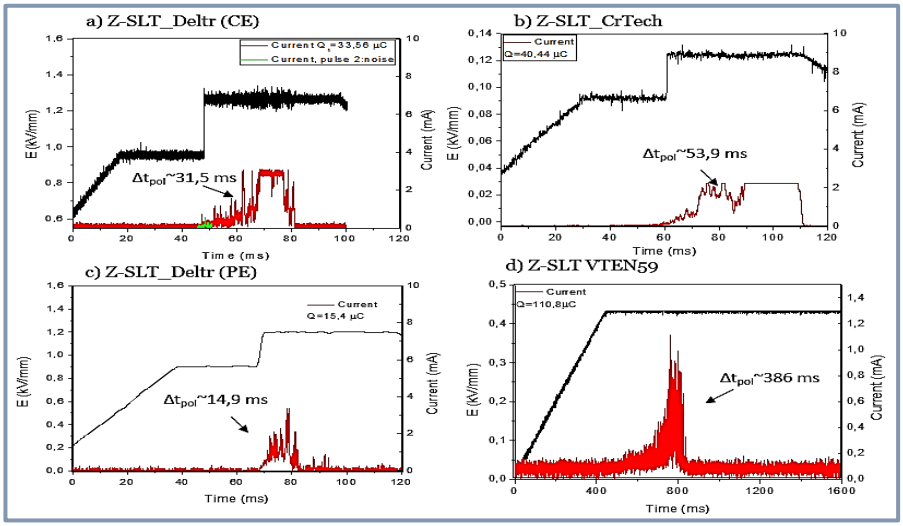

Fig. 3. 16 Applied voltage and poling current as a function of time in stoichiometric LT crystals: Z-SLT Deltr (a), Z-SLT CrTech (b), periodically poled Z-SLT_CrTech and d) Z-SLT VTEN59, the limited current was 3 mA. The duration of poling (t_{pol}) is indicated in each case.

The domain reversal takes much longer time in the stoichiometric crystals comparing to congruent crystals. For example, in the case of congruent samples, the poling time (t_{pol}) was around 2 ms whereas it was longer than 14 ms in stoichiometric samples (the t_{pol} are indicated in Fig. 3.16). All single domain samples were completely poled after one pulse of electric field. The values of E_f were close to the values reported in the literature for the stoichiometric and nearly stoichiometric LT crystals [20], [23], [46], the differences were in the error range. Moreover, the electric field required to pole the Z-SLT_CrTech sample was almost 10 times lower than of the Z-SLT_Deltr sample, which indicated that the first one had composition closer to the stoichiometric one.

In the case of poly-domain VTE treated stoichiometric Z-SLT_VTEN59 crystal, the transient current also presented a spiky shape. However, it appeared not immediately after the application of the maximum field but after 300 ms, which was not typical for single-domain crystals (Fig. 3.16-d). Similarly, the important delay in creation of domains under applied electric field was observed in MgO doped crystals [29]. This is related to the rate of the initial nucleation of new domains, which is slower in MgO doped crystals, as compared to undoped ones. Moreover, the observed current was very small (~1 mA) but the poling time was very long (~386 ms). After the application of the first pulse at 0.480 kV/mm, the domains were completely reversed. The delivered charges are compared to the calculated values in Table 3.4. In all the cases, the total amount of delivered charges during the poling was slightly higher than the expected one, which indicates that the domains were completely reversed.

3.3.3 Electric field poling of 42° rotated Y-cut LT crystals

In the case of 42 ° rotated Y-cut LT crystals (θ_R = 42°), the ferroelectric axis is rotated by angle $\theta z=90-\theta_R$ from the surface normal. Thus, the applied electric field, E_c, P_s and the patterned period Λ_{surf} (for periodically poled crystals) are affected by the rotation of ferroelectric axis, as it is indicated in the Fig. 3.17. The electric field is applied across to the thickness of crystal and is parallel to the surface normal (n). However, the ferroelectric axis is rotated by an angle (θz). Therefore, according to D. Hum thesis [48], the E_c and P_s can be calculated using the following Eq.s:

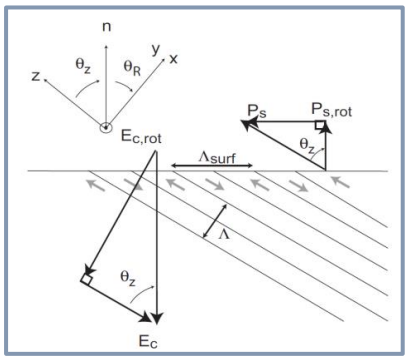

Fig. 3.17 Coercive electric field and polarization in rotated-cut crystals [48].

$$E_{c,rot} = \frac{E_c}{Cos\theta_R} \qquad Eq.\ 3.6$$

$$P_{s,rot=}P_s Cos\theta_R \qquad Eq.\ 3.7$$

For 42 RY-CLT, θ_R=42°, hence, E_c is expected to be 28.46 kV/mm and P_s=44.59 μC/cm²

We used SAW grade Fe doped and undoped 42 RY-LT crystals, having a thickness of 250 μm and 350 μm. The wafers, initially congruent (CLT) and single domain, were supplied by Yamaju ceramics and KOIKE Corp. Co. VTE treated samples with different Li_2O stoichiometries were poled: sub-congruent (42 RY- sub-CLT), nearly stoichiometry (42 RY-

NSLT) and stoichiometric (SLT) crystals. The supplier, initial domain state, doping, Li_2O concentration (measured on the surface by Raman Spectroscopy), size, the temperature, time and concentration of powders used in VTE treatments of the used 42 RY-LT crystals are given in Table 3.5.

Table 3. 5 Supplier, initial domain state, doping, Li2O content, size and treatment condition of 42 RY-LT crystals used for poling. l, w and h stands for length, width, and thickness, respectively.

Sample name	***Doping***	***%Li_2O on surface (± 0.05), mol%***	***Size (lxwxh) mm***	***Treatment***	***Domain state***	***Supplier***
42 RY-CLT_SP	Undoped	48.50	32x25x0.25	Untreated	Single	Yamaju ceramics
42 RY-CLT_DP	Undoped	48.50	32x25x0.25	Untreated	Single	Yamaju ceramics
42 RY-CLT_PPLT	Undoped	48.50	32x25x0.25	Untreated	Single	Yamaju ceramics
42 RY-subCLT_A1250	Undoped	48.20±0.2	30x30x0.25	Annealed at 1250°C for 48h	Poly	Yamaju ceramics
42 RY- CLT_A750	Undoped	48.45	50x30x0.35	Annealed at 750°C for 10h	Poly	Yamaju ceramics
42 RY-CLT :Fe	Fe doped	48.50	32x25x0.25	Untreated	Single	KOIKE Co.
42 RY-CLT :Fe_2	Fe doped	48.50	50x30x0.35	Untreated (polished)	Single	KOIKE Co.
42 RY-CLT :Fe_PPLT	Fe doped	48.50	32x25x0.35	Untreated (periodic electrodes)	Single	KOIKE Co.
42 RY-CLT :Fe_A500	Fe doped	48.50	32x25x0.25	Annealed 500°C for 10h	Single	KOIKE Co.
42 RY-CLT :Fe_A750	Fe doped	48.44	32x25x0.25	Annealed 750°C for 10h	Poly	KOIKE Co.
42 RY-subCLT :Fe_VTEN61	Fe doped	47.32	33x30x0.25	VTE: powder 40%mol of Li_2O**	Poly	KOIKE Co.
42 RY-NSLT_VTEN41	Undoped	49.75	32x25x0.25	VTE: powder 60%mol of Li_2O (recycled)*	Poly	KOIKE Co.
42 RY-SLT_VTEA2_60	Undoped	50.00	50x30x0.35	VTE: powder 60%mol of Li_2O *	Poly	KOIKE Co.
42 RY-NSLT:Fe_VTEN74	Fe doped	49.59	50x30x0.35	VTE: powder 60%mol of Li_2O (recycled)*	Poly	KOIKE Co.
42 RY-NSLT:Fe_VTEN62	Fe doped	49.95	32x25x0.25	VTE: powder 60%mol of Li_2O (recycled)*	Poly	KOIKE Co.
42 RY-NSLT:Fe_VTEN60	Fe doped	49.87	32x25x0.25	VTE: powder 60%mol of Li_2O (recycled)*	Poly	KOIKE Co.

** VTE treatments at 1250°C for 48h;*

*** VTE treatment at 1300°C for 48h (see Chapter 2 for more details).*

3.3.3.1. Undoped congruent and sub-congruent 42 RY-LT crystals

In this section, we are going to present the electrical poling of undoped congruent and sub-congruent 42 RY-CLT crystals. The quality of the surface, the electrode type, calculated poling charges (using Eqs. 3.1 and 3.7), expected and experimental values of E_c are summarized in Table 3.6. The estimation of charges was done taking into account that the value of P_s value is 44.58 µC/cm² and 40.87 µC/cm² for 42 RY-CLT and 42 RY-SLT samples, respectively.

Table 3. 6 Comparison of theoretical (th) values of poling charges and electric coercive field (E_c) with experimental values of charges (exp) and electric forward field (E_f) for undoped congruent and sub-congruent 42 RY-LT crystals. PE stands for periodical electrodes, and CE - circular electrode, DP and SP mean double polished and single polished, respectively.

Sample	***%Li₂O on surface (± 0.05), mol%***	***Polishing***	***Type of electrode***	***Electrode area (cm²)***	***Q_{th} (µC)***	***Q_{exp} (µC)***	***$E_{c\,th}$ (±0.9 kV/mm)***	***$E_{f\,exp}$ (kV/mm)***
42 RY-CLT_DP	48.50	DP	CE	1.13	101±13	116±13	28.5	≤34.9
42 RY-CLT_SP	48.50	SP	CE	1.54	137±14	186±14	28.5	≤34.4
42 RY-CLT_PPLT	48.50	SP	PE	0.44	39±2	47±2	28.5	≤32.9
42 RY-sub CLT_A1250	48.20±0.2	SP	CE	0.79	70±11	86±11	32.1±6*	≤42.1
42 RY-CLT_A750	48.45	SP	CE	1.33	118±13	121±13	29.4	≤31.4

**Sample with concentration gradient of 0.2 mol% of Li_2O*

The poling of 42 RY-CLT requires an application of higher electric field as compared to that used for the poling of Z-CLT. In particular, it was more difficult to have a successful poling at RT of 42 RY-CLT samples with 350 µm of thickness and with sub-congruent composition (<48.5 mol% of Li_2O), because dielectric breakdown usually occurred before poling.

The nucleation of domains can be affected by the quality of surface of the crystal (defects and polishing) [38, p. 95], [39, p. 49]. In our work, we have used 42 RY-LT SAW grade single-side polished wafers. Thus, we compared the poling procedure for single-side polished (SP) and double-side polished (DP) 42 RY- CLT wafers with thickness of 250 µm. To inverse the polarization direction of uniformly poled 42 RY-CLT_DP, the 1st waveform of electric field (Fig. 3.7-a) with the direction opposite to the polarization projection to the surface normal and the maximum value of $E_{f,max}$= 32 kV/mm was applied (higher than the Ec=28.5 kV/mm). However, the current of poling was not observed. Then the electric field was increased to 34.9 kV/mm. The observed switching current after this pulse is shown in Fig. 3.18 a (the red curve). The quantity of delivered charges were slightly smaller than the expected value ($Q_{experimental}$ = 98.5 µC < $Q_{expected}$=101 µC). Thus, a second pulse at the same voltage was needed to complete the poling process. The total quantity of charges obtained during two poling cycles were 116 µC, close to the theoretical value. To confirm that the crystal was well poled, a third pulse was applied and no more current was observed.

Moreover, negative current wasn't found, which indicated that there was no backswitching. The E_f was 34.9 kV/mm and it was higher than the calculated value (28.5 kV/mm).

The poling of a single polished (SP) sample was done, as well. In this case, electric fields (E_{fmax}) varying from 28.8 to 34.4 kV/mm were applied. At 34.4 kV/mm, the reversal of domains was observed, then a second pulse with the same voltage was applied and no more current was observed. The 42 RY-CLT_SP was completely re-poled after the application of one pulse (E_f=34.4 kV/mm). The charges, delivered during the pulse with E_{fmax} =34.4 kV/mm, were higher than the theoretical value ($Q_{experimental}$ = 186 μC >$Q_{expected}$=137 μC). The reversal of the polarization direction in uniformly poled SP and DP wafers with polarization directed towards the polished surface seems to be similar as the E_f used for poling and delivered charges are equivalent (Fig. 3.18). We found that it is possible to reverse the polarization in one–side polished uniformly poled crystals, the

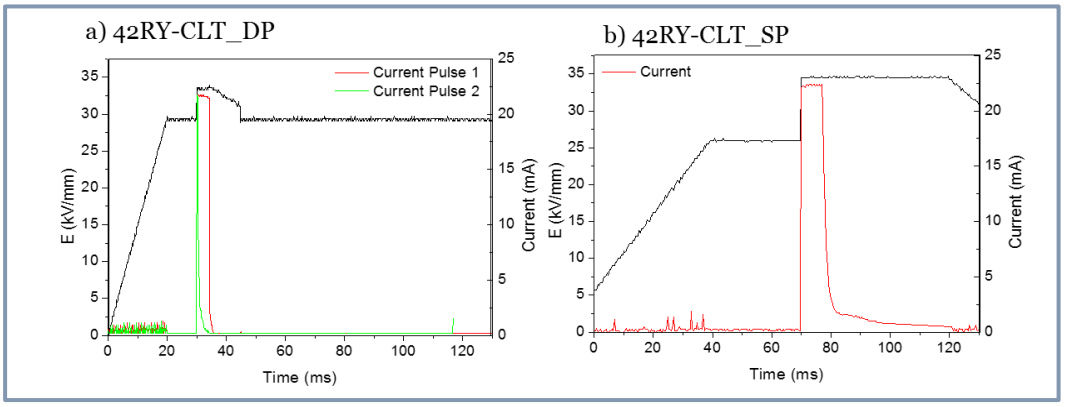

Fig. 3. 18 Waveforms of electric field, used for poling, and transient current, observed during poling of undoped 42RY-CLT: double-side polished crystal (a) and single-side polished wafer (b).

polishing quality of wafers seems do not affect significantly the poling processing.

The areas with reversed polarization direction in DP and SP wafers were revealed by etching the surface with concentrated HF and by polishing the surface, respectively (Fig. 3.19). The re-poled area can be clearly distinguished in both samples. The Fig. 3.19-a shows the schematic representation of different areas in the re-poled sample: (1) a small area (~0.07 cm²) in the zone delimited by O-ring where LiCl was not filled-up; (2) the o-ring mark and (3) the area in contact with the LiCl electrodes. The first two areas kept their original domain state whereas the polarization of the area covered by liquid electrodes was reversed.

In order to validate completely the technique used for poling of congruent 42 RY-LT crystals, we prepared a periodically poled 42 RY-LT crystal (42 RY-CLT_PPLT) because the poled zones can be visualized/identified easily. The complete reversal of polarization was achieved after the application of 2 pulses with $E_{f,max}$= 32.9 kV/mm. The electric charges generated during the cycles of poling were slightly higher than the theoretically estimated ones ($Q_{expected}$=39±2 μC, $Q_{experimental}$=47±2 μC). The periodical structure of domains was revealed by polishing of the surface during 1 hour and it was visualized by optical microscope (Fig. 3.20-a) and interferometer (Fig. 3.20-b, c, d). The period of photoresist used was 600 μm, with a ratio of 1:1 between the cover and uncovered areas, whereas the ratio between unpoled and poled area was 1.15:1. The well-defined inverted zones with the expected period let us confirm our poling procedure. There is a difference in height of

~110 nm in areas with positive and negative projections of Z+ axis. This indicates that the difference in polishing rate in +48° Z and -48° Z directions is around 3.6 nm/min.

In 42 RY-CLT_PPLT sample, a forward poling (opposite to the initial polarization) was performed at a voltage E_f, and then, the direction of the field was reversed (reversal poling,

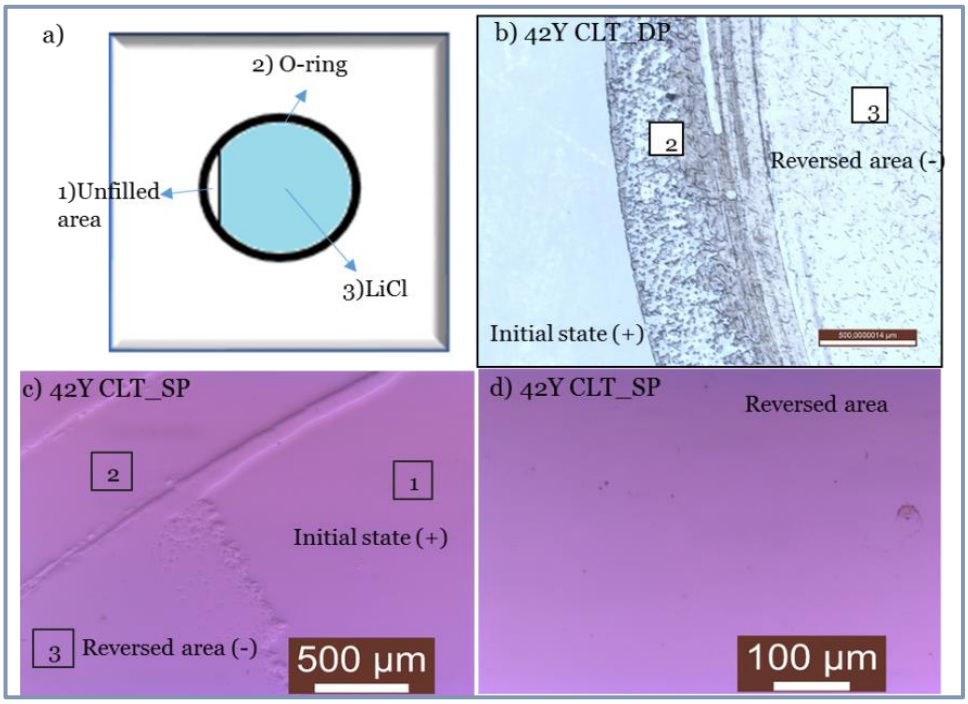

Fig. 3. 20 Schematic representation of the different zones in the poled sample, which were identified in the optical images of the surface of 42YCLT_DP (b) and 42YCLT_SP samples (c, d), obtained after poling.

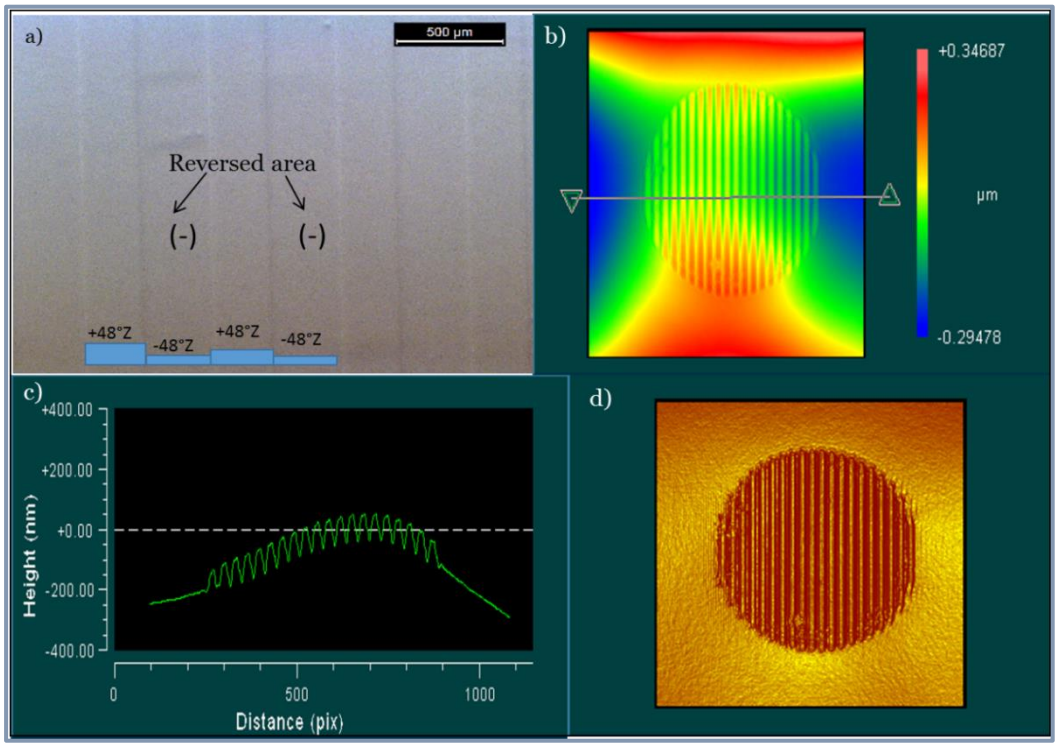

Fig. 3. 20 Surface of periodically poled 42 RY-CLT after polishing during 1 hour observed by means of optical microscope (a) and mapped with interferometer (b-d): profile of the surface, showing a difference in height of the domains with +48° Z and -48°Z directions (c) and the 2D projections of the surface, showing the inverted areas (b and d).

E_r=24 kV/mm). The value of E_{int} was estimated according to the Eq. 1.7 in Chapter 1, the value found was 4.5 kV/mm, which is slightly lower than of the observed for Z-CLT crystals, E_{int}=5 kV/mm, or E_{int}=6.72 kV/mm for 42 RY-LT (taking into account the angle of rotation) [46]. This probably indicates that we applied a too high field for backwards reversion of polarization.

The poling of sub-congruent (42 RY-subCLT) was carried out by using the same procedure as for congruent crystals (described above). The difficulty is that the E_c of these kind of samples is considerably higher than that of the congruent ones. Thus, electrical poling of many sub-congruent samples at room temperature was not successful due to dielectric breakdown. However, we were able to pole uniformly several poly-domain 42 RY-LT crystals annealed at high temperatures in the air (without equilibration powders). For example, one crystal was annealed at 1250 °C for 48 h (sample 42 RYCLT_A1250). During annealing, crystal lost some amount of Li_2O and after annealing crystal presented Li_2O concentration gradient with the lowest Li_2O concentration of 48.29 mol% of Li_2O on the surface. The concentration gradient on the surface of sample was around 0.2 mol% of Li_2O. Thus the E_c expected was 32.1±6 kV/mm. To homogeneously pole this crystal, we applied 7 poling cycles gradually increasing the applied maximum field from 38.1 to 42.1 kV/mm and we exchanged twice the direction of the electric field. The poling was completed by 3 pulses of electric field with maximum value of 42.1 kV/mm. The necessity to apply much higher E_f than the expected E_c probably could be explained by the presence of the concentration gradient.The transferred charges during poling were estimated by integration of the current peak (by using Eq. 3.1), the Fig. 3.21 shows the transient current obtained during poling of this sample. The experimental charges were higher than the theoretically estimated ones (Q_{th}=70±11 μC, Q_{exp}=86 μC), therefore we assumed that the poling was complete.

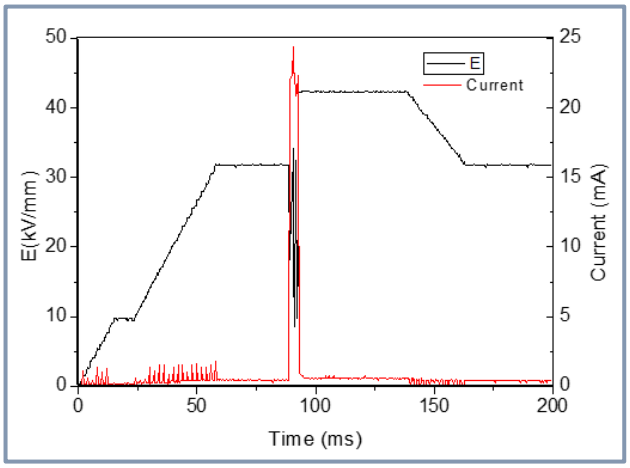

Fig. 3.21 Waveforms of electric field used for poling, and transient current, observed during poling of undoped 42RY- LT crystal, annealed at 1250°C for 48 h (42 RY-subCLT_1250 sample).

The electric field values used for the poling of undoped congruent and sub-congruent 42 RY-LT crystals and total quantity of delivered charges during the complete poling procedure of these crystals are summarized and compared to the E_c and expected value of charges in Table 3.6. From the results presented above, it can be observed that all crystals were poled by applying the values E_f higher than the effective E_c. The total quantity of delivered charges was close to the expected ones in the limits of errors. It should be noted that the poling processes for initially single-domain crystals and poly-domain crystals are different. Indeed, to pole uniformly the poly-domain crystals it is necessary to apply several pulses at high voltages and to change the direction of the electric field for several times. The present concentration gradient required the application of the E_f much higher than the

expected maximum E_c field (corresponding to the lowest Li_2O concentration present in the crystal).

3.3.3.2. Iron doped congruent and sub-congruent 42 RY-LT crystals

As mentioned above, iron doped 42 RY-LT are commonly used in SAW device industry due to the fact that the iron doping improves flexural strength of the crystals. Therefore, we tried to optimize VTE treatments and electrical poling for these type of crystals, as well.

The samples used in this section were SAW grade wafers with initially congruent composition and thickness of 250 or 350 µm. Crystals were treated by VTE using different concentrations of Li_2O in equilibration powders. The preparation conditions and composition of studied crystals are summarized in Table 3.5. The electrode type, the theoretical and experimental values of electric field and charges are given in Table 3.7.

Table 3.7 Comparison of experimental and theoretical values of poling charges and electric coercive field with the forward electric field used for poling for congruent and sub-congruent 42 RY- LT:Fe crystals. Number of cycles of electric field with $E_{f,\,max} > E_c$ applied to pole completely 42 RY- LT:Fe crystals are given, as well. PE stands for periodical electrodes, and CE - circular electrode.

Sample	***%Li_2O on surface (± 0.05), mol%***	***Poling type***	***No. pulses***	***Electrode area (cm^2)***	***Q_{th} (µC)***	***Q_{exp} (µC)***	***E_c (kV/mm)±0.9***	***E_f (kV/mm)***
42 RY- CLT:Fe	48.5	CE	19	2.14	191±14	181±14	28.5	≤32.6
42 RY- CLT:Fe_2	48.5	CE	10	2.27	202±15	255±15	28.5	≤32.6
42 RY- CLT :Fe_3	48.5	CE	12	0.88	78±8	45±8	28.5	≤31.69
42 RY-CLT:Fe_PPLT	48.5	PE	7	0.88	79±7	63±7	28.5	≤32.6
42 RY-CLT:Fe_A500	48.5	CE	1	0.87	77±12	79±12	28.5	≤32.3
42 RY-CLT:Fe_A750	48.44	CE	43	0.87	77±12	65±12	29.6	≤44
42 RY-CLT:Fe_VTEN78	48.46	CE	72	2.27	202±15	180±15	29.2±	≤48.5
42 RY-sub-CLT:Fe_VTEN61	47.32	CE	40	0.87	77±12	61±12	50.6	≤53.6

First, we tried to reverse the polarization in the single-domain 42 RY-CLT:Fe crystal. The applied maximum electric field was 32.6 kV/mm. At this electric field, the transient current was observed. But the delivered charges were only of 53 µC, whereas the Q_{th} expected was 191 µC. Then several additional poling cycles with slightly increased E_{max} (32.9 kV/mm) were applied. After 3 pulses at this field, the current started to decrease gradually. We had to apply 16 cycles with the same waveform of the electric field until the transient current disappeared. To be sure that only displacement current was observed, we repeated the poling cycle several additional times. The peak of the transient current during the last cycles (14-16th cycles) was very small (Q=2 µC) and finally only the displacement current with Q=0.35 µC

(related to crystal capacitance) remained (Fig. 3.22-a). At this stage we expected that the poling was complete. The electric charges delivered at each cycle were added in order to estimate the total quantity of charges, and the charges corresponding to the displacement current were subtracted. It was close to the expected value ($Q_{experimental}$~181±14 µC < Q_{th}~191 µC) in the error range. The inverted area was clearly identified after polishing the surface (Fig. 3.22-b).

The dynamics of domain reversal in iron doped LT crystals (42 RY-LT:Fe) is different from that in the undoped crystals. The main difference between the inversion of domains in single-domain undoped and iron doped 42 RY-LT crystals is that we have to apply tens of pulses (19 pulses in this case) in order to have a complete inversion in iron doped crystals, because at each poling cycle the quantity of delivered charges was very small. The E_f used for iron doped crystals was similar to that used for undoped crystals.

As mentioned above, the quantity of delivered charges was very small during each poling cycle. Thus, when the first waveform of electric field was used, the peaks of transient current and displacement currents were overlapped. This made difficult the identification of appearance/disappearance of transient current and the initiation/ termination of the inversion process. Thus, in the case of 42 RY-LT:Fe crystals, we preferred to use the 2nd waveform (Fig. 3.7-c), in which the voltage is increased gradually in the 2nd stage. In this case, the intense displacement current peak is replaced by several less intense peaks. The comparison of intensity and width of these peaks helps the identification of (dis)appearance of transient current. Several wafers coming from the same box were poled and the same trend was observed. The poling began at E_f around 32.6 kV/mm but to complete it 9–25 pulses were necessary.

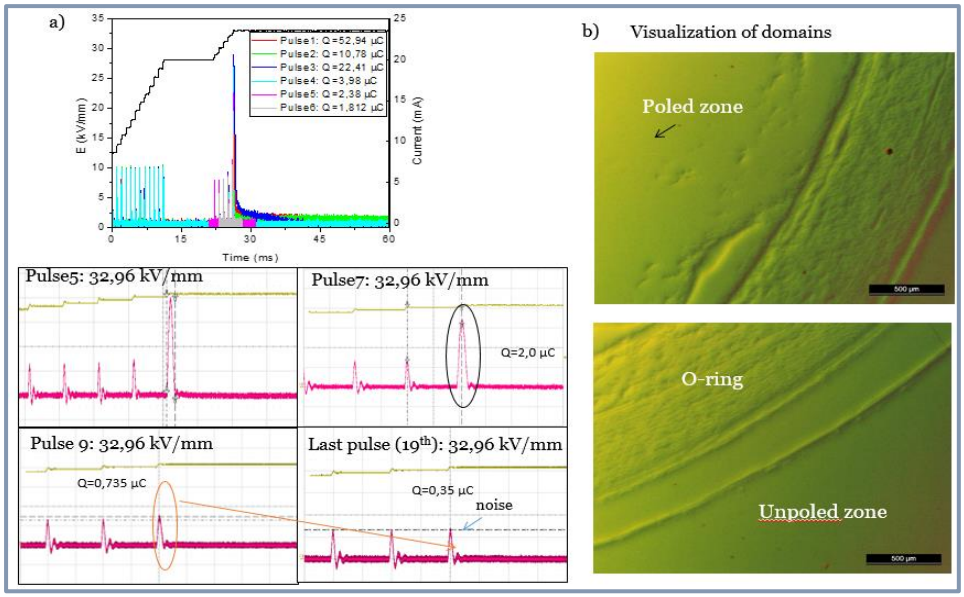

Fig. 3. 22 Displacement and transient current peaks observed during the different poling cycles of 42RY-CLT:Fe, done by using 2nd waveform of the electric field (a). Optical images of inverted and non-inverted areas after 19 poling cycles, revealed by polishing the surface of the sample.

To facilitate the poling of 42 RY-CLT:Fe samples, we tried to pole the annealed congruent crystals at 500 °C during 10 h. The poling was achieved during the first cycle with E_{fmax}= 32.3 kV/mm. The delivered charges were close to the expected ones (Table 3.7). Thus, we can expect that the inversion process was complete. Hence, it seems that the annealing at

a temperature below T_c facilitates the poling because the mobility of the Li ions is increased at high temperature [24].

We tried to pole the 42 RY-CLT:Fe crystal annealed at temperatures higher than T_c (at 750 °C for 10 h), as well. This crystal was poly-domain after annealing. The E_c expected for this sample was 32.3 kV/mm. The maximum of applied electric field was gradually increased from 28.8 kV/mm to 44 kV/mm. At 44 kV/mm we observed the first appearance of transient current and it was necessary the application of 43 cycles at this field in order to complete the poling. The experimental charges were close to the expected value, in the error ranges (see Table 3.7). Similarly, a poly-domain crystal with Li_2O concentration (48.46 mol%) close to the congruent one obtained after VTE treatment (VTEN78) was poled after the application of 72 pulses at 36.5 kV/mm, whereas the E_c estimated was 29.3 kV/mm. It seems that the poling of poly-domain 42 RY-CLT:Fe samples required the application of much higher E_f than the single-domain crystals.

This poling procedure was tested also on the sub-congruent 42 RY-subCLT:Fe samples. The poly-domain 42 RY-subCLT:Fe _VTEN61 crystal, with 47.32 mol% of Li_2O on the crystal surface, was poled. The estimated E_c of this crystal was 50.6 kV/mm. Several pulses of very high voltages across the sample were applied. It was necessary to switch the direction of the electric field for three times in order to observe the beginning of the domain reversal. In order to eliminate completely the transient current, 40 poling cycles with E_{max}=53.6 kV/mm were applied.

In order to understand better the process of poling of 42 RY-CLT:Fe wafers, a periodically poled domain structure was prepared, by using a wafer with a thickness of 350 µm. The poling was performed by the application of 7 poling cycles with E_{max}=32.6 kV/mm, higher than the E_c expected (28.5kV/mm) without changing the direction of the field (Fig. 3.23-a). The charges delivered during these cycles were slightly smaller than the theoretically estimated ones ($Q_{experimental}$~63±7 µC<$Q_{theoretical}$~79±7 µC).

The periodic domain structure on the surface of the crystal was revealed by polishing

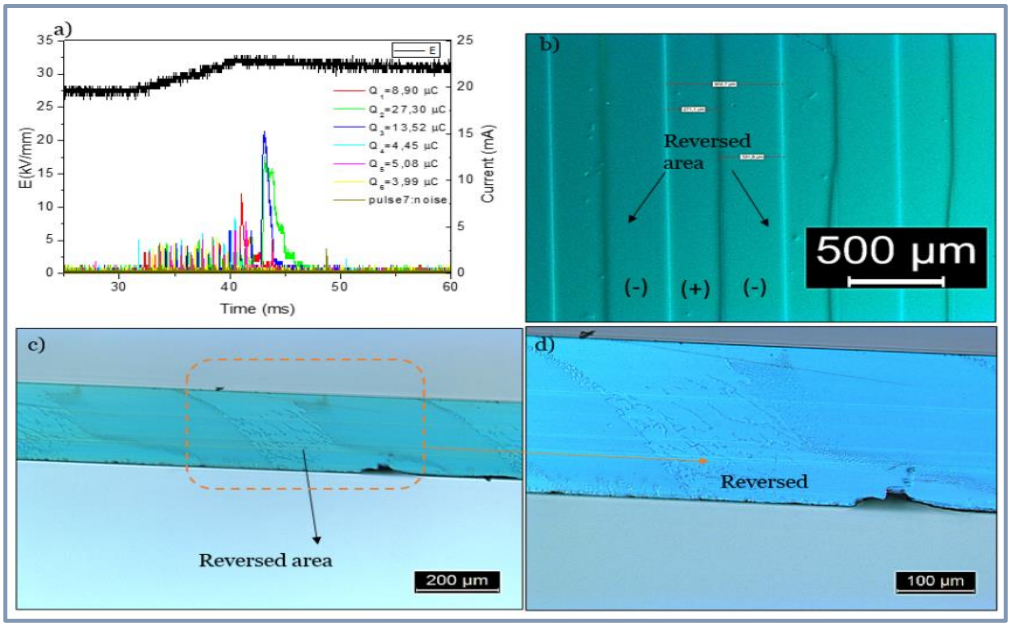

Fig. 3.23 Waveform of applied electric field and observed transient current peaks during periodical poling of 42RY-CLT:Fe (a), periodical domain structure observed on the surface by means of

(Fig. 3.23-b). It must be noted that on the surface the inverted areas are wider than the unpoled ones. This indicates that the crystal was over-poled - the domains spread laterally to the regions covered by the photoresist [14], [16], [49].

Furthermore, in order to observe the propagation of domains in the depth of the crystal, the cross-section of the crystal was cut and polished, followed by etching with concentrated HF. Then the cross section was studied by means of optical microscope. It can be clearly seen in the images of the cross section, that the domain walls were parallel to the ferroelectric axis and the width of inverted zones were large only in the zone close to the surfaces (Fig. 3.23-c, d). The width of the inverted domain decreased almost twice in the depth of the crystal. This indicates that the domains had a difficulty to propagate in the depth of the crystal. Moreover, it can be observed that there are some residual micro-domains in the reversed area. Gopalan et. al [44] found that after poling of Z-CLT crystals, there were some unreversed micro-domains, which consisted in local regions having an internal field slightly higher than in the neighbour areas, and therefore, these region were not poled. This indicates that iron cations are strong pining centres for the domain propagation.

Finally, we have modified the poling procedure for 42 RY-LT:Fe crystals. In the following experiments, the electric field was applied in one direction in order to reverse the direction of polarization in iron doped congruent crystals (sample 42 RY-CLT:Fe_2) (forward poling) , and then, the field was switched in the opposite direction (reversal poling). The forward and reversal electric fields, E_f and E_r, were 32.6 kV/mm and 22.9 kV/mm, respectively. The E_{int} was estimated to be around 4.9 kV/mm. The values were close to the reported values in the literature (Table 3.7). This operation was repeated several times (application of 5 pulses in forward direction and 5 pulses in reversal direction). It was observed that the quantity of charges increased with the number of cycles, as illustrated in the Fig. 3.24-a, b. It should be noted that in the first cycle, the obtained charges were considerably smaller than the expected value (Q_{th}=202μC), therefore, this cycle was not considered as complete poling. During the 3^{rd} -5^{th} cycles, the quantity of delivered charges was bigger than the expected one. In this case the over-poling might be expected. We considered that the poling was complete when the quantity of delivered charges started to saturate with the increasing number of cycles (Fig. 3.24-b). Since during the last cycle the direction of the electric field was in the same direction as the initial polarization of the crystal. There should not be observed any difference between the poled and unpoled areas if the poling was complete. In order to verify this, the polished cross section of the zone where polarization was reversed several times was observed after etching with HF (the Fig. 3.24-c). No domain structure was observed on it. The vertical lines are the marks of the blade used for dicing of the crystal. Single domain state was also observed on the surface of this crystal after etching it with concentrated HF (Fig. 3.24 d)

For comparison purposes, another 42 RY-CLT:Fe crystal was incompletely poled (named 42 RY-CLT:Fe_3). In this case, the sample was poled by applying electric field of E_{fmax}=31.69 kV/mm in one direction (forward poling) for 12 times. In the first cycle of poling the sample was partially reversed and the quantity of charges were 21 μC, almost four times lower than the expected value (79 μC), then 11 more cycles of poling were done but the total quantity of charges was 45 μC. Thus, it is expected to have a partially poled sample. After poling, the polished cross section and surface of samples were etched with HF for 1 h. The Fig. 3.25 illustrates the ferroelectric domains observed by optical microscope and SEM. The nucleation of the domains was observed on the surface and their propagation followed the ferroelectric axis. The geometry of the nucleated domains was similar to those reported for Z-CLT crystals [45].

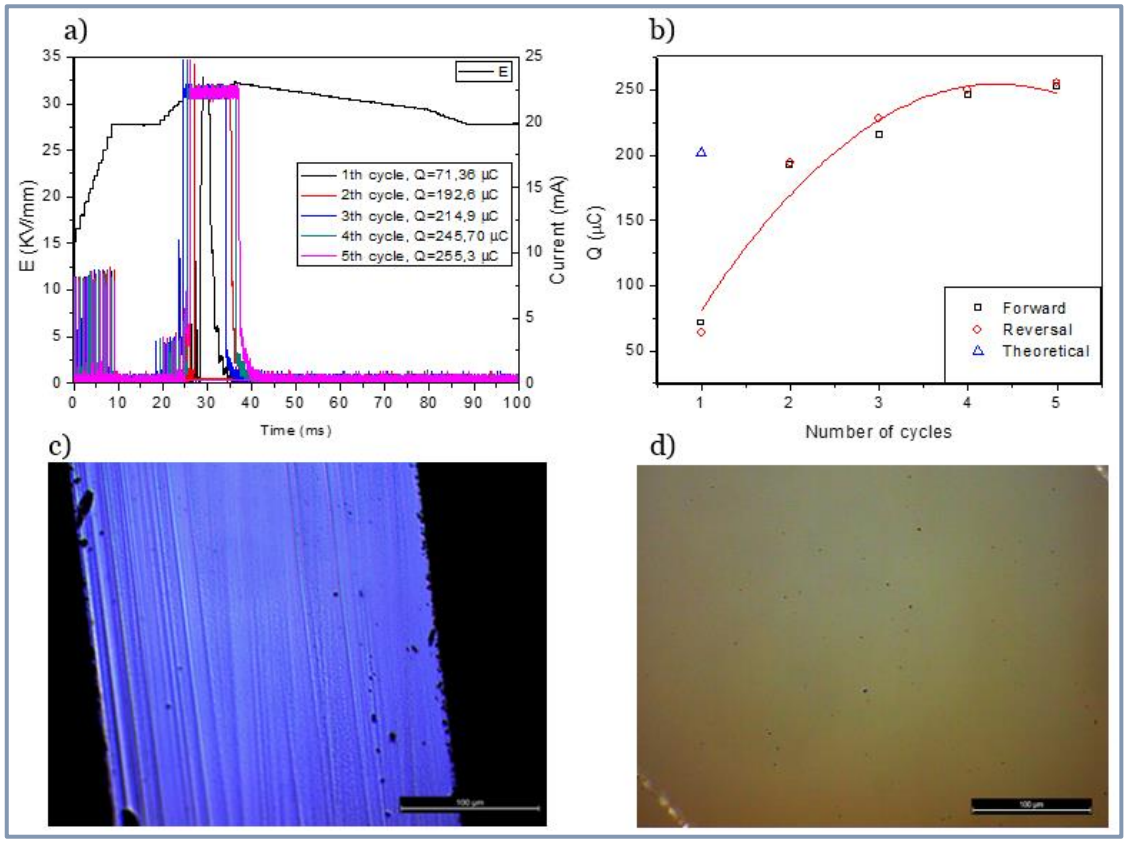

Fig. 3. 24 Transient current as a function of time and number of inversions of the electric field direction during the poling of 42RY-CLT:Fe (a). Evolution of the quantity of delivered charges with the number of inversion cycles (b). Optical image of cross section and surface of the re poled zone in the 42RY-CLT:Fe crystal (etched with HF 48 mol% during 1 hour) (c) and (d), respectively.

To summarize, switching of electric field direction several times facilitates the poling of iron doped 42 RY-CLT:Fe crystals and allows to complete the domain reversal in several poling cycles. Tens of cycles would be needed if the subsequent poling cycles with the same direction of the field were applied. It is important to note that the switching of the field direction was not necessary for domain reversal in undoped single-domain crystals. This could be explained by the fact that iron cations create pining centers for domain walls and/or introduce the local depolarization fields [37], which can be eliminated by the switching the direction of electric field several times. Based on our experimental observations, the poling of 42 RY-CLT:Fe crystals usually requires E_f slightly smaller than for the undoped crystals

(see Table 3.7 and Table 3.6). In the next section the poling on stoichiometric samples will be presented.

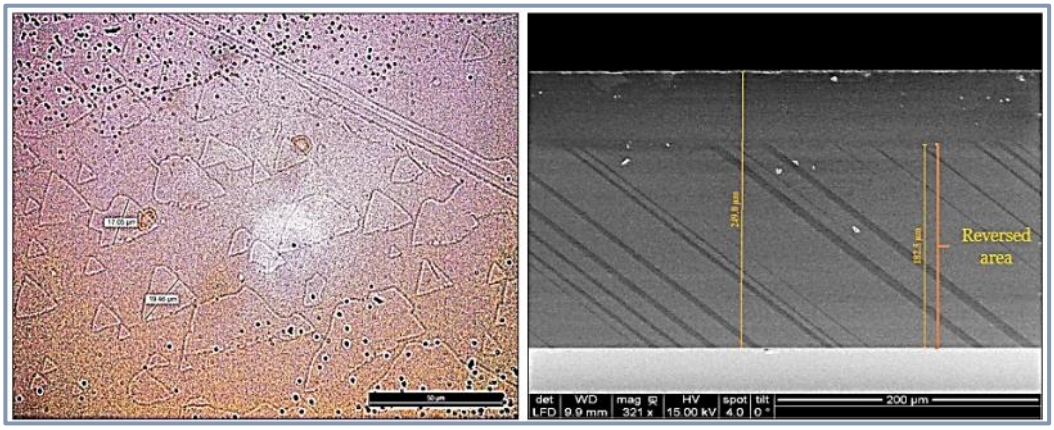

Fig. 3. 25 Optical images of the surface of 42RY-CLT:Fe crystals partially re-poled (a) and SEM image of cross section of the same crustal (etched with HF 48 mol% durina 1 hour) (b).

3.3.3.3 Iron doped and undoped stoichiometric and nearly stoichiometric 42 RY-LT crystals

Finally, poling of iron doped and undoped 42 RY-LT crystals, having stoichiometric and nearly stoichiometric compositions, was optimized. Li_2O concentration of the crystals was in the range from 49.5 to 49.99 mol% (Table 3. 5).Crystals with sizes of 25x30 mm², ¼ and 4 inches were used in our experiments. The thickness of the crystals was 250 or 350 µm.

First, we tried to do homogenous poling of poly-domain undoped stoichiometric 42 RY-SLT_VTEA2_60. The poling was successful after two pulses at E_f=0.57 kV/mm, which was very close to the expected E_c for this crystal (Table 3.8). The current was observed when the maximum voltage was applied and is given in the Fig. 3.26. It can be observed that the shape of peaks is similar to that obtained in stoichiometric crystals of Z-cut LT. Moreover, it appeared not immediately after the application of the maximum field but after 8 ms. The quantity of delivered charges was 142±11 µC, close to the theoretical value (154 µC). Then the electric field was applied in the opposite direction (forward poling) at 0.51 kV/mm and the domain reversal by delivering 149±11 µC charges was observed again. This indicates that the internal field of the 42 RY-SLT crystals was 0.028 kV/mm, which agrees well with the reported small values of E_{int} for Z-SLT obtained by VTE [23].

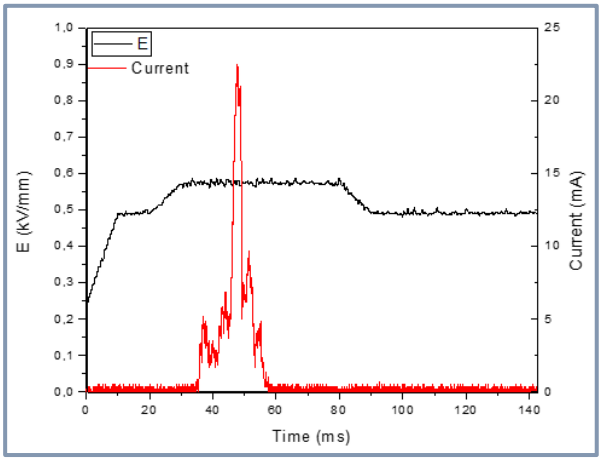

Fig. 3. 26 Transient current as a function of time during poling of 42RY-SLT-VTEA2_60 crystal.

During our poling experiment of (nearly) stoichiometric 42 RY-NSLT crystals, we noticed that the application of the electric fields with intensity much higher than their E_c resulted in the considerable stresses and the cracking of the crystals (Fig. 3.27-b). For

example, when the electric field of 14.4 kV/mm was applied across the 42 RY-NSLT_VTEN41 crystal with E_c=5.1 kV/mm, the domain reversal occurred during the first stage-field rising and the crystal was cracked after the poling procedure (Fig. 3.27-a).

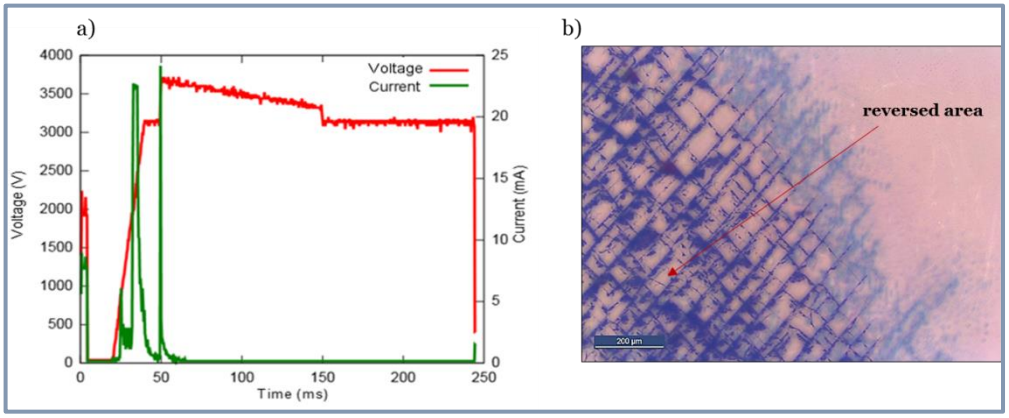

Fig. 3. 27 Transient current observed during domain reversal in 42RY- NSLT_VTEN41 (a). Optical image of surface of poled crystal surface, revealed by etching with HF during 1h, showing cracks produced by stresses in the poled area due to the application of high electric fields (b).

Table 3. 8 Comparison of experimental and theoretical values of poling charges and electric coercive field with the forward electric field used for poling for stoichiometric and nearly stoichiometric iron doped an undoped 42 RY-LT crystals. Number of cycles of electric field with $E_{f,max} > E_c$ applied to pole completely 42 RY- LT crystals are given, as well. PE stands for periodical electrodes, and CE - circular electrode.

Sample	***%Li_2O on surface (± 0.05), mol%***	***Poling type***	***No. pulses***	***Electrode area (cm^2)***	***Q_{th} (μC)***	***Q_{exp} (μC)***	***E_c (kV/mm) ±0.4***	***E_f (kV/mm)***
42 RY-SLT_VTEA2_60	50.00	CE	2	1.89	154±11	149±11	0.55	≤0.57
42 RY-NSLT_VTEN41	49.75	CE	2	1.77	144±10	163±10	5.1	≤14.4
42 RY-NSLT :Fe_VTEN60	49.87	PE	22	0.32	26±3	-	2.8	≤4.8
42 RY-NSLT :Fe_VTEN62	49.95	CE	20	0.64	52±7	50±7	1.3	≤1.6
42 RY-NSLT :Fe_VTEN74	49.59	CE	18	2.54	208±23	184±23	9.7	≤16

Then, we tried to do periodical poling on a 42 RY-NSLT:Fe_VTEN60, having 49.87 mol% of Li_2O. We applied electric field from 1.2 kV/mm to 5.6 kV/mm in one direction but peaks with important intensity were not observed. Then, the field was switched in the opposite direction, starting from 1.6 kV/mm to 11.2 kV/mm. At E_{fmax}=5.6 kV/mm, some peaks with very low intensity were observed (Fig. 3.28, second cycle). Finally, the direction of electric field was reversed again. In this third cycle, at 4.8 kV/mm, the tiny multi-peaks with low intensity of transient current were observed. This was a result typical for iron doped crystals and multi-peak shape for stoichiometric samples. Then, we applied 22 pulses of

electric field, varying from 5.6 to 16.5 kV/mm, along the same direction. It was very difficult to identify the presence of transient current because its intensity was very close to the noise (Fig. 3.28). Thus, we stopped the poling procedure without being sure that the homogenous poling was complete and we etched the surface and the cross section of the crystal with concentrated HF during 1 hour in order to study the domain structure. We observed periodical domain structure with residual micro-domain inclusions on the crystal surface by means of optical microscope (Fig. 3.29-a). These micro-domains had an elongated hexagonal shape (Fig. 3.29-b) similar to that reported in literature [8], [27]. The diameter of these domains was around 6 μm. It can be clearly seen in the optical images of the cross-section of the crystal that the electrical poling was not complete (Fig. 3.29-c and d). The surface layer of around 100 μm was homogenously re-poled and the remaining part of the crystal had poly-domain structure with many small-nucleated domains. This indicates that we needed to apply even more poling cycles to complete the poling. Therefore, in the future experiments, we applied similar strategy as for the congruent iron doped crystals.

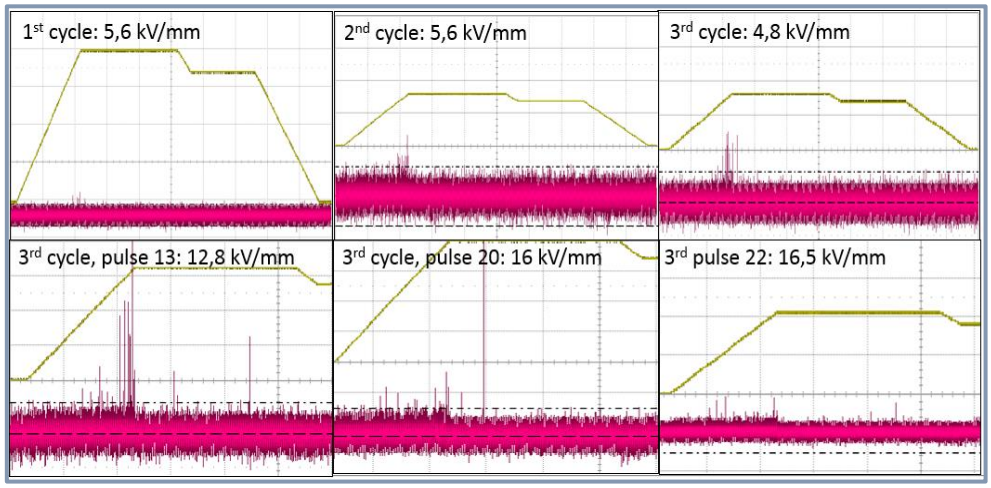

Fig. 3. 29 Transient current peaks observed during the poling of a 42 RY-NSLT:Fe (VTEN60) crystal

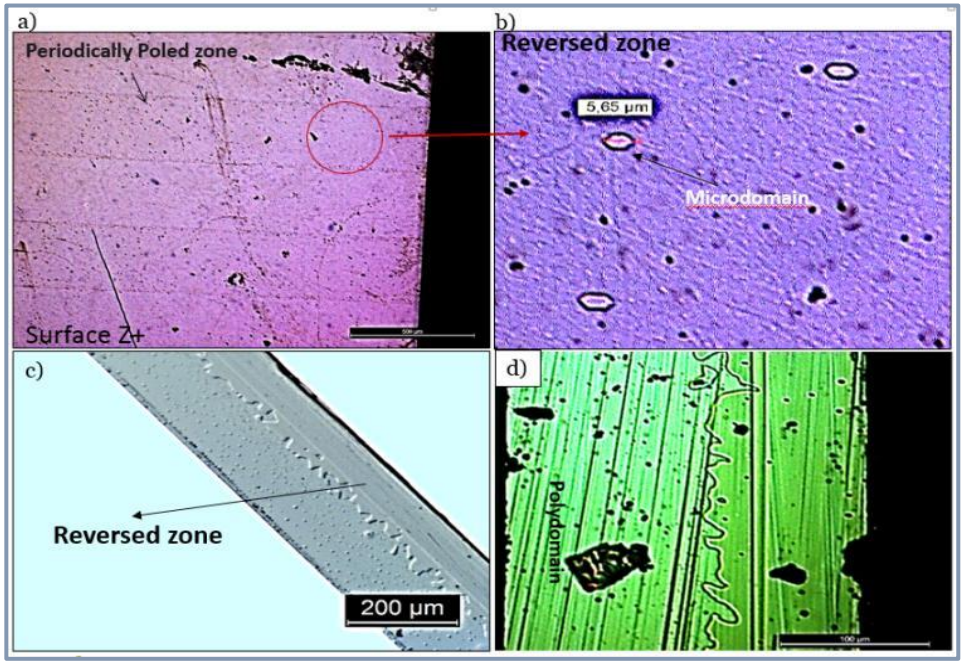

Fig. 3. 29 Optical images of domains in the VTEN60, revealed by etching with HF concentrated for 1 hour: Periodic structure formed on the surface (a), residual microdomains in reversed zone (b), cross section of the crystal, showing a layer in the re-poled area and some residual microdomains (c, d).

Another iron doped crystal, treated by VTE, with nearly stoichiometric composition (42 RY-NSLT :Fe_VTEN62), was poled by switching several times the direction of the electric field. The direction had to be switched six times at 1.3 kV/mm before the observation of the reasonable transient current representing the quantity of delivered charges close to the expected ones (Fig. 3.30-a and Table 3.8). After we applied several additional cycles at the higher voltage (2.4-4.8 kV/mm) to be sure that the poling was complete. During these cycles transient current totally disappeared. After poling, the domain structure were also visualized on the surface and on the cross section (Fig. 3.30 b-d). It should be noted that on the surface the poled and unpoled areas are separated by the mark of the O-ring. Furthermore, the uniform poled area was observed on the cross section of the crystal (Fig. 3.30-c). Whereas the layered domain structure was observed in the unpoled area (Fig. 3.30-d). Thus, we concluded that the homogenous poling was successful.

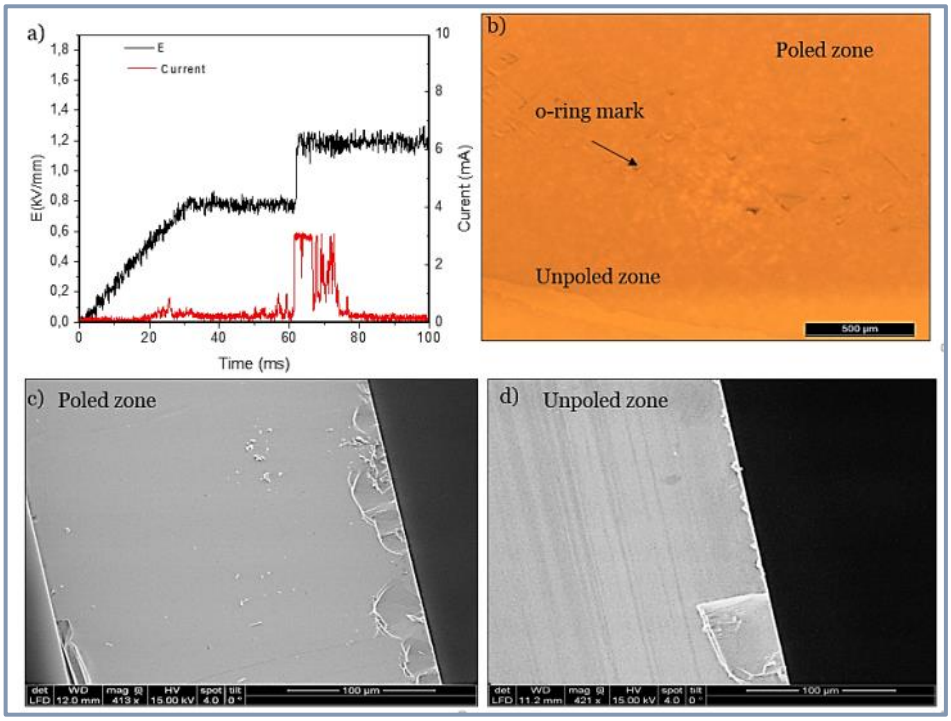

Fig. 3. 30 Transient current as a function of time during poling of 42RY- NSLT :Fe_VTEN62 (a), surface of the poled crystal after polishing (b), cross section of the sample, etched with HF, showing the poled and unpoled areas, (c) and(d), respectively.

In summary, the homogenous poling of iron doped 42 RY-SLT and NSLT crystals, treated by VTE, can be obtained by switching the direction of the field at $E_f > E_c$ several times. Similar strategy has to be applied as in the case of the congruent iron doped crystals (Table 3.7). Moreover, transient current during poling of 42 RY-NSLT:Fe also presents poly-peak nature like in the case of 42 RY-SLT crystals.

Finally, the dependence of E_f field values on the composition of the crystals was estimated from our experimental results (Fig. 3.31). E_f decreases linearly with the increase of the Li_2O concentration within the crystal and can be described by:

$$E_f = 1069.41 - 21.38\,[\%Li_2O \text{ or } X_{Li_2O}] \qquad \text{Eq. 3.8}$$

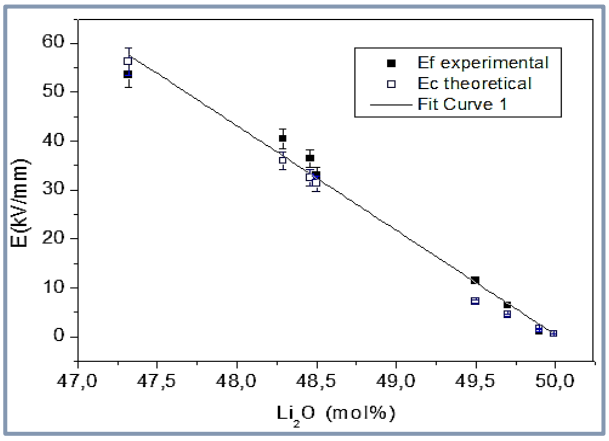

Fig. 3. 31 Forward electric field, E_f, as a function of Li_2O content in the doped and undoped 42 RY- LT crystals.

The E_f values were very close to the E_c values estimated from the Li_2O concentration in the crystals using Eq. 1.11 (see Chapter 1), reported in [25, p. 33].

3.4 Conclusions

In this chapter, I have presented some theoretical aspects of domain reversal in LT crystals. The principles and mechanisms of domain reversal by electric field poling were explained. Furthermore, the effects of Li non-stoichiometry and doping on the poling dynamics: the domains nucleation and the domains wall motion were discussed. Then, the experimental techniques used for the poling of Z-cut and 42 RY-LT crystals at room temperature were described. We have used a basic poling technique reported in several literature works [31], [38], [39]. We used two kind of samples: (i) single-domain crystals in which we reversed the polarization direction; (ii) poly-domain crystals, which were poled homogenously. We have worked on the undoped and iron doped crystals having different Li_2O non-stoichiometry. The optimization of domain reversal in iron-doped crystals required many experiments and observations. Polishing and etching by HF were used to reveal the domain structure. However, polishing was useful technique only for the flat crystals. In the case of warped crystals and cross-sections of the crystals, we preferred to use chemical etching.

To summarize, all LT crystals were poled by applying an electric field slightly higher than the coercive field. The quantity of charges delivered during complete domain reversal corresponds well to the calculated values within the error limits. In agreement with literature, E_f decreases linearly with the increase of Li concentration in the crystals. One or two poling cycles were necessary to reverse the polarization direction in the single-domain undoped crystals regardless of its composition. In contrast to single-domain crystals, the direction of the electric field had to be changed several times to homogenously pole poly-domain crystals. Furthermore, the poling of several sub-congruent crystals using similar procedure as for congruent crystals was done, as well. However, the application of very high electric fields was necessary, often inducing a dielectric breakdown of air. Thus, many of our poling test were unsuccessful for sub-congruent crystals. The poling dynamics (which is reflected in the transient current) of poly-domain NSLT and SLT crystals, prepared by VTE treatment, is different from the congruent and sub-congruent samples. In fact, the transient current in NSLT and SLT samples rarely reaches the limit current. The peaks of current are

accompanied by the creation of spikes because the motion of domains walls is carried out like “jumps”. On the other hand, the poling process is affected by the Li concentration, the defects, the homogeneity of crystals and its initial polarization state. Thus, the procedure for poling of poly-domain crystals with different concentration is essentially the same, but with some particularities. The magnitude of voltage applied and the number of poling cycles needed to obtain a completely domain reversed crystal might be different. This made the poling process difficult. In contrast to poly-domain crystals, the domain reversal in initially poled crystals was more reproducible.

Moreover, the possibility to pole 42 RY-LT:Fe crystals having different Li_2O concentrations (from sub-congruent to stoichiometric compositions) at room temperature was tested, as well. It was found that the Fe impurities have a significant effect on the poling dynamics probably by creation of pinning centers or depolarization fields. If the field was applied only in one direction, several tens of poling cycles were needed to achieve complete domain reversal. More efficient domain reversal in iron doped crystals was achieved by switching the direction of the electric field several times. Besides, it was shown that an annealing at temperatures lower than T_c made easier the domain reversal in these crystals.

According to literature, the E_c decreases [5], [50], [51] and cation mobility increases with temperature. Thus, high-temperature poling is a common technique used in literature to pole poly-domain samples. Moreover, high-temperature poling would be preferable for sub-congruent samples, in order to reduce the risk of the dielectric breakdown. Although, an experimental set up for poling at high temperatures (< 210 °C) was prepared, for the reason of a time limit it was not possible to optimize the poling procedure at high temperatures.

3.5 References

[1] K. Nassau and H. J. Levinstein, "Ferroelectric behavior of Lithium Niobate," *Appl. Phys. Lett.*, vol. 7, no. 3, pp. 69–70, Aug. 1965.
[2] K. Nassau, H. J. Levinstein, and G. M. Loiacono, "Ferroelectric lithium niobate. 2. Preparation of single domain crystals," *J. Phys. Chem. Solids*, vol. 27, no. 6–7, pp. 989–996, Jun. 1966.
[3] P. F. Bordui, R. G. Norwood, C. D. Bird, and G. D. Calvert, "Compositional uniformity in growth and poling of large-diameter lithium niobate crystals," *J. Cryst. Growth*, vol. 113, no. 1–2, pp. 61–68, Aug. 1991.
[4] A. A. Ballman and H. Brown, "Ferroelectric domain reversal in lithium metatantalate," *Ferroelectrics*, vol. 4, no. 3, pp. 189–194, Nov. 1972.
[5] C. C. Battle, S. Kim, V. Gopalan, K. Barkocy, M. C. Gupta, Q. X. Jia, and T. E. Mitchell, "Ferroelectric domain reversal in congruent LiTaO3 crystals at elevated temperatures," *Appl. Phys. Lett.*, vol. 76, no. 17, pp. 2436–2438, Apr. 2000.
[6] V. Gopalan and T. E. Mitchell, "In situ video observation of 180° domain switching in LiTaO3 by electro-optic imaging microscopy," *J. Appl. Phys.*, vol. 85, no. 4, pp. 2304–2311, Feb. 1999.
[7] S. Kim, V. Gopalan, and A. Gruverman, "Coercive fields in ferroelectrics: A case study in lithium niobate and lithium tantalate," *Appl. Phys. Lett.*, vol. 80, no. 15, pp. 2740–2742, Apr. 2002.
[8] V. Gopalan, T. E. Mitchell, and K. E. Sicakfus, "Switching kinetics of 180° domains in congruent LiNbO3 and LiTaO3 crystals," *Solid State Commun.*, vol. 109, no. 2, pp. 111–117, Dec. 1998.
[9] M. Yamada, N. Nada, M. Saitoh, and K. Watanabe, "First-order quasi-phase matched LiNbO3 waveguide periodically poled by applying an external field for efficient blue second-harmonic generation," *Appl. Phys. Lett.*, vol. 62, no. 5, pp. 435–436, Feb. 1993.
[10] L. E. Myers, R. C. Eckardt, M. M. Fejer, R. L. Byer, W. R. Bosenberg, and J. W. Pierce, "Quasi-phase-matched optical parametric oscillators in bulk periodically poled LiNbO_3," *J. Opt. Soc. Am. B*, vol. 12, no. 11, p. 2102, Nov. 1995.
[11] S. Zhu, Y. Zhu, Z. Zhang, H. Shu, H. Wang, J. Hong, C. Ge, and N. Ming, "LiTaO3 crystal periodically poled by applying an external pulsed field," *J. Appl. Phys.*, vol. 77, no. 10, pp. 5481–5483, May 1995.
[12] G. D. Miller, "Periodically poled lithium niobate: modeling, fabrication, and nonlinear-optical performance," Ph.D.Thesis, Stanford University, California, 1998.
[13] Y.-L. Chen, J.-J. Xu, X.-J. Chen, Y.-F. Kong, and G.-Y. Zhang, "Domain reversion process in near-stoichiometric LiNbO3 crystals," *Opt. Commun.*, vol. 188, no. 5–6, pp. 359–364, Feb. 2001.
[14] S. Grilli, P. Ferraro, S. De Nicola, A. Finizio, G. Pierattini, P. De Natale, and M. Chiarini, "Investigation on reversed domain structures in lithium niobate crystals patterned by interference lithography," *Opt. Express*, vol. 11, no. 4, pp. 392–405, Feb. 2003.
[15] R. V. Roussev, R. Route, J. Schaar, K. Urbanek, M. M. Fejer, D. Jundt, and C. Kajiyama, "Periodically poled vapor transport equilibrated lithium niobate for visible light generation," 2006, vol. 6103, pp. 610302-610302–7.
[16] A. C. Busacca, C. L. Sones, V. Apostolopoulos, R. W. Eason, and S. Mailis, "Surface domain engineering in congruent lithium niobate single crystals: A route to submicron periodic poling," *Appl. Phys. Lett.*, vol. 81, no. 26, pp. 4946–4948, Dec. 2002.
[17] V. Shur, E. Rumyantsev, R. Batchko, G. Miller, M. Fejer, and R. Byer, "Physical basis of the domain engineering in the bulk ferroelectrics," *Ferroelectrics*, vol. 221, no. 1, pp. 157–167, Jan. 1999.
[18] V. Y. Shur, "Kinetics of ferroelectric domains: Application of general approach to LiNbO3 and LiTaO3," in *Frontiers of Ferroelectricity*, Springer US, 2006, pp. 199–210.
[19] S. Kim, V. Gopalan, K. Kitamura, and Y. Furukawa, "Domain reversal and nonstoichiometry in lithium tantalate," *J. Appl. Phys.*, vol. 90, no. 6, pp. 2949–2963, Sep. 2001.
[20] K. Kitamura, Y. Furukawa, K. Niwa, V. Gopalan, and T. E. Mitchell, "Crystal growth and low coercive field 180° domain switching characteristics of stoichiometric LiTaO3," *Appl. Phys. Lett.*, vol. 73, no. 21, pp. 3073–3075, Nov. 1998.

[21] S. Kim, V. Gopalan, K. Kitamura, and Y. Furukawa, "Domain reversal and nonstoichiometry in lithium tantalate," *J. Appl. Phys.*, vol. 90, no. 6, pp. 2949–2963, Sep. 2001.
[22] Y. Furukawa, K. Kitamura, E. Suzuki, and K. Niwa, "Stoichiometric LiTaO3 single crystal growth by double crucible Czochralski method using automatic powder supply system," *J. Cryst. Growth*, vol. 197, no. 4, pp. 889–895, Mar. 1999.
[23] L. Tian, V. Gopalan, and L. Galambos, "Domain reversal in stoichiometric LiTaO3 prepared by vapor transport equilibration," *Appl. Phys. Lett.*, vol. 85, no. 19, pp. 4445–4447, Nov. 2004.
[24] V. Gopalan, V. Dierolf, and D. A. Scrymgeour, "Defect–Domain Wall Interactions in Trigonal Ferroelectrics," *Annu. Rev. Mater. Res.*, vol. 37, no. 1, pp. 449–489, 2007.
[25] L. Tian, "Nanoscale probing and photonic applications of ferroelectric domain walls," Ph.D.Thesis, Pennsylvania State University, Pennsylvania State, 2006.
[26] V. Y. Shur, A. R. Akhmatkhanov, I. S. Baturin, and E. V. Shishkina, "Polarization reversal and jump-like domain wall motion in stoichiometric LiTaO3 produced by vapor transport equilibration," *J. Appl. Phys.*, vol. 111, no. 1, p. 14101, Jan. 2012.
[27] V. Y. Shur, A. I. Lobov, A. G. Shur, S. Kurimura, Y. Nomura, K. Terabe, X. Y. Liu, and K. Kitamura, "Rearrangement of ferroelectric domain structure induced by chemical etching," *Appl. Phys. Lett.*, vol. 87, no. 2, p. 22905, Jul. 2005.
[28] D. A. Scrymgeour, V. Gopalan, A. Itagi, A. Saxena, and P. J. Swart, "Phenomenological theory of a single domain wall in uniaxial trigonal ferroelectrics: Lithium niobate and lithium tantalate," *Phys. Rev. B*, vol. 71, no. 18, p. 184110, May 2005.
[29] A. Kuroda, S. Kurimura, and Y. Uesu, "Domain inversion in ferroelectric MgO:LiNbO3 by applying electric fields," *Appl. Phys. Lett.*, vol. 69, no. 11, pp. 1565–1567, Sep. 1996.
[30] K. Mizuuchi, A. Morikawa, T. Sugita, and K. Yamamoto, "Electric-field poling in Mg-doped LiNbO3," *J. Appl. Phys.*, vol. 96, no. 11, pp. 6585–6590, Dec. 2004.
[31] F. Bassignot, "Nouveau type d'oscillateur exploitant des transducteurs à domaines ferroélectriques alternés et des matériaux de guidage pour l'excitation d'ondes ultrasonores d'interface," Ph.D.Thesis, Université de Franche-Comté, Besançon, 2011.
[32] Y. Kong, S. Liu, and J. Xu, "Recent Advances in the Photorefraction of Doped Lithium Niobate Crystals," *Materials*, vol. 5, no. 10, pp. 1954–1971, Oct. 2012.
[33] Roditi International Co., "Lithium Tantalate Properties." [Online]. Available: http://www.roditi.com/SingleCrystal/Lithium-Tantalate/LiTaO3-Properties.html. [Accessed: 15-Jun-2015].
[34] M. G. Clark, F. J. DiSalvo, A. M. Glass, and G. E. Peterson, "Electronic structure and optical index damage of iron-doped lithium niobate," *J. Chem. Phys.*, vol. 59, no. 12, pp. 6209–6219, Dec. 1973.
[35] W. T. Hsu, Z. B. Chen, C. C. Wu, R. K. Choubey, and C. W. Lan, "Optical Properties of Mg, Fe, Co-Doped Near-Stoichiometric LiTaO3 Single Crystals," *Materials*, vol. 5, no. 2, pp. 227–238, Jan. 2012.
[36] F. Träger, *Springer Handbook of Lasers and Optics*, 2nd ed. Kassel, Germany: Springer Science & Business Media, 2012.
[37] V. I. Kovalevich, L. A. Shuvalov, and T. R. Volk, "Spontaneous polarization reversal and photorefractive effect in single-domain iron-doped lithium niobate crystals," *Phys. Status Solidi A*, vol. 45, no. 1, pp. 249–252, Jan. 1978.
[38] E. Courjon, "Transducteurs à domaines ferroélectriques alternés pour composants à ondes de surface appliqués au traitement du signal radio-fréquence par composants passifs," Ph.D.Thesis, Université de Franche-Comté, 2009.
[39] A. Martinez, "Convertisseur en longueur d'onde intgré sur le niobate de lithium périodiquement inversé. Étude de la génération de fréquence différence indépendante de la polarisation," Ph.D.Thesis, Université Franche-Comté, Besançon, 2002.
[40] X. Liu, K. Terabe, M. Nakamura, S. Takekawa, and K. Kitamura, "Nanoscale chemical etching of near-stoichiometric lithium tantalate," *J. Appl. Phys.*, vol. 97, no. 6, p. 64308, Mar. 2005.
[41] C. L. Sones, S. Mailis, W. S. Brocklesby, R. W. Eason, and J. R. Owen, "Differential etch rates in z-cut LiNbO3 for variable HF/HNO3 concentrations," *J. Mater. Chem.*, vol. 12, no. 2, pp. 295–298, Jan. 2002.
[42] K. Nassau, H. J. Levinstein, and G. M. Loiacono, "The domain structure and etching of ferroelectric Lithium Niobate," *Appl. Phys. Lett.*, vol. 6, no. 11, pp. 228–229, Jun. 1965.

[43]K. Nassau, H. J. Levinstein, and G. M. Loiacono, “Ferroelectric lithium niobate. 1. Growth, domain structure, dislocations and etching,” *J. Phys. Chem. Solids*, vol. 27, no. 6–7, pp. 983–988, Jun. 1966.
[44]V. Gopalan and T. E. Mitchell, “Wall velocities, switching times, and the stabilization mechanism of 180° domains in congruent LiTaO3 crystals,” *J. Appl. Phys.*, vol. 83, no. 2, pp. 941–954, Jan. 1998.
[45]V. Gopalan and M. C. Gupta, “Origin of internal field and visualization of 180° domains in congruent LiTaO3 crystals,” *J. Appl. Phys.*, vol. 80, no. 11, pp. 6099–6106, Dec. 1996.
[46]V. Gopalan and M. C. Gupta, “Observation of internal field in LiTaO3 single crystals: Its origin and time-temperature dependence,” *Appl. Phys. Lett.*, vol. 68, no. 7, pp. 888–890, Feb. 1996.
[47]V. Y. Shur, E. V. Nikolaeva, E. I. Shishkin, V. L. Kozhevnikov, A. P. Chernykh, K. Terabe, and K. Kitamura, “Polarization reversal in congruent and stoichiometric lithium tantalate,” *Appl. Phys. Lett.*, vol. 79, no. 19, pp. 3146–3148, Nov. 2001.
[48]D. Hum, “Frequency conversion in near-stoichiometric lithium tantalate fabricated by vapor transport equilibration,” Ph.D.Thesis, Standford University, Standford, California, 2007.
[49]F. Bassignot, E. Courjon, F. Henrot, T. Baron, and S. Ballandras, “New microfabrication method to invert micrometric ferroelectric domains on lithium niobate wafers for RF applications,” in *Applications of Ferroelectric and Workshop on the Piezoresponse Force Microscopy (ISAF/PFM), 2013 IEEE International Symposium on the*, 2013, pp. 283–286.
[50]M. Houé and P. D. Townsend, “Thermal polarization reversal of lithium niobate,” *Appl. Phys. Lett.*, vol. 66, no. 20, pp. 2667–2669, May 1995.
[51] H. Ishizuki, I. Shoji, and T. Taira, “Periodical poling characteristics of congruent MgO:LiNbO3 crystals at elevated temperature,” *Appl. Phys. Lett.*, vol. 82, no. 23, pp. 4062–4064, Jun. 2003.

Chapter 4

Effect of Li non-stoichiometry and domain structure on acoustical properties of BAW and SAW devices based on $LiTaO_3$ crystals

4.1 Introduction

The application of piezoelectric LT single crystals for Surface Acoustic Wave (SAW) devices has been discussed in Chapter 1. The most of SAW filters are based on the 42° rotated Y-cut X propagating $LiTaO_3$ crystals (42 RY-LT, common notation or XYl/42, according to the IEEE standard notation)[1] due to its piezoelectric properties such as good electromechanical coupling factor (K^2= 7-10 %) and a relatively low Temperature Coefficient of Frequency (TCF)[2]. In 42 RY-LT crystals, the wave velocities of leaky wave depend mainly on C_{44} and C_{66} elastic stiffness constants, as will be demonstrated later. In this work, we are interested in the learning about the relationship between elastic constants and crystal composition because several wave propagation properties, such as the TCF, depend directly on these constants and contribute to the performance of SAW filters. Therefore, we will focus on the investigation of the effect of Li non-stoichiometry on the temperature dependence of elastic constants, mainly C_{44} and C_{66}.

It has been previously reported that elastic constants depend on the Li composition. The effect of Li non-stoichiometry on the elastic constants has been evaluated at room temperature for LT and LN crystals with nearly congruent compositions in the range from 48.28 to 48.55 mol% of Li_2O [3], [4]. As it was discussed in the Chapter 1, the elastic constants of LT and LN increase with the increase of Li_2O content, with exception to the C_{44} of LN, which decreases when stoichiometric composition is approached [3]. Therefore, the wave propagation characteristics are modified with change in Li_2O concentration, as well. It has been shown that longitudinal, shear and LSAW velocities increase with the reduced Li_2O non-stoichiometry. The change in wave velocities as a function of composition depends on the crystal cut. For example, in the case of 33 RY-X LT cut crystals, velocity of LSAW increases by 23.8 m/s by adding 1 mol % of Li_2O [3]. In the case of LN crystals, most of velocities along different directions increase with the reduced Li deficiency. However, several shear and LSAW velocities decrease when the Li content increase slightly. Furthermore, density of LT and LN also changes with the Li non-stoichiometry. It decreases by 18.26 kg/m^3 and by 6.94 kg/m^3 when Li_2O concentration is increased by 1 mol% in LT and LN crystals, respectively.

On the other hand, it has been demonstrated that the ferroelectric domain structure affects the elastic constants, as well. The elastic constants are slightly higher for poly-domain

LT crystals than those of the single domain material. The increase in the values of the elastic constants are in a range from 1.67 % to 7.97 % [5]. Consequently, the acoustic properties of materials are also significantly affected by poly-domain structure. For example, the LSAW velocities of 112.2RX-Y LT poly-domain crystals is 2.7 % larger than that of the single-domain crystals in, measured in, being larger than the velocity of the poly-domain wafer[6].

The objective of this work was to understand the effect of Li concentration and the effect of domains on the acoustical properties (TCF and K^2) of 42 RY-X LT crystals. Moreover, since the performance of acoustic filters, based on these crystals, depends mainly on C_{44}, the estimation of its dependence on temperature, stoichiometry and domains state was also required. This knowledge will allow us to correlate the Li non-stoichiometry and the performance of SAW filters on 42 RY-X LT crystals.

In this chapter, I start with a review of different methods used for estimation of elastic constants and thereafter I present our used approach. Then, I explain the experimental techniques used for fabrication of devices and their characterization. Later, I present the simulations done for different applications of BAW and SAW devices and the experimental results.

4.2 Theoretical considerations

4.2.1 Estimation of elastic properties of LT and LN

The elastic constants can be characterized by measuring the velocity of waves propagating in materials. There are several methods for determining elastic properties of LT and LN. The methods, used in literature, can be classified in:

1) Impedance measurement;
2) Ultrasonic velocity measurement;
3) Brillouin spectroscopy;

In impedance measurement, electrodes are deposited on the surface of the plates with different crystallographic orientations and the impedance of the thickness modes of vibration in plates is measured. The elastic constants of LT and LN can be estimated from the measurement of velocities of BAW propagating along the X, Y and Z-axis, by using the Eqs.1.41-1.50 given in the Chapter 1. The effective elastic constant characterizing the propagation of an elastic wave along the thickness of an arbitrary crystal cut can always be estimated from the resonance frequency, according to the following equation [7]:

$$C^E = 4t^2 \rho f_r^2, \qquad Eq.\ 4.1$$

where t is the thickness of plate, f_r is the resonance frequency and ρ is the mass density. All six independent elastic constants can be obtained by studying of appropriate crystal cuts and the direction of the applied electric field. For this purpose, two configurations of excitation are possible: thickness field excitation and lateral field excitation, which have been described in the Chapter 1 (section 1.4.2.1). In the Table 4.1, we list the plate orientations and the type of excitation used to characterize the different elastic constants of LN and LT [8].

Another method used for the estimation of elastic properties of LN and LT is based on the measurement of ultrasonic phase velocity by means of the ultrasonic pulse-echo technique [9]. This method was widely used for the estimation of elastic constants and has been improved in order to get results with an accuracy of four significant digits [10]–[12]. The experimental set up consists in a film transducer (in ZnO or X-cut LN), a cylindrical buffer rod of synthetic silica (SiO_2) glass, a coupling material (pure water or a thin layer of a bonding material) and the sample to be measured. The structure of the testing probe is shown in the Fig. 4.1. First, the transducer converts the electrical radio frequency signals into ultrasonic waves which propagate through the silica buffer rod, the coupling material and the sample. Then, the ultrasonic waves are reflected into two signals: from the front surface of the specimen, V_1, and from the back surface, V_2. These signals are superposed in the time domain by the double pulse method and the frequency is swept. Finally, the velocity of bulk acoustic waves, V, is determined from the frequency interval in the interference waveform, Δf, and the thickness of the sample, h, using the following equation:

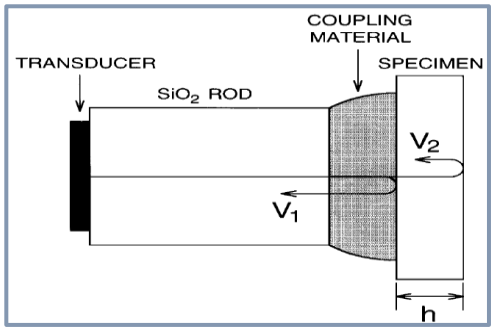

Fig. 4.1 Experimental set up for measurement of ultrasonic velocities using the double-pulse interference method [2].

$$V = 2\Delta f h. \qquad \textit{Eq. 4.2}$$

By this method, shear wave velocities can be measured whenever they are independent of the electric displacement. Otherwise, shear velocities are usually measured by the impedance method [10].

Furthermore, the dielectric constants are obtained by measuring the capacitance of a plate with full electrodes at a frequency sufficiently lower than the lowest resonance frequency. Density can be determined using the Archimedes method. An improvement of the latter technique is the use of a line focus Beam (LFB) system. The details of this method are described in Ref. [13]. LFB system allows focusing an acoustic field at defined angles, which enhances the accuracy of the method.

Table 4.1 Different crystallographic cuts and excitation modes allowing the determination of elastic constants of LT and LN crystals

Elastic constant	***Cut plate***	***Vibration mode***	***Type of excitation***
C_{11}	X	Pure extensional	Lateral field excitation
C_{33}	Z	Pure extensional	Thickness field excitation
C_{44}	Z	Pure shear	Lateral field excitation
C_{66}	Y	Pure shear	Lateral field excitation
C_{13}	Y rotated	Quasi shear (QS), Quasi extensional (QE), Thickness extensional (TE)	Lateral field excitation
C_{14}	Y rotated	Quasi shear (QS), Quasi extensional (QE)	Lateral field excitation

Another approach used for characterization of elastic properties is Brillouin spectroscopy. In this technique a laser beam directed on the surface of crystal produces

acoustic vibrations in the material, then the light is scattered at a slightly different frequency. This difference of frequency ($\Delta\upsilon^B$) is defined by:

$$\Delta\upsilon^B = \left(\frac{V}{\lambda}\right)(n_i^2 + n_S^2 - 2n_i n_s\, cos\theta)^{1/2}, \qquad Eq.\ 4.3$$

where λ is the photon laser wavelength, n_i and n_s are the incident and scattered refractive index, respectively, V is the sound velocity, and θ is the angle between the incident and scattered light. The velocity of transverse acoustic phonons propagating along the c-axis of LT and LN crystals, is related to the C_{44} elastic constant by $C_{44}=\rho V^2$ [14]. The angle θ can be modified, allowing the measurement of the wave velocity for different directions of propagation [15].

All here-presented methods have advantages and drawbacks. For example, the convenience of ultrasonic microscopy is the possibility to evaluate directly the elastic properties in a determined direction and with a better accuracy, compared to the other methods. However, not all velocities can be estimated and usually impedance and ultrasonic microscopy are complementary techniques. The Brillouin spectroscopy allows the estimation of elastic constants. Nevertheless, the accuracy is lower than the accuracy of ultrasonic method [16].

In this work we have used the impedance measurement because it allows the estimation of elastic constants and also other acoustical properties of interest for our project, such as the electromechanical coupling factor and the evolution of frequency with temperature. On the other hand, the dependence of the velocity of Rayleigh waves (RW) and LSAW on the elastic stiffness was estimated for 42 RY-X LT substrates by means of numerical analysis, in order to estimate the sensitivity of these wave velocities to each independent elastic constant [17]. The results are summarized in the Table 4.2. The C_{44} and C_{66} elastic constants have the most important influence on the variation of frequency of RW and LSAW in 42 RY-X LT. Similarly, we have realized the analysis on the relationship between resonance frequency and the variation of elastic constants in Z-cut and 42 RY-LT crystals, which will be presented in the next sections.

Table 4.2 Dependence of SAW velocities on elastic constants in 42 RY-X LT. Where $V_{LSAW\ ref}$ and $V_{RW\ ref}$ are the leaky surface acoustic wave and Rayleigh wave velocities, respectively.

	LSAW				Rayleigh wave		
$V_{LSAW\ ref}$:	**3929.03**	**dV (m/s)**	**$dV/V_{LSAW\ ref}$ (ppm)**	**$V_{RW\ ref}$:**	**3037.77**	**dV (m/s)**	**$dV/V_{RW\ ref}$ (ppm)**
dC_{11}	3924.99	-4.04	-1028.24	dC_{11}	3030.85	-4.1	-1310.54
dC_{13}	3931.42	2.39	608.29	dC_{13}	3037.91	0.14	44.75
dC_{14}	3926.11	-2.92	-743.86	dC_{14}	3039.82	2.47	789.52
dC_{33}	3925.34	-3.69	-939.63	dC_{33}	3036.96	-0.63	-201.38
dC_{44}	3911.47	-17.56	**-4469.29**	dC_{44}	3027.14	-11.51	**-3679.09**
dC_{66}	3920.45	-8.58	**-2183.75**	dC_{66}	3023.37	-17.09	**-5462.7**

4.2.2 Dependence of frequency of BAW resonators on elastic constants

The dependence of frequency on the elastic constants and the dependence of the electromechanical coupling factor on the piezoelectric moduli have been investigated analytically. For this purpose, we created a script in Scilab, which is given in Annex A.3.1. The analysis was done considering a piezoelectric BAW resonator where the wave propagates along the plate thickness. We start from the tensors (in matrix representation) of elastic, piezoelectric and permittivity constants given in Chapter 1 (Eq.1.23-1.25). Then, the matrices are rotated according to the crystal orientation of plate, defined by the Euler angles (ψ, θ, φ). The rotation is performed in such a way that the thickness coincides with x_2 axis in the local frame. Afterwards, the [3x3] matrix of piezoelectrically-stiffened elastic constants defining the Christoffel coefficients Γ_{ij} in local axes is calculated as follows:

$$[\Gamma] = \begin{bmatrix} C_{66}^E + \frac{{e_{26}}^2}{\varepsilon_{22}} & C_{26}^E + \frac{e_{22}e_{24}}{\varepsilon_{22}} & C_{46}^E + \frac{e_{24}e_{26}}{\varepsilon_{22}} \\ C_{26}^E + \frac{e_{22}e_{24}}{\varepsilon_{22}} & C_{22}^E + \frac{{e_{22}}^2}{\varepsilon_{22}} & C_{24}^E + \frac{e_{22}e_{24}}{\varepsilon_{22}} \\ C_{46}^E + \frac{e_{24}e_{26}}{\varepsilon_{22}} & C_{24}^E + \frac{e_{22}e_{24}}{\varepsilon_{22}} & C_{44}^E + \frac{{e_{24}}^2}{\varepsilon_{22}} \end{bmatrix} \qquad \textit{Eq. 4.4}$$

The corresponding system of eigenvalues and eigenvectors is obtained. And then, we determine the wave velocities and the polarization direction of three modes: Slow Shear (SS), Fast Shear (FS) and Thickness Extension (TE).

Then, we obtain the natural (open circuit) frequency, f, of a BAW resonator from the wave velocity ,V, and the corresponding eigenvalue, $\bar{C}$, of the Christoffel matrix in local axes:

$$V = \sqrt{\frac{\bar{C}}{\rho}}, \quad f = \frac{nV}{2h}, \qquad \textit{Eq. 4.5}$$

where ρ is the density and h is the thickness of the piezoelectric substrate. Considering that LT and LN belong to the $3m$ point group, these crystals possess only 6 independent elastic coefficients. Assuming that there is a small change in an independent elastic constant C_n within the restricted set, $C_n \in [C_{11}, C_{13}, C_{14}, C_{33}, C_{44}, C_{66}]$, the variation of the frequency δf with this considered constant C_n is readily expressed in terms of successive partial derivatives:

$$\delta f = f - f_0 = \frac{\partial f}{\partial C_n}\delta C_n + \frac{1}{2}\frac{\partial^2 f}{\partial C_n^2}\delta^2 C_n \ , \qquad \textit{Eq. 4.6}$$

where f_o is the initial frequency. This second order expansion allows the numerical estimation of the partial derivatives $\partial f_n/\partial C_n$ by performing small arbitrary fractional changes δC in the computation of the frequency as follows:

$$C_n = C_{0n}(1 + \delta C)$$

$$\frac{\partial f_n}{\partial C_n} = \frac{4f_1 - f_2 - 3f_0}{2\delta C\ (C_{0(n)})} \ , \qquad \textit{Eq. 4.7}$$

where C_{on} is the initial value of elastic constant, f_1 and f_2 are the modified frequencies upon incrementing C_n by δC and $2\delta C$, respectively. To facilitate the comparison between the obtained partial derivatives for different vibrational modes in various crystal cuts, we can turn them into a normalized (dimensionless) form ($\%\gamma$), which we take the liberty to call "contributions" for the sake of convenience:

$$\%\gamma = \frac{|\partial f_n/\partial C_n|}{\sum_{n=1}^{6}|\partial f_n/\partial C_n|} \qquad \textit{Eq. 4.8}$$

A fully linear relationship between f and the C_n would actually be required to have here-defined quantities exactly represent the contributions of each independent elastic constant to the frequency. Nevertheless, they are useful to help understanding the influence of small variations of the material constants on the behavior of resonators from various orientations.

Similarly, a small variation in a piezoelectric coefficient e_n, where $e_n \in [e_{15}, e_{22}, e_{31}, e_{33}]$ produces a change of the electromechanical coupling factor (K^2). This variation can be expressed in terms of partial derivatives as follows:

$$\delta K^2 = K^2 - K_0^2 = \frac{\partial K^2}{\partial e_n}\delta e_n + \frac{1}{2}\frac{\partial^2 K^2}{\partial e_n^2}\delta^2 e_{ij}\,, \qquad \textit{Eq. 4.9}$$

this expression enables to determine the partial derivatives $\partial K^2/\partial e_n$ when piezoelectric coefficients vary by δe:

$$e_n = e_{0(n)}(1+\delta e)$$

$$\frac{dK_n^2}{\partial e_n} = \frac{4K_1^2 - K_2^2 - 3K_0^2}{2\delta e\ e_{0(n)}}, \qquad \textit{Eq. 4.10}$$

where K_0^2 is the initial value of elastic constant, K_1^2 and K_2^2 are the modified frequencies upon incrementing e_n by δe and $2\delta e$, respectively. Thus, the "contribution",%β (given in percents), of piezoelectric coefficients in the variation of K^2, for each mode can be estimated by:

$$\%\beta = \frac{|\partial K_n^2/\partial e_n|}{\sum_{n=1}^{6}|\partial K_n^2/\partial e_n|} \qquad \textit{Eq. 4.11}$$

Two type of BAW resonators were studied: *i)* plates in Thickness Field Excitation (TFE), having a thickness of 250 μm; *ii)* resonators based on high aspect ratio ridge structures

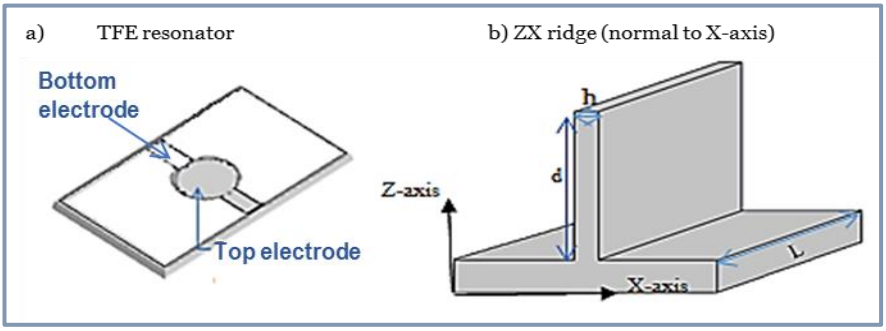

Fig. 4.2 Schematic representation of BAW resonators configured in: thickness field excitation (a) and high aspect ratio ZX ridge resonator structured on Z-cut LT wafers (b)

(hereafter called ridges). The Fig. 4.2 shows an example of each type of BAW resonator.

In the case of the TFE plates, the 42 RY-LT and Z-cut LT orientations were analyzed, where the wave propagates perpendicularly to the thickness. These crystallographic orientations corresponds to the YXl/42 and YXl/90, according to the IEEE standard notation [1]. In the case of ridge resonators, three different orientations of ridges were investigated: (i) ridge normal to X-axis in Z-cut LT wafer (ZX-LT), (ii) ridge parallel to X-axis in Z-cut LT wafer (ZY-LT), (iii) ridge normal to X-axis in 42RY-LT wafer (42RYX-LT). It should be stressed that the ZX and 42RYX-LT configurations are expected to have similar behaviour

because the ridges are in the same X plane, although the second one is simply rotated by 42 degrees around its own normal. The ridge resonator is geometrically defined by its length , *L*, depth, *d*, and thickness, *h*, as illustrated in the Fig. 4.2 b. The numerical analysis was done considering that the ridge is a plate of 20 μm of thickness and it was rotated according the Euler angles (φ, θ, ψ) as indicated in the Table 4.3.

The contributions of different elastic constants to the variation of resonance frequency (%γ), as well as the variation of electromechanical coupling (%β) with piezoelectric coefficients were estimated from the Eqs. 4.8 and 4.11, respectively. The results obtained for BAW in TFE and for ridges resonators are summarized in the Tables 4.3 and 4.4, respectively. Concerning the resonator in TFE configuration, it was found that the slow shear, fast shear and thickness extension modes can be excited in the both type of plates (Table 4.3). In the case of Z-cut LT resonator, the SS mode purely depends on C_{66}, while in the case of the other modes, C_{11}, C_{14} and C_{44} contributed, as well. In the case of FS and TE modes, the piezoelectric coefficients e_{15} and e_{22} have a contribution to the variation of K^2. On the other hand, in the case of 42 RY-LT plate, the mode SS depends on C_{14}, C_{44} and C_{66}. In the case of FS and TE modes, the variation of frequency depends on almost all independent elastic constants, with exception to C_{66} of the modes FS and TE. In similar way, all piezoelectric constants have a contribution to the frequency variation of the modes FS and TE, while the mode SS is not piezoelectrically coupled.

Table 4.3 Contribution in percent of different elastic and piezoelectric constants to the variation of frequency and K^2, % γ and %β, respectively, of SH, FS and TE modes in Z-cut LT and 42RY-LT BAW in TFE configuration resonators. The contributions noted by an asterisk indicate the change in elastic constant that induces negative shift of frequency. The Euler angles representing studied crystal cuts are given, as well.

Orientation of plate	***Mode:***		***SS***	***FS***	***TE***
Z-cut LT **(φ, θ, ψ)=0,0,0**	*Velocity (m/s)*		*3306*	*3335*	*6213*
	Frequency (MHz)		*6.6*	*6.7*	*12.4*
	%γ	**C_{11}**	0	3.0	68.7
		C_{14}	0	28.3	28.3*
		C_{44}	0	68.7	3.0
		C_{66}	100	0	0
	% β	**e_{15}**	0	82.9	17.1
		e_{22}	0	17.1*	82.9
42RY- LT **(φ, θ, ψ)=0,42,0**	*Velocity (m/s)*		*3306*	*3335*	*6213*
	Frequency (MHz)		*6.6*	*6.7*	*12.4*
	%γ	**C_{11}**	0	24.5	9.4
		C_{13}	0	46.2*	16.2
		C_{14}	49.9	7.1	34.9*
		C_{33}	0	21.7	7
		C_{44}	22.4	0.5	32.5
		C_{66}	27.7	0	0
	% β	**e_{15}**	0	34.4	40.9
		e_{22}	0	23.9*	22.1
		e_{31}	0	21.5*	19.9
		e_{33}	0	20.2	17.1

Frequency dependence on elastic constants and the variation of K^2 with piezoelectric constants of ridge resonators are summarized in the Table 4.4. The frequency shift of the TE

modes is ruled by C_{11} in ZX and 42 RYX resonators. In the case of ZY structure, the frequency of this mode is also mainly defined by C_{11} but with contributions from C_{14} and C_{44}. The frequency of SS mode for ZY ridge resonators is purely dependent on C_{66}, while C_{14}, C_{44} and C_{66} contribute to the frequency of this mode in the case of ZX and 42 RYX ridges. The frequency shift of FS mode in ZY structure is mainly dependent on C_{44}, although a contribution from C_{14} and C_{11} is also seen. The frequency of ZX and 42 RYX ridges, in the FS mode, is also dependent on C_{44} but it is mainly defined by C_{14} and to a lesser extent by C_{66}.

Table 4.4. Contribution in percent of different elastic constants to the variation of frequency and K^2, % γ and %β, respectively of SH, FS and TE modes in ZY, ZX and 42RYX ridge resonators. The contributions noted by an asterisk indicate the change in elastic constant that induces negative shift of frequency. L stands for the length, d - the depth, and t- the thickness (Fig. 4.2 b). The Euler angles representing studied crystal cuts are given, as well.

Orientation of ridge	***Mode:***		***SS***	***FS***	***TE***
ZY **Ridge parallel to X-axis** **L//X** **d// Z** **h// Y** **(φ, θ, ψ)=0,0,0**	*Velocity (m/s)*		*3536*	*3677*	*5611*
	Frequency (MHz)		*88.4*	*91.9*	*140.3*
	%γ	**C_{11}**	0	3.0	68.7
		C_{14}	0	28.3	28.3*
		C_{44}	0	68.7	3.0
		C_{66}	100	0	0
	% β	**e_{15}**	0	82.9	17.1
		e_{22}	0	17.1*	82.9
ZX **Ridge normal to X-axis** **L//Y** **d// Z** **h// X** **(φ, θ, ψ)=90,0,0**	*Velocity (m/s)*		*3301*	*3924*	*5588*
	Frequency (MHz)		*82.5*	*98.1*	*139.7*
	%γ	**C_{11}**	0	0	100
		C_{14}	48.8	48.7*	0
		C_{44}	17.7	33.5	0
		C_{66}	33.5	17.8	0
	% β	**e_{15}**	42.1	57.9	0
		e_{22}	57.9*	42.1	0
42RYX **Ridge parallel to X-axis** **L//Y** **d// Z** **h// X** **(φ, θ, ψ)=90,0,-42**	*Velocity (m/s)*		*3301*	*3924*	*5588*
	Frequency (MHz)		*82.5*	*98.1*	*139.7*
	%γ	**C_{11}**	0	0	100
		C_{14}	48.8	48.7*	0
		C_{44}	17.7	33.5	0
		C_{66}	33.5	17.8	0
	% β	**e_{15}**	42.1	57.9	0
		e_{22}	57.9*	42.1	0

4.3 Experimental Techniques

4.3.1 Fabrication of BAW and SAW structures

BAW devices were fabricated in order to investigate the impact of Li-non stoichiometry and ferroelectric domain state on electro-acoustical properties and to estimate the temperature dependence of C_{44} elastic constant. Two types of BAW resonators, based on 42RY-LT and Z-cut LT single crystals with different stoichiometries and domain structures, were fabricated for the generation of different types of acoustic modes: a) thickness field excitation (TFE) in piezoelectric plates; b) thickness field excitation of shear modes in high aspect ratio *ridge* structures, which we called ridge resonators. The dimensions of the plates

used experimentally in this study were 25x30 mm² with a substrate of thickness of 250 µm. This plate size was adapted to the diameter of the crucible used for VTE treatment of the crystals. In the next sections I will give detailed description of the experiments conducted for the fabrication and characterization of each type of devices.

4.3.1.1 Fabrication of BAW resonators for thickness field excitation

Untreated 42RY-LT crystals, provided by Yamaju Ceramics, and crystals treated by VTE (with different Li content) were used as substrates for BAW resonators. The main steps for fabrication of BAW resonator in thickness field excitation configuration are listed below and are schematically represented in the Fig. 4.3 :

1. Cutting of wafers by using an automatic dicing saw DISCO DAD 320, equipped with a high-speed spindle with an ultra-thin diamond blade to dice the wafer into samples with size of 25x30 mm².
2. Polishing back and front side of each sample by using a polishing disc in felt and a suspension of colloidal silica as abrasive, which has a grain size of 50 nm.
3. Deposition of gold electrodes with thickness of 90±10 nm on both sample surfaces by using by magnetron sputtering (machine MP 500 Plassys) at room temperature. The metal was deposited during 2 min. by using a current of 0.3 A, pression of 70 mbar and Ar presence.

4.3.1.2 Fabrication of ridge structure for BAW resonator

Commercially available congruent iron doped 42RY-CLT and Z-CLT, having the thickness of 250 µm and 500 µm, respectively, were used for the fabrication of ridge resonators. Nearly stoichiometric and single domain (Z-NSLT) crystals with composition of 49.95 mol% of Li_2O were supplied by Deltronics (USA). Single-domain Z-cut LT plates were used for the fabrication of ridges, as well.

The 42RY-LT crystals with several Li concentrations, from congruent (48.5 mol% of Li_2O to near stoichiometric, 49.99 mol% of Li_2O) were used. Congruent (42RY-CLT) crystals were provided by Yamaju Ceramics and the crystals having different Li contents were prepared by the VTE process, followed by electrical field poling at room temperature.

The ridge structures were fabricated according to the technology developed at FEMTO-ST. Details about fabrication of ridges can be found in the Refs. [18], [19]. The process for the fabrication of ridges resonators is described below and illustrated in the Fig. 4.3 a:

1. *Dicing-polishing of single crystal.* It is carried out by using an automatic dicing saw machine DISCO DAD 3500. The blades used for dicing have a width of 200 µm. Several characteristics are important to control the ridge fabrication: the thickness (h), the depth (d) and the length (L). In the first step, two parallel cuts are made on the substrate, separated by a desired width or thickness. Parallelism is involved in total thickness variation (TTV) of the final structure, so its regulation is important for confining acoustic waves. The variation of thickness of ridge depends of its length, therefore the TTV of long ridges will be larger than this of short ridges. The verticality of sidewalls is also a critical parameter, it should be close to 90° in order to have an homogeneity in depth of ridges. This may affect its electrical response. Roughness of sidewalls should be small (<10 nm rms) because it may increase the propagation losses.

2. *Deposition of electrodes*. After cutting, samples were metallized with aluminum using sputtering technique. The aluminum was deposited during 3 min. by using a current of 0.51-0.53 A, Ar and a pression of 70 mbar. It is known that sputtering leads to a bad conformality of depositions on the vertical walls. We had a choice between sputtering and evaporation techniques. Both methods are directional (bad coverage of vertical walls), but sputtering results in more conformal thickness. Thus, this method was chosen because atoms are sputtered in several directions, allowing deposition of metal in a vertical structure. In this way, electrodes of 60±10 nm of thickness were deposited on the sidewalls of the ridge structures.

3. *Protection step*. In this step a drop of photoresist S1813 is applied on the device surface, followed by an annealing at 90°C during 25 minutes in an oven.

4. *Cut-away*. The metal deposited on the top of ridge is removed by cutting 2-5 µm of material along the structure. A second cut is done in the plane of electrodes, as well, in order to isolate electrically the electrodes. Finally, photoresist is removed. In this work, all the steps of dicing were carried out by Blandine Guichardaz, from the Technological Center MIMENTO at FEMTO-ST Institute. After fabrication, the devices were inspected by using optical microscope and SEM. SEM images of fabricated ridge-resonators are shown in the Fig. 4.3 b.

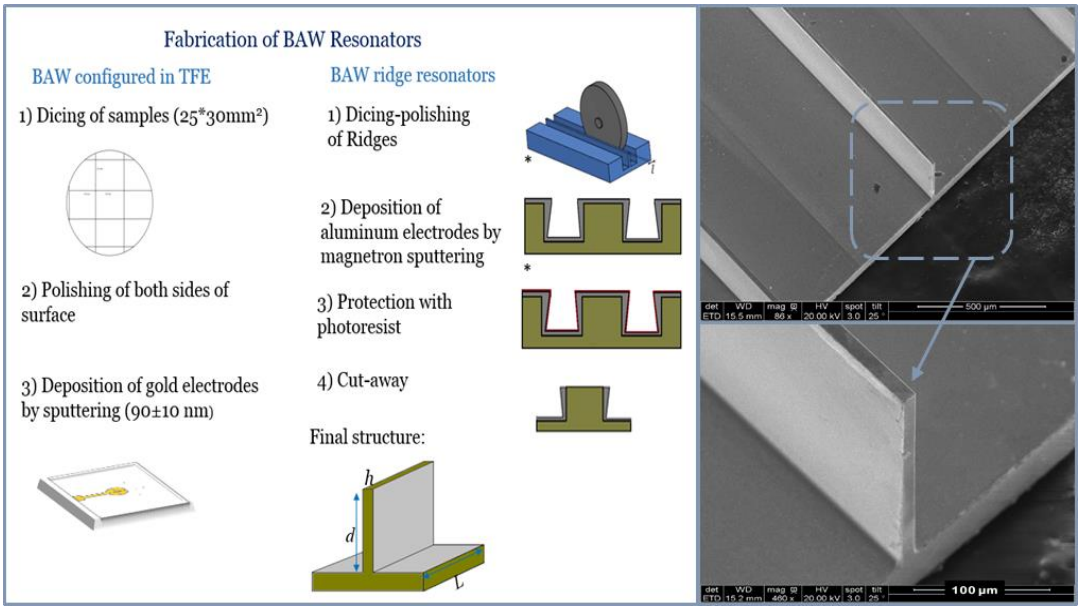

*Figure 4.3 Flow chart showing the necessary steps for BAW device fabrication (a). SEM image of ridge resonators realized on 42RY-LT crystals (b). * Images modified from [19]*

4.3.1.3 Fabrication of SAW devices

SAW filters were fabricated on substrates of undoped 42RY-LT crystals. Crystals were VTE treated and then uniformly poled in the middle zone of the crystal. The wafers were provided to the company frec|n|sys for the realization and characterization of SAW filters. According to the design of filters, the metal thickness required is 800 nm. The photolithography technique used was lift-off. It requires a photoresists having a thickness three times more important than metal thickness. Therefore, the photoresist should be at least 2.4 µm thick. It is suitable for a pattern with a strip width of 2 µm. Then, it is important to use a photoresist allowing to get shapes with an aspect ratio larger than the one used in typical process. For this reason, the AZ nLOF 2035 photoresist was used. The wafer was coated by the photoresist and then it was baked at 110 °C for 3 min. Then, the wafer was exposed to UV light by using an exposure dose

of 500 mJ/cm². After this stage, the exposed regions of the photoresist were developed with AZ 326 MIF. Afterwards, the Al-Cu 2% alloy with thickness of 800 nm was deposited on the surface of wafer by evaporation. Finally, the wafer was immerged in an acetone bath to remove the remaining resist by lifting-off the metal deposited on the top of the resist. The electrical characterization of BAW and SAW devices will be described in following sections.

4.3.2 Measurements of acousto-electrical properties

4.3.2.1 Characterization of BAW resonators in TFE configuration

The electrical characterization of BAW and SAW devices consists essentially in the measurement of electrical parameters of resonators such as admittance and impedance as a function of frequency. The BAW resonators in TFE configuration were characterized by using a set up allowing to connect the ground to the back electrode of device and the top electrode to the Vector Network Analyzer (VNA) Agilent E5100A. The Fig. 4.4 shows the experimental set up used for admittance measurements. The frequency response was investigated in the range from 11 to 40 MHz.

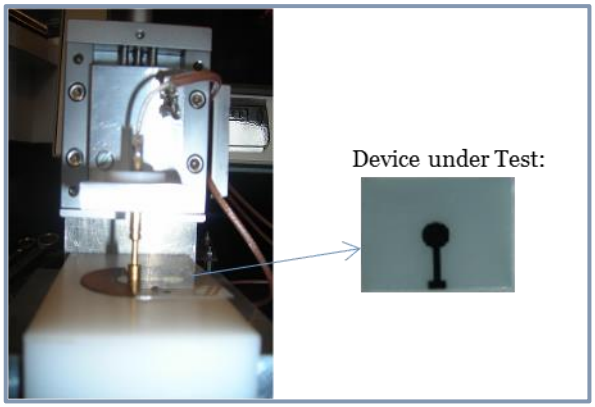

Fig. 4.4 Experimental set-up used for electrical characterization of a BAW resonators in TFE configuration

4.3.2.2 Characterization of ridge resonators and SAW devices.

The experimental set up, used for the characterization of ridge resonators was composed of the Vector Network Analyzer (VNA) ROHDE & SCHWARZ, which allows to measure frequencies from 100 kHz to 8.5 GHz and a probe station connected to the VNA. The a pair of RF probes are aligned through a microscope (Suss Microtec PM5) onto the test device (Fig. 4.5). The first step of measurements is the calibration of probes by means of a calibration substrate following the usual protocol (open, short, match). The frequency response of ridges resonators was investigated in the range from 50 to 200 MHz. Measurements at different temperatures, in the range from 25°C to 100°C, were performed by placing a sample on a hot plate. The accuracy in temperature was ±1 °C. The first order TCF and the K^2 were estimated in the range from 30°C to 100°C, by using Eqs. 1.55 and 1.64 (Chapter 1), respectively.

SAW devices were characterized by frec|n|sys company by using a similar experimental set-up. The heating of sample was done by using a chuck that enables to hold the sample by vaccum and the temperature of sample.

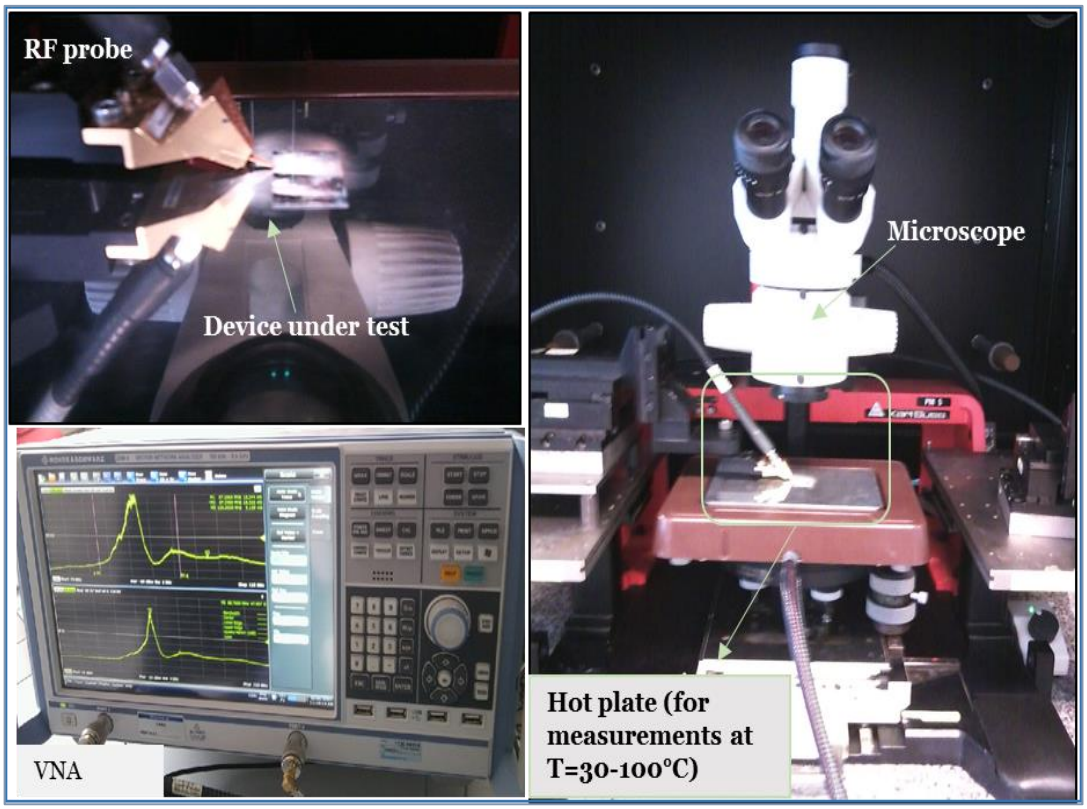

Figure 4.5 Experimental set-up for admittance measurements, showing the VNA, the RF probes and the hot plate used for characterizations at different temperatures.

4.4 BAW resonators based on 42 RY-LT and Z-cut LT single crystals

In this section I will present the simulations and experimental results of different configurations of BAW resonators: i) thickness field excited (TFE) BAW resonators, ii) lateral field excited (LFE) BAW resonators, iii) ridge resonators. Firstly, I will introduce the simulation tools used in this work and then the results of simulations and their comparison with experimental results.

4.4.1 Simulation tools of acoustic devices

The Finite Elements Method (FEM) is a technique that allows the modeling of physical phenomena by using the numerical solution of partial differential equations. In FEM, a complex structure is discretized in sub-domains called finite element. Each element is formed by points called nodes, which are related to the other ones by equations. By solving the equation for each element it is possible to estimate the field variables of the studied physical phenomenon in the whole structure. The set of elements forms a mesh, whose density, *d*, defines the accuracy of modeling [20]. On the other hand, the boundary elements method (BEM, also called boundary integral method BIM) is an alternative numerical method. In the case of this method, the conjugate field variables (e.g. stresses and strains) can be uniquely determined over the entire frontier of a studied domain so that the equations obeyed by the field variables inside the enclosed domain are automatically satisfied. Thereby, from the user's viewpoint the main difference between FEM and BEM is that the latter one requires the

discretization only on the surface (or boundaries) of the domain [21]. Although BEM drastically reduces the number of degrees-of-freedom of a given problem, it generally results in well-filled matrices, at the difference of FEM which results in sparse matrices.

The simulation tools used here are based on a combination of finite elements and boundary elements and allow the modeling of structure in two and three dimensions (2D and 3D, respectively). These modeling tools were developed by several members of the CoSyMA group of the Time & Frequency Department at FEMTO-ST. More details about its performances and building principles can found in the Refs.[22], [23].

Several BAW resonators, based on LT, were simulated in order to investigate the acoustical properties of resonators in TFE, LFE and ridge configurations. Moreover, simulations taking into account the effect of temperature were also realized in order to compare theoretical results with experimental ones. In the next sections, the simulations and experimental characterization of BAW resonators will be presented.

4.4.2 BAW resonators in thickness field excitation configuration

4.4.2.1.2 Simulations

Prior to the modeling of 2D structures, some calculations were done in order to optimize the thickness of electrodes. The energy trapping model was used for estimation of the electrode thickness required to excite only the main frequency response issued by modes converging at infinity, in order to avoid spurious responses arising from the numerous lateral resonances. This model takes into account the nature of substrate, its dispersion constants, the metal to be deposited and the dimension of electrodes. We found that the required thickness was between 50 and 150 nm. The detailed description of this study is given in the Annex A 4.2. Then, a BAW resonator in TFE configuration, based on 42 RY-LT was modeled in 2D. It consists of a plate with thickness of 250 µm, where the both surfaces were metallized using Al electrodes with thickness of 100 nm. A schematic representation of the transversal section of the plate used for modeling in 2D is represented in the Fig. 4.6 a. The plate has a width, w, of 25 mm and the diameter of electrodes ,b, of 6 mm. The Fig. 4.6 b illustrates the mesh employed for these simulations, the position of electrodes and the applied electric potential. The software used for these simulations (EMMIX 2) enables the choice of the material, its orientation and the electrical conditions. In this case the whole plate with real

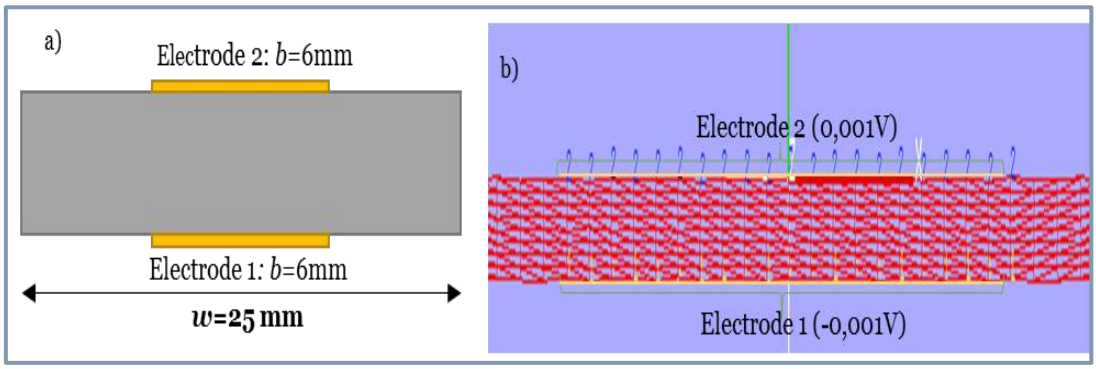

Fig.4.6 Schematic representation of TFE resonator based on 42RY-LT and Z-cut LT single crystals, where w is the width of resonator and b is the diameter of electrode (a); mesh used for modeling in 2D indicating the electric potential that was applied (b).

dimensions was considered, without boundary conditions.

Plates of 42RY-LT and Z-cut LT were investigated by doing this kind of simulations. Their frequency response is shown in the Fig. 4.7. We observed the resonant frequencies of the fundamental mode and of the third overtone at 12.26 and 40.17 MHz, respectively. These frequencies agree well with the analytically computed, 12.4 and 37.2 MHz for the fundamental and the 3rd overtone modes, respectively. The same simulation was done for Z-cut LT and the similar resonant frequencies were found at 12.29 MHz and 39.16 MHz. On the other hand, the Fig. 4.8 shows the isovalues of displacement along Y-axis, for the 42RY-LT and Z-cut LT BAW resonators. In both resonators, the TE mode is excited at 12.26 and 12.29 MHz, respectively.

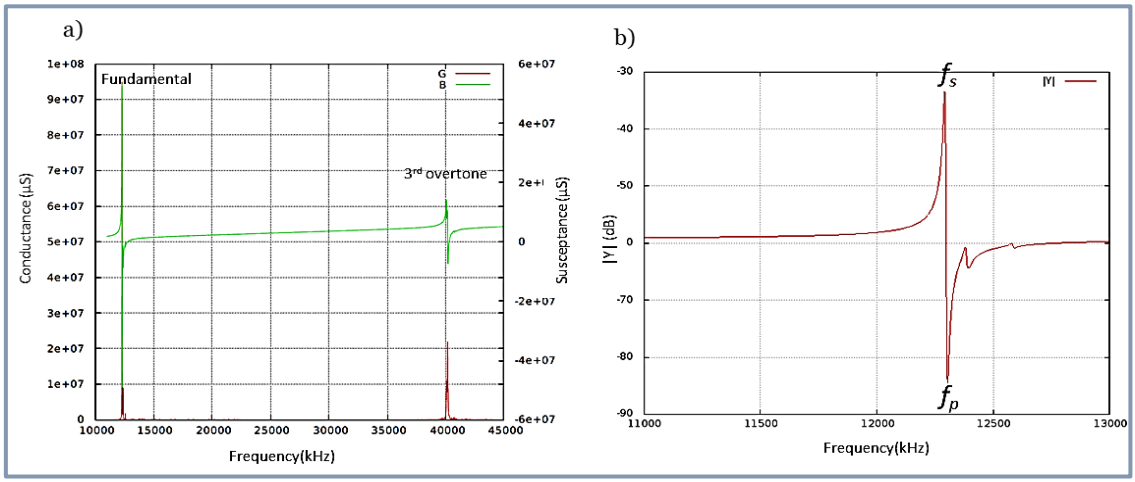

Fig.4.7 Response at fundamental frequency (12.26 MHz) and 3rd overtone (40.17 MHz) of TE modes in TFE resonator based on 42RY-LT (a). Modulus of admittance, indicating the position of series , f_s, and parallel frequencies , f_p (b).

Furthermore, according to the Ref. [1, p. 49], the K^2 of each resonator was determined from the parallel, f_p, and series, f_s, frequencies of the module of admittance |Y| by using the Eq. 1.51 (Chapter 1). The results of simulations are summarized in the Table 4.5. It should be noted that resonators based on 42RY-LT present higher K^2 than Z-cut LT ones. Besides, these resonators present a well-defined TE mode. Thus, these kind of resonators were experimentally done, as will be presented in the next section.

Table 4.5 Electromechanical coupling factors, series and parallel frequencies, obtained from 2D simulations, of BAW resonators in TFE configuration, based on 42 RY-LT and Z-cut LT crystals.

Substrate	**f_s (MHz)**		**f_p (MHz)**		**K^2 (%)**
	fundamental	*3rd overtone*	*fundamental*	*3rd overtone*	
42 RY-LT	12.27	40.17	12.74	40.14	8.89
Z cut LT	12.29	39.16	12.42	39.21	2.59

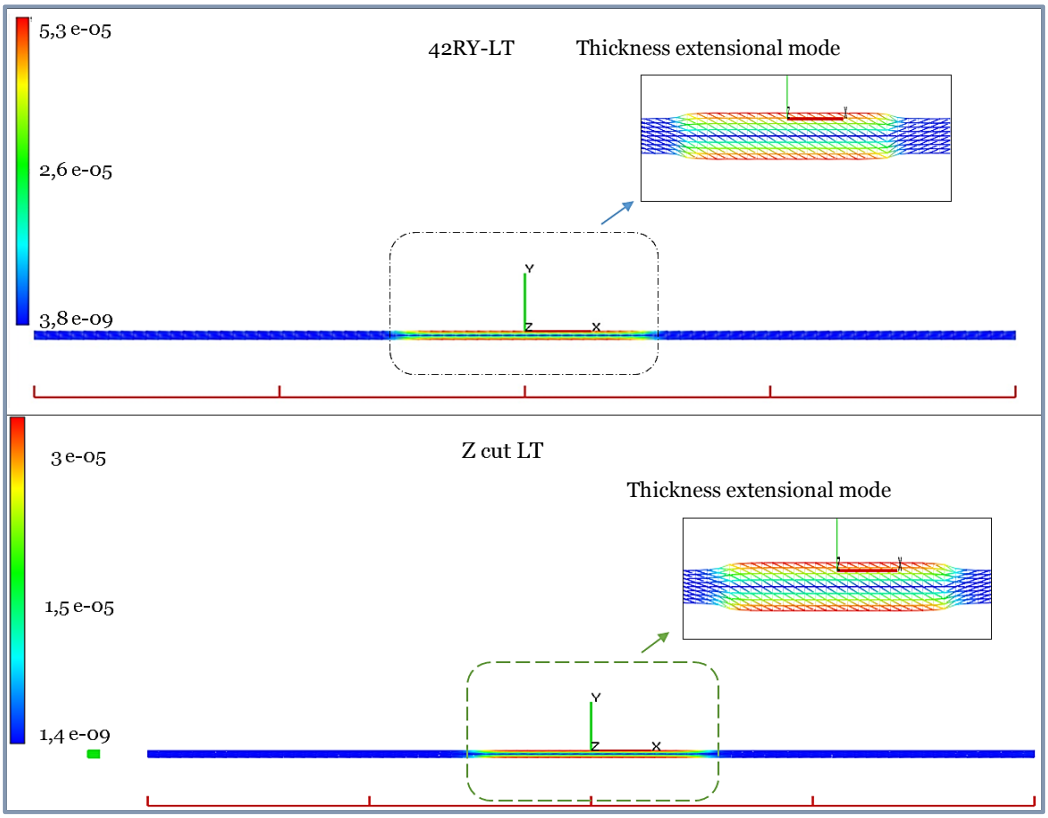

Fig. 4.8 Simulation in 2D of BAW resonators based on 42RY-LT and Z-cut LT. The color scale shows the isovalues of displacement along Y of the thickness extensional mode, excited at 12.26 and 12.29 MHz for both plates, respectively. Note that the indicated X, Y, Z axis do not represent crystal axis.

4.4.2.1.3 Experimental characterization

The admittance of TFE resonators was measured as a function of frequency close to 12 and 36 MHz, corresponding to the resonance frequency of fundamental mode and of 3rd overtone, respectively (Fig. 4.9). At 12 MHz, the admittance presents many modes near the resonance frequency. Thus, it was difficult to estimate the f_s and f_p, but K^2 was approximatively 4 %. It was almost two times smaller than the theoretical K^2 (8%). On the other hand, the signal at 36 MHz was better defined but the experimental K^2 was only 0.05%, while at least 0.86% was expected theoretically.

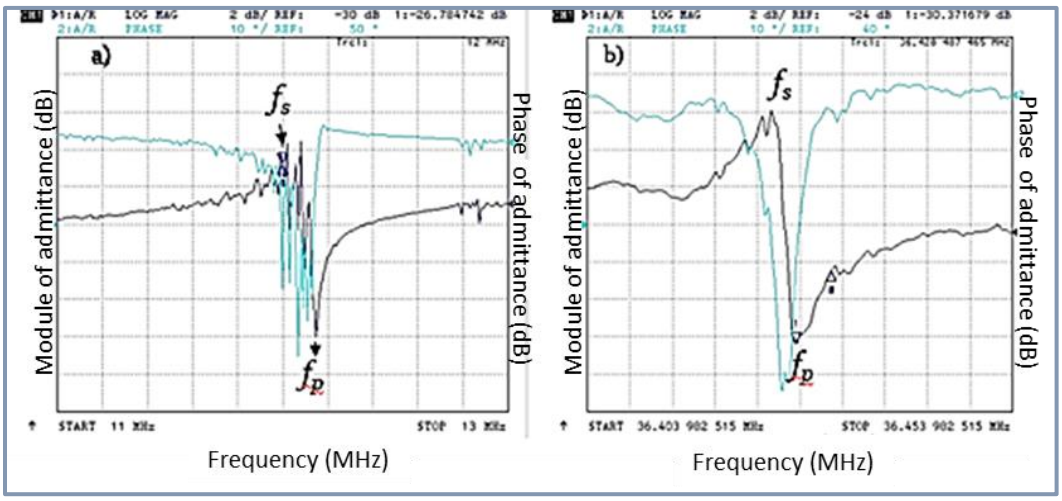

Fig. 4.9 Modulus of admittance as a function of frequency of TFE resonators based on 42RY-X LT in the frequency ranges close to 12 MHz (a) and 36 MHz (b).

The differences between theoretical and experimental results were significant. Several aspects need to be considered in order to explain this behavior. Firstly, the used plates were re-polished on the backside, which could introduce some defects of parallelism and could affect the characteristics of propagation [24]. Moreover, the simulations were done in 2D, but the whole size of plate was not considered. It may happen that the large size of the plate induces spurious responses with very small separation in frequency, which indicates that energy trapping is not efficient. Several 42RY-LT crystals with different Li non-stoichiometries, from subcongruent to stoichiometric concentrations were characterized at 36 MHz. From admittance responses, K^2 was estimated for each sample, the results are presented in the Fig. 4.10. It should be noted that the VTE treated samples presented in this part were poly-domain. In the Fig. 4.10, the K^2 of single and poly-domain 42 RY-CLT are compared. The latter was obtained by annealing the crystal at 750°C during 10 h. The K^2 of the polydomain sample is ten times smaller than the K^2 of the single-domain one, as expected, because the piezoelectric excitation is strongly affected by the polydomain state. However, the comparison of K^2 of polydomain samples is not possible because the volume ratio of naturally occurring domains differs from sample to sample. Nevertheless, the K^2 of poly-domain stoichiometric 42 RY-SLT was higher than that of congruent single-domain crystal. This indicates that reduced Li non-stoichiometry ameliorates electromechanical coupling. Further experiments on single domains samples are required in order to identify the relationship between Li_2O concentration and the K^2. The values of K^2 obtained here were very small, which makes difficult the comparison between samples and affects the reliability of results.

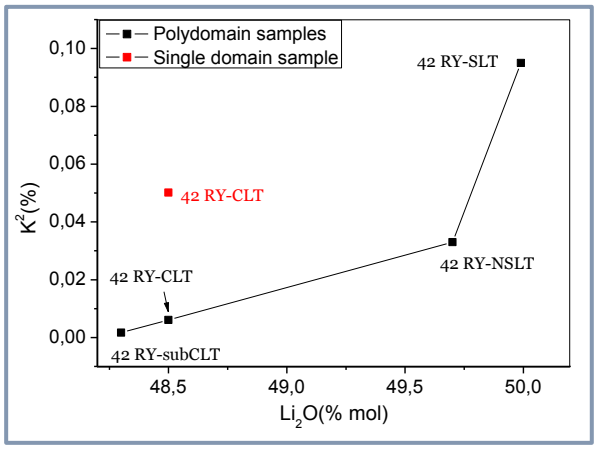

Fig. 4.10 Evolution of K^2 with Li_2O in polydomain and single-domain crystals with different Li-non stoichiometry

Furthermore, although the excitation of the TE mode of BAW resonators on 42RY-LT can give information about C_{11}, C_{13}, C_{14}, C_{33} and C_{44} but not on C_{66}. The contribution of C_{44} is not predominant. For this reason, we looked for another configuration able to excite shear modes. Another way to excite the shear modes is using a resonator in lateral field excitation (LFE), which will be presented in the next section.

4.4.3 BAW resonators in lateral field excitation configuration

4.4.3.1 Simulations

BAW resonators configured in LFE were investigated in order to excite the shear modes depending on C_{44} elastic constants. Unlike TFE, whose orientation of plate defines the direction of the wave propagation and that of the excitation, the LFE configuration allows to choose directions of excitation [25]. The first simulation tests were done with 42RY-LT crystals. According to both, analytical and numerical studies, lateral field excitation can also

drive three modes: TE, FS and SS, having different lateral coupling coefficients (K_t). The values of K_t, in the case of LFE resonators, based on 42RY-LT crystals, were estimated using the following equation:

$$K_t = \frac{\left[\left(e_{16}-\frac{\varepsilon_{12}}{\varepsilon_{22}}\right)u_1+\left(e_{12}-\frac{\varepsilon_{12}}{\varepsilon_{22}}e_{22}\right)u_2+\left(e_{14}-\frac{\varepsilon_{12}}{\varepsilon_{22}}e_{24}\right)u_3\right]}{\left(\varepsilon_{11}-\frac{\varepsilon_{12}^2}{\varepsilon_{22}}\right)^{1/2}(\bar{C})^{1/4}} \qquad \textit{Eq .4.12}$$

where e_{ij} are the piezoelectric coefficients, ε_{ij} are the permittivity constants and u is the wave displacement.

We firstly simulate a structure having two electrodes of same size on top of plate of width (w) of 25 mm (see Fig. 4.11 b). Their dimensions are:

- Diameter of electrodes (b_1 and b_2)= 6 mm
- Thickness of electrode= 100 nm
- Thickness plate (h)= 250 µm

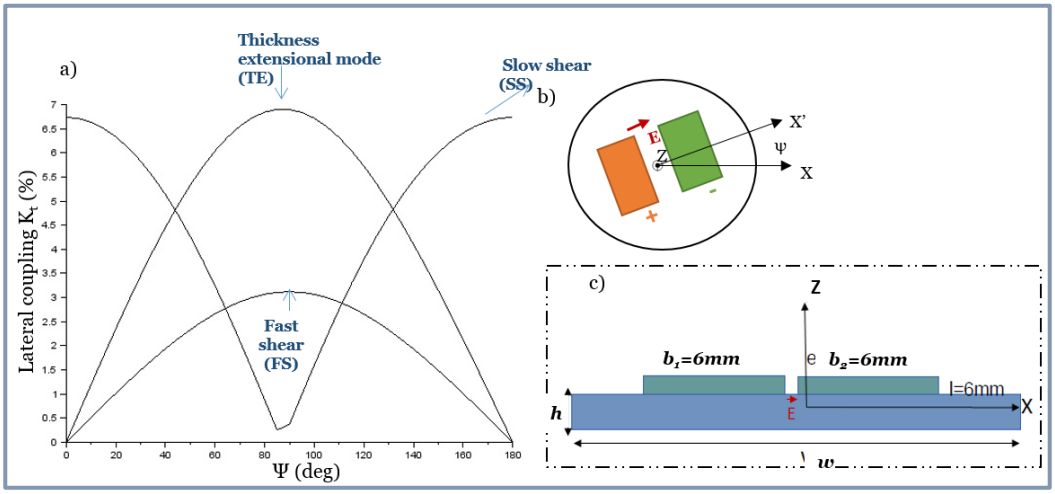

Fig.4.11 Lateral field coupling factor, K_t, (in %) of TE, FS and SS modes of 42RY-LT plate as a function of the electric field angle ψ relative to X-axis (a). Schematic representation of lateral field excited BAW resonator: top (b) and side views (c).

- Gap between electrodes= 1 mm

The K_t as a function of the orientation of the electric field for the different excited modes is represented in the Fig. 4.11. We consider that the wave propagates along the thickness of the plate (Z-axis). The electric field is applied along X-axis, in the plane of plate, and its direction is defined by a rotation in counterclockwise about the Z-axis, which is denoted by the angle ψ.

Additionally, two configurations of electrodes were simulated:

- *1st Configuration*. The electric field is applied along the X-axis (Fig. 4.12 a).
- *2nd Configuration*. The electric field is perpendicular to the X-axis (Fig. 4.12 b). The frequency response, obtained for the two configurations show several shear modes at frequencies between 6 and 7 MHz. The frequency response of resonator in the 2nd configuration was less spurious than that of the 1st configuration.

The excited modes in the resonators in LFE configuration were analyzed in the frequency region from 6 to 7.5 MHz. The Fig. 4.13 shows the mesh and the isovalues of displacement along Y direction of the different modes. The identified modes were: slow shear mode at 6.73 MHz, fast shear mode at 6.77 MHz and flexure mode at 7.02 MHz.

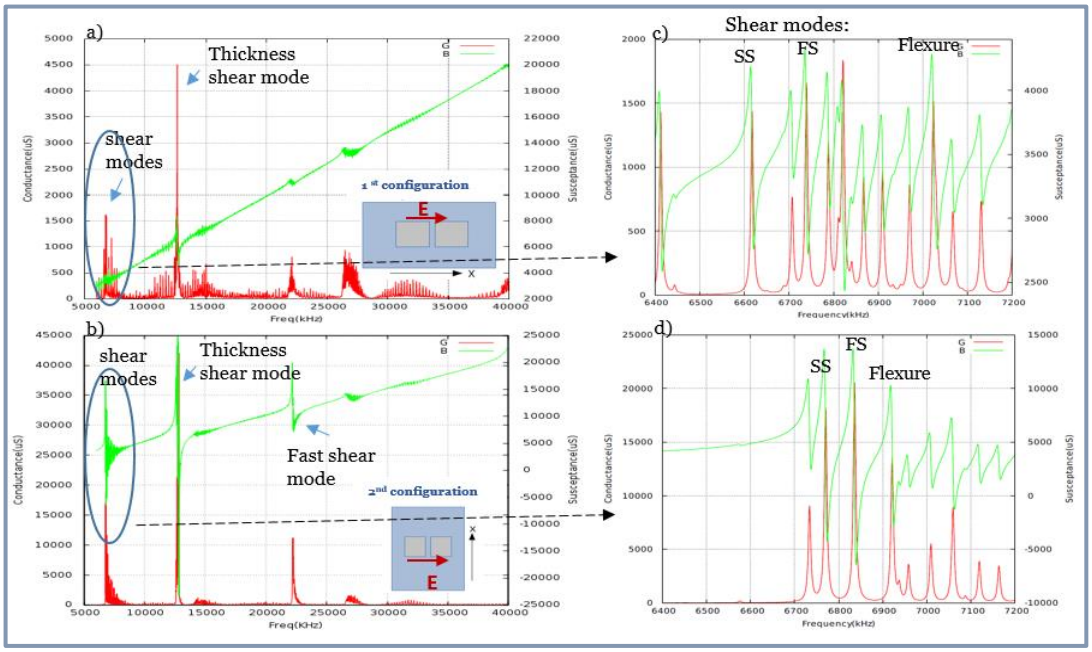

Fig.4.12 Frequency response of BAW resonator in LFE configuration, excited by the application of electric field parallel (a) and normal to X-axis (b). Zoom of the frequency range corresponding to the shear modes for the 1st and 2nd configurations (c) and (d) respectively.

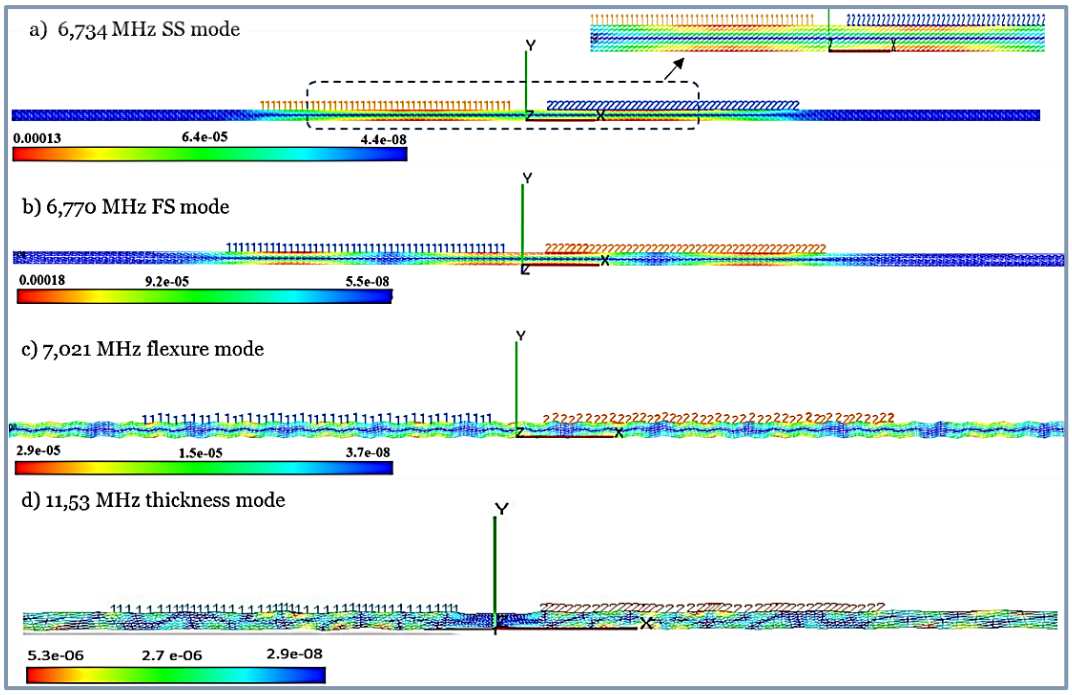

Fig. 4.13 2D simulations of BAW resonator in LFE configuration based on 42RY-LT. The isovalues of displacement along X shows the SS mode at 6.734 MHz (a), the FS mode at 6.77 MHz (b), the flexure mode at 7.021 MHz and the thickness shear mode at 11.53 MHz (d).

The K^2 of each resonator was estimated from the harmonic response obtained by 2D simulations, by using the Eq. 1.64 (Chapter 1). The f_s, was taken from the frequency of

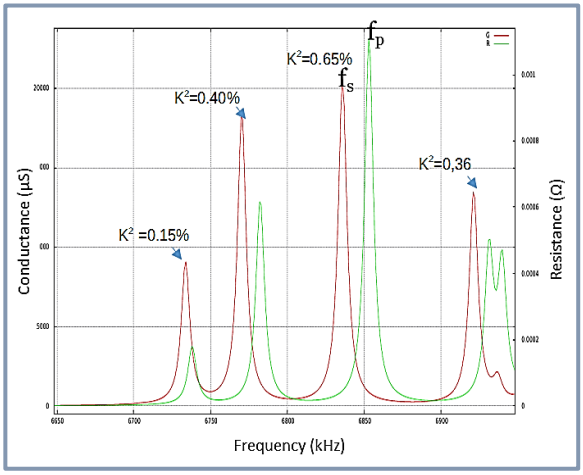

Fig. 4.14 Frequency response and electromechanical coupling factor of BAW resonators in LFE configuration of shear modes, in the frequency range from 6.6 MHz to 7 MHz. obtained by 2D simulations.

maximum conductance and the f_p, corresponds to the frequency of maximum resistance. In both configurations, K^2 is very small, between 0.15 and 0.65%, depending on the frequency (Fig. 4.14). These values, analytically estimated, are close to K^2_t=0.49%. We did simulations by using electrodes on the top and on the bottom in order to increase the coupling but similar values of K^2 were found (0.21-0.46%).

The simulations carried out in this part was done using 100 nm thick gold electrodes. In order to find a better coupled configuration, the effect of the thickness and geometry of electrodes were studied, as well, and will be detailed in the next section.

4.4.3.2 Optimization of parameters

2D Simulations using BAW resonators in LFE configuration based on 42RY-LT crystals, with gold electrodes were done. We kept the 2nd configuration, where the direction of the electric field is normal to X-axis, because it had a better frequency response. We analyzed the effect of the variation of thickness of electrodes and the gap between electrodes on K^2 of FS mode, in order to find a better-coupled response.

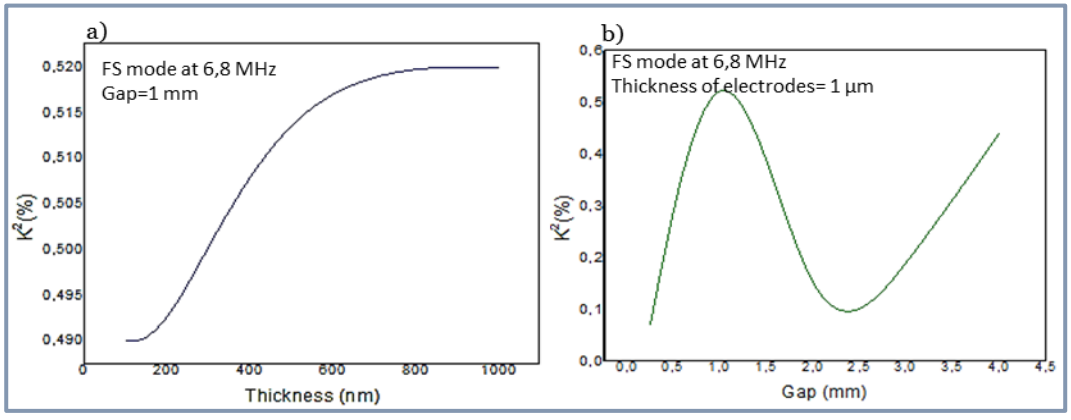

Fig.4.15 Electromechanical coupling factor of FS mode of LFE BAW resonator as a function of the thickness of gold electrodes (a) and the gap between electrodes (b).

The Fig. 4.15 a shows the dependence of K^2 on the thickness of electrodes. It can be observed that the electromechanical coupling factor increases slightly with thickness until 600 nm and then, it remains almost constant. On the second hand, the K^2 shows a maximum value at gap of 1 mm. The K^2 decreases when gap between electrodes is increased from 1 mm to 2.5 mm. Further increase of gap (> 2.5 mm) tends to ameliorate coupling (Fig. 4.15 b). The K^2 was slightly improved with the optimized thickness and the gap. However, the optimized K^2 values remained small. Furthermore, the analysis of this configuration was complicated by the existence of many spurious modes near the resonance frequency. The mode excited in this configuration presents very low values of K^2 and this makes the comparison of several samples complicated.

The BAW resonators based on Z-cut LT substrates were studied, as well. We used a gap of 3 mm and all the other parameters were the same as in the case of 42RY-LT resonators. The Fig. 4.16 shows the simulated frequency response and the excited modes. The frequency response is highly coupled at 7.21 MHz. The K^2 of this mode is 18.11%. However, it shows also a second mode at 7.28 MHz with large intensity near the resonance frequency. This mode is slightly less coupled than the previous one, it presents K^2=12.91%. According to modal analysis, the modes excited at these frequencies are thickness-shear modes, the displacement of isovalues along the X-direction are presented in the Fig. 4.16 d. Although this resonator shows a highly coupled mode, several spurious modes occur in its close vicinity and this may make difficult the distinction of the main mode during the measurements, realized at different temperatures. Further amelioration of performance of this structure can be achieved by using simetrical excitation of both sides of crystals in order to homogeneize the horizontal electrical

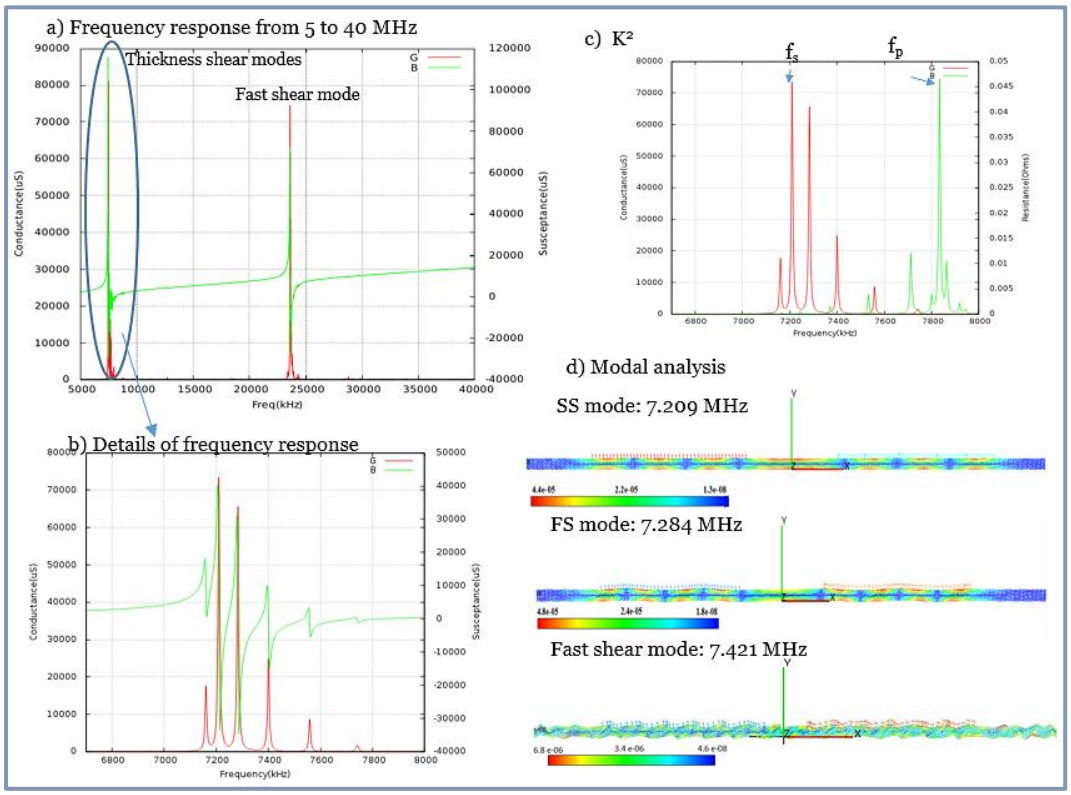

Fig. 4.16 2D simulation of BAW resonator in LFE configuration based on Z-cut LT: frequency response (a), detail of the frequency response in the region between 6.5 and 8 MHz (b), estimation of K^2 (c), and isovalues of displacement in X direction, showing the excitation of shear thickness modes (d).

field. But we decided do not continue this developement and to study ridge structures.

In summary, several BAW resonators, based on 42RY-LT and Z-cut LT plates, were simulated in order to find a configuration allowing the excitation of shear modes, which depends on C_{14}, C_{14} and C_{66}. The first BAW resonator modeled was in TFE configuration. In the case of the resonator structured on Z-cut LT, the TE mode depends mainly on C_{11}. When 42RY-LT crystals are used as a substrate, the TE mode depends mostly on C_{44} and C_{14}. But all the others elastic constants have a slight contribution, as well. Therefore, the study of TFE resonators based on 42 RY-LT can give information about elastic constants C_{44} and C_{14}. Thus, these resonators were fabricated and characterized experimentally. However, the experimental response at 12 MHz presented many spurious modes around the resonance frequency. At 36 MHz, the signal was better defined but with very weak coupling. Moreover, lateral field excited BAW resonators, based on 42 RY-LT have been simulated, as well. Although shear modes, which are interesting for estimation of C_{44}, were present in the frequency response. We observed weakly coupled and spurious modes. Furthermore, the same structure, using Z-cut LT as piezoelectric substrate, was studied. It was found that the thickness-shear mode was well coupled (K^2=18.11%) at frequency close to 7 MHz. However, unwanted modes appeared close to the shear mode, as well.

On the other hand, it was previously shown (in Section 4.2.2) that the FS mode of ridges resonators in ZY configuration depends mainly on C_{44}. For this reason, these resonators were simulated and realized experimentally.

4.4.4 BAW resonator based on ridge structures

4.4.4.1 Simulations of ridge resonators

BAW resonators based on ridges structures have been studied in order to excite the shear modes depending on C_{44} elastic constant. The frequency response of ZY, ZX and 42RYX ridge resonators depend on C_{44}, C_{14} and C_{66} elastic constants (as discussed in the Section 4.2.2). In the ZY configuration the changes of C_{44} have a larger influence on the frequency.

ZY, ZX and 42 RYX ridge resonators were simulated in 2D by combined finite element / boundary element analysis, allowing to take into account the influence of the clamping by the substrate on the vibrations of the ridge. The Fig. 4.17 shows the mesh used for these simulations. The electric potential was applied on the sides of the ridges (surfaces Ref.1 and Ref.2, which corresponds to the ZY planes in the case of ZX ridges). The simulated frequency response of each configuration is given in the Fig. 4.17 a-c. It can be seen that the main mode is very well defined in the all three cases.

In the case of the ZY resonator, two modes at 90.9 MHz and 139 MHz, which corresponds to FS and to the TE modes, were present, respectively. These results agree well with the estimations by numerical analyses (presented in the Section 4.2.2). The modal analysis indicates that the shear mode is excited at 90.9 MHz. This mode is highly coupled (K^2=9.5%) and it depends mainly on C_{44} but also on C_{14}, to a lesser extent. Therefore this configuration will allow us to determine qualitatively the temperature dependence of C_{44}.

The frequency responses of ZX and 42 RYX ridges show only the presence of the FS mode at 95.5 MHz and 94.9 MHz, respectively. It was previously demonstrated that the variation of frequency in ZX and 42 RYX resonators, depends on C_{44}, C_{14} and C_{66} in different

degrees (68.7%, 28.3% and 17.8%, respectively). Therefore, the study of the FS mode on these

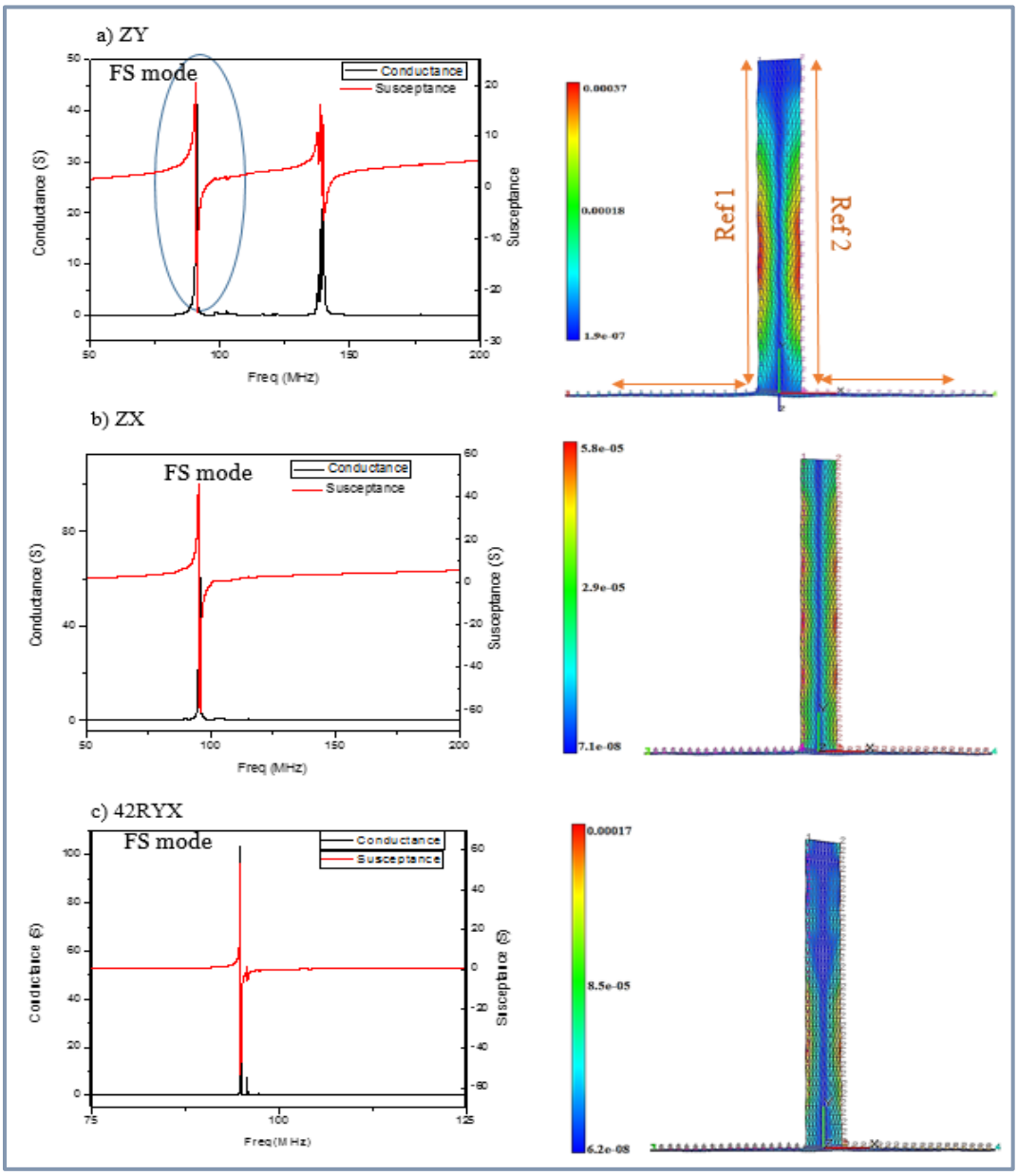

Fig. 4.17 Frequency response (left) and modal analysis (right) obtained from 2D simulations of ridge resonators: Ridge ZY , parallel to X-axis (a); ZX ridge, perpendicular to X-axis (b); 42RYX LT ridge, normal to X-axis (c). In all resonators the Fast shear mode is excited.

resonators will give information about the behaviour of shear modes and will allow us to deduce qualitatively the joint temperature dependence of C_{14}, C_{44} and C_{66} elastic constants from the measurements of the variation of frequency with temperature, as will be seen later. On the second hand, the frequency response of ridge resonators were simulated at different temperatures in order to estimate the theoretical values of TCF and the temperature dependence of K^2, which will be detailed in the next section. For this reason, we will focus in the investigation of FS mode in all three configurations of ridges.

4.4.4.1.1 Simulation of temperature dependence of frequency and K².

2-D simulations of the temperature dependence of frequency and K² have been performed for each type of resonators. For this purpose, the harmonic admittance was simulated at temperatures in the range from 25 to 140 °C. In this range of temperatures the frequency dependence on temperature is nonlinear. Then, in order to estimate the first order of TCF, the data were taken only from 30 to 100 °C. The thermal derivatives were estimated by using the software EMMIX2, taking into account the thermal expansion of the used materials. The Fig. 4.18 shows an example of theoretical conductance and the resistance as a function of frequency of FS mode of 42 RYX-LT resonators at different temperatures. The f_s shifts towards higher frequencies when the temperature is increased from 25 to 105 °C. In contrast, the f_p goes toward lower frequencies, with the increase of temperature from 25 to 105°C. The temperature coefficient of frequency (TCF) of ridge resonators was estimated by using Eq. 1.55 (Chapter 1). Furthermore, the K² was estimated by using the Eq. 1.64 (Chapter 1) at different temperatures. The temperature dependence of f_s and f_p (TCF_s and TCF_p, respectively) and the K² obtained by 2D simulation are given in the Table 4.6.

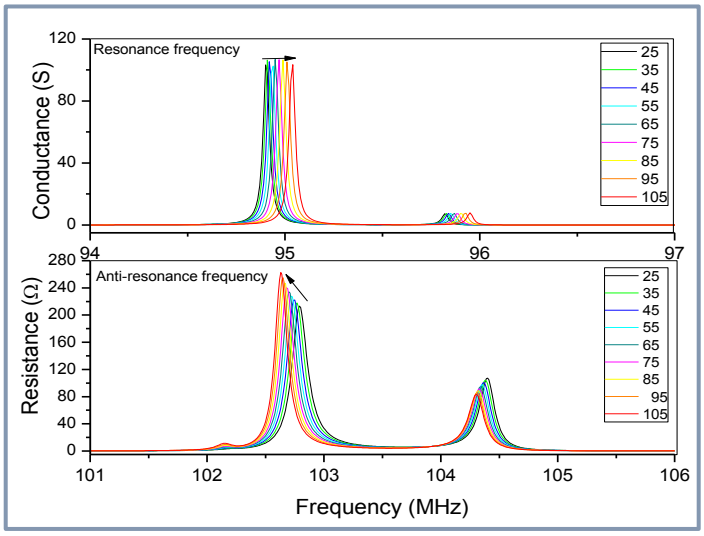

Fig. 4.18 Conductance and resistance of 42RYX LT resonator estimated at different temperatures

Table 4.6 Temperature coefficients of resonance and anti-resonance frequencies (TCFs and TCFp, respectively) estimated theoretically in the temperature range from 30 to 100 °C for FS mode of ZX, ZY and 42 RYX ridge resonators, by using a quality factor Q=1000. K² of FS mode at room temperature is indicated, as well.

Sample	***TCF_s (±5 ppm/°C)***	***TCF_p (±5 ppm/°C)***	***K² (±1%)***
ZY-LT	-19	-38	9.5
ZX-LT	6	-7	13.2
42RYX-LT	18	-20	17.6

It should be noted that in the case of 42 RYX and ZX ridge resonators the f_s presents a positive TCF, whereas the TCF_s in ZY ridge resonator is negative. Smallest TCF_s is expected for FS mode of ZX ridge resonator. In contrast, in the case of anti-resonance frequency, the TCF_p of all resonators is negative. Concerning the K^2, it was found that the FS mode of ridge resonators based on Z-cut crystals is less coupled (8-13 %) comparing to that of ridge resonator in 42 RY-LT crystals (17.6 %). Similar results were found in the case of BAW resonators in TFE configuration. On the second hand, the effect of temperature on the K^2 was simulated, as well (Fig. 4.19). It can be observed that the K^2 of FS mode in all resonators diminishes slightly with temperature. The 42 RYX-LT ridge resonators present the most important variation of K^2 with temperature (-0.007%/°C).

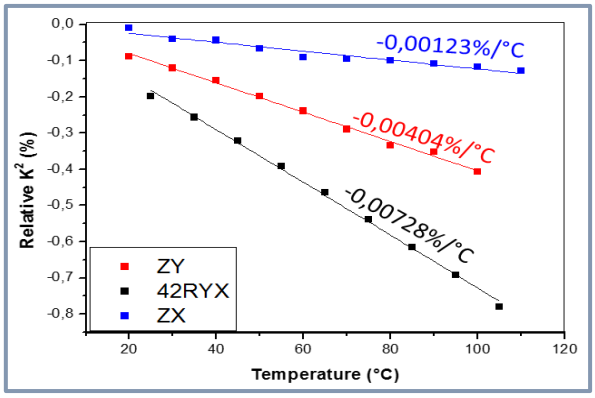

Fig. 4.19 Temperature dependence of K^2 for ridge resonators based on Z-cut and 42 RY-LT crystal

4.4.4.1.2 Simulation of the dependence of TCF and K^2 on quality factor.

The dependence of the TCF of resonance and anti-resonance frequencies (TCF_s and TCF_p, respectively) and of the K^2 values on the quality factor, Q, of the FS mode, were also investigated for ZY, ZX and 42 RYX ridges. For this purpose, the value of Q was varied from 5 to 1000. The results are presented in the Fig. 4.20. In general, it can be seen that the TCF_s increases with Q until Q~150 and then it remains almost constant, while the TCF_p tends to decrease with the increase of Q. The TCF_p of the FS mode becomes independent on the quality factor at Q>500 for ZX and ZY ridge resonators, and at Q>300 for 42 RYX-LT ridge resonators. It should be noted that the TCF varies differently for each kind of resonator. The TCF values of ZX show the most important sensitivity to the variation of quality factor. Its TCF_s decreases by 64.6% and the TCF_p increases by 71% when Q increases from 5 to 1000.For example, in the case of ZX ridges, the TCF_s is 17.7 ppm/°C at Q=5 and diminishes to 6 ppm/°C when Q=1000. However, in the case of the ZY and 42 RYX-LT ridge resonators, the effect of quality factor is less important but remains considerable. Furthermore, at Q<150, the K^2 increases with the decrease of Q. The most significant variation of K^2 as a function of Q was found in the case of ZX resonators, as well. Thus, it is very important to obtain high Q values experimentally as low Q can strongly affect the TCF and the K^2. The quality factor tends to modify the profile of modes and at low quality factors the identification of resonance frequency might be not precise. We do not believe that K^2 might increase at low Q values. Therefore, it indicates that in the case of resonators with low Q, we can overestimate the K^2 and the TCF values might be false, as well.

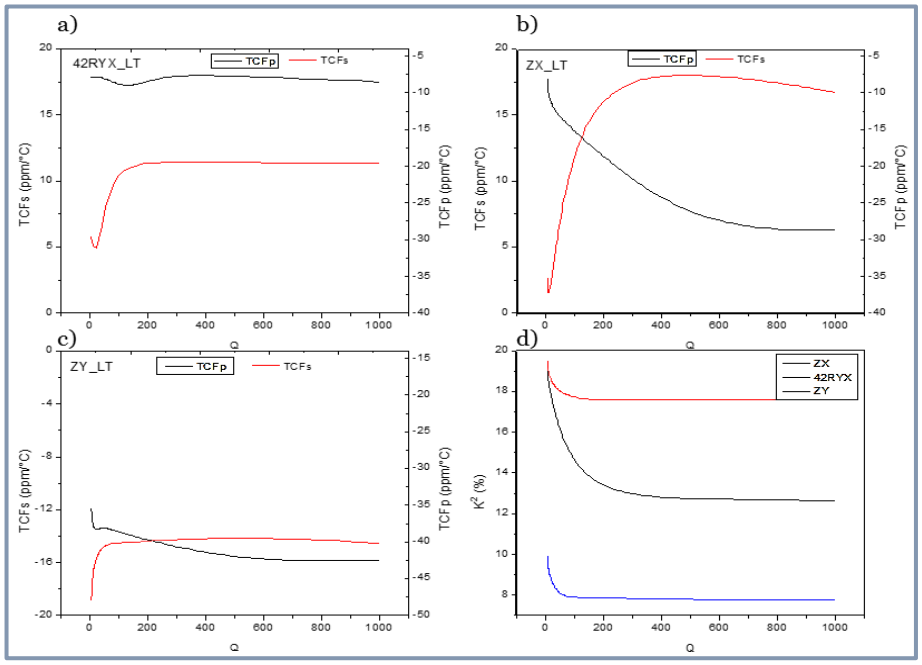

Fig. 4.20 Dependence of TCF_s and TCF_p and K^2 on quality factor (Q) of different ridge resonators: 42 RYX-LT (a); ZX-LT (b); ZY-LT (c); variation of K^2 with quality factor (d).

4.4.4.1.3 Simulation of the temperature dependence of elastic constants

Simulations of the evolution of effective elastic constants of 42 RY-LT crystals and Z-cut LT crystals with temperature have been performed in one dimension, by using a software called Matx, which is available in the used set of simulation tools. The temperature dependence of effective elastic constants was simulated from 20 to 125 °C. The investigated orientation was YXl/90, according to the IEEE standard-176 Rev. 1949[1]. This orientation corresponds to the ZX crystal orientation in the orthogonal reference system, used for the description of ridge resonators, respectively. These constants can be estimated from the excitation of the TE and FS modes in ridge resonators. The Fig. 4.21 illustrates their temperature dependence. C_{11} and C_{16} have the close values and decrease with increase of temperature. C_{44} decreases with temperature, as well. Whereas, the effective C_{14} increases with temperature.

According to the Table 4.4, in the case of ZX and 42 RYX ridges, the elastic constant having the highest influence on the variation of frequency is C_{14}. This could explain the positive TCF obtained for the ZX and 42 RYX ridges, described in the previous section. In the case of ZY ridges resonators, the frequency depends mostly on C_{44} and in a lesser amount on C_{14}, thus, the TCF is negative.

Comparing to the other BAW resonators discussed above, ridge resonators allowed the excitation of the shear mode in both geometrical configurations of ridges and the simulations predicted the existence of a main mode highly coupled without spurious modes. Therefore, these resonators were fabricated and characterized, as we present in following sections.

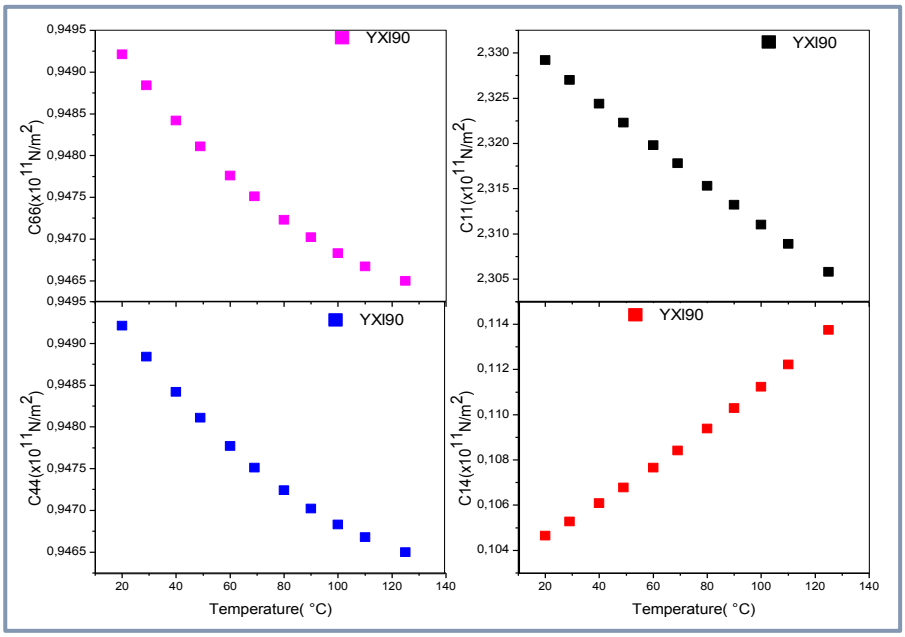

Fig. 4.21 Temperature dependence of effective stiffened elastic constants of crystals of YXl/90 LT crystal

4.4.4.2 Experimental results

We have observed during the first characterizations of ridge frequency response, that it contained many spurious resonances close to the main resonance. Therefore, we have investigated different geometrical parameters of ridge structures, in order to ameliorate the quality of frequency response. The effect of the depth (*d*), thickness (*h*) and length (*L*) of ridges on the frequency response was investigated by keeping constant one parameter and varying the other ones. For this purpose, several tests were experimentally conducted. The Table 4.7 summarizes the different geometrical configurations used for these experiments. The ridges resonators were electrically characterized by admittance measurements. The Fig. 4.22 shows the frequency response for different ridge resonators. The ridge structure with t=20 µm, d=200µm and L=5mm find the "cleanest" frequency response comparing to their geometrical configuration.

Table 4.7 Geometrical parameters (d, h and L) used for the optimization of frequency response of ridges resonators

Sample	***Depth (d), µm***	***Thickness (h), µm***	***Length (L), µm***
		Variation of h	
1	200	4	5
2	200	10	5
3	200	20	5
4	200	50	5
		Variation of h	
5	300	4	5
6	300	10	5
7	300	20	5
8	300	50	5
		Variation of L	
9	200	10	5
10	200	10	10
11	200	10	20

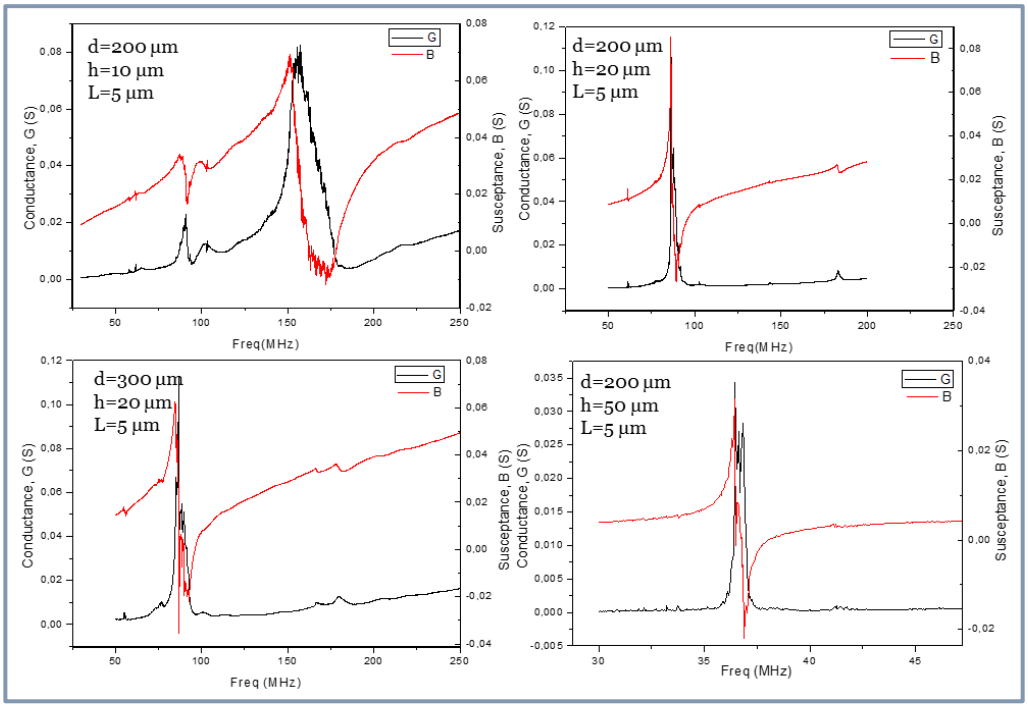

Fig. 4.22 Conductance and susceptance as a function of frequency measured experimentally of 42 RYX-CLT ridge resonators with different geometrical parameters (d, h and L).

Ridge structures were realized in Z-cut LT and 42 RY-LT crystals with different Li concentration in the range from congruent (CLT, 48.5 mol% of Li_2O) to nearly stoichiometric (NSLT, 49.9 mol% of Li_2O) compositions. The measured frequency responses of ZY-CLT and 42 RYX-CLT ridges are shown in Fig. 4.23 b and d, respectively. They are compared to the simulation results (Fig.4.23 a and c). The same modes were found theoretically and experimentally. Nevertheless, there is a slight difference in the theoretical and experimental resonance frequencies due to a deviation of the actual thickness of ridge resonators from the theoretical value of 20 µm. The experimental ridge thickness varied from 18 µm to 20 µm in different devices. Moreover, the experimental frequency responses of all ridge structures realized on different substrates presented several close resonances corresponding to different modes in a narrow sweep range, which affected the accuracy of estimation of acoustical parameters from experimental data. For this reason, the conductance and the resistance signals were fitted separately by using independent damped harmonic oscillator profiles using Unifit procedure (written by I. Gregora), running under IgorPro interface. An example of fitting of the signal is given in the Fig. 4.23 e. Furthermore, the simulations did not take into account some experimental aspects, such as the surface quality of the ridges, and the loss generation due to the clamping of the ridge by the substrate [26].

In order to facilitate the analysis of results, first I will present the results obtained on FS mode of resonators based on Z-cut LT crystals and then the results on resonators based on the 42 RY-LT crystals.

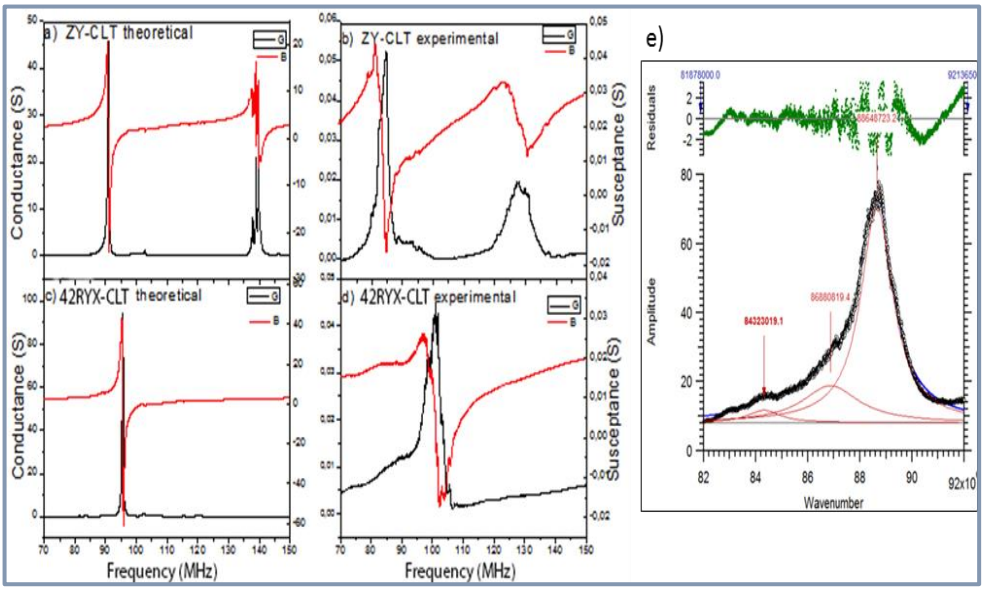

Fig. 4.23 Conductance and susceptance as a function of frequency simulated and measured experimentally of ZY-CLT (a and b) and 42RYX-CLT ridge resonators (c and d); fitting of experimental curves by using independent oscillator profiles (e).

4.4.4.2.1 Ridges based on Z cut LT crystals

The K^2, TCF_s and TCF_p of FS mode of ZX, ZY and resonators realized on CLT and SLT wafers are given in Table 4.8. The experimental quality factor (Q) was estimated by using the Eq. 1.65, mentioned in the Chapter 1. In order to estimate the K^2, the f_s and f_p were taken from the maximum of the conductance and the resistance, respectively (Fig. 4.24), and then, K^2 was obtained by using the Eq. 1.64 (in Chapter 1). It has been shown previously that the Q factor could false the values of TCF and the K^2 (according to the simulation presented in the Fig. 4.20). The simulated values of TCF and K^2, corresponding to the experimental Q, are compared to the experimentally measured TCF and K^2 in the Table 4.8. In this way, theoretical results must be close to the experimental ones. Therefore, these theoretical results are only indicative and some difference with experimental results might be expected if the K^2 and TCF are dependent on Li_2O concentration.

Table 4.8 . TCF_s, TCF_p and K^2 calculated theoretically (Theo.) and measured experimentally (Exp.) of FS mode of ZX and ZY ridges resonators based on CLT and SLT single crystals. The experimental Q factors of devices are given, as well. The theoretical values noted by an asterisk were obtained considering only the Q factor but it did not take into account the stoichiometric composition of crystals.

Sample	***Li_2O (±0.05%mol)***	***Quality factor (Q)***	***TCF_s (±7 ppm/°C)***		***TCF_p (±7 ppm/°C)***		***K^2 (±3%)***	
			Theo.	***Exp.***	***Theo.***	***Exp.***	***Theo.***	***Exp.***
ZY-CLT	48.5	33.89	-19	-34	-38	-40	8	7
ZY-SLT	49.95	40.21	-13*	-18	-41*	-43	8*	10
ZX-CLT	48.5	36.18	15	13	-24	-19	13	11
ZX-SLT	49.95	94.14	11*	22	-12*	-12	13.5*	17

In the case of congruent crystals, the experimentally measured K^2 agrees with the theoretically expected ones. K^2 decreased by 0,01 %/°C when temperature increased from 30°C to 100 °C range, which agreed well with expectations. In the case of ZY-CLT ridge resonators, it was difficult to identify f_s and to calculate precisely K^2 (Fig. 4.24 a). Nevertheless, the Fig. 4.24 b

shows the module of admittance as a function of frequency of these samples. It can be seen that the K^2 is almost the same in SLT and CLT samples.

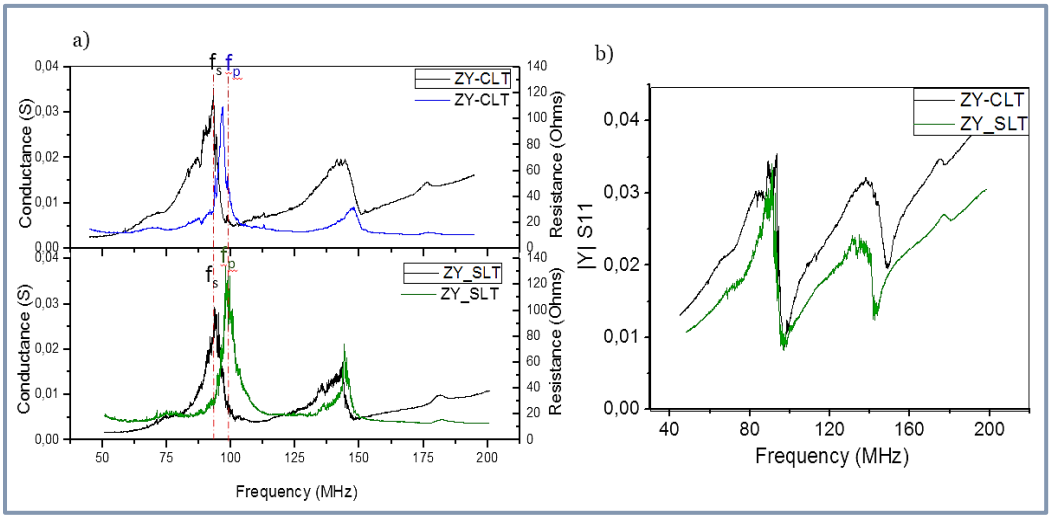

Fig. 4.24 Estimation of K^2 for ZY-CLT and ZY_SLT ridge resonators (a); comparison of the frequency dependence of the module of admittance for congruent and stoichiometric samples (b).

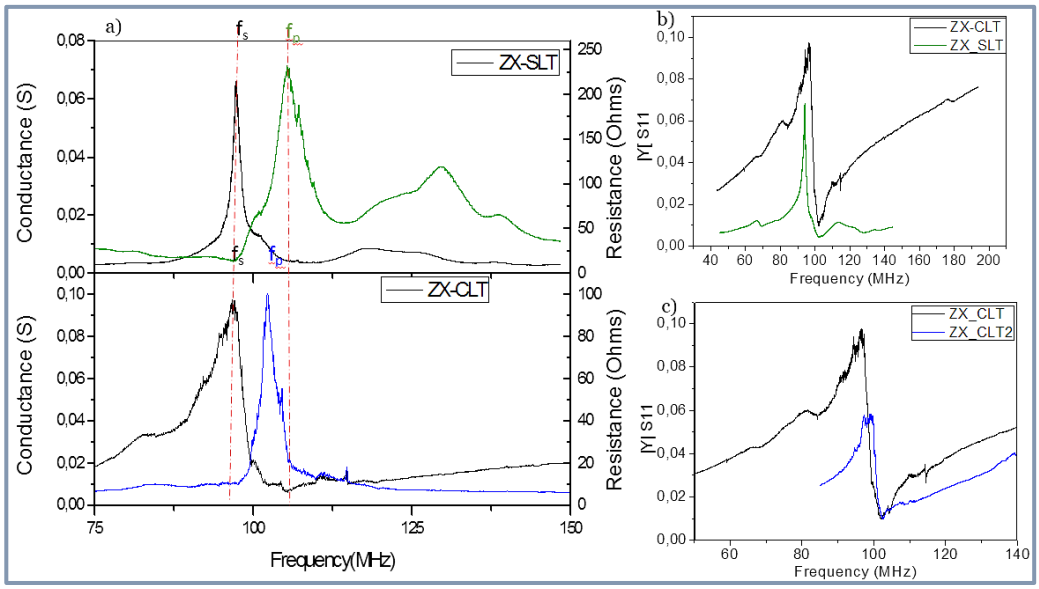

Fig. 4.25 Estimation of K^2 for ZX-CLT and ZX_SLT ridge resonators (a). Comparison between the module of admittance for congruent (ZX_CLT) and stoichiometric sample (ZX_SLT) (b). Module of admittance of two ZX ridges based on LT crystals with congruent composition (c).

In the case of ZX-LT resonators, the K^2 of resonators based on SLT crystals seems to be slightly higher than that of CLT samples, according to the conductance and resistance peaks shown in the Fig.4.25 a. However the f_s frequency was difficult to identify again. The comparison of frequency of the module of admittance indicates that the K^2 of ZX ridges based on CLT and SLT are probably close (Fig. 4.25 b). Therefore, the results on K^2 should be considered with some reserve because our data quality does not allow to estimate accurately the K^2 parameter (Table 4.8). Moreover, it was found that the quality of signals varies significantly from sample to sample. For example, the module of admittance of two ridge resonators based on untreated ZX-CLT crystals, with the same composition, had very different

signal (Fig. 4.25 c) These resonators were fabricated separately and in different regions of the same wafer. There are several possible origins of these discrepancies. First, even if the fabrication procedure of resonators is the same, the state of the blade used for dicing might be different. It depends on the wear of the blade, which can affect the roughness of the walls of resonator. Moreover, the TTV affects directly the quality factor, which should be improved. Finally, the thickness of the electrodes was very thin, 60 nm. Thus, it was difficult to ensure good contact during the electrical measurements.

On the second hand, the temperature dependence of f_s of FS mode of ZX-LT and ZY-LT resonators based on of stoichiometric and congruent samples is shown in Fig. 4.26. The TCF_p was negative in the case of all studied ridge orientations whereas the TCF_s of ZY and ZX resonators were negative and positive, respectively. Theoretically predicted and experimentally measured values of TCF_s and TCF_p for different studied ridge orientations had the same sign. In the case of ZY-CLT resonators, the magnitude of the absolute value of TCF_s was higher than the expected values, while the value of TCF_p agrees well with the predictions (Table 4.8). The absolute value of the TCF_s for ZY-SLT ridge resonators was lower than the measured coefficient for congruent material but close to the theoretical value for ZY-CLT. The TCF_p of ZY-SLT and ZY-CLT resonators did not present significant difference and both experimental results are close to the simulated value.

In the case of ZX-CLT ridge resonators, there is a good agreement between experimental and theoretical values of TCF_p. The TCF_s of stoichiometric and congruent materials are similar, in the range of the errors. In summary, the results show that in the case of ZY-resonators, stoichiometric material leads to a lower TCF_s. Since this configuration depends mainly on C_{44} elastic constant, it could be an indication that the change with temperature of the C_{44} elastic coefficient is lower in stoichiometric LT than in congruent one. But further experiments are needed to confirm this. In next section the results of resonators in 42 RY-cut LT crystals will be discussed.

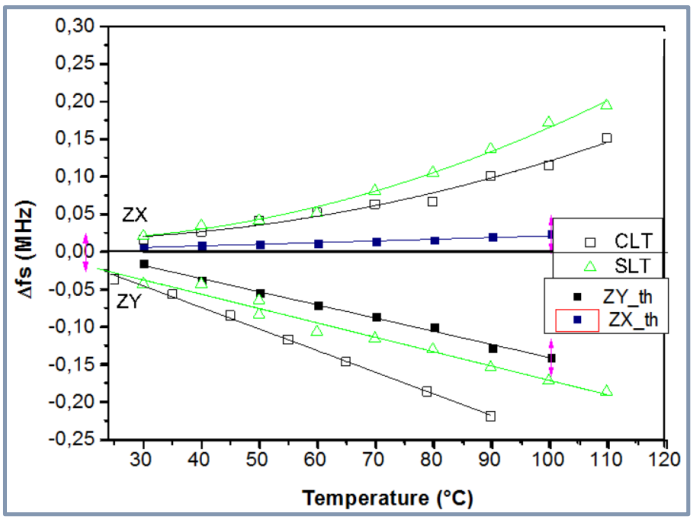

Fig.4.26 Temperature dependence of resonance frequency (fs) on Z cut LT crystals with congruent (CLT) and stoichiometric composition (SLT) and comparison with theoretical results (ZY_th and ZX_th).

4.4.4.2.2 Ridges based on iron doped 42 RY-cut LT crystals

Several iron doped 42RY-LT crystals with different stoichiometries and domain state were characterized. The nearly stoichiometric crystals were prepared by VTE with Li-rich powders (60 %mol of Li_2O) at 1250°C during 48 h. The powders were re-used several times. For this reason, the crystals had different Li_2O concentrations. After VTE treatment, the samples were poled in the central area and then, the ridges were cut in the re-poled and the

unpoled (poly-domain) areas. The congruent poly-domain crystal (42 RYX-CLT poly-domain) was obtained after annealing at 750°C during 10 h.

The experimental and theoretical values of K^2, TCF_s and TCF_p of FS mode of 42RYX-LT resonators are given in the Table 4.9. The theoretical values of TCF were simulated by using the experimental values of quality factors. The simulations were done by using a Q factor from 10 to 45, without taking into account the Li non-stoichiometry effect. It was found that the theoretical value of TCF_s of FS mode in 42RYX-LT resonators was 18 ppm/°C in all cases. The TCF_p varied from -31 to -27 ppm/°C and the values of K^2 were ~18 %.

The Fig. 4.27 illustrates the frequency response obtained in resonators based on single and polydomain 42RYX-LT crystals and with different Li_2O concentrations. In the case of crystals with congruent composition, there is a good agreement between theoretical and experimental values. The signal was notably weak in the case of poly-domain sample with congruent composition (Fig. 4.27 a). Therefore, the electromechanical coupling factor is very affected by the poly-domain state. The Fig. 4.27 b, c, d shows the modulus of admittance for poly-domain and re-poled resonators based on 42 RY-NSLT crystals. The signal obtained in VTEN74 and VTEN56 re-poled and poly-domain is almost the same, whereas the signal of the VTEN70 poly-domain sample is very different from that corresponding to the re-poled one. In the case of VTEN74 and VTEN56 samples, we had a doubt if the poling process was complete. Furthermore, it can be seen that the amplitude of admittance of the reference sample (single domain 42 RYX- CLT) is higher than that corresponding to the stoichiometric material. It seems that in the case of the VTE treated samples, there are more losses. But it's difficult at this stage to identify their origin. As it was previously shown, different quality of responses were obtained even in untreated samples, which is associated to the fabrication of resonator. Moreover, the higher losses might be associated to the poling quality of treated samples. This made the analysis of the experimental data very complicated.

Table 4.9 TCF_s, TCF_p and K^2 calculated theoretically (Theo.) and measured experimentally (Exp.), of 42 RYX resonators based on LT crystal with different compositions and domain states.

Sample	***Domains state***	***%Li_2O in crystal (±0.05 mol%)***	***Q***	***TCF_s (±7 ppm/°C)***		***TCF_p (±7 ppm/°C)***	
				Theo.	***Exp.***	***Theo.***	***Exp.***
42RYX-CLT	single domain	48.5	33.19	18	18	-29	-36
42RYX-CLT polydomain	polydomain	48.5	10.60		-110.01		-89.9
42RYX-VTEN74	re-poled	49.6	44.45		6.14		-10
42RYX-VTEN74 polydomain	polydomain	49.6	37.32		15.85		10.07
42RYX-VTEN56	re-poled	49.7	38.27		6.13		-6.52
42RYX-VTEN56 polydomain	polydomain	49.7	18.33		6.3		-8.79
42RYX-VTEN70	re-poled	49.9	32.45		14		-31.4
42RYX-VTEN70 polydomain	polydomain	49.9	14.29		12		-9.64

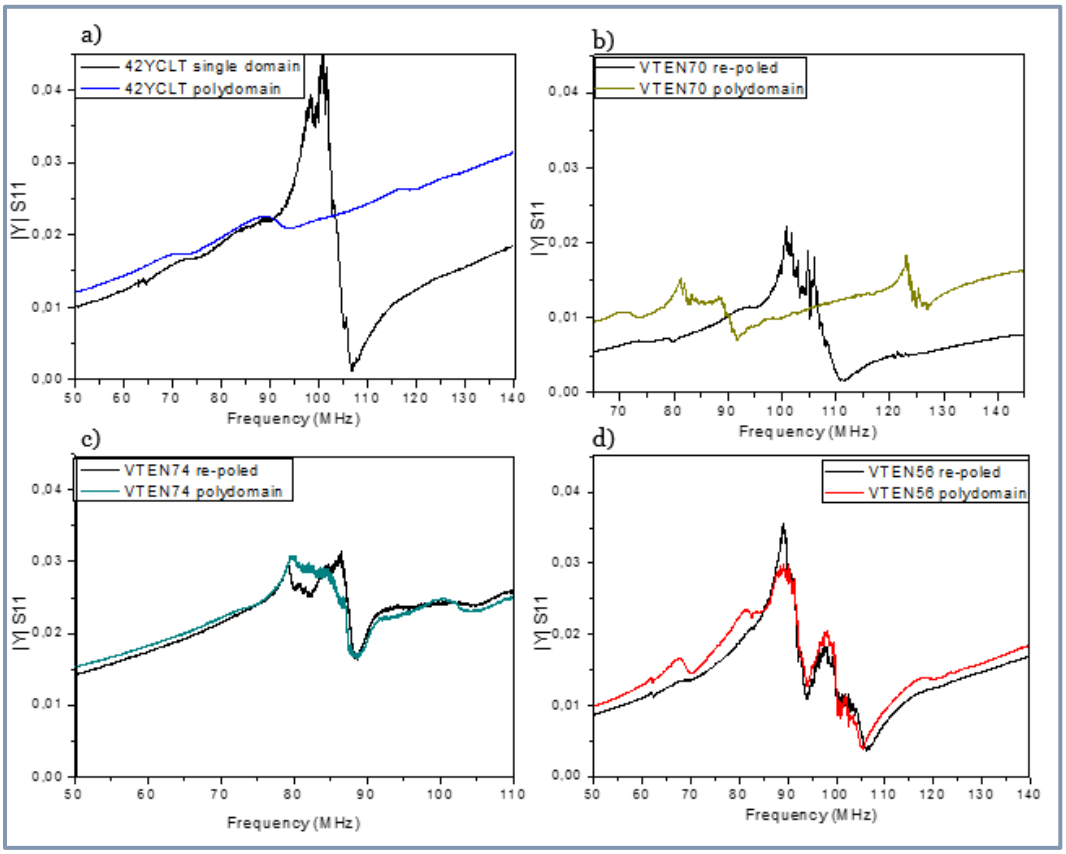

Fig. 4.27 Effect of domain state on electrical response of ridge resonators based on 42 RY-LT crystals with different stoichiometries: congruent, 48.5 mol% of Li_2O (a), VTEN70, 49.9 mol% of Li_2O (b), 49.5 % mol of Li_2O (c), 49.7 mol% of Li_2O (d).

The temperature dependence of resonance and antiresonance frequencies for poly-domain and single domain (re-poled) samples is presented in Fig. 4.28. In the case of re-poled samples, the TCF_s is always positive and the TCF_p is negative, which agrees with theoretical predictions for congruent crystals. In the case of poly-domain samples, the TCF_s is positive in VTE-treated samples, but it's negative for the 42RYX-CLT. In the case of antiresonance frequency, the TCF_p of almost all poly-domain samples is negative, with exception to that of VTEN74 sample. Therefore, in the case of polydomain samples, experimental values of TCF might be very different from the predicted ones for single domain crystals. This indicates that the ferroelectric domains are the responsible of this particular behavior. Furthermore, in literature reports, it has been demonstrated the existence of differences in acoustical properties between single and polydomain LT crystals. For example, the velocity of BAW is reduced by 1.59 % in polydomain Y-cut LT crystals and the elastic constants might increase by 1.2 % [10]. Besides, it has been reported that a layer with inverted polarization modifies the piezoelectric response of SAW devices, which modifies the electric response [27]. This confirms the important role of ferroelectric domains in device performance.

It was difficult to identify the Li-non stoichiometry effect on the electromechanical coupling factor by studying the ridge resonators. Because the signal was irreproducible and presented several spurious modes, which affected the accuracy of estimation of acoustical parameters from experimental data. Moreover, we were not sure about the complete poling process in the case of some samples (VTEN56 and VTEN74), where residual domains might be present. The same doubts concern the analysis of Li non-stoichiometry effect on TCF. Thus, we preferred to study SAW resonators and filters, which allows to estimate K^2 and TCF in a more confident way (see next section).

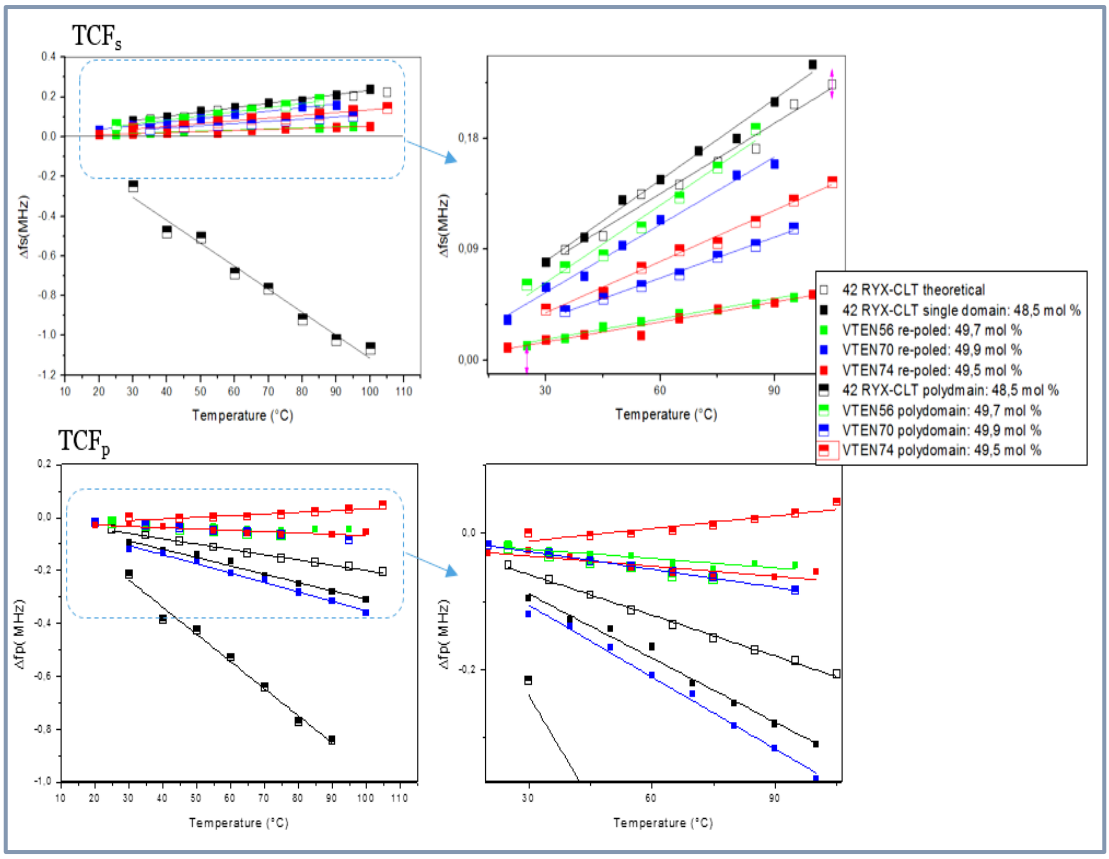

Fig.4.28 Experimental and theoretical values of TCF_s and TCF_p of ridges resonators based on single domain and polydomain 42 RY-LT crystals with different Li_2O concentration.

4.5 SAW devices based on 42 RY-X LT crystals

4.5.1 Simulation of SAW devices and comparison with experimental results.

SAW filters based on undoped 42RY-X LT with different Li compositions were investigated, as well. The design, simulation, fabrication and characterization of SAW filters were done by the company frec|n|sys. For this purpose, two single-port resonators have been combined to form a ladder filter. The main test vehicle consists in a single-port resonator, whose design is given in the Fig. 4.29 a and their geometrical parameters are detailed in the Table 4.10. The Fig. 4.29 b shows the ladder-type filter, it consists in a 4L-cells cascade.

Table 4.10 Geometrical parameters of the resonators forming the ladder filter where a is the finger width, p is the period, a/p corresponds to the metallization ratio, h is the thickness and λ is the wavelength [28].

Resonator	***a/p***	***h/λ (%)***	***IDT period (μm)***	***IDT electrode number***	***Mirror period (μm)***	***Mirror electrode number***	***Acoustic aperture (μm)***
Series	0,6	8,2	4,88	58	4,95	35	400
Parallel	0,6	7,9	5,06	56	5,14	35	400

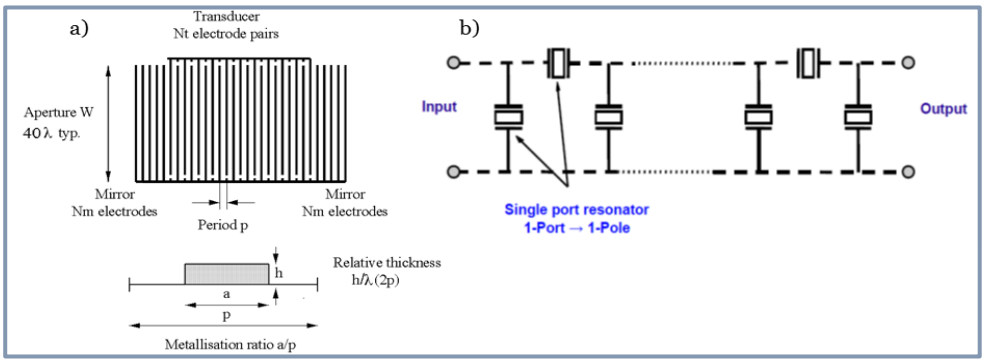

Fig. 4.29 Schematic representation of a single port synchronous resonator used as vehicle test and the definition of geometrical parameters (a). and ladder-type filter with 4L cascaded cells (b) [28]

The frequency response of filter, obtained by simulation, is shown in the Fig. 4.30. It illustrates the combination of impedance elements of the filter. The resonance frequency of the series resonator coincides with and anti-resonance frequency of the parallel resonator, in the center of the pass-band filter (Fig. 4.30 a). The transfer function or $|S_{12}|$ parameter of filter have a relative bandwidth of 3.75%, insertion losses of 1 dB and attenuation better than 50 dB (Fig. 4.30 b).

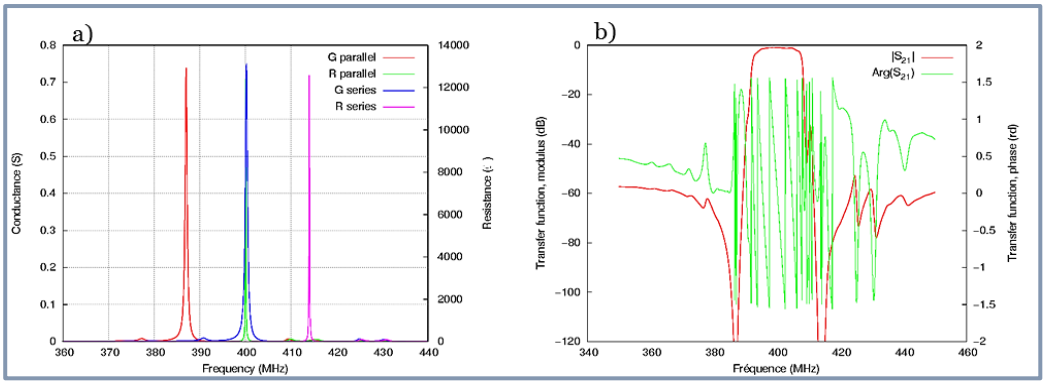

Fig. 4.30 Impedance elements on 42RY-XLT for the fabrication of a low loss pass-band filter: coincidence of resonance (G) and antiresonance (R) of the series and parallel branches of the filter (a). Modulus and phase of transfer function of filter (b).

SAW ladder-type filters were fabricated on quarters of wafers of undoped 42 RY-X LT crystals with congruent composition (42 RY-X CLT_reference sample). The resonators have been characterized electrically by admittance measurements. The Fig. 4.31 a shows the transfer function of eight filters with four cascaded cells of the 42 RY-X CLT_reference sample and its comparison to simulated signal ($|S_{12}|_{th}$). The experimentally measured transfer function is similar to the theoretical one. However, there is not a perfect coincidence of resonance and anti-resonance frequencies of the parallel and series branches, which produces

some ripples in the band. The dip presented on experimental $|S_{12}|$ is due to overestimated K^2 in the design. Dip in the upper passband edge seen in simulations is upper stopband edge of parallel resonator, which is not perfectly described in simulation. The experimental attenuation level is quite different to the predicted one, mainly on the lower edge of the passband. It is due to the experimental capacitance ratio between parallel and series resonator was different from the used one in simulations. Fig. 4.31 b shows a comparison of simulated and measured experimentally reflection coefficient $|S_{11}|$. Hump in S11 in passband center is due to the low K^2 in experimental results. Finally, the experimental and simulated $|S_{12}|$ of filter with 3 cascaded cells were compared (Fig.4.31 c). The experimental results fitted well with the simulated ones.

The single port resonators were simulated, as well. The simulations were done by adjusting the theoretical parameters (velocity, conductance, reflectivity, leakage factor etc.) in order to find the best fit to experimental results. The Fig. 4.32 shows the comparison between the theoretical and experimentally measured admittance of the series resonator. There is a slight difference between experimental and theoretical results. The susceptance is well predicted but the conductance is overestimated (Fig. 4.32 a). Then, the conductance was reduced by 7.5% and the reflection by 14%. The wave characteristics used for fitting were: wave velocity of 4070 m/s, conductance of 1.49×10^{-6} S/m and reflection coefficient of 8.58%.

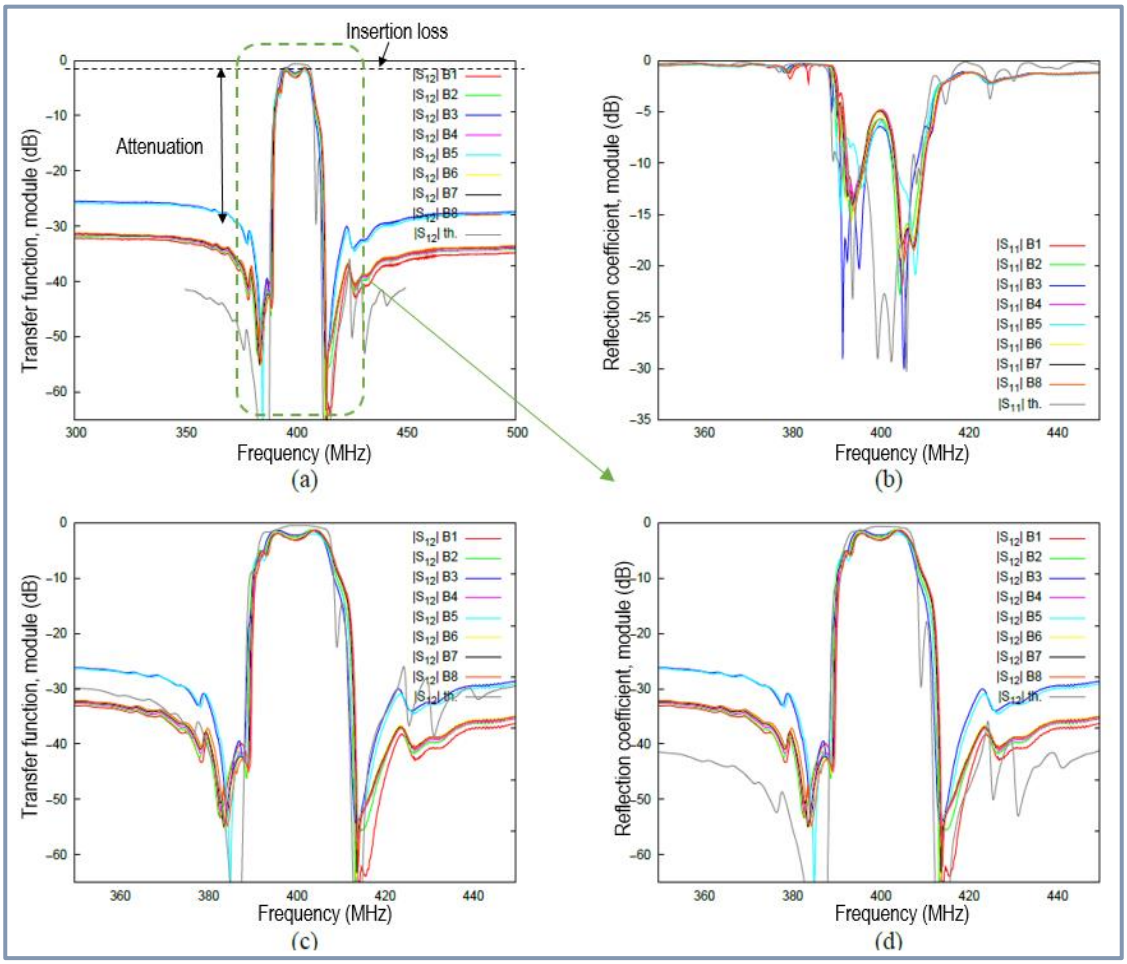

Fig. 4.31 Results of characterization of filters based on 42 RY-X CLT crystals: measured and simulated transfer function, S_{12}, of filters with 4 cascaded cells (B1-B8) (a); measured and simulated reflection coefficient, S_{11} (b); comparison of experimental and theoretical transfer function of filters with 3 cascaded cells filter (c); zoom on the passband of filters with 4 cascade elements (d).

Finally, a good agreement between experimental and theoretical conductance, susceptance and resistance responses were achieved (Fig. 4.32 b and c).

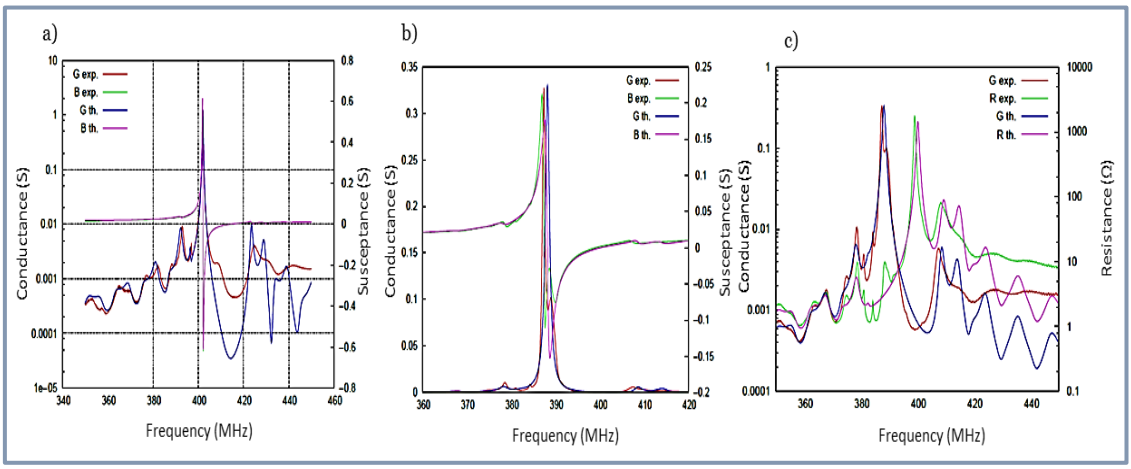

Fig.4.32 Comparison of theoretical and experimentally measured admittance of single port resonator based on 42 RY-X CLT crystals: response without velocity adjustment (a); conductance, susceptance and resistance after adjustment of parameters (b and c).

4.5.2 SAW filters on 42 RY-X LT crystals with different Li stoichiometries and domain states

SAW filters were fabricated on substrates of 42 RY-X LT crystals having different Li_2O concentrations and domain states: an untreated crystal, used as a reference, a sample annealed at 750°C during 48h (42 RY-X CLT_A3) and two samples treated by VTE with compositions close to the stoichiometric one (42 RY-X SLT_A2 and 42 RY-X NSLT_A5). In the case of crystal with congruent concentration, a sample was re-poled in the middle by reversing the polarization in the opposite direction and then switching it back, in order to check our poling quality. The samples, after annealing or VTE treatment, were homogeneously poled in the central region. However, the sample A3 wasn't completely poled because it required the application of a very high voltage (E_f>31.5 kV/mm) and during the poling a dielectric breakdown was observed. The Table 4.11 indicates the applied treatment and the Li_2O content in each sample.

Table 4.11 Properties and treatment conditions of 42 RY-X LT substrates, used for preparation of SAW devices.

Sample	***Treatment***	***%Li_2O in crystal (±0.05 mol%)***
42 RY-X CLT_reference	untreated	48.5
42 RY-X CLT_re-poled	re-poled in the middle of sample	48.5
42 RY-X CLT_A3	Annealed at 750°C for 48 h	48.5
42 RY-X NSLT_A5	VTE at 1300°C for 24h then at 1250°C for 10 h, by using powders with X_{Li2O}=60 mol%	49.9
42 RY-X SLT_A2	VTE at 1250°C, 48h by using powders with X_{Li2O}=60 mol%	~50

The SAW devices were fabricated on poled and poly-domain areas, in order to investigate if there was a difference in the signal due to the possible presence of polydomain state. However, few if any important changes were found, probably because the surface of the tested device was rather single domain. It is actually possible because SAW waves propagate only on surface layer and VTE samples often presented layered domain structure as it was shown in the Chapter 3. Thus, if this layer has homogenous properties, the wave that propagates on the surface will be as it was in a single domain region. Several filter parameters were estimated at room temperature from the transfer function as it is indicated in the Fig. 4.33. The center frequency (f_c), the upper and lower edge frequencies (f_h and f_l, respectively) were taken at a -20 dB level. The frequency of argument (F_o) was chosen in the mid band at the 0° phase level. The bandwidth (BW) was estimated by using the Eq. 1.59 (Chapter 1).

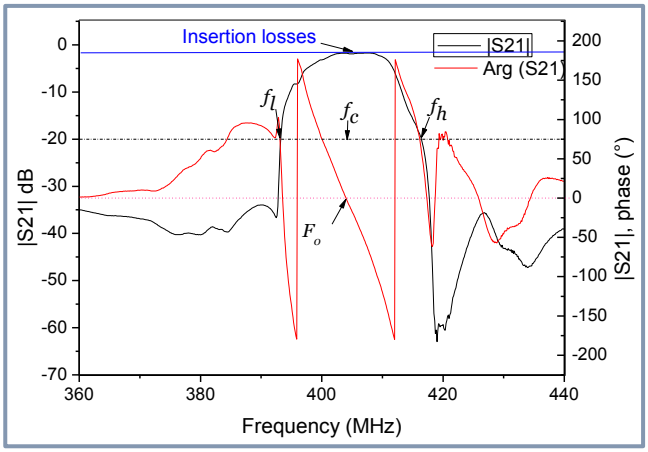

Fig. 4.33Parameters of SAW filters measured at room temperature: f_c, f_l and f_h are the center frequency, the lower and upper edge frequencies of the pass band, respectively, measured at a level of -20 dB. The F_o is the frequency measured at the phase 0° level. The insertion loss was measured taking f_c as a reference point.

The Fig. 4.34 shows the transfer function $|S_{12}|$ and the reflection coefficient $|S_{11}|$ of the SAW filters based on congruent 42 RY-X CLT crystals single and poly-domain. The 42 RY-X CLT_reference and the 42 RY-X CLT_re-poled samples have very similar responses. The values of f_c, f_l, f_h, F_o, IL and BW are almost identical (see Table 4.12). In contrast, in the case of the poly-domain sample (42 RY-X CLT_A3), the response of the filter is very different as compared to the reference devices, it presented many ripples in the band (Fig. 4.34 c). The bandpass was strongly affected, the BW decreased from 5.72% to 4.39%, the insertion losses were 1.4 dB in the case of the reference untreated sample, while the IL was 14.30 for the poly-domain sample. The transfer function and the reflection coefficient show spurious responses that can be interpreted as reflected signals. It should be noted that in this case the position of the spectra moved down to low frequencies. According to the shape of the band and the insertion loss, it can be deduced that the electromechanical coupling in this sample was strongly diminished, which should be confirmed by the characterization of resonators. There are several aspects to take into account in order to explain the origin of the poor response obtained in this sample. Firstly, the sample wasn't completely poled, then the poly-domain structure was probably the responsible for such spurious response. Moreover, this sample was polished in its backside in order to visualize the domains after poling. This can be the origin of the strong reflected signals observed in the filter response, as well.

Table 4.12 Parameters of SAW filters based on 42 RY-X LT crystals at 25 °C.

Sample	Domains state	f_c	f_l (MHz)	f_h (MHz)	F_o	IL (dB)	BW (±0.05%)
42 RY-X CLT_reference	single-domain	400.91	389.48	412.23	399.90	1.40	5.67
42 RY-X CLT_reference	single-domain	402.53	391.21	413.84	401.47	1.37	5.62
42 RY-X CLT_re poled	single-domain (re-poled)	401.40	390.38	412.42	400.16	1.07	5.49
42 RY-X CLT_A3	poly-domain	389.49	380.97	398.02	391.85	14.30	4.37
42 RY-X NSLT_VTEA5	single-domain (re-poled)	406.66	394.42	418.89	405.49	1.73	6.03
42 RY-X SLT_VTEA2	single-domain (re-poled)	404.82	393.24	416.34	403.99	1.53	5.71

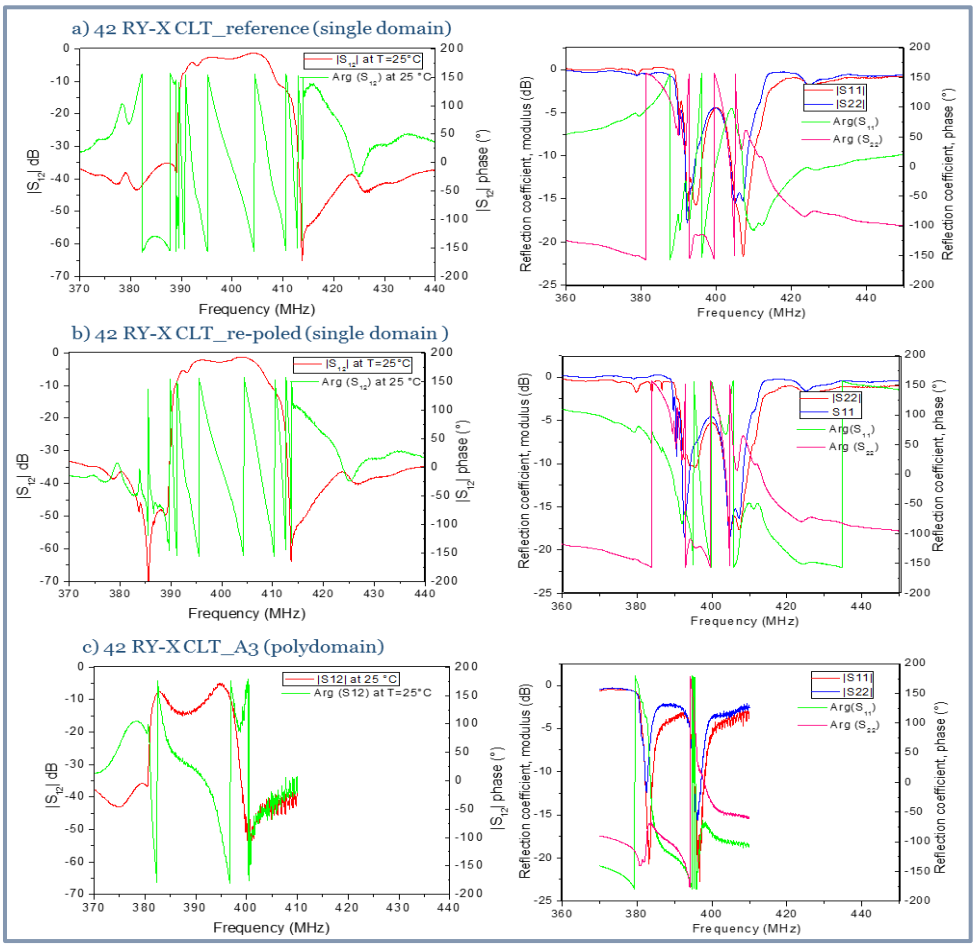

Fig. 4.34 Filter transfer function $|S_{12}|$ and reflection coefficient measured in different devices based on 42 RY-X CLT crystals:42 RY-X CLT_reference (a), 42 RY-X CLT_re -poled (b) and 42 RY-X CLT_A3 (c).

The Fig. 4.35 presents the reflection coefficient and the transfer function measured in 42 RY-X CLT-reference, 42 RY-X SLT_VTEA2 and 42 RY-X NSLT_VTEA5 samples. In the case of filters fabricated on nearly stoichiometric and stoichiometric crystals, the filter band parameters such as the ripple, bandwidth and insertion loss do not exhibit important changes as compared to response of the reference sample. We found that the f_c increases by 2-4 MHz as compared to the reference sample (see Table 4.12). The shift of frequencies to higher values maybe due to the actual thickness of electrodes was 780 nm instead of 800 nm. However, the origin of this can be also an effect of Li concentration in the crystal since it has been reported in literature that the velocity of shear waves, and therefore, the frequency, changes with the Li content in crystals [3]. The IL values are slightly higher, -1.53 dB in 42 RY-X SLT_VTEA2 sample, instead of -1.37 dB in reference sample. However, the BW of SAW filters based on stoichiometric crystals is slightly higher than of the congruent sample (5.99 % instead of 5.72%). Therefore, the coupling was slightly increased with the decrease of Li deficiency.

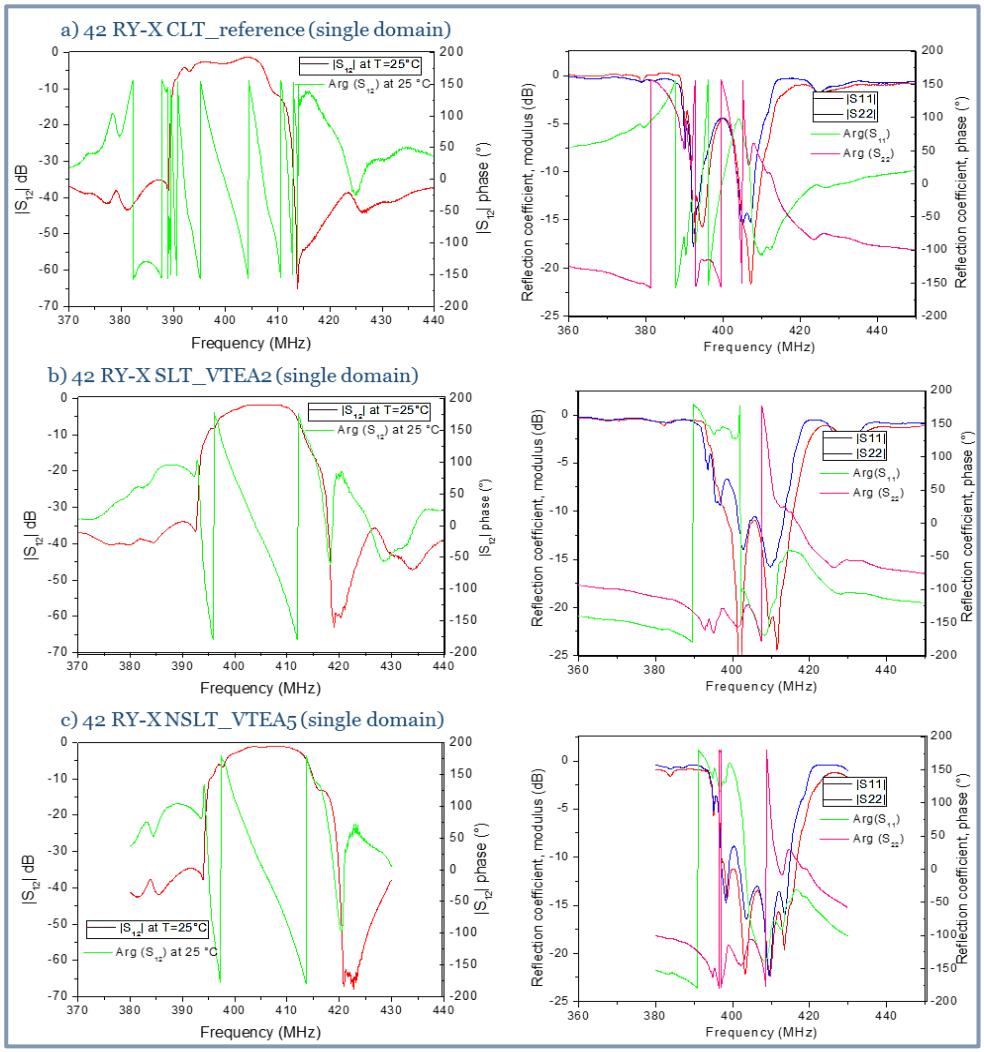

Fig. 4.35 Filter transfer function $|S_{12}|$and reflection coefficient measured in different devices based on 42RY-X CLT single domain crystals:42 RY-X CLT_reference (a), 42 RY-X NSLT_VTEA2, 50 mol% of Li_2O (b), 42 RY-X NSLT VTEA5, 49.9 mol% of Li_2O (c).

4.5.2.1 Estimation of TCF and K² in SAW devices

The thermal stability of filter response was investigated, as well. For this purpose, the devices were characterized from 25 to 100°C. The temperature dependence of the transfer function of SAW filters built on substrates of 42 RY-X LT with different Li_2O concentrations and domain states is shown in Fig. 4.36. The first order temperature coefficient of frequency was estimated from the temperature variation of the minimum of lower and upper edges of the passband (f_{lm} and f_{hm}, respectively) at f_l and f_h taking-20 dB as a reference level and at F_o (see Fig. 4.36 a). The values of TCF are summarized in the Table 4.13.

Table 4.13 Temperature coefficient of different frequencies: f_l, f_h measured at a transition band level of – 20 dB. The frequencies f_{lm} and f_{hm} were taken in the minimum of the lower and upper edges of the passband, respectively. F_o is the frequency at phase of 0°in the mid band. K² of SAW devices based on 42 RY-X crystals with different domain states and Li non-stoichiometries is indicated, as well.

Sample	***%Li_2O in crystal (±0.05 mol%)***	***TCF_{lm} (±3 ppm/°C)***	***TCF_{hm} (±3 ppm/°C)***	***TCF_l (±2 ppm/°C)***	***TCF_h (±2 ppm/°C)***	***TCF_o (±2 ppm/°C)***	***K^2 (±0.1%)***
42 RY-X CLT_reference	48.5	-38.5	-32.00	**-31.2**	**-41.32**	-42.34	7.0
42 RY-X CLT_re-poled	48.5	-28.8	-33.00	**-33.0**	**-40.9**	-42.8	7.0
42 RY-X CLT_A3	48.5	-27.6	-28.5	**-19.2**	**-21.9**	-24.1	2.5
42 RY-X NSLT_VTEA5	49.9	-31.4	-37.4	**-31.4**	**-40.8**	-42.4	7.3
42 RY-X SLT_VTEA2	50	-23.1	-34.03	**-29.0**	**-46.6**	-34.9	7.1

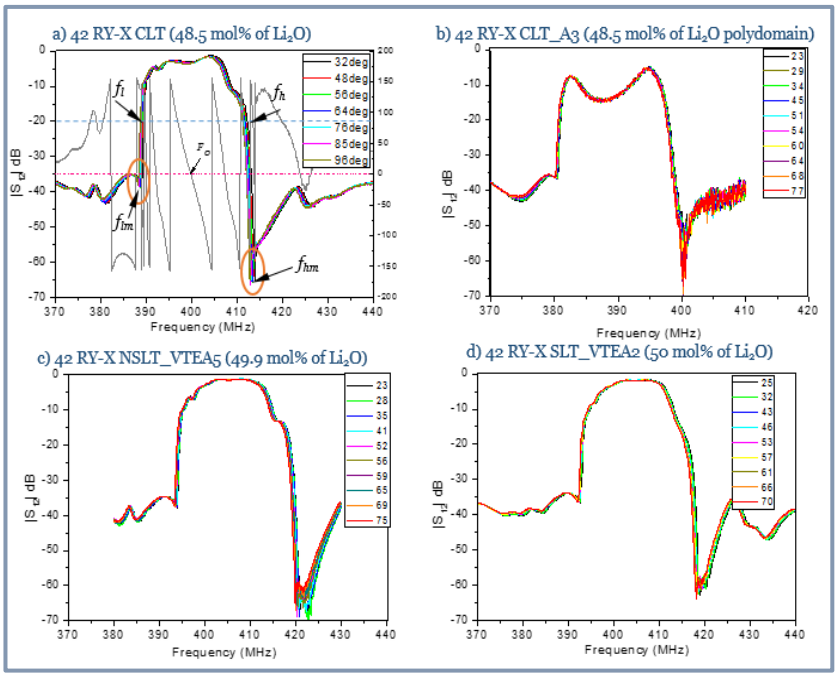

Fig.4.36 Temperature dependence of the transfer function of filters on 42 RY-XLT: reference sample (a), polydomain sample (b), 42 RY-X NSLT_VTE A5 (c) and42 RY-X NSLT_VTEA2 sample (d).

The TCF_{lm} and TCF_{hm}, taken from the frequencies in the minimum of the lower and upper edge of the passband, respectively, shows that the VTE treated and the re-poled samples have smaller absolute value of TCF_{lm} than the reference sample (see Table 4.13). Moreover, it seems that the stoichiometric sample (42 RY-X SLT_VTEA2) has a TCF_{lm} lower than the reference. The TCF_{hm} is almost the same in all samples, in the range of errors. However, the signal of upper edge of filter was often noisy, which made difficult to select properly the value of f_{hm} (see Fig. 4.37). Therefore, the results of TCF_{lm} and TCF_{hm} should be considered with reserve. Then, we chose another reference point in order to have results that are more reliable. The frequencies of the upper and lower edge of pass band were taken at -20 dB as reference level. In this area, the f_l and f_h obtained at different temperatures were clearly distinguished (Fig. 4.37).

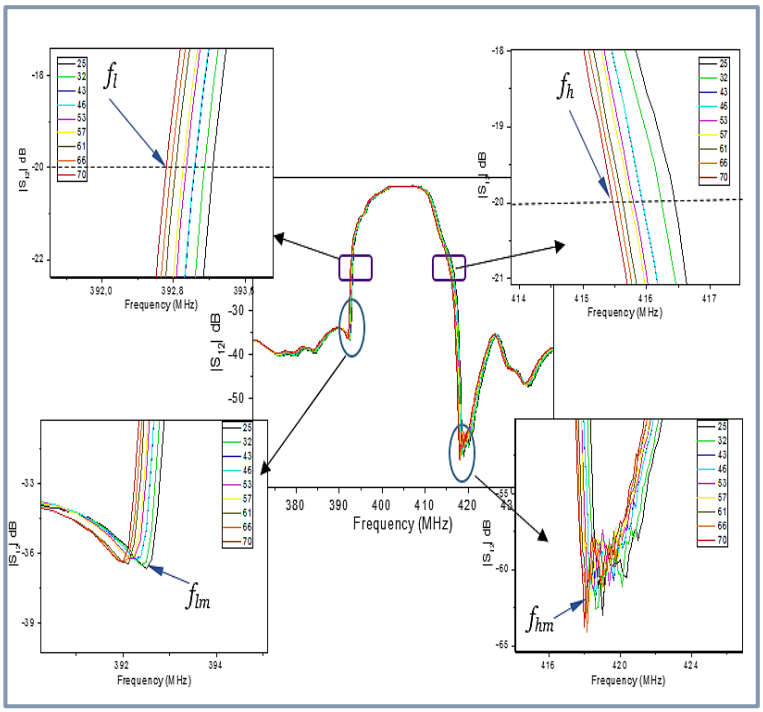

Fig. 4.37 Position of different frequencies used for estimation of TCF in the lower and upper frequencies of the edges of pass band of the 42 RY-X LT_VTE A2 SAW filter.

The relative TCF_l and TCF_h of all studied samples are given in Fig. 4.38. The reference sample had a TCF_l of -31.2 ppm/°C and a TCF_h of -41.32 ppm/°C, which is close to the reported one (-40 ppm/°C)[29]. Furthermore, the re poled sample had a TCF_l and TCF_h very similar to those of reference (-33 ppm/°C and -40.9 ppm/°C), respectively. Thus, it seems that there are no differences between the reference and the re-poled samples. Moreover, the TCF_l and TCF_h are similar in congruent and stoichiometric samples, in the accuracy range (see Table 4.13). It indicates that the changes in Li stoichiometry does not have important effects on the TCF values.

In the case of the 42 RY-X CLT_A3 sample, it has the same Li content as the untreated sample, but it is polydomain. This sample showed a TCF_l and TCF_h less negative than the reference. Therefore, it indicates that the polydomain state can be responsible for the diminution of TCF.

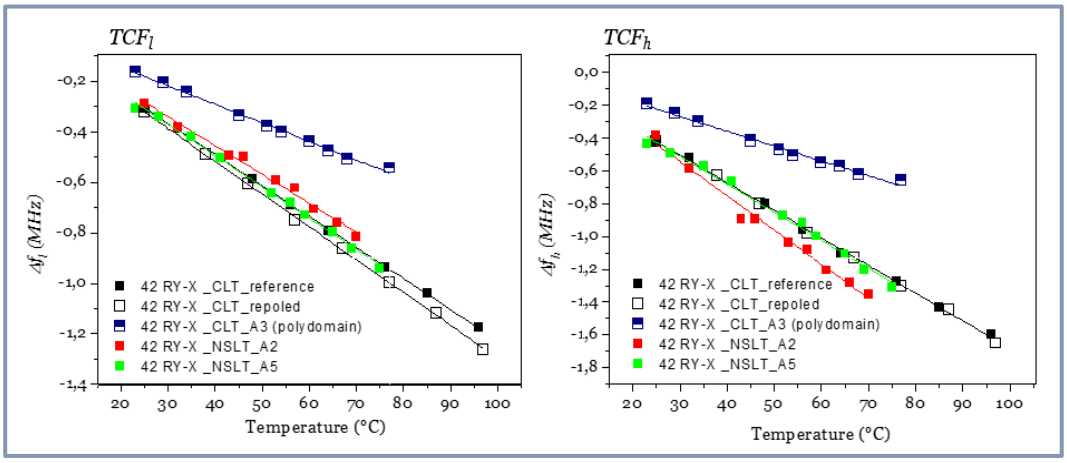

Fig. 4.38 Relative temperature coefficient of lower (TCF_l) and upper frequencies (TCF_h) of SAW filters based on 42 RY-X LT crystals with different Li stoichiometries and domain states.

On the second hand, the coupling factor of series and parallel resonators was estimated from the RLC parameters from the equivalent circuit. The Fig. 4.39 shows the model of *m-BVD (modified Butterworth Van Dyke)* circuit that was employed, where R_s stands for the stray resistance. R_1, L_1 and C_1 are the motional resistance, inductance and capacitance, respectively. C_0 and R_0 are the parallel capacitance and resistance. This model can be expressed with the following function:

$$Y = \frac{1}{jC_0\omega} + R_0 \qquad Eq.\ 4.13$$

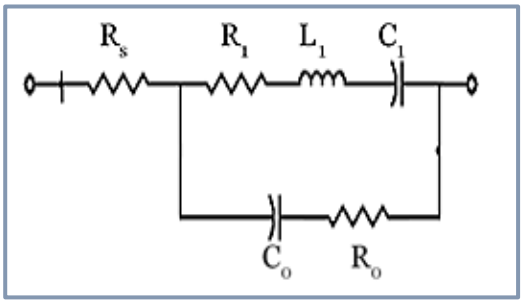

Fig. 4.39 Equivalent circuit model used for characterization of series and parallel single port resonators.

All the RLC parameters were obtained by using a script that fits the experimental with the modeled admittance, after several iterations, the program gives the better adjusted values. The Fig. 4.40 shows an example of the comparison of experimentally measured and theoretically estimated admittance in a single resonator based on 42 RY-X LT crystals, treated by VTE. The modeled response is in a good agreement with the experimentally measured one. Then the K^2 was estimated from the values of C_0 and C_1, by using the Eq. 1.73 described in the Chapter 1. The values of K^2 of each sample are summarized in the Table 4.13.The reference sample showed K^2 of 7.00 %, close to the expected one (7.6%)[29]. The re-poled sample had the same K^2 value. The nearly stoichiometric samples had K^2 of 7.1 and 7.3 %, slightly higher than that of untreated sample. The K^2 of the

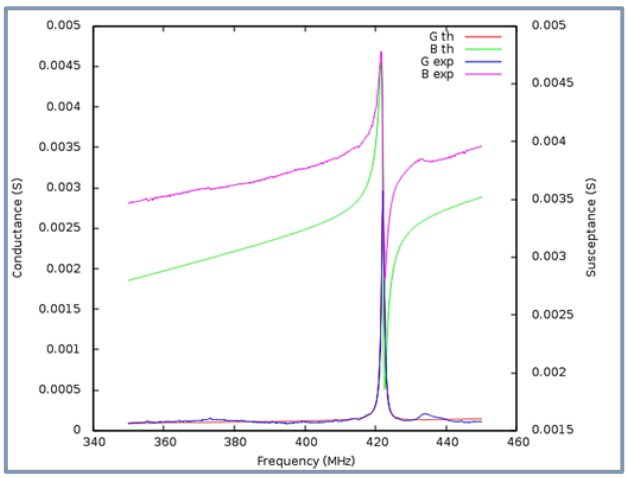

Fig. 4.40 Experimental and theoretical conductance and susceptance as a function of frequency of single port of 42 RY-X-NSLT_VTEA2 sample

poly-domain sample (42 RY-X_CLT_A3) diminished almost three times regarding to the reference sample. Therefore, it confirms that the poly-domain structure diminishes drastically the piezoelectric coupling, as observed in the case of ridges resonators.

In summary, in this part, we analyzed the effect of Li stoichiometry on the TCF and K^2 of SAW filters and resonators. In contrast to the frequency response obtained by ridge resonators, the signal quality of filters allowed a more accurate estimation of TCF. However, it was demonstrated that the reference level used to take the frequencies values is very important and it influences strongly the results. The TCF of SAW filters based on 42 RY-X LT crystals with congruent and nearly stoichiometric compositions were almost the same, in the range of errors. The temperature changes of the lower edge (TCF_l) of the passband of filters based on stoichiometric 42 RY-X crystals is almost the same than that on congruent crystal. The upper frequency at -20 dB level on the right side of the passband (f_h) changes slightly faster in the case of the stoichiometric sample as compared to the congruent one. These differences might be related to the change of K^2 and its temperature variation with Li_2O non-stoichiometry. The K^2 of stoichiometric samples was slightly higher than that of congruent ones. Thus, the filter based on stoichiometric crystals presented less ripples in the passband. However, in the case of poly-domain samples, the K^2 and the absolute value of TCF were smaller than those of untreated sample. Thus, the poly-domain state affects the acoustic properties of devices and it is probably the responsible for the diminution of TCF and K^2.

4.6 Conclusions

In this chapter, we investigated the dependence of variation of frequency on the elastic constants of different BAW resonators based on LT as a piezoelectric substrate. Depending on the orientation of the crystals and the disposition of resonators, elastic constants have different contributions to the variation of frequency. We focused on the search of a configuration allowing the excitation of shear modes dependent on C_{44} elastic constants. Different configurations of BAW resonators (TE, LFE and ridges) were simulated in 2D. The simulations of BAW resonators in LFE configuration, realized on 42 RY-LT crystals showed shear modes interesting for the estimation of C_{44} but with a very low K^2. Thus, this configuration was not suitable for experimental characterization. On the second hand, according to simulations, the thickness excited BAW resonators based on 42 RY-LT crystals depended mainly on C_{44} and C_{14}. However, experimental results did not agree with predictions. The theoretical K^2 was about 8% but the signal measured experimentally had many spurious modes at the fundamental frequency. Besides, the values of K^2 of 3rd overtone, were very small. There are several possible explanations. Firstly, the size of the plates was probably too big regarding the size of electrodes. Secondly, the parallelism of plates after polishing its back side, unpolished initially, could be defective.

Finally, the problem might be in the contact or resistivity of electrodes. However, since in this configuration the contribution of C_{44} to the variation of frequency is rather modest, we decided to try another configuration. Hence, ridge resonators were investigated. The ridges presented a highly coupled signal and the shear modes could be excited. For this reason, we realized experimentally this kind of resonators. Furthermore, according to theoretical analysis, the FS mode of ridge resonators parallel to X-axis (ZY-LT) depended mainly on C_{44}.

Other configurations of ridge resonators (ZX and 42RYX) were tested as well, in which FS mode depends on C_{44}, C_{14} and C_{66}.

In the case of ridge resonators based on Z-cut LT crystals, the theoretical and experimental TCF_s and TCF_p had the same sign. Furthermore, in the case of ZY ridge resonators fabricated in stoichiometric crystals, the TCF_s of the FS mode was less negative than compared to the TCF_s of congruent material (-18 and -31 ppm/C°, respectively), but close to the theoretical value for ZY-CLT. The TCF_p and K^2 of stoichiometric sample were similar to those of congruent sample. The results show that in ZY ridge configuration, stoichiometric material could provide a lower temperature coefficient of series frequency, which is dependent on C_{44}. In the case of ZX ridge resonators, the TCF_p, the TCF_s and K^2 of stoichiometric and congruent materials were similar. Z-cut LT stoichiometric crystals were single domain, thus, the observed changes in TCF might be attributed to the stoichiometry effect or the quality of ridges structures. However, the poor quality factor of ridges resonators did not allow to obtain reliable conclusions.

On the second hand, the study of ridge resonators based on re-poled and poly-domain 42 RY-LT crystals indicates that the presence of domains affects significantly the properties of devices. For example, the K^2 decreases strongly in poly-domain samples and the TCF varies considerably. The results obtained on ridge resonators fabricated on iron doped 42 RY-LT crystals were not conclusive due to the poor quality signal. Thus, the accurate estimation of K^2 and the TCF of these samples was not possible. Besides, we had a doubt about the complete reversal domain in some of these samples.

Furthermore, SAW filters were fabricated on substrates of undoped 42 RY-LT crystals with different Li_2O concentrations and domain states. The experimentally measured transfer function and reflection coefficient were in good agreement with expected results. The SAW filters based on nearly stoichiometric crystals (42 RY-X NSLT_VTEA5 and 42 RY-X SLT_VTEA2) showed a bandwidth and insertion loss similar to the untreated samples. However, the poly-domain sample with congruent concentration (42 RY-X CLT_A3) shows an increase of insertion losses and unwanted reflections in the edges of the pass band.

The quality of signal of SAW filters allowed the estimation of TCF and K^2 with better accuracy than in the case of ridge resonators. In the case of filters, the better method was to take the frequency values at a band transmission level of -20 dB because in this part the curves did not showed an ambiguous behavior with temperature. The TCF, estimated from the lower and upper frequency edge of bandpass in the transfer function of filters were compared. It was found that the TCF of untreated and nearly stoichiometric samples were very similar. The K^2 of nearly stoichiometric samples was slightly higher than that of the congruent sample. However, in the case of the poly-domain sample, the TCF_l and TCF_h were reduced with respect to the reference sample, by 12 ppm/°C and 19.4 ppm/°C, respectively. This sample presented K^2=2.5%, i.e the coupling was reduced three times with respect to that of the untreated single domain sample.

Finally, these last results allows us to conclude that the Li stoichiometry does not affects significantly the properties of acoustic devices studied here, i.e, the TCF and the K^2. However, it was demonstrated that the polydomain state in the substrate affects strongly the acoustic properties of devices.

4.7 References

[1] "IEEE Standard on Piezoelectricity," *ANSIIEEE Std 176-1987*, p. 0_1-, 1988.
[2] O. Kawachi, S. Mineyoshi, G. Endoh, U. M. Ueda, O. Ikata, K.-Y. Hashimoto, and M. Yamaguchi, "Optimal cut for leaky SAW on LiTaO/sub 3/ for high performance resonators and filters," *IEEE Trans. Ultrason. Ferroelectr. Freq. Control*, vol. 48, no. 5, pp. 1442–1448, Sep. 2001.
[3] J. Kushibiki, I. Takanaga, S. Komatsuzaki, and T. Ujiie, "Chemical composition dependences of the acoustical physical constants of LiNbO3 and LiTaO3 single crystals," *J. Appl. Phys.*, vol. 91, no. 10, pp. 6341–6349, May 2002.
[4] J. Kushibiki, H. Ishiji, T. Kobayashi, N. Chubachi, I. Sahashi, and T. Sasamata, "Characterization of 36/spl deg/YX-LiTaO/sub 3/ wafers by line-focus-beam acoustic microscopy," *IEEE Trans. Ultrason. Ferroelectr. Freq. Control*, vol. 42, no. 1, pp. 83–90, Jan. 1995.
[5] I. Takanaga and J. Kushibiki, "Elastic constants of multidomain LiTaO3 crystal," *J. Appl. Phys.*, vol. 86, no. 6, pp. 3342–3346, Sep. 1999.
[6] J. Kushibiki, H. Takahashi, T. Kobayashi, and N. Chubachi, "Quantitative evaluation of elastic properties of LiTaO3 crystals by line-focus-beam acoustic microscopy," *Appl. Phys. Lett.*, vol. 58, no. 9, pp. 893–895, Mar. 1991.
[7] T. Yamada, H. Iwasaki, and N. Niizeki, "Piezoelectric and Elastic Properties of LiTaO3: Temperature Characteristics," *Jpn. J. Appl. Phys.*, vol. 8, no. 9, p. 1127, Sep. 1969.
[8] A. W. Warner, M. Onoe, and G. A. Coquin, "Determination of Elastic and Piezoelectric Constants for Crystals in Class (3m)," *J. Acoust. Soc. Am.*, vol. 42, no. 6, pp. 1223–1231, Dec. 1967.
[9] R. T. Smith, "Elastic, piezoelectric, and dielectric properties of lithium tantalate", *Appl. Phys. Lett.*, vol. 11, no. 5, pp. 146–148, Sep. 1967.
[10] J. -i. Kushibiki, I. Takanaga, M. Arakawa, and T. Sannomiya, "Accurate measurements of the acoustical physical constants of LiNbO/sub 3/ and LiTaO/sub 3/ single crystals," *IEEE Trans. Ultrason. Ferroelectr. Freq. Control*, vol. 46, no. 5, pp. 1315–1323, Sep. 1999.
[11] J. Kushibiki and I. Takanaga, "Elastic properties of single- and multi-domain crystals of LiTaO3," *J. Appl. Phys.*, vol. 81, no. 10, pp. 6906–6910, May 1997.
[12] I. Takanaga and J. -i. Kushibiki, "A method of determining acoustical physical constants for piezoelectric materials by line-focus-beam acoustic microscopy," *IEEE Trans. Ultrason. Ferroelectr. Freq. Control*, vol. 49, no. 7, pp. 893–904, Jul. 2002.
[13] J.-I. Kushibiki and N. Chubachi, "Material Characterization by Line-Focus-Beam Acoustic Microscope," *IEEE Trans. Sonics Ultrason.*, vol. 32, no. 2, pp. 189–212, Mar. 1985.
[14] A. de Bernabé, C. Prieto, and A. de Andrés, "Effect of stoichiometry on the dynamic mechanical properties of LiNbO3," *J. Appl. Phys.*, vol. 79, no. 1, pp. 143–148, Jan. 1996.
[15] V. Hinkov, M. Barth, and K. Dransfeld, "Acoustic properties of proton exchanged LiNbO3 investigated by Brillouin scattering," *Appl. Phys. A*, vol. 38, no. 4, pp. 269–273, Dec. 1985.
[16] T. Błachowicz, "Study of the elastic properties of the lithium tantalate crystal by the Brillouin laser light scattering," *Arch. Acoust.*, no. Vol. 25, 1, pp. 23–34, 2000.
[17] U. Röesler, "Wave velocity dependence on elastic constants, personal information provided by TDK Co.," Dec-2012.
[18] F. Henrot, F. Bassignot, B. Guichardaz, G. Ulliac, E. Courjon, J.-Y. Rauch, and S. Ballandras, "New acoustic resonator based on a ridge built in a periodically poled ferroelectric material for RF applications," in *Applications of Ferroelectrics held jointly with 2012 European Conference on the Applications of Polar Dielectrics and 2012 International Symp Piezoresponse Force Microscopy and Nanoscale Phenomena in Polar Materials (ISAF/ECAPD/PFM), 2012 Intl Symp*, 2012, pp. 1–4.
[19] F. Henrot, F. Bassignot, C. Guyot, J.-Y. Rauch, B. Guichardaz, and S. Ballandras, "Highly coupled resonator based on ridge-shaped periodically poled materials for radio-Frequency applications," in *European Frequency and Time Forum International Frequency Control Symposium (EFTF/IFC), 2013 Joint*, 2013, pp. 933–936.
[20] "Introduction to Finite Element Analysis." [Online]. Available: http://www.sv.vt.edu/classes/MSE2094_NoteBook/97ClassProj/num/widas/history.html.].
[21] "The Boundary element Method." [Online]. Available: http://www.boundary-element-method.com/.

[22]S. Ballandras, R. Lardat, M. Wilm, T. Pastureaud, A. Reinhardt, N. Champavert, W. Steichen, W. Daniau, V. Laude, R. Armati, and G. Martin, "A mixed finite element/boundary element approach to simulate complex guided elastic wave periodic transducers," *J. Appl. Phys.*, vol. 105, no. 1, p. 14911, Jan. 2009.
[23]S. Ballandras and W.Steichen, "Composants acoustiques utilisés pour le filtrage Modèles et outils de simulation," *Techniques de l'ingénieur Matériaux pour l'électronique et dispositifs associés*, p. E 2 001-1-32, 10-Nov-2010.
[24]R. A. Moore, J. T. Haynes, and B. R. McAvoy, "High Overtone Bulk Resonator Stabilized Microwave Sources," in *1981 Ultrasonics Symposium*, 1981, pp. 414–424.
[25]A. Ballato, E. R. Hatch, M. Mizan, T. Lukaszek, and E. R. Tilton, "Simple Thickness Plate Modes Driven by Lateral Fields," in *39th Annual Symposium on Frequency Control. 1985*, 1985, pp. 462–472.
[26]F. Henrot, F. Bassignot, B. Guichardaz, G. Ulliac, E. Courjon, J.-Y. Rauch, T. Baron, and S. Ballandras, "Acoustic resonator based on periodically poled lithium niobate ridge," *IEEE Trans. Ultrason. Ferroelectr. Freq. Control*, vol. 60, no. 8, pp. 1556–1563, Aug. 2013.
[27]K. Nakamura and H. Shimizu, "Local domain inversion in ferroelectric crystals and its application to piezoelectric devices," in *Ultrasonics Symposium, 1989. Proceedings., IEEE 1989*, 1989, pp. 309–318 vol.1.
[28]S. Ballandras, "Personal information communicated by Frec'n'sys society."
[29]Roditi International Co., "Lithium Tantalate Properties." [Online]. Available: http://www.roditi.com/SingleCrystal/Lithium-Tantalate/LiTaO3-Properties.html.

5. General conclusion and perspectives

One of the limitations of present SAW filter technology, based on LT and LN crystals, is the sensitivity of frequency to temperature, which is mainly induced by the temperature derivatives of elastic constants of the material.

The effect of Li non-stoichiometry on the physical and structural properties of LN and LT was widely studied in literature. My PhD supervisor A. Bartasyte has started to work in this field in 2008, during her stay at Oxford University. Later, she joined University of Lorraine, where she focused on the relationship between the non-stoichiometry and acoustical properties. The patents based on the acoustical and optical characterizations of VTE treated samples were applied at University of Lorraine and University of Oxford, respectively. I did my master training and my first year of PhD on this topic, at University of Lorraine, as well. At the beginning of my 2nd PhD year I have moved to FEMTO-ST following my supervisor A. Bartasyte. At FEMTO-ST, I integrated the groups MINAMAS and COSYMA. The many-years experience of COSYMA group and my co-supervisor B. Dulmet on the SAW and BAW devices, their simulations, fabrication, and characterization, as well as electrical poling of LN and LT crystals added a new dimension to my PhD topic. Therefore, my PhD topic was redefined by using more fundamental studies of materials and devices by adding several alternative approaches to demonstrate the relationship between acoustical performance and Li_2O non-stoichiometry in LT and LN.

The aim of this thesis was the investigation of the effect of Li_2O non-stoichiometry in LT and LN single crystals on the performance of acoustic wave devices. I put a particular emphasis on the investigation of possibilities to reduce TCF in 42 RY-X LT crystals, the improvement of the stability at high power densities of 128 RY-X LN wafers, without reduction of K^2 and without increase of losses. For this purpose, I had to complete several tasks, including the fabrication of LT and LN crystals with different Li stoichiometry, their homogenous electrical field poling, the simulation of BAW and SAW devices, and their micro-fabrication and electrical characterization.

At the initial stage of my PhD, an exhaustive study about the VTE process in LT and LN crystals was performed, in order to produce homogenous crystals with controlled Li_2O concentration. Although there are many reports on VTE treatment of LN crystals, little was done on LT crystals. Therefore, a detailed study of effects of all parameters involved in VTE treatment (e.g. duration, temperature, Li_2O concentration in powders and crystal cut) on Li_2O volatility, in- and out-diffusion of Li_2O, and concentration gradients was done. The VTE treatments enabling to obtain different Li_2O concentrations with homogenous distribution in wide compositional range was optimized for different cuts of LT crystals. Comparing to literature works, we did an additional effort to obtain homogenous LT crystals with intermediate Li_2O concentrations in between the congruent and stoichiometric ones. The Li_2O concentration in crystals and its gradients were accurately measured by means of Raman spectroscopy. We established the empirical equations presenting the dependence of Li_2O content in treated crystals on treatment time, temperature and Li_2O concentration in equilibration powders. We found that the treatment time and temperature parameters affected strongly the Li_2O concentration and homogeneity of

treated crystals. At higher VTE temperatures, shorter treatment durations were needed in order to obtain crystals with homogenous composition. However, the composition of equilibration powders changes very quickly at high VTE temperatures (≥1300 °C). This makes difficult to precisely control the Li_2O non stoichiometry in treated crystals. Therefore, we selected 1250 °C as an optimal temperature for the treatments of LT crystals. In agreement with literature, we observed that the diffusion of Li is anisotropic, being a faster process along Z-axis of LT crystals. In the case of X-cut LT, Y-cut LT, 42 RY-LT and Z-cut LT crystals with stoichiometric and intermediate Li_2O concentrations, treatments longer than 24 h at 1250 °C are required to obtain homogenous crystals. Homogenous, twin- and crack-free 42 RY-LT crystals with Li_2O concentration in the compositional range from 47.3 to 50 mol% were prepared. Sub-congruent 128 RY-LN crystals with 47.9 mol% of Li_2O on the crystal surface were obtained as well. The VTE process was carried out at temperatures below T_c, thus, the poly-domain structure was not expected.

In the next stage, we have considered the possibility to transfer the VTE technology from small samples to 4 inches wafers. However, it was found that 4 inches LT wafers were warped after the thermal treatments at high temperatures (the bow height of 1 mm after 48 h at 1250 °C). Although we have tried to optimize the treatment temperature, duration and cooling/heating rates in order to reduce the warping of wafers, and we succeeded to reduce it to the order of 100 μm, the values of bowing height remained too high for industrial fabrication lines. Thus, we used small crystals to prepare the samples for further micro-fabrication of SAW and BAW devices.

After the VTE treatment, LT crystals were poly-domain and had to be uniformly poled. For this purpose, we used the technique of electric field poling at room temperature. Undoped and iron doped LT crystals with different orientations (Z-cut and 42 RY-LT), compositions (47.3-50 mol% of Li_2O), and various initial ferroelectric domain states (single and poly-domain) were poled. In the case of initially single domain crystals, only one or two poling cycles were needed to reverse the polarization and the process was reproducible. Although the procedure for poling of poly-domain (VTE treated) crystals was basically similar to that used for single domains crystals, some particularities were observed. The poling process was more difficult in the case of poly-domain undoped LT crystals as higher voltages and bigger number of poling cycles were needed in order to obtain a complete domain reversal. On the second hand, the poling of iron doped 42 RY-LT crystals required many experiments and observations because the poling dynamics was different from the undoped LT crystals. When the electric field was applied only in one direction, many poling cycles were needed to completely reverse the direction of polarization. It was found that by switching the direction of electric field several times the domain reversal process was facilitated. Moreover, the poling dynamics, reflected in the transient current, in stoichiometric and nearly stoichiometric crystals was different from that of the congruent ones. The uniform poling of undoped SLT and NSLT was achieved successfully at room temperature. In contrast, the poling of sub-congruent 42 RY-LT crystals was often unsuccessful due to the extremely high magnitudes of voltage required to reverse the polarization of these crystals.

After the preparation of crystals with different Li_2O concentration and uniform electrical poling, the crystals were used for fabrication of BAW and SAW devices. We focused our investigations on the effect of Li-non stoichiometry of LT crystals on the temperature dependence of elastic constants, mainly C_{44} and C_{66}. For this purpose, we have investigated several

configurations of BAW resonators allowing the excitation of shear modes, dependent on C_{44} and C_{66} elastic constants. According to simulations, ridge resonators showed a highly coupled signal and the possibility to excite the shear modes. Then, ridges resonators were fabricated from congruent and nearly stoichiometric Z-cut LT and 42 RY-LT crystals. In the most of cases, the frequency response, TCF and K^2 values of untreated crystals measured experimentally, were in agreement with theoretical results. However, the poor quality factor of ridge resonators did not allow to obtain reproducible results and to conclude on Li non-stoichiometry effect, due to the presence of spurious modes near the resonance frequency.

Finally, SAW filters were fabricated on substrates of undoped 42 RY-LT crystals with congruent and nearly stoichiometric composition. Although the investigation of sub-congruent and stoichiometric crystals was wanted, it was not possible to prepare the sub-congruent LT crystals with single-domain state, due to the difficulties in electrical poling of these compositions, as mentioned above. The experimentally measured transfer function and reflection coefficient were in a good agreement with the expected results and were very similar for untreated and VTE treated samples. This time, the quality of signal was satisfactory and it allowed the estimation of TCF and K^2 with better accuracy than in the case of ridge resonators. We have observed that the method used to estimate the TCF strongly affected the results. Thus, it is important to study the frequencies in the region where the frequency response does not shows an ambiguous behavior with temperature. We have obtained representative and reliable results by estimation of TCF values from the lower and upper frequency edges of the bandwidth in the transfer function of filters. We have found that the TCF and K^2 of untreated and nearly stoichiometric crystals were very close. However, in the case of congruent poly-domain crystals, a strong decrease of the electromechanical coupling factor from 7% (for the untreated sample) to 2.5%, was observed. Furthermore, the poly-domain sample showed a reduced TCF from -19.2 ppm/°C (the TCF of congruent 42 RY-X LT crystals was -31.5 ppm/°C). Therefore, we can conclude that the variation of Li_2O non-stoichiometry in the congruent-stoichiometric composition range in LT crystals does not change significantly the values of TCF and K^2. However, the presence of a poly-domain structure in crystal affects strongly these properties.

Perspectives

In order to evaluate the effect of Li non-stoichiometry in the congruent-subcongruent composition range (<48.5 mol % of Li_2O) on the acoustical performance of 42 RY-X LT devices, the high temperature poling procedure has to be optimized. The poling at high temperature can facilitate the process because the electric coercive field decreases with temperature. We prepared an experimental set-up to pole the crystals at temperatures < 210 °C. However, it was not possible to optimize the technique due to time limitations.

Furthermore, the treatment of 128 RY-LN crystals was done at the end of project and the fabrication of devices was not possible due to the limitation of time, as well. The realization of SAW devices based on 128 RY-LN VTE treated crystals and the test of their stability at high power density will be done in future.

It would be also interesting to investigate Li_2O non-stoichiometry effect on the temperature evolution of complete set of elastic, piezoelectric and dielectric constants of LN and LT.

6. Résumé

Effet de la non stœchiométrie en Li sur la performance des dispositifs à ondes élastiques à base de monocristaux de $LiTaO_3$ et $LiNbO_3$

I. Introduction

Les dispositifs à ondes élastiques de surface (O.E.S) constituent des éléments essentiels dans les systèmes de communication mobile. Ils sont utilisés comme filtres passe–bande, résonateurs où lignes à retard. La plupart des filtres de radiofréquence sont réalisés à base de niobate et tantalate de lithium (LT et LN). Ces deux matériaux présentent des propriétés piézoélectriques intéressantes, par exemple un coefficient de couplage électromécanique élevé, K^2= 7% pour le LT coupe YXl/42, avec la propagation d'onde selon l'axe X, ou 42 RY-X LT (notation utilisée dans ce travail) (*Réf. 2, Chap. 4*). Dans le cas d'un filtre, cette caractéristique permet d'élargir la bande passante et d'assurer de faibles pertes d'insertion. Cependant, ces dispositifs présentent une importante sensibilité à la température, définie par le Coefficient de Température de la Fréquence (CTF=-40 ppm/°C pour le 42 RY-X LT) (*Réf. 29, Chap. 4*). Cette sensibilité affecte le centrage de la bande passante et peut donc introduire une incertitude dans l'utilisation des filtres. Ainsi, une des principales problématiques reste de trouver un moyen de minimiser la valeur du CTF. Plusieurs approches ont été étudiées, parmi les plus explorés se trouve la compensation en température par la liaison de deux matériaux ayant des CTF de signes opposés. Par exemple, une couche de SiO_2 (avec un CTF positif), est déposée sur un substrat de $LiTaO_3$ ou $LiNbO_3$ (CTF négatif). Le CTF diminue à mesure que la couche de SiO_2 augmente (*Réf. 104 et 105, Chap. 1*). Cependant, le facteur de couplage diminue et les pertes d'insertion augmentent. Ceci est dû aux parties convexes à la surface de SiO_2 déposé sur les électrodes (*Réf. 108, Chap. 1*). Une autre méthode consiste en l'utilisation d'une couche avec direction de polarisation inversée à la surface du substrat utilisé pour les dispositifs à ondes élastiques de surface (*Réf. 123 et 124, Chap. 1*). La frontière des domaines ferroélectriques agit comme un court-circuit, ce qui fait diminuer la valeur du CTF mais aussi le K^2. Le principal problème avec cette technique est la difficulté de contrôler précisément l'épaisseur de la couche de polarisation inversée, ce qui n'est pas pratique pour une production à l'échelle industrielle. Par conséquent, il est nécessaire d'explorer des méthodes alternatives permettant la réduction du CTF sans dégrader d'autres propriétés.

D'autre part, l'effet de la concentration de Li_2O sur les propriétés élastiques de LT et LN a été publié dans plusieurs travaux (*Réf. 3 et 4, Chap. 4*). En effet, la vitesse de propagation d'une onde de surface augmente avec la teneur en Li_2O dans les monocristaux de LT coupe Y, à raison de 15.4 m/s/mol%. D'autre part, le CTF dépend principalement des constantes élastiques et de la dilatation thermique du matériau (*cf. Eq. 1.55, page 25*). Il a été démontré que la dilatation thermique selon l'axe X ne change pas avec la concentration de Li_2O dans les monocristaux de LT et LN (*Réf. 126, Chap. 1*). En conséquence, un changement dans les constantes élastiques pourrait modifier le coefficient CTF.

Une méthode qui permet de modifier la teneur en Li_2O est le traitement d'équilibration par transport en phase vapeur ou d'après son acronyme en anglais *Vapor transport equilibration* (VTE) (*Réf. 11, Chap. 2*). Il consiste en un traitement à haute température où il y a un échange d'ions de Li entre les cristaux et les poudres d'équilibration, par diffusion en état solide. Le traitement VTE va nous permettre de modifier les propriétés de LT et LN qu'on trouve dans le commerce, avec une composition dite congruente (CLT=48.5 mol % en Li_2O et CLN=43,38 mol% en Li_2O (*Réf. 18 et 21, Chap. 1*). Ainsi, en ajoutant ou en enlèvent du Li_2O, la composition des monocristaux s'approche ou s'éloigne de la composition dite stœchiométrique (50 mol% de Li_2O). La non-stœchiométrie en Li affecte fortement les propriétés physiques et structurales des matériaux LT et LN. Par exemple, les paramètres de maille (*a* et *c*) diminuent avec la teneur en Li_2O et la température de Curie (T_c) augmente linéairement avec la concentration de Li (*voir Tableau 1.1, page 13*). D'autre part, le champ coercitif diminue de deux ordres de grandeur quand la concentration de Li_2O augmente de congruente à stœchiométrique (48,5 à 50 mol%).

Des études récentes ont mis en évidence la possibilité de réduire la valeur du CTF des lignes à retard à base de monocristaux de LT coupe 36 RY. La composition de ces cristaux a été modifiée grâce à la méthode VTE. Le CTF a été réduit de -37,2 ppm/°C à -7,1 ppm/°C dans le cas d'un monocristal de LT coupe 36 RY avec une composition intermédiaire entre congruente et stœchiométrique (49,43 mol%) (*Réf. 126, Chap. 1*). Cependant, lors du traitement VTE, le LT est recuit à une température supérieure à la T_c. Durant le refroidissement, le cristal repasse en dessous de la T_c et devient alors multi-domaine, ce qui peut affecter les caractéristiques de propagation des ondes et peut être à l'origine de la diminution du coefficient de couplage et du CTF. Donc, il est d'abord nécessaire d'avoir une structure mono-domaine (avec une polarisation uniforme) afin de découpler l'effet de la non-stœchiométrie de Li et les domaines ferroélectriques sur les propriétés des dispositifs à ondes élastiques.

L'objectif de cette thèse est d'étudier l'effet de la non-stœchiométrie en Li et l'effet des domaines ferroélectriques sur les propriétés des dispositifs à O.E.S à base de LT et LN. Dans le cas des dispositifs à base des monocristaux de LT coupe YXl/42 (42 RY-LT), on espère une amélioration du CTF sans dégradation d'autres propriétés (coefficient de couplage électromécanique et pertes d'insertion). D'autre part, on cherche à améliorer la stabilité de dispositifs utilisés à haute densité de puissance dans le cas des monocristaux de 128 RY-X LN. À cet effet, nous allons diviser ce projet en trois tâches principales :

1) Modification de la concentration de Li_2O dans les monocristaux de LT et LN en utilisant la méthode VTE : optimisation du procédé VTE ainsi que le transfert technologique du traitement VTE vers wafers de 4 pouces.
2) Développement de la technique d'inversion de domaines ferroélectriques pour différents cristaux de LT (42 RY-LT et coupe Z) traités par VTE, possédant différentes compositions : congruentes (48,5%mol Li_2O), sous congruentes (<48,5%mol Li_2O) et proche de stœchiométrique (49,8-50%mol Li_2O).
3) Fabrication et caractérisation de dispositifs à ondes élastiques de volume (O.E.V) et de surface sur des monocristaux de LT et LN avec différentes concentrations de Li_2O, traités par VTE, afin d'évaluer les effets du changement de la concentration en Li dans les cristaux sur les propriétés des dispositifs.

Ce projet a été mené dans le cadre d'une Conventions Industrielle de Formation par la Recherche (CIFRE) entre la société TDK, l'Institut FEMTO-ST et l'association Nationale de Recherche Technologique (ANRT).

II. Modification contrôlée de la concentration de Li dans les monocristaux de $LiTaO_3$ et $LiNbO_3$

D'après le diagramme de phase des systèmes Li_2O-Ta_2O_5 et Li_2O-Nb_2O_5, les niobate et tantalate de lithium monophasés $Li_{1-x}Nb(Ta)_{1+x}O_{3+2x}$ peuvent exister dans une grande gamme de compositions entre 46,5 et 50 mol% de Li_2O (*cf. Fig. 1.5, page 7*). Bien que la plupart de monocristaux de LT et LN aient une composition congruente (CLT et CLN), des cristaux avec une composition stœchiométrique (SLT et SLN) sont produits parce qu'ils possèdent moins de défauts intrinsèques (lacunes de Li et anti-sites de Nb) comparés aux cristaux congruents. SLT et SLN montrent plusieurs avantages par rapport au CLT et CLN, comme des pertes réfractives moins importantes (*Réf. 59-61, Chap. 1*) et un champ coercitif plus petit, ce qui facilite le processus d'inversion de domaines ferroélectriques (*Réf. 34-35, Chap. 1*).

Les différentes méthodes pour l'obtention de cristaux stœchiométriques sont : Czochralski (CZ) (*Réf. 3-5, Chap. 2)*, Czochralski avec l'utilisation d'un double creuset (DCCZ) (*Réf. 6-8, Chap. 2*), croissance de monocristaux à partir d'un germe (TSSG) (*Réf. 10, 11 et 20, Chap. 2*) et équilibration par transport en phase vapeur (VTE) (*Réf. 14-17, Chap. 2*). Une comparaison de méthodes et leurs principaux avantages et les inconvénients sont résumés dans le *Tableau 2.1, page 53*. Les principaux problèmes des méthodes CZ et TSSG sont la fissuration et le mâclage dû aux gradients thermiques présents dans le système utilisé pour la croissance des cristaux. La méthode de DCCZ produit des monocristaux de bonne qualité mais elle nécessite de faire un rigoureux contrôle des paramètres pendant la croissance des cristaux. La méthode VTE peut fournir des cristaux avec une composition plus proche de stœchiométrique compare aux deux autres méthodes. En plus, il est possible de produire des cristaux homogènes, sans fissures et sans mâcles. Cependant, cette méthode est appropriée pour les wafers avec une épaisseur ≤ 3 mm, mais les wafers subissent une déformation importante pendant le traitement à haute température.

Dans ce travail, nous avons utilisé la méthode VTE car il est relativement facile de contrôler les paramètres pour produire des monocristaux de bonne qualité. En outre, la méthode VTE permet de produire des cristaux avec diffèrent stœchiométrie de façon simultanée.

Le VTE consiste à un traitement de recuit d'un cristal de LT ou LN de composition congruente (à une température au-dessous de sa température de fusion) à proximité des poudres d'équilibration d'une composition diffèrent à celle des cristaux. Le dispositif expérimental utilisé pour le traitement VTE est montré dans la *Fig. 2.5, page 59*. Nous avons utilisés des creusets en alumine avec différents diamètres, en fonction de la taille des échantillons.

Les poudres d'équilibration ont été synthétisées à partir de Li_2CO_3 et Ta_2O_5 ou Nb_2O_5, en différentes fractions molaires (X_{Li2O}) :

a) Poudre monophasé ($Li_{1-x}Nb(Ta)_{1+x}O_{3+2x}$), avec $46.5 \leq X_{Li2O} \leq 50$ mol%
b) Poudre enrichie en lithium, composé des phases [$LiNb(Ta)O_3 + Li_3Nb(Ta)O_4$], avec $75 > X_{Li2O} > 50$ mol %
c) Poudre appauvrie en lithium, composé des phases [$Li_{0.93}Nb(Ta)_{1.07}O_{3.14} + LiNb(Ta)_3O_8$], avec $25 < X_{Li2O} < 46{,}5$ mol %

À haute température, il y a un transfert d'oxyde de lithium de la poudre vers le cristal par transport en phase vapeur et il y a une diffusion de Li^+, de laquelle résulte la modification de la composition ou stœchiométrie du cristal. La diffusion en état solide est menée par la différence de potentiel chimique entre le cristal et la poudre et c'est un processus qui finit lorsque l'équilibre entre le potentiel chimique de la poudre et le cristal est atteint *(Réf. 15-16, Chap. 2*). Les poudres enrichies en lithium constituent une source infinie d'oxyde de lithium, tandis que dans le cas des poudres appauvries en lithium, le Li^+ diffuse du cristal vers les poudres d'équilibration.

Dans le traitement VTE, les paramètres qui ont l'influence la plus importante sur la qualité et la composition des cristaux sont la durée, la température du traitement et la concentration en Li_2O des poudres d'équilibration. La durée de VTE dépend de l'épaisseur et de la coupe des cristaux, ainsi que de la composition des poudres. En général, les cristaux plus épais requièrent des traitements plus longs afin de les rendre homogènes. De plus, les traitements réalisés avec des poudres appauvries en lithium doivent être plus longs que ceux réalisés avec poudre enrichies en lithium. Dans le cas des cristaux de LN de 0.5 mm, traités à 1100°C, le temps nécessaire pour produire cristaux homogènes de composition sous-congruente (<48.38 mol% de Li_2O) et stœchiométrique (50 mol% de Li_2O) a été respectivement de 400 h et 60 h (*Réf. 16, Chap. 2*). De plus, il a été publié que la diffusivité de Li^+ est anisotrope, généralement, elle est plus rapide selon l'axe Z (*Réf. 28, Chap. 2*) et elle augmente avec la concentration de Li_2O dans les cristaux (*Réf. 31, Chap. 2*). Cependant, la plupart de ces résultats correspondent aux cristaux de LN. Bien que LT et LN soient deux matériaux similaires, les mêmes conditions de traitement ne peuvent pas être appliquées parce qu'ils n'ont pas exactement les mêmes propriétés. Par exemple, la température de fusion des cristaux de LN est 1240 °C tandis que celle du LT est 1650 °C (*Réf. 29, Chap. 4*). D'autre part, aucune investigation détaillé de l'homogénéité des cristaux de LT traités par VTE n'a été publiée. C'est pourquoi, dans le cadre de nos travaux, nous nous focalisons tout d'abord sur l'optimisation des paramètres du traitement VTE pour les cristaux de LT.

II.1 Optimisation des paramètres du traitement VTE des cristaux de LT.

Nous avons réalisé diffèrent séries d'expériences afin d'étudier l'influence de la température du traitement, la durée du traitement et la composition des poudres d'équilibration sur la concentration en Li_2O des cristaux et leur homogénéité. Pour ce faire, nous avons utilisé des cristaux de LT coupe X, Y et Z avec composition initial de 48.5 mol % en Li_2O et polies simple face (SAW grade). Nous avons utilisé des échantillons de 5 x 20 mm^2 et 500 µm d'épaisseur et les expériences suivantes ont été réalisées :

- Effet de la température et la concentration des poudres d'équilibration.
- Effet de la durée du traitement

Ensuite, nous avons utilisé les méthodes de diffraction de rayons X et spectroscopie Raman pour évaluer la concentration en Li_2O présente dans les poudres d'équilibration et dans les cristaux, respectivement. Pour la diffraction de rayons X nous avons utilisé un diffractomètre haute résolution Cu Kα1, λ=1.5418Å, afin d'identifier et de quantifier les phases secondaires (Li_3TaO_4 et $LiTa_3O_8$) présentes dans les poudres d'équilibration contenant deux phases. En ce qui concerne les cristaux, la concentration locale en Li_2O (avec une résolution latérale de 2 µm et une profondeur de champ de 7 µm) a été estimée à partir de partir de mesures par spectroscopie Raman. La caractérisation a été réalisée avec le spectromètre Jobin-Yvon/Horiba LabRam HR en mode micro-Raman, en configuration de polarisation croisée. Nous avons mesuré plusieurs points à la surface des cristaux et après une découpe–polissage, nous avons réalisé une cartographie sur la section transversale des cristaux, dans des intervalles de 1-5 µm, afin de vérifier l'homogénéité des échantillons (*cf. Fig. 2.8, page 62*). L'erreur dans les mesures effectuées a été de ±0.06 à ±0.15 mol % en Li_2O.

Etant donné que la pression partielle des vapeurs de Li_2O est un élément clé dans le traitement VTE, car il définit la concentration en lithium des cristaux traités et leur homogénéité, dans un premier temps, nous avons étudié la volatilisation et les pertes de Li_2O en fonction de la composition des poudres d'équilibration et la température de traitement. Les pertes de Li_2O dans les poudres d'équilibration ont été déterminées à partir de la mesure de leur concentration avant et après traitement VTE, réalisé à 1250 °C et 1300 °C pendant 24 h. Nous avons observé que les pertes de Li_2O sont plus importantes dans les poudres enrichies en lithium. De plus, la volatilisation de Li_2O est 9 fois plus importante à 1300 °C comparé à celle de 1250 °C dû au fait que les vapeurs de Li_2O se volatilisent plus rapidement avec l'incrément de la température (*cf. Fig. 2.14, page 68*). D'autre part, nous avons estimé l'effet de la durée d'utilisation des poudres et la température du traitement sur leur teneur en lithium. Nous avons trouvé que la teneur en Li_2O diminue linéairement avec la durée du traitement. La vitesse de pertes de Li_2O a été de 0.1716 mol%/h et 0.019 mol%/h pour les poudres utilisées à 1300 et 1250°C, respectivement (*cf. Fig. 2.15, page 68*). Ce qui indique que la perte de Li_2O est plus rapide à plus haute température. Par conséquent, les cristaux traités avec des poudres enrichies en Li à plus haute température peuvent avoir une concentration plus grande de Li_2O. Cependant, quand le changement en concentration de Li_2O est réalisé plus rapidement, il est plus difficile de contrôler précisément la composition des cristaux et leur homogénéité. Donc, nous avons préféré utiliser des températures plus bases que 1300 °C.

Une fois qu'il a été clarifié l'importance de la température et la concentration de Li_2O dans les poudres sur la concentration des vapeurs de Li_2O, nous allons montrer les résultats obtenus concernant l'optimisation des paramètres du VTE réalisé sur des cristaux de LT.

II.1.1 Effet de la température et composition des poudres d'équilibration sur la concentration des cristaux.

Les cristaux ont été traités avec des poudres d'équilibration avec 40, 50 and 60 mol% en Li_2O à différentes températures (1150°C, 1200 °C, 1250 °C and 1300 °C) pendant 10 h. Nous avons choisi cette durée parce qu'un gradient de concentration est espéré, donc cela nous permettra d'étudier l'effet de la température et la concentration de poudres sur la diffusion de ions de Li. Le récapitulatif des conditions utilisées pour ces séries d'expériences se trouve dans le *tableau 2.4, page 69*. Après les traitements VTE à différentes températures, nous avons évalué la concentration de Li_2O dans la section transversale et la surface des cristaux par spectroscopie Raman. Les profils de concentration des cristaux de LT, coupe X, Y and Z sont illustrés dans la *Fig. 2.16, page 71*. Ils montrent un gradient de concentration, le contenu maximum de Li_2O se trouve à la surface et il diminue à mesure que la profondeur du cristal augmente. Dans le cas des cristaux traités en utilisant des poudres avec 50 et 60 mol% de Li_2O, le gradient de concentration diminue avec l'augmentation de température du fait que la volatilisation et la diffusion de Li^+ augmentent avec la température, donc, la distribution de Li devient plus homogène. Par contre, les cristaux traités avec des poudres appauvries en lithium ont des gradients de concentration qui augmentent avec la température car à plus haute température, les cristaux peuvent perdre plus de Li_2O (*cf. Fig. 2.17, page 73*).

De plus, à une température donnée, les gradients de concentration diminuent avec la concentration de Li_2O dans les poudres. Les cristaux traités en utilisant des poudres avec 40 mol% de Li_2O ont montré le plus petit gradient de concentration. Leur concentration moyenne a été proche de celle de cristaux congruents (48,28-48,5 mol%) car la sortie de Li^+ des cristaux est un processus qui requièrt plus de temps, jusqu'à 400 h dans le cas des cristaux de LN (*Réf. 17, Chap. 2*).

Par ailleurs, la diffusion de Li+ est anisotrope, étant plus rapide dans le cas de la coupe Z du LT., ce qui est en accord avec les résultats publiés dans la littérature (*Réf. 28 et 31, Chap. 2*). La diffusivité de Li_2O pour la coupe Z des cristaux de LT est plus rapide que celle des coupes Y et X, étant $2.29x10^{-12}$ m^2/s, $1.67\ x10^{-12}$ m^2/s et $9.9x10^{-12}$ m^2/s pour les coupes X, Y et Z de LT, respectivement. De plus, le coefficient de diffusivité de Li^+, estimé expérimentalement, augmente exponentiellement avec la température et avec la concentration de Li_2O (*cf. Fig. 2.19, page 75*), ce qui est en accord avec les résultats publiés dans la littérature *(Réf. 28, 29 et 31, Chap. 2*).

À partir de ces résultats, nous pouvons déduire que la concentration de Li_2O dans les cristaux traités par VTE dépend principalement de la température et de la teneur en Li_2O dans les poudres d'équilibration. En outre, la diffusion de Li+ est plus rapide selon l'axe Z dans les cristaux de LT. La température que nous avons utilisée dans les traitements suivants a été 1250 °C car celle-ci permet l'obtention de cristaux plus homogènes, comparés à ceux obtenus à 1150 °C et 1200 °C. De plus, à 1250°C, la volatilité de la vapeur de Li_2O est moins importante comparée à celle obtenue à 1300°C, ce qui nous permettra de contrôler plus facilement la durée de traitement VTE nécessaire pour produire des cristaux avec une concentration souhaité.

II.1.2 Optimisation de la durée du traitement VTE pour la fabrication de cristaux homogènes.

Les cristaux ont été traités par VTE en utilisant une température de 1250 °C et des poudres d'équilibration avec 60 mol% en Li_2O. Le temps de traitement a varié de 5, 10, 24, 48 et 64 h. Les profils de concentration des cristaux de LT, coupe X, Y et Z sont illustrés dans la *Fig. 2.20, page 76*). Les cristaux traités pendant de courtes durés (5-10 h) ont une concentration en Li_2O stœchiométrique et elle diminue à mesure que la profondeur du cristal augmente. Les gradients de concentration que présente la coupe Z des cristaux de LT sont plus petits comparés à ceux des autres coupes, cela est dû au fait que la diffusion est plus rapide selon l'axe Z, comme il a été discuté précédemment. La différence de concentration entre la surface et le milieu des cristaux (ΔC_{Li2O}) diminue exponentiellement avec la durée du traitement car les ions de Li ont plus de temps pour se distribuer de façon homogène dans les cristaux (*cf. Fig. 2.21, Page 77*). Les résultats expérimentaux montrent que plus de 24 h de traitement à 1250 °C sont nécessaires pour produire des cristaux homogènes. D'après les résultats publiés par P.F. Bordui et al. (*Réf. 17, Chap. 2*) sur le VTE des cristaux de LN. Le traitement réalisé à 1100°C avec l'utilisation de poudres riches en Li, requièrt entre 100 et 200 h, tandis que 300-400 h sont nécessaires pour les cristaux traités à 1050°C.

En ce qui concerne la relation entre la concentration de Li_2O dans les poudres d'équilibration et la concentration de Li_2O dans les cristaux, nous avons trouvé une relation non linéaire. Le contenu de Li_2O dans les cristaux augmente exponentiellement avec l'incrément de la quantité de Li_2O dans les poudres d'équilibration (*cf. Fig. 2.23, Page 78*).

Finalement, nous avons observé la surface et la section transversale des cristaux traités par VTE. Nous avons trouvé des mâcles dans certains cristaux traités avec poudres de X_{Li2O}= 60 mol% pendant de courtes durées, en raison des gradients de concentration de Li_2O. Cependant nous avons également trouvé des mâcles dans les cristaux homogènes, traités pendant 48 et 64 h. Donc, il s'avère que le gradient de concentration n'est pas le seul responsable de la présence de mâcles dans les cristaux. Il est connu que le refroidissement rapide produit des mâcles dans les cristaux de LT et LN (*Réf. 8 et 22, Chap. 2*). Dans le cas du four utilisé pour l'optimisation des paramètres, le refroidissement naturel était trop rapide (il faut 20 h pour descendre de 1250°C à la température ambiante, vitesse approximative de 60 °C/h), ce qui aurait pu produire les mâcles. Donc, nous espérions avoir des cristaux de meilleure qualité en réduisant la vitesse de refroidissement. Pour cette raison, nous avons utilisé un autre four (ROHDE) qui permet de réduire la vitesse de refroidissement dans les traitements VTE ultérieures.

Les cristaux de LT coupe YXl/42 de composition initiale congruente (nommés 42 RY-CLT ci-après) de 250 µm d'épaisseur ont été traités dans le four qui permet une vitesse de refroidissement plus longue (~27 °C/h). Après le traitement VTE à 1250 °C pendant 48 h, les cristaux ont présenté une distribution homogène de Li_2O à la surface et dans leur section transversale (*cf. Fig. 2.27, page 81*). Les cristaux 42 RY-CLT de 350 µm d'épaisseur, traités avec les poudres d'équilibration pauvres en Li (40 mol%) ont montré un petit gradient de concentration à la surface. Cependant les cristaux de même épaisseur traités avec poudres d'équilibration riches en lithium ont montré une distribution de Li_2O homogène.

Nous avons mesuré la rugosité des cristaux par microscopie de force atomique (AFM). Nous avons observé que les cristaux de 42 RY-LT traités par VTE ou simplement recuits, sans

l'utilisation des poudres, ont une rugosité plus importante que celle d'un wafer non traité. Mais, après la réalisation d'un polissage pendant 1 heure et demie et nous avons réussi à réduire la rugosité jusqu'à l'obtention de valeurs de rugosité similaires à celle des cristaux de référence (*voir Tableau 2.10, page 84*). Finalement, nous avons observé la section transversale de cristaux traités à 1250 °C pendant 48 h. Les cristaux sont homogènes et ils ne présentent pas de mâcles.

II.2 Traitement VTE des cristaux de LN.

Dans ce travail, nous sommes intéressés à l'obtention des cristaux 128 RY-CLN sous-congruents avec ~47.5 mol % en Li_2O, afin de réduire leur champ coercitif de 50% (E_c~31.5 kV/mm) et ainsi évaluer la stabilité des dispositifs à ondes élastiques réalisées à partir de ces substrats. A cette fin, nous avons traité plusieurs échantillons et wafers de 4 pouces, par VTE en utilisant les poudres d'équilibration appauvries en Li (X_{Li2O}=25 et 40 mol%). Les cristaux de LN ont été traités à 1050 °C et plusieurs durées de traitement ont été investiguées : 5, 10, 25, 99 et 400 h. Ensuite, la concentration de Li_2O dans les cristaux a été estimée dans la section transversale en utilisant la spectroscopie Raman, où nous avons réalisé une cartographie dans des intervalles de 5 µm, afin de vérifier l'homogénéité des échantillons. Les profils de concentration sont montrés dans la *Fig. 2.32, page 86*, on peut y observer qu'il y a un petit gradient de concentration dans tous les cristaux à la surface. De plus, le gradient de concentration augment avec la durée de traitement car en augmentant le temps, la majeure partie du Li+ est diffusée de la surface du cristal vers les poudres d'équilibration. D'autre part, les concentrations moyennes dans les cristaux traités entre 5 et 99 h sont proches de celles du cristal congruent (47.99-48.34) et après 400 h de traitement avec des poudres de X_{Li2O}=40 mol %, nous avons obtenu des cristaux avec une concentration à la surface de 47.65 mol%. Ceci indique qu'il faut plus de 400 h pour obtenir des cristaux avec la composition visée.

Nous avons optimisé le traitement VTE pour les échantillons de LT de petite taille (20x30 ou 50x50 mm^2). Cependant, afin de fabriquer les dispositifs à O.E.S dans les lignes industrielles, en utilisant de procédures standardisées, il est important d'avoir des wafers de 4 pouces traités par VTE. Mais, les premières expériences réalisées sur wafers de 4 pouces de LT ont montré que les cristaux recuits présentent une importante courbure. Donc, afin de réduire cette déformation, nous avons réalisé plusieurs expériences, détaillées dans ce qui suit.

II.3 Transfert technologique du procédé VTE

Dans le traitement VTE nous utilisons un creuset intérieur de support. Les wafers ont été positionnés avec la face initialement polie (Z^+) vers le haut ou la face rugueuse (Z^-) vers le haut (*voir Fig. 2.35, page 87*). D'abord nous avons placé des wafers de 4 pouces sur des creusets de différents diamètres (de 15 à 60 mm) afin d'évaluer l'effet du diamètre du creuset, la taille et la polarité des cristaux sur la courbure des wafers. Les cristaux ont été recuits à 1250 °C pendant 10 h et après ils ont été mesurés en utilisant différents méthodes :

1) *Mesure d'épaisseur*.- un palpeur HEIDENHAIN a été utilisé pour mesurer l'épaisseur des wafers sur différents points.

2) *Interférométrie laser*.- la planéité de la surface des wafers a été mesurée avec un interféromètre laser. La surface des wafers est scannée et le profil de la surface indique le rayon de courbure.
3) *Mesure de rayon de courbure*.- Dans cette méthode nous avons utilisé un appareil (FSM) qui permet de scanner la surface des wafers et calculé leur rayon de courbure, lequel est lié à la valeur de la flèche (Δh_3).

Le *Tableau 2.12, page 88* montre les valeurs de Δh_3 trouvés pour chaque configuration. Le signe négatif de Δh_3 indique que la forme du wafer est concave tandis que le signe positif indique une forme convexe. Les valeurs plus petites de Δh_3 (22- 25 µm) ont été trouvées lorsque les cristaux ont été posés sur un creuset de 15 mm de diamètre. Cette valeur est inférieur à la valeur de flèche requise pour travailler avec les wafers de 4 pouces dans les lignes industrielles est de ±40 µm. Cependant, pour le traitement VTE il faut une durée d'au moins 24 h, donc nous avons investigué l'effet de la durée de recuit sur la courbure des wafers.

Nous avons observé qu'après 10 h de recuit à 1250°C, les wafers positionnés avec la face Z^+ vers le haut deviennent concaves et ceux positionnés avec la face Z^- vers le haut, deviennent convexes. De plus, la courbure des wafers augmente fortement avec la durée de recuit. En effet, après 48 h de recuit à 1250 °C, la courbure des wafers est autour de 1100 µm, une telle valeur n'est pas acceptable pour l'utilisation des wafers dans les lignes industrielles. Ensuite, nous avons utilisé deux creusets de support pour positionner les wafers, mais les valeurs de Δh_3 pour les wafers de 42 RY-CLT de 250 µm d'épaisseur restaient grandes (1000 µm).

L'effet de la température de recuit sur la courbure des wafers a été déterminé également. Les valeurs de Δh_3 augmentent drastiquement avec la température de traitement de 1200 à 1300 °C (*cf. Fig. 2.37 a et c, page 90)*. De plus, dans le cas des wafers positionnés avec la face Z+ vers le haut, ils ont présenté une forme concave après recuit à 1200 °C et 1250 °C. Tandis que les wafers recuits à 1275 et 1300 °C ont eu une forme convexe. Ce changement de signe fait supposer qu'à partir d'une certaine température, les cristaux changent de comportement. Donc, dans les expériences suivantes, nous avons utilisé un recuit en deux étapes, la première consiste en un recuit à 1250 °C durant un temps déterminé (t1), suivi d'un recuit à 1300 °C pendant 10 h. De plus, cette fois, nous avons utilisé des wafers plus épais (350 µm) car ils ont montré une courbure moins important comparé à celle des wafers de 250 µm.

Les wafers avec une épaisseur de 350 µm, recuits à 1250 °C pendant 24 h, puis ayant subi une deuxième étape à 1300 °C pendant 10 h ont montré une valeur acceptable de Δh_3 (12 µm). Par conséquent, nous avons utilisé ces conditions pour faire des traitements VTE sur des wafers 42 RY-CLT, en utilisant des poudres d'équilibration avec 40 et 60 mol% de Li_2O. Bien que des faibles valeurs de Δh_3 aient été espérées, nous avons obtenu des wafers très déformés, probablement à cause de l'interaction entre les wafers et les poudres d'équilibration. Plus d'expériences peuvent être envisagées afin de réduire la courbure des wafers, par exemple, en changeant la position des wafers lors du traitement, en passant de la position horizontale à la verticale, ou en utilisant des wafers plus épais (de 0.5 ou 1 mm). Cependant, dû au temps milité du projet, il n'a pas été possible de le réaliser. En conséquence, nous avons utilisé des échantillons d'un quart de wafer de 4 pouces pour le traitement VTE et pour la fabrication de dispositifs à ondes élastiques.

En outre, nous avons traité des wafers de 4 pouces de 128 RY-CLN et 350 µm d'épaisseur, avec des poudres d'équilibration avec 25 et 40 mol% de Li_2O. Ces wafers ont été

traités durant 5-400 h à 1050 °C. La valeur de Δh_3 obtenue après 5 h de traitement a été similaire à celle de l'échantillon de référence (23 µm) et après 400 h de traitement le Δh_3 a été de 59 µm, une valeur légèrement au-dessus de celle de la référence, mais qui peut tout de même être utilisée pour la fabrication de dispositifs à O.E.S sur les lignes industrielles, ainsi que leur caractérisation.

En conclusion, dans cette partie, nous avons trouvé les meilleures conditions de durée et température pour le traitement VTE sur les cristaux de LT, qui permettent l'obtention de cristaux homogènes, lesquels vont être utilisés pour l'étude de l'effet de Li non-stœchiométrie sur les propriétés des dispositifs acoustiques. Cependant, lors du traitement VTE, le $LiTaO_3$ est recuit à une température supérieure à la T_c et perd sa polarisation initiale, il devient alors multi-domaine. Donc, il est d'abord nécessaire de lui rendre sa nature mono-domaine (avec une polarisation uniforme), la méthode employée à cette fin sera expliquée dans la section suivante.

III. Inversion de domaines dans les cristaux de $LiTaO_3$

Nous avons utilisé la technique d'inversion de domaines ferroélectriques par application d'un champ électrique afin de produire des cristaux avec une polarisation uniforme. Nous nous sommes basés sur les travaux de thèse réalisés par E. Courjon et F. Bassignot (*Réf. 31 et 38, Chap. 3*) concernant l'inversion de domaines ferroélectriques de la coupe Z des cristaux de LN et LT afin d'adapter cette technique à des cristaux avec une orientation oblique (tournées 42 degrés de l'axe Y) et avec une état initial multi-domaine.

Dans cette technique, il est nécessaire d'appliquer un champ supérieur au champ coercitif (E_c) dans la direction opposée à la polarisation spontanée du cristal. La principale problématique que celle-ci présente est que l'on a besoin d'appliquer une très haute tension afin de générer champ électrique supérieur au champ coercitif (E_c ~21 kV/mm) et parfois cela induit des contraintes ou peut générer des claquages dans l'air, ce qui peut amener à la fissuration des cristaux pendant cette opération.

Le banc de polarisation utilisé pour l'inversion de domaines par champ électrique, ainsi que la cellule de polarisation sont illustrés dans les *Fig. 3.4 et 3.5, page 103 et 104, respectivement*. Le banc de polarisation consiste en un amplificateur de tension, connecté à un générateur de signal. La courbe d'impulsion est définie par un ordinateur. La *Fig. 3.7, page 106* montre les courbes d'impulsion utilisées dans ce travail. La tension est appliquée selon la courbe d'impulsion, à travers l'épaisseur des cristaux. Le voltage appliqué, et le courant produit ont été monitorés par un oscilloscope LeCroy Waverunner 610Zi, connecté à l'amplificateur. Ces deux signaux nous renseignent à propos de la dynamique de l'inversion de domaines. L'amplificateur travaille en régime saturé, donc le courant maximal que le système peut atteindre est 22.5 mA. Pendant l'inversion de domaines, il y a un transfert de charges afin de compenser l'inversion, laquelle génère un courant. Lorsque l'inversion de domaines se produit, un pic de courant monte jusqu'à la valeur de courant saturé et après il descend à zéro, lors de la finalisation de l'inversion de domaines. Un exemple de courbe de courant et tension observée lors de l'inversion de domaines des cristaux congruents de 42 RY-CLT, de 250 µm d'épaisseur, est montré dans la *Fig. 3.6, page 104*.

Les charges, Q, générées pendant l'inversion des domaines sont quantifiées par l'intégration de l'aire sous la courbe de courant, I_{pol}, en fonction du temps, t :

$$Q = \int I_{pol} dt = 2P_s A, \qquad \textit{Eq. 1}$$

où P_s et A sont la polarisation spontanée et l'aire de la région inversée, respectivement.

Afin d'assurer l'inversion complète des domaines, plusieurs impulsions, à la même tension ou légèrement plus haute, ont été appliquées. Finalement, la quantité de charges obtenue expérimentalement (par intégration de t et I_{pol}) est comparée à celle estimée théoriquement à partir de la valeur de P_s et de l'aire de la région inversée. Lorsque les valeurs de Q théoriques et expérimentales ont été similaires, nous avons considéré que l'inversion des domaines dans les cristaux était complète.

III.1 Inversion de domaines ferroélectriques sur la coupe Z de $LiTaO_3$

Tout d'abord, afin d'optimiser la méthode d'inversion de domaines sur les cristaux traités par VTE, nous avons réalisé l'inversion de domaines sur la coupe Z des cristaux commerciaux de LT, de composition congruente (Z-CLT) et stœchiométrique (Z-SLT), provenant de différents fournisseurs. La concentration de Li_2O dans les cristaux, la qualité de polissage, les méthodes de fabrication, leur état des domaines initial et les fournisseurs sont indiqués dans le *Tableau 3.3, page 112*. Les cristaux commerciaux sont initialement mono-domaines. Donc, la comparaison des paramètres utilisés pour l'inversion de domaines du LT congruents et stœchiométriques initialement mono-domaines a été faite pour évaluer l'effet de la stœchiométrie et les défauts intrinsèques relatifs aux méthodes de fabrication des cristaux stœchiométriques. Après, nous avons adapté cette méthode à l'inversion de domaines d'échantillons traités par VTE, et donc, initialement multi-domaines.

Afin de faciliter l'évaluation de l'effectivité de la méthode d'inversion de domaines utilisés, nous avons réalisé des structures périodiquement polarisées. Pour ce faire nous avons fabriqué une structure périodique isolante, défini par lithographie optique, permettant l'isolation électrique sur l'une des faces des wafers (Z^+). Nous avons utilisé une résine positive Shipley 1828 avec une épaisseur de 3.2 µm pour la définition de réseaux alternés de 600 µm de période.

Le champ coercitif des cristaux congruents (Z-CLT) est ~21 kV/mm, donc la tension maximale que l'on doit appliquer afin d'inverser les domaines de cristaux de 500 µm d'épaisseur est 10.5 kV. Nous avons appliqué plusieurs impulsions électriques avec une augmentation graduelle de 7.2 kV à 10.32 kV, à cette dernière tension nous avons observé un pic de courant qui indique l'inversion de domaine. A cette tension correspond un E_c=20.6 kV/mm, une valeur proche de celle reportée dans la littérature (*Réf. 7 et 8, Chap. 3*). Cependant, la quantité de charges expérimentalement obtenue était deux fois plus petite que celle estimée théoriquement. Ensuite, nous avons continué à appliquer un champ E_{fmax}=20.72 µm, plusieurs fois, jusqu'à la disparition du pic de courant. Après, nous avons inversé la direction du champ électrique et nous avons observé une inversion de domaines complète à un E_c=16.6 kV/mm avec l'application d'une seule impulsion.

Afin d'observer la structure de domaines de la surface périodiquement polarisée de l'échantillon, nous avons fait un polissage pendant 1 heure. L'image de la structure périodique obtenue est montrée dans la *Fig. 3.15, page 113*. On peut y observer les régions avec différentes polarisations (Z+ et Z-), révélées par polissage. Cela est possible grâce à la différence de dureté des domaines selon l'orientation de leur polarisation.

Dans le cas des échantillons stœchiométriques (50 mol% de Li_2O) et proche de stœchiométrique (49.95 mol% de Li_2O), nous avons utilisé l'application d'une tension de deux ordres de grandeur plus petite que celle des cristaux congruents. Ainsi nous avons trouvé des champs coercitifs très petits pour ces échantillons, entre 0.2 et 1 kV/mm. Dans le cas des échantillons initialement mono-domaines, nous avons appliqué seulement deux impulsions afin d'avoir une inversion complète des domaines. Les courbes de tension et de courant en fonction du temps pour tous les échantillons stœchiométriques sont présentées dans la *Fig. 3.16, page 114*. On peut y observer des pics de courant similaires à ceux reportés dans la littérature (*Réf. 26 et 47, Chap. 3*).

L'inversion de domaines des échantillons stœchiométriques est considérablement plus longue que celle des échantillons congruents. Par exemple, le temps d'inversion (t_{pol}) est de 2 ms pour les cristaux congruents tandis que pour l'inversion de domaines des cristaux stœchiométriques le t_{pol} est entre 14 et 386 ms, en fonction de l'échantillon. Dans le cas des échantillons stœchiométriques obtenus par VTE (échantillon Z-SLT_VTEN59), le courant a présenté une forme de pics, également. Cependant elle n'apparut qu'après 300 ms, ce qui n'a pas été observé pour les cristaux initialement mono-domaines. Dans tous les cas, la quantité totale de charges générées pendant l'inversion de domaines a été plus grande que celles estimée, ce qui indique que les domaines ferroélectriques ont été complètement inversés. Après, nous avons observé la section transversale des échantillons dans la région polarisée. Nous avons constaté la présence des structures périodiques, révélées par gravure humide avec HF concentré (48 % pendant 1 heure), ce qui confirme que l'inversion de domaines a été complète.

III.2 Inversion de domaines sur des cristaux de LT coupe Y roté de 42 degrés (42 RY-LT)

Dans le cas des cristaux 42 RY-LT (θ_R = 42°), l'axe ferroélectrique est tourné d'un angle $\theta z=90-\theta_R$ par rapport à la normale à la surface. Donc, le champ coercitif ($E_{c,R}$), la polarisation spontanée (P_s) et la période des structures périodiques (Λ_{surf}) sont affectés par la rotation de l'axe ferroélectrique. Ainsi, le $E_{c,R}$ est divisé par $Cos\theta_R$ comparé au E_c des cristaux de LT coupe Z ($E_{c,R}$~28.46 kV/mm et E_c=21 KV/mm, respectivement) et le $P_{s,R}$=44.59 μC/cm².

Nous avons utilisé des cristaux de 42 RY-LT qualité SAW, dopés et non dopés Fe, avec une épaisseur de 250 μm et 350 μm, car ils sont les wafers utilisés dans l'industrie pour la fabrication de dispositifs à O.E.S. Nous avons réalisé l'inversion de domaines de cristaux de 42 RY- LT avec différentes compositions : congruente (48.5%mol Li_2O), sous congruente (<48.5%mol Li_2O) et proche de la stœchiométrique (49.8-50%mol Li_2O). Le Tableau 3.5 indique les caractéristiques des cristaux utilisés, leur concentration, leur état initial de domaines, et les conditions utilisées pour leur préparation par le traitement VTE.

Etant donné que l'inversion de domaines des cristaux congruents de 42 RY-LT requièrt un champ électrique plus élevé comparé à celui des cristaux de LT coupe Z, il a été plus compliqué d'achever le processus avec succès, en raison des claquages diélectriques produits lors de l'application d'une tension très haute. En outre, nous avons testé l'inversion de domaines sur des cristaux polis simple face et double face, afin d'observer les différences entre les deux. Cependant, nous avons trouvé des valeurs de E_c très similaires. Par conséquent, que la qualité de polissage n'affecte pas le processus d'inversion de domaines.

Afin de valider complètement la technique d'inversion de domaines sur les cristaux 42 RY-LT de composition congruente, nous avons préparé des structures isolées périodiquement. De cette manière, les zones inversées peuvent être identifiées plus facilement. L'inversion complète de la polarisation des cristaux 42 RY-LT non dopés Fe a été achevée avec l'application de deux impulsions à $E_{f,\ max}$=32.9 kV/mm et les charges produites expérimentalement ont été proches de celles estimées. Ensuite, nous avons fait un polissage pendant 30 minutes sur la surface de l'échantillon afin de visualiser le réseau périodique de domaines. Nous avons observé une structure périodique bien définie, ce qui valide la technique utilisée pour inverser la polarisation de domaines ferroélectriques (*cf. Fig. 3.20, page 119*).

Dans le cas des cristaux de composition sous-congruente, nous avons utilisé la même technique pour l'inversion de domaines. La difficulté dans ce cas a été la nécessité d'appliquer une tension considérablement plus haute, ce qui a souvent produit des claquages diélectriques et en conséquence nous n'avons pas réussi l'inversion de domaines de ce type d'échantillons dans la plupart des cas. Malgré les difficultés, après la réalisation d'un grand nombre d'expériences, nous avons réussi à inverser la polarisation de cristaux avec une composition très proche de congruent (48.4 mol% en Li_2O) et un échantillon sous congruent (47.32 mol% en Li_2O), voir *Tableau 3.7 page 121*.

Le champ électrique utilisé pour l'inversion de domaines des cristaux 42 RY-LT non dopés Fe, avec une composition congruente et sous congruente, ainsi que les charges générées sont montrés dans le Tableau 3.6. L'inversion de la polarisation uniforme de tous ces cristaux a été achevée par l'application de champs électriques plus grands que le champ coercitif espéré. Les quantités totales de courant généré sont proches de celle estimées théoriquement. De plus, afin d'inverser la polarisation des domaines ferroélectriques, l'application de plusieurs impulsions (2 ou 3) à très haute tension a été nécessaire, ainsi que le changement de direction de la polarisation du champ électrique plusieurs fois.

Nous avons appliqué la même procédure pour l'inversion de domaines des cristaux 42 RY-LT dopés Fe (42 RY-LT :Fe). Cependant, nous avons trouvé une différence dans la dynamique d'inversion des domaines dans les cristaux dopés Fe, vis-à-vis de celle des cristaux non dopés. Ainsi, dans le cas des cristaux dopés Fe, initialement mono-domaines, on doit appliquer d'avantage d'impulsions électriques (>20 impulsions) afin d'obtenir l'inversion complète des domaines, puisque chaque cycle produit une petite quantité de charges. En plus, il a été nécessaire d'inverser la direction d'application du champ électrique plusieurs fois. En utilisant cette méthode, la quantité de charges augmente après chaque cycle, ce qui facilite l'inversion complète de domaines ferroélectriques (*cf. Fig. 3.24, page 125*). Dans le cas des cristaux non dopés Fe, ce changement de direction du champ électrique, dans plusieurs cycles, n'est pas nécessaire. La différence peut être due au fait que les cations de Fe introduisent des

centres de dépolarisation locale, empêchant la propagation des domaines (*Réf. 37, Chap. 3*), ce qui peut être éliminé par le changement de direction du champ électrique plusieurs fois.

Dans le cas des cristaux 42 RY-LT (non dopés Fe) de composition proche stœchiométrique et stœchiométrique (49.5-50 mol% en Li_2O), l'inversion de domaines a nécessité l'application d'un champ coercitif de deux ordres de magnitude inférieur à celui utilisé pour les cristaux de composition congruente, (E_f~0.57 kV/mm et E_f~32 kV/mm, pour les cristaux stœchiométriques et congruent, respectivement). Cependant, l'inversion de domaines dans le cas des cristaux 42 RY-LT dopé Fe s'est avérée plus compliquée. En effet, l'inversion de domaines dans ces échantillons s'est produite après l'application de plusieurs impulsions et le changement de direction du champ électrique (*Tableau 3.8, page 127*) et dans certains échantillons l'inversion complète de domaines n'a pas été possible.

Finalement, la présence de domaines ferroélectriques à la surface et dans la section transversale des cristaux a été révélée en utilisant les techniques de polissage et attaque chimique, avec HF concentré (48 mol%) pendant 1 heure. Les structures des domaines ont été observées par microscopie optique et microscopie électronique à balayage.

L'inversion de domaines s'est avérée une technique compliquée à maîtriser, d'autant plus que la cinétique de formation de domaines était différente pour les matériaux selon leur composition chimique. Finalement nous avons compris la façon dont l'inversion de domaines doit être effectuée, ainsi que le moyen de vérifier celle-ci. Dans les cas des échantillons de composition sous congruente, l'inversion de domaines à haute température est préférable, afin de réduire les risques de claquage. Bien que nous ayons préparé un dispositif expérimental pour réaliser l'inversion de domaines à haute température (≤210 °C), nous n'avons pas eu le temps d'optimiser ce procédé. Mais le procédé d'inversion de domaines à température ambiante nous a permis tout de même de produire des cristaux traités par VTE, avec une polarisation uniforme, lesquels ont été utilisés pour fabriquer des dispositifs à ondes élastiques de surface et de volume, abordés dans la section suivante.

IV. Effet de la non-stœchiométrie en Li et de la structure de domaines sur les propriétés acoustiques des dispositifs à ondes élastiques de volume et de surface à base de monocristaux de LT

IV.1 Résonateur à ondes élastiques de volume à base de $LiTaO_3$

La réponse fréquentielle des filtres SAW qui utilisent le mode de cisaillement de la coupe 42 RY-X LT dépend principalement des constantes élastiques C_{44} et C_{66} (*Tableau 4.2, page 138*). Rappelons-nous que dans ce travail nous sommes intéressés par l'effet de la concentration en Li_2O des monocristaux sur les propriétés élastiques et leur comportement avec la température, puisque le coefficient de CTF et les propriétés de propagation des ondes dépendent des constantes élastiques.

Nous avons estimé analytiquement la dépendance de la fréquence avec la variation des constantes élastiques de LT, coupe Z et coupe 42 RY-X, pour les trois modes : cisaillement lent, cisaillement rapide et extension-compression. Deux types de résonateurs à ondes de volume ont été étudiés : i) un résonateur fonctionnant en mode de cisaillement d'épaisseur

(TFE), ii) résonateurs à haut facteur de forme réalisés sur des monocristaux de LT, appelés « *ridges* » ci-après. Dans le cas de la coupe Z de LT, les résonateur configurés en TFE ont montré que la variation de la fréquence dépend principalement de la variation de C_{66} dans le mode de cisaillement lent tandis que le changement de la fréquence dépend plus de la variation de C_{44} dans le mode de cisaillement rapide. Dans le cas de la coupe 42 RY-LT configurée en TFE, le mode de cisaillement lent dépend de C_{14}, C_{44} et C_{66}. Les modes de cisaillement rapide et d' extension-compression, dépendent quant à eux de presque toutes les constantes élastiques, sauf la constante C_{66}. D'autre part, des simulations en 2D de résonateurs à ondes de volume avec différentes configurations (TFE, ridges et un résonateur à excitation par champ latéral) ont été faites, afin d'exciter les modes dépendant de C_{44} et C_{66}. Les résultats des simulations ont montré que les résonateurs configurés en TFE, avec la coupe Z de LT, ainsi que les « ridges » permettent d'exciter les modes de cisaillement, avec un bon couplage (K^2=7% et 18%, respectivement). Les résonateurs à excitation par champ latéral permettent l'excitation des modes de cisaillement, également. Cependant, la réponse en fréquence des résonateurs de test s'est avérée perturbée par l'apparition de modes parasites qui pourraient compliquer les mesures lors de la caractérisation des dispositifs. De plus, le K^2 est resté faible, de l'ordre de (0.01-0.06%). Alors, nous avons procédé à la fabrication des deux premiers types de résonateurs (TFE et ridges). La procédure utilisée pour la fabrication de chaque dispositif est résumée sur la *Fig. 4.3, page 144*.

Les résonateurs ont été caractérisés en mesurant l'admittance en fonction de la fréquence, avec un testeur sous pointes et un analyseur de réseaux. Les dispositifs expérimentaux utilisés pour la caractérisation des résonateurs configurés en TFE et ridges sont montrés dans les *Fig. 4.4 et 4.5*, respectivement (*pages 145-146*).

Nous avons mesuré l'admittance des résonateurs configurés en TFE dans une plage de fréquences de 12 à 36 MHz, ce qui correspond au mode fondamental et à la troisième harmonique, respectivement. Des modes parasites, proches de la fréquence de résonance dans le mode fondamental, ont été trouvés. Donc, l'estimation du facteur de couplage (K^2) s'est avérée compliqué à déterminer avec exactitude. Dans le cas de la troisième harmonique, le signal a été plus propre mais le K^2 estimé a été de 0.05%, tandis que la valeur estimée théoriquement était de 0.86%. Les différences signifiantes entre les résultats théoriques et expérimentaux peuvent être dues à plusieurs facteurs. Par exemple, le parallélisme des substrats et la taille des plaques par rapport à celle des électrodes. En effet, les défauts de parallélisme peuvent détériorer les propriétés de propagation (*Réf. 24, Chap. 4*) et la large taille de la plaque peut entraîner des réponses parasites dans une plage étroite de fréquences. Nous avons arrêté ce type de résonateurs car dans tous les essais nous avons trouvé des réponses très faiblement couplées et nous nous sommes focalisés sur l'étude de l'autre type de résonateur (ridges), lequel permet d'obtenir l'excitation des modes de cisaillement, avec un fort couplage, d'après les simulations.

Nous avons simulé et réalisé expérimentalement des résonateurs ridges avec plusieurs orientations, sur les substrats de LT, coupe Z et coupe 42 RY-LT :

i) Ridge parallèle à l'axe X, utilisant la coupe Z de LT comme substrat (ZY)
ii) Ridge perpendiculaire à l'axe X, utilisant la coupe Z de LT comme substrat (ZX)
iii) Ridge parallèle à l'axe X, utilisant la coupe Z de LT comme substrat (42 RYX)

D'après les mesures d'admittance, la réponse fréquentielle montre la présence de modes parasites et l'estimation du CTF et K^2 a été complexe pour la plupart des dispositifs. Une optimisation des paramètres des « ridges » a été effectuée expérimentalement, afin d'améliorer la qualité de la réponse fréquentielle. Cependant celle-ci dépend des conditions expérimentales pendant la fabrication des dispositifs, telles que la qualité de la surface, laquelle est liée à l'état de la lame utilisée pendant la découpe, le parallélisme, et l'homogénéité des électrodes. Néanmoins, une méthode de traitement des données permettant d'ajuster les données expérimentales aux sommes des fonctions d'oscillateur a été utilisée pour obtenir la valeur des fréquences de résonance et anti-résonance. A partir de ces données, l'évolution de la fréquence avec la température, et donc, le CTF ont été évalués pour chaque dispositif. Le K^2 a été estimé avec *l'Eq. 1.64, page 29*, à partir de la fréquence série (f_s) et de la fréquence parallèle (f_p), mesurées à partir du maximum de la conductance et la résistance, respectivement.

Une série de résonateurs avec différents stœchiométries en Li et uniformément polarisés a été préparée et caractérisée sur des substrats de 42 RY-LT. De plus, des substrats de la coupe Z du LT (Z-LT) avec composition congruent et stœchiométrique provenant de l'industrie ont été également étudiés.

Dans le cas des résonateurs ridges ZY et ZX, le CTF de la fréquence parallèle (CTF_p) a été négatif, tandis que le CTF de la fréquence série (CTF_s) des résonateurs ZY et ZX ont été négatif et positif, respectivement, ce qui est en accord avec les résultats obtenus par simulation (*voir Tableau 4.8, page 162*).

Plusieurs différences dans la performance des échantillons congruents et stœchiométriques ont été trouvées. Par exemple, dans les substrats Z-LT, avec les ridges parallèles à l'axe X (ridges ZY), l'échantillon stœchiométrique, avec 49.95 %mol Li_2O a montré un CTF=-18 ppm/°C, tandis que l'échantillon congruent (48.5%%mol Li_2O), avec les ridges orientés dans la même direction, a présenté un CTF de -34 ppm/°C. Cependant le CTF de l'échantillon stœchiométrique et proche de celui estimé théoriquement pour le matériau congruent.

Ces résultats ont montré que dans le cas des résonateurs ZY, le matériau stœchiométrique présente un CTF_s plus petit. Etant donné que cette configuration dépend principalement de la constante C_{44}, cela pourrait indiquer que la variation de constante C_{44} avec la température est plus petite dans le matériau stœchiométrique que dans le matériau congruent. Cependant, il est nécessaire de faire plus d'expériences pour confirmer ces résultats. Dans le cas des résonateurs ZX, le CTF_s des échantillons stœchiométriques et congruents sont similaires. D'autre part, le K^2 des échantillons stœchiométriques est légèrement plus grand que celui des échantillons de composition congruente. Cependant les valeurs de K^2 doivent être considérées avec réserve car la qualité du signal ne permet pas d'estimer avec suffisamment de précision le facteur de couplage.

En ce qui concerne les cristaux de la coupe 42 RY-LT, nous avons préparé des « ridges » perpendiculaires à l'axe X. Plusieurs cristaux traités par VTE, avec différents stœchiométries et uniformément polarisés (dans la plupart des cas) ont été utilisés pour leur fabrication. Afin de connaître l'effet de la structure de domaines sur les propriétés des dispositifs, nous avons caractérisé une région multi-domaine et une région avec une polarisation uniforme. Les

résultats expérimentaux et ceux obtenus par simulation sont montrés dans le *Tableau 4.9, page 165*. Dans cette configuration, nous avons trouvé que la f_s augmente avec la température, ce qui donne des valeurs positives de CTF_s. Par contre, la f_p diminue avec la température, donnant un CTF_p négatif. Les wafers de 42 RYX-LT non traités, de composition congruente ont un CTF_s =18 ppm/°C et un CTF_p=-36 ppm/°C, ce qui est en accord avec les résultats prédits par simulation.

La *Fig. 4.27, page 166*, montre la réponse fréquentielle des résonateurs fabriqués sur des substrats de 42 RY-LT mono-domaines et multi-domaines, avec différentes concentrations en Li_2O. En comparant l'échantillon de composition congruente, mono et multi-domaine, on constate une forte réduction dans l'amplitude du signal, ce qui indique que la structure multi-domaine a fait diminuer le facteur de couplage électromécanique (*cf. Fig. 4.27 a*). D'autre part, dans les cas des résonateurs à base des cristaux 42 RY-LT proches de la composition stœchiométrique, on a observé que parfois, la réponse fréquentielle obtenue dans les régions mono et multi-domaine ont été très similaires. Cela a été le cas pour les échantillons VTEN 74 et VTEN 56. Ces échantillons stœchiométriques ont montré un CTF_s plus proche de que celui du matériau congruent : 6.14 et 6.13 ppm/°C. Cependant nous avons un doute sur la complète inversion des domaines de ces échantillons.

En outre, nous avons constaté une réduction dans l'amplitude du signal des échantillons stœchiométriques en comparaison avec les échantillons congruents, mais à ce stade, il a été difficile d'identifier son origine. Lors de la caractérisation de résonateurs « ridges » fabriqués sur un même substrat (non traité), nous avons trouvé des réponses fréquentielles et des amplitudes du signal différentes, ce qui est associé à la fabrication des résonateurs, dû à un défaut de parallélisme ou un mauvais contact électrique, par exemple. De plus, la perte du signal peut être due à la qualité de polarisation uniforme des échantillons. Les résultats obtenus par la caractérisation des « rigdes » n'ont pas été reproductibles et le signal a souvent présenté des modes parasites. Il a donc été difficile de faire l'analyse de données expérimentales (K^2 et CTF) avec une certitude suffisante. En conséquence, nous avons préféré étudier d'autres structures, résonateurs et filtres à ondes de surface (O.E.S), ce qui nous permettra l'estimation des CTF et le couplage de manière plus concluante.

IV.2 Dispositifs à ondes élastiques de surface à base $LiTaO_3$

Des cristaux de 42 RY-LT traités par VTE et uniformément polarisés ont été fournis à la société Frec'n'sys afin de réaliser et caractériser de résonateurs et des filtres à ondes élastiques de surface. Le filtre à éléments d'impédance est constitué de résonateurs simple-port arrangés en 4 cellules L en cascade (*cf. Fig. 4.29, page 167*). La fonction de transfert $|S_{12}|$ de différents filtres fabriqués sur un substrat de 42 RY-LT non traité (référence), obtenue par simulation et expérimentalement, sont montrés dans la *Fig. 4.31, page 169*. On peut observer un bon accord entre les résultats théoriques et expérimentaux. Cependant, il n'y a pas une correspondance parfaite entre la fréquence de résonance et antirésonance des branches en parallèle et en série, ce qui produit des ondulations dans la bande passante, dû à une surestimation du K^2 dans les simulations. D'autre part, les atténuations théorique et expérimentale sont différentes en raison du fait que le ratio de capacités électriques (C_1/C_0) expérimentales a été distinct de celui utilisé dans les simulations. En ce qui concerne le

coefficient de réflexion $|S_{11}|$, l'écart entre les réponses simulée et théorique est dû à la valeur de K^2, également.

Les filtres ont été fabriqués sur des substrats avec différentes concentrations en Li_2O et différent état des domaines : i) 42 RY-LT congruent et mono-domaine, utilisé comme référence, ii) 42 RY-LT congruent avec une région polarisée dans une direction opposé, puis retourné à leur état de polarisation original, iii) 42 RY-LT multi domaine (recuit à 750 °C pendant 48 h), iv) deux échantillons de composition stœchiométrique. Le traitement appliqué à chaque substrat et leur composition sont indiqués dans le *Tableau 4.11, page 170*. Les dispositifs ont été fabriqués dans les régions mono-domaine et multi-domaine afin d'investiguer l'effet des domaines sur leur réponses fréquentielles. Cependant, nous n'avons pas observé de changement important entre les deux régions, dû probablement au fait que la surface des échantillons était plutôt mono-domaine. En effet, cela est tout à fait possible car d'après les observations faites sur la section transversale des cristaux multi domaines, nous avons observé que les structures multi domaines forment des couches avec la même polarisation. De cette façon, cette couche présente des propriétés homogènes et l'onde se propage comme si elle était dans une région mono-domaine.

La fonction de transfert et le coefficient de réflexion des filtres basés sur des cristaux de composition congruente, mono-domaine et multi-domaine sont montrés dans la *Fig. 4.34, page 172*. L'échantillon de référence et l'échantillon re-polarisé ont montré des réponses fréquentielles très similaires. En revanche, la réponse de l'échantillon multi domaine a été très différente de celle de l'échantillon de référence. L'amplitude de la bande passante a été diminuée de 5.72% à 4.39%, les pertes d'insertion ont été dix fois plus importantes et la bande passante a présenté des ondulations. Il y a plusieurs aspects à considérer afin d'expliquer l'origine de la mauvaise réponse obtenue dans cette échantillon. Tout d'abord, cet échantillon n'a pas été uniformément polarisé, donc la présence d'une structure multi-domaine est probablement la responsable d'une telle réponse. De plus, la face arrière de cet échantillon a été polie, afin de visualiser les domaines après le processus d'inversion de domaines, ce qui peut être à l'origine des réflexions observés dans le signal.

Dans le cas des filtres fabriqués à base de cristaux de composition stœchiométrique et proche de stœchiométrique, les paramètres des filtres tels que la largeur de bande et les pertes d'insertion sont très similaires à ceux des échantillons de référence. La seule différence que nous avons trouvée a été le décalage de la fréquence centrale, f_c, par 2-4 MHz, par rapport à celle de l'échantillon de référence. Ce décalage peut être expliqué car l'épaisseur des électrodes a été 780 nm au lieu de 800 nm. Cependant, cela peut être dû à un effet de la concentration de Li_2O dans les cristaux. En effet, des études publiées ont montré que la vélocité des ondes de cisaillement , et donc, la fréquence, changent avec la teneur en Li dans les monocristaux de LT, de composition proche de congruent (*Réf. 3, Chap. 4*). D'autre part, la largeur de bande des filtres basés sur des cristaux stœchiométriques ont montré une légère augmentation comparée à celle des cristaux congruents (5.99% au lieu de 5.72%). Ce qui indique que le facteur de couplage électromécanique a augmenté avec la diminution de défauts intrinsèques dans le LT.

IV.2.1 Estimation du CTF et K^2 dans les dispositifs à ondes élastiques de surface

Nous avons investigué la sensibilité à la température des filtres à O.E.S. A cette fin, la réponse fréquentielle a été mesurée à une température de 25 à 100 °C. La dépendance de la température de la fonction de transfert $|S_{12}|$ mesurée dans les échantillons avec diffèrentes concentrations en Li et diffèrents états de domaines est représentée sur la *Fig. 4.36, page 174*. Nous avons pris la variation de la fréquence avec la température sur plusieurs points de la fonction de transfert, dans le minimum inférieur (f_{lm}) et le minimum supérieur (f_{hm}) de la bande passante et dans la limite inférieure (f_l) et supérieure (f_h) de la bande passante en prenant le niveau -20 dB comme référence (*cf. Fig. 4.36, page 174*). Cependant le signal de f_{hm} a montré une réponse bruitée, ce qui empêche de sélectionner correctement les valeurs de cette fréquence. Par conséquent, nous avons utilisé seulement les valeurs en utilisant le niveau d'atténuation de -20 dB comme référence, puisqu'à cet endroit on peut observer clairement la variation des fréquences avec la température.

Les CTF_l et CTF_h relatifs de tous les échantillons sont montrés sur la *Fig. 4.38, page 176* et leurs valeurs sont indiquées sur le *Tableau 4.13, page 174*. Le CTF_l et le CTF_h de l'échantillon de référence ont été -31.2 et -41.32 ppm/°C, respectivement. Ces valeurs sont proches du CTF reporté pour le 42 RY-X LT congruent (-40 ppm/°C) (Réf. 29, Chap. 4). De plus, l'échantillon de composition congruent re-polarisé uniformément montre des valeurs proches. (CTF_l=-33 et CTF_h=-40.9 ppm/°C). Donc, il apparaît qu'il n'y a pas de différences entre l'échantillon de référence et celui re-polarisé.

En ce qui concerne les échantillons de composition stœchiométrique et proche de stœchiométrique, les valeurs de CTF_l et le CTF_h ont été très similaires à ceux des échantillons congruents. Ceci indique que les changements en stœchiométrie n'ont pas un effet important sur la sensibilité des filtres à la température.

Dans le cas de l'échantillon de composition congruent et multi-domaine, les valeurs absolues de CTF_l et CTF_h ont été plus proches de zéro comparée à celles de référence, ce qui indique que l'état multi domaine peut être le responsable de la réduction du CTF.

D'autre part, le coefficient de couplage électromécanique des résonateurs en série et parallèle a été estimé à partir des paramètres RLC du circuit équivalent. Nous avons utilisé le modèle de Butterworth Van dyke modifié pour estimer la résistance motionnelle, R_1, la capacité motionnelle, C_1, l'inductance motionnelle, L_1, et la capacité statique, C_0. Nous avons estimé le K^2 à partir des valeurs de C_1 et C_0, en utilisant l'*Eq. 1.73, page 30*. Les valeurs de K^2 sont indiquées dans le *Tableau 4.13, page 174*. L'échantillon de référence a montré un K^2 de 7.00%, proche de celui reporté dans la littérature (*Réf. 29, Chap. 4*). L'échantillon re-polarisé a montré la même valeur de K^2 que l'échantillon de référence. Finalement, les échantillons de composition stœchiométrique et proche de stœchiométrique ont montré un K^2 légèrement plus élevé que celui de la référence, mais dans la plage des erreurs. En contraste, le K^2 de l'échantillon multi-domaine a fortement diminué en comparaison avec l'échantillon de référence (de 7% à 2.5%). Cela confirme le fait que la structure multi-domaine fait diminuer drastiquement le couplage piézoélectrique, comme nous avons observé dans le cas des résonateurs ridges, également.

V. Conclusions et perspectives

Parmi les principales limitations que présentent les technologies de filtres à ondes élastiques basés sur les monocristaux de LT et LN se trouve la sensibilité de la fréquence à la température, laquelle est due principalement aux changements des constantes élastiques des matériaux avec la température. Un autre problème est le disfonctionnement de dispositifs soumis à haute densité de puissance, suite à une inversion de domaines dans le substrat piézoélectrique. Afin de répondre à ces problématiques, au cours de cette thèse nous avons proposé une nouvelle approche visant à améliorer les propriétés des substrats.

L'objectif de cette thèse était l'investigation de l'effet de la non-stœchiométrie en Li_2O dans la performance des dispositifs à ondes élastiques de surface et de volume à base de monocristaux de LT et LN. Nous nous sommes focalisés sur la possibilité de réduire le CTF des cristaux 42 RY-X LT et sur l'amélioration de la stabilité à hautes densités de puissance des dispositifs à base de 128 RY-X LN, sans la détérioration d'autres propriétés, tels que le couplage électromécanique et les pertes d'insertion.

Tout d'abord, nous avons travaillé sur la méthode qui permet de modifier la composition des cristaux de LT et LN. À cet effet, nous avons fait une étude exhaustive sur le procédé VTE de LT et LN, afin de produire des cristaux homogènes avec une concentration contrôlée en Li_2O. Bien qu'il existe des nombreuses études sur le VTE des cristaux de LN, très peu de travaux ont été publiés sur le VTE des cristaux de LT. Par conséquent, nous avons décidé de faire une étude détaillée sur l'effet des paramètres impliqués dans le procédé VTE (par exemple la durée, la température et la concentration des poudres d'équilibration) sur la concentration de Li_2O dans les poudres et les cristaux, ainsi que l'anisotropie et la diffusion de Li. Nous avons optimisé le traitement de VTE pour différentes coupes de LT. Ceci a permis la production de cristaux avec une distribution homogène de Li_2O dans une grande plage de composition entre sous-congruente et stœchiométrique (<48.5-50 mol%). La concentration en Li_2O dans les cristaux traités par VTE a été mesurée avec précision en utilisant la technique de Spectroscopie Raman. Nous avons obtenu des équations empiriques, permettant d'établir une relation entre la concentration en Li_2O des cristaux et les conditions utilisées lors du traitement VTE. Nous avons trouvé que la durée de traitement et la température sont des paramètres qui affectent significativement la concentration et l'homogénéité des cristaux traités. En général, plus haute est la température de traitement, plus courts sont les traitements nécessaires. Cependant la composition des poudres d'équilibration change très rapidement à hautes températures (≥ 1300 °C) due à la volatilisation de Li_2O. Ce qui rend difficile de contrôler la concentration en Li_2O dans les cristaux avec un précision suffisante. Alors, nous avons choisi 1250°C comme la température idéale permettant d'obtenir des cristaux homogènes à une durée de traitement raisonnable. D'autre part, nous avons observé que la diffusion de Li est anisotrope, étant plus rapide selon l'axe cristallographique Z des cristaux de LT, ce qui est identique dans le cas des cristaux de LN, d'après les résultats publiés dans la littérature. Dans le cas de la coupe X, Y, Z et 42 RY des cristaux de LT, avec une composition stœchiométrique et intermédiaire, des traitements plus longs que 24 h à 1250°C sont nécessaires pour l'obtention de cristaux homogènes. Avec ces conditions, nous avons préparé de cristaux sans fissures et sans mâcles.

De plus, nous avons considéré l'idée de réaliser un transfert technologique du traitement VTE de petits échantillons vers wafers de 4 pouces, afin de pouvoir préparer les

dispositifs à O.E.S dans les lignes industrielles. Cependant, les wafers de 4 pouces de LT se sont déformés significativement après les traitements à haute température (avec une fléché de 1 mm après être recuits à 1250°C pendant 48 h). Pour faire face à ce problème, nous avons essayé d'optimiser la température de traitement, la durée et les vitesses de refroidissement. Dans les cas des cristaux 42 RY-LT, nous avons réussi à réduire la déformation à des valeurs de l'ordre de 100 µm. Cependant, de telles valeurs restent encore trop grandes pour pouvoir être utilisées pour la fabrication de dispositifs dans les lignes industrielles. Donc, nous avons utilisé des quarts de wafers de quatre pouces pour les suivantes étapes de fabrication de dispositifs à base de 42 RY-LT. Dans les cas de wafers de 4 pouces de 128 RY-LN, traités par VTE pendant 400 h, nous avons réussi à obtenir une légère déformation de 59 µm, de telles valeurs nous permettent de préparer des dispositifs dans les lignes industrielles et de leur caractériser.

Après avoir effectué le traitement VTE, les cristaux de LT sont multi-domaines et ils doivent être polarisés uniformément. A cette fin, nous avons utilisé la technique d'inversion de domaines par application d'un champ électrique à température ambiante. Avec cette technique, nous avons polarisé uniformément différentes coupes de cristaux de LT (Z et 42 RY) dopés et non dopés Fe, avec différentes compositions entre congruente et stœchiométrique, avec différents états de domaines initiaux. Bien que la procédure pour l'inversion de domaines des cristaux traités par VTE soit essentiellement la même que celle utilisée pour les cristaux initialement mono-domaines, nous avons observé certaines particularités. Ainsi, l'inversion de domaines dans le cas de cristaux initialement multi-domaines a été plus compliquée car nous avons besoin d'appliquer une tension plus intense et la quantité d'impulsions est également plus grande, afin d'inverser complètement les domaines ferroélectriques. De plus, dans le cas des cristaux 42 RY-LT dopés Fe, nous avons appliqué des champs électriques plus intenses ainsi qu'un plus grand nombre d'impulsions. Finalement, nous avons trouvé que lorsqu'on change la direction de polarisation entre chaque cycle, plusieurs fois, le processus d'inversion de domaines devient plus facile.

En outre, la dynamique d'inversion de domaines, reflétée dans la forme de la courbe du courant, des échantillons stœchiométriques et proche stœchiométriques a été différente de celle des échantillons de composition congruente. Finalement, nous avons réussi à faire la polarisation uniforme à température ambiante des échantillons de composition congruente, stœchiométriques et de composition intermédiaire. Cependant l'inversion de domaines des échantillons sous-congruents a été plus problématique et nous avons souvent eu des claquages avant de réussir l'inversion de domaines. Ceci est dû au fait que l'inversion de domaines de ce type d'échantillon nécessite de l'application de champs électriques considérablement plus intenses.

Après la préparation de cristaux avec différentes concentrations en Li_2O et polarisation uniforme, nous avons procédé à la fabrication de dispositifs à ondes élastiques de surface et de volume. Nous avons focalisé notre étude sur l'effet de la non stœchiométrie en Li sur la dépendance en température des constantes élastiques C_{44} et C_{66}. A cette fin nous avons préparé différents types de résonateurs permettant l'excitation des ondes de cisaillement. D'après les simulations, les résonateurs à ondes de volume à haute facteur de forme (appelés « ridges ») ont montré un signal fortement couplé et la possibilité d'exciter les modes de cisaillement. Alors, ces structures ont été fabriquées sur de substrats de LT, coupe Z et 42 RY.

Dans la plupart des cas, la réponse fréquentielle, le CTF et le K^2 des cristaux non traités, mesurés expérimentalement, ont été en accord avec les résultats théoriques, obtenus par simulation en 2D. Cependant, le faible facteur de qualité des résonateurs ridges n'a pas permis l'obtention de résultats reproductibles et en conséquence les résultats n'ont pas été concluants.

Finalement, des filtres à ondes de surface ont été fabriqués sur des substrats de 42RY-LT de composition congruente et stœchiométrique. La préparation de substrats mono domaine de composition sous congruente n'a pas été possible en raison des difficultés rencontrées pendant le processus d'inversion de domaines, mentionné précédemment. D'autre part, la fonction de transfert et le coefficient de réflexion mesurés ont été en accord avec les résultats prédits par les simulations. Cette fois-ci la qualité du signal a été satisfaisante, ce qui a permis l'estimation du CTF et le K^2 avec une meilleure précision que dans le cas des résonateur ridges. Nous avons trouvé que le CTF des échantillons de référence et des échantillons de composition stœchiométrique et proche de stœchiométrique ont été très similaires. En revanche, dans le cas de l'échantillon multi-domaine, le CTF a été plus proche de zéro comparé à celui du congruent, étant -19.21 ppm/°C et -31.5 ppm/°C pour l'échantillon multi-domaine et l'échantillon non traité, respectivement.

En ce qui concerne le facteur de couplage, nous avons observé une légère augmentation dans les échantillons stœchiométriques et une forte diminution (de 7% à 2.5%) dans le cas d'un échantillon multi-domaine. Par conséquent, nous pouvons conclure que la variation de la non stœchiométrie en Li, dans l'intervalle de composition congruent-stœchiométrique (48.5-50 mol%) ne change pas significativement les valeurs du CTF. Cependant, l'état multi domaine des cristaux produit une diminution du CTF mais il produit une diminution du facteur de couplage, également, ainsi qu'une augmentation des pertes d'insertion.

Perspectives

Il est important d'évaluer l'effet de la non stœchiométrie en Li des échantillons de composition sous-congruente sur les propriétés des dispositifs. A cette fin il est nécessaire d'obtenir des cristaux mono-domaines. Malgré tous nos efforts, l'inversion de domaines à température ambiante n'a pas été possible en raison du haut champ coercitif. Dans ce cas il est plus approprié de faire l'inversion de domaines à haute température, car le champ coercitif diminue avec la température. Dans le cadre de cette thèse nous avons préparé un dispositif expérimental permettant de faire ladite inversion à haute température (<210°C). Cependant, nous n'avons pas eu le temps d'optimiser cette technique.

De plus, le traitement VTE sur les échantillons de 128 RY-LN a été fait à la fin de ce projet, et donc nous n'avons pas eu le temps de préparer les dispositifs. La réalisation de dispositifs à ondes élastiques de surface à base de 128 RY-LN traités par VTE et l'évaluation de leur stabilité à haute densité de puissance va être faite prochainement.

Finalement, il pourrait être intéressant d'investiguer l'effet de la non stœchiométrie en Li sur l'évolution avec la température de toutes les constants élastiques, piézoélectriques et diélectriques des matériaux LN et LT.

7. Annex

A1.1 Chemical composition dependence on acoustic properties of LT and LN

Table A.1.1 Effect of composition on elastic properties of LN

		48.28 Li_2O mol %	48.41 Li_2O mol %	48.55 Li_2O mol %	Gradient (/mol %)
Elastic constant ($\times 10^{11}$ N/m^2)	c_{11}^E	1.9844	1.9883	1.9916	0.027
	c_{12}^E	0.5433	0.5463	0.5489	0.021
	c_{13}^E	0.6794	0.6811	0.6820	0.010
	c_{14}^E	0.0758	0.0779	0.0799	0.015
	c_{33}^E	2.3382	2.3431	2.3459	0.028
	c_{44}^E	0.5996	0.5984	0.5973	−0.008
Piezoelectric constant (C/m^2)	e_{15}	3.631	3.659	3.682	0.191
	e_{22}	2.394	2.408	2.419	0.093
	e_{31}	0.332	0.328	0.320	−0.045
	e_{33}	1.896	1.878	1.870	−0.094
Dielectric constant	$\varepsilon_{11}^S/\varepsilon_0$	45.1	45.1	45.0	−0.26
	$\varepsilon_{33}^S/\varepsilon_0$	26.8	26.6	26.5	−1.33
Density (kg/m^3)	ρ	4643.5	4642.8	4641.7	−6.94

Table A.1.2 Effect of composition on elastic properties of LT

		48.35 Li_2O mol %	48.50 Li_2O mol %	48.66 Li_2O mol %	Gradient (/mol %)
Elastic constant ($\times 10^{11}$ N/m^2)	c_{11}^E	2.3264	2.3300	2.3333	0.022
	c_{12}^E	0.4620	0.4643	0.4653	0.011
	c_{13}^E	0.8356	0.8341	0.8358	0.000
	c_{14}^E	−0.1077	−0.1061	−0.1054	0.008
	c_{33}^E	2.7530	2.7574	2.7614	0.027
	c_{44}^E	0.9513	0.9514	0.9521	0.002
Piezoelectric constant (C/m^2)	e_{15}	2.609	2.634	2.650	0.132
	e_{22}	1.818	1.826	1.844	0.084
	e_{31}	−0.143	−0.090	−0.114	0.094
	e_{33}	1.804	1.792	1.779	−0.080
Dielectric constant	$\varepsilon_{11}^S/\varepsilon_0$	41.7	41.7	41.7	0.00
	$\varepsilon_{33}^S/\varepsilon_0$	41.9	41.7	41.4	−1.70
Density (kg/m^3)	ρ	7463.4	7460.6	7457.9	−18.26

Table A.1.3 Effect of chemical composition on acoustic properties of LT crystals (Kushibiki, 2002)

		48.35 Li_2O mol %	48.50 Li_2O mol %	48.66 Li_2O mol %	Gradient (/mol %)
Longitudinal velocity (m/s)	X cut	5583.1	5588.4	5593.4	33.7
	Y cut	5738.9	5745.2	5752.6	44.6
	Z cut	6169.3	6174.5	6179.3	32.8
	33° Y cut	6324.2	6333.3	6339.8	50.9
Shear velocity (m/s)	Y cut	3534.1	3536.0	3538.9	15.4
	Z cut	3570.2	3571.0	3572.9	8.8
	33° Y cut	3353.9	3358.4	3362.4	27.6
LSAW velocity (m/s)	Y cut	3229.3	3232.0	3234.5	17.1
	Z cut	3314.3	3318.8	3322.8	28.0
	33° Y cut	3133.7	3137.7	3141.0	23.8
Dielectric constant	$\varepsilon_{11}^T/\varepsilon_0$	52.6	52.8	53.0	1.13
	$\varepsilon_{33}^T/\varepsilon_0$	43.7	43.4	43.1	−2.00
Density (kg/m^3)	ρ	7463.4	7460.6	7457.9	−18.26

Table A.1.4 Effect of chemical composition on acoustic properties of LT crystals (Kushibiki, 2002)

		48.28 Li_2O mol %	48.41 Li_2O mol %	48.55 Li_2O mol %	Gradient (/mol %)
Longitudinal velocity (m/s)	X cut	6536.7	6543.7	6550.0	48.9
	Y cut	6795.2	6805.1	6813.7	68.5
	Z cut	7322.2	7327.2	7332.0	36.3
	128° Y cut	7149.7	7157.8	7165.0	56.5
Shear velocity (m/s)	Y cut	3938.8	3940.4	3941.8	11.0
	Z cut	3593.2	3590.0	3587.3	−21.9
	128° Y cut	3508.5	3500.8	3493.7	−54.6
LSAW velocity (m/s)	Y cut	3445.6	3444.8	3443.9	−6.2
	Z cut	3868.8	3875.3	3881.3	46.1
	128° Y cut	3658.5	3662.1	3665.2	24.9
Dielectric constant	$\varepsilon_{11}^T/\varepsilon_0$	82.9	83.6	84.2	4.72
	$\varepsilon_{33}^T/\varepsilon_0$	28.6	28.4	28.2	−1.51
Density (kg/m^3)	ρ	4643.5	4642.8	4641.7	−6.94

A 1.1.2: Orientation of crystalline plates

The wafers are usually cut at a defined angle, the wafers of LN and LT used in this work have the orientation indicated below:

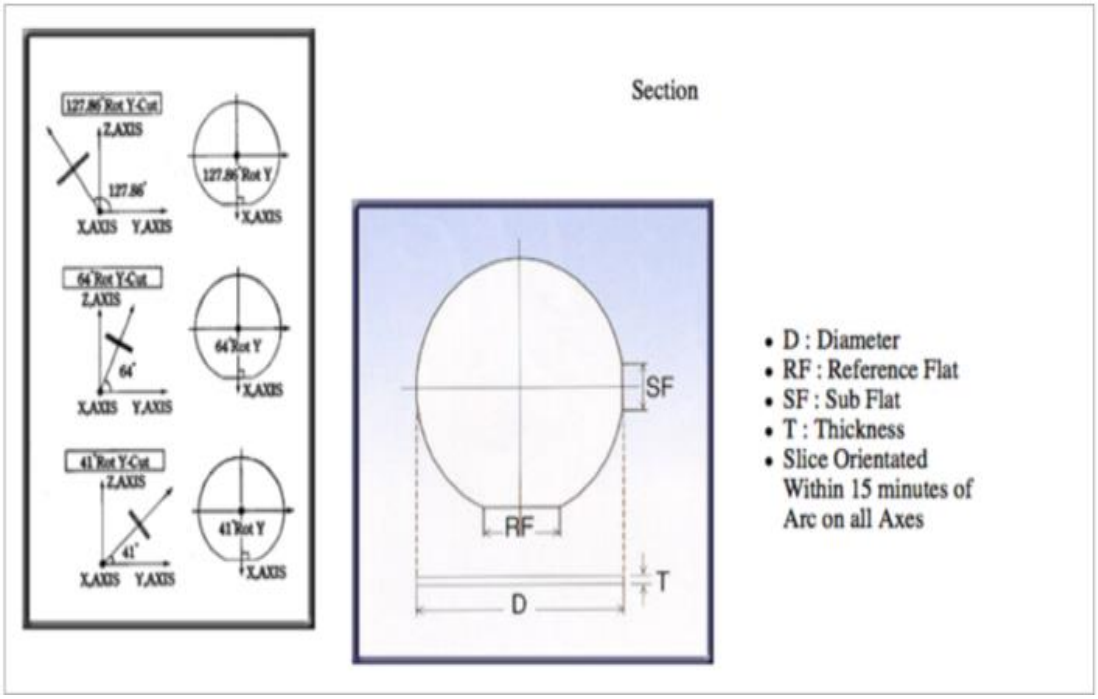

Fig.A.1. Orientation of wafers commercially available

A.2.1 Crystallographic database of $LiTaO_3$, Li_3TaO_4 and $LiTa_3O_8$ phases

This crystallographic information file (CIF) contains the data in a paper accepted for publication in Acta Crystallographica Section B. It has been peer reviewed under the auspices of the IUCr Commission on Journals. Full details of the Crystallographic Information File format are given in the paper "The Crystallographic Information File (CIF): a New Standard Archive File for Crystallography" by S. R. Hall, F. H. Allen and I. D. Brown [Acta Cryst. (1991), A47, 655-685]. From the CIF it can be found the following information about crystals:

- Chemical formula
- Chemical formula weight
- Chemical melting point
- Symmetry cell setting
- Symmetry space group
- Lattice parameters
- Cell volume
- Cell formula units, Z, which allows the estimation of crystal density
- The position of the atoms in the asymmetric unit cell
- The atom oxidation number

$LiTaO_3$:

_ _publ_author_name
'Hsu, R.'
'Maslen, E. N.'
'du Boulay, D.'
'Ishizawa, N.'
_publ_section_title
;
Synchrotron X-ray Studies of LiNbO~3~ and LiTaO~3~
;
_journal_issue 3
_journal_name_full 'Acta Crystallographica Section B'
_journal_page_first 420
_journal_page_last 428
_journal_volume 53
_journal_year 1997
_chemical_formula_analytical LiTaO~3~
_chemical_formula_sum 'Li O3 Ta'
_chemical_formula_weight 235.9
_chemical_melting_point 1923
_chemical_name_systematic lithium_tantalate
_space_group_IT_number 161
_symmetry_cell_setting trigonal
_symmetry_space_group_name_Hall 'R 3 -2"c'
_symmetry_space_group_name_H-M 'R 3 c :H'
_audit_creation_method
from_xtal_archive_file_using_CIFIO
_cell_angle_alpha 90.000(10)
_cell_angle_beta 90.000(10)
_cell_angle_gamma 120.000(13)
_cell_formula_units_Z 6
_cell_length_a 5.154(3)
_cell_length_b 5.154(3)
_cell_length_c 13.783(3)
_cell_measurement_reflns_used 6
_cell_measurement_temperature 293
_cell_measurement_theta_max 41.288
_cell_measurement_theta_min 41.283
_cell_volume 317.1(3)

****

Li_3TaO_4

Li-O-Ta # Li3TaO4rt # 1200044

data_1200044

_audit_creation_date 2013-05-21

_audit_creation_method;

Pearson's Crystal Data browser;

#_database_code_PCD 1200044

Entry summary

_chemical_formula_structural Li3TaO4

_chemical_formula_sum Li3O4Ta

_chemical_name_mineral ?

_chemical_compound_source ?

_chemical_name_structure_type Li3TaO4,mS64,15

_chemical_formula_weight 265.8

_chemical_melting_point ?

Bibliographic data

_publ_section_title 'Reinvestigation of b-Li3TaO4'

_journal_coden_ASTM ACSEBH

_journal_year 2003

_journal_volume 59

_journal_page_first i80

_journal_page_last i82

_journal_language English

loop_

#publ_author_name _publ_author_address

'Du Boulay D.';
Tokyo Institute of Technology
Laboratory of Materials and Structures
Yokohama / Kanagawa
Japan;
'Sakaguchi A.';
Tokyo Institute of Technology
Laboratory of Materials and Structures
Yokohama / Kanagawa
Japan;
'Sude K.';
Tokyo Institute of Technology
Laboratory of Materials and Structures
Yokohama / Kanagawa
Japan;
'Ishizawa N.';
Tokyo Institute of Technology
Laboratory of Materials and Structures
Yokohama / Kanagawa
Japan;

Standardized crystallographic data
_cell_length_a 8.508
_cell_length_b 8.516
_cell_length_c 9.338
_cell_angle_alpha 90
_cell_angle_beta 116.869
_cell_angle_gamma 90
_cell_volume 603.5
_cell_formula_units_Z 8
_symmetry_Int_Tables_number 15
_symmetry_space_group_name_H-M C12/c1
loop_
_symmetry_equiv_pos_site_id
_symmetry_equiv_pos_as_xyz
1 'x, y, z'
2 '-x, -y, -z'
3 '-x, y, 0.5-z'
4 'x, -y, 0.5+z'
5 '0.5+x, 0.5+y, z'
6 '0.5-x, 0.5-y, -z'
7 '0.5-x, 0.5+y, 0.5-z'
8 '0.5+x, 0.5-y, 0.5+z'
loop_
_atom_type_symbol
_atom_type_oxidation_number
O 0
Ta 0
Li 0
loop_
_atom_site_label
_atom_site_type_symbol
_atom_site_Wyckoff_symbol
_atom_site_symmetry_multiplicity
_atom_site_fract_x
_atom_site_fract_y
_atom_site_fract_z
_atom_site_occupancy
O4 O f 8 0.0564 0.1106 0.6114 1
O2 O f 8 0.0606 0.3611 0.1178 1
Ta1 Ta f 8 0.07894 0.14081 0.12484 1
O1 O f 8 0.1643 0.1228 0.3608 1
Li1 Li f 8 0.1836 0.3816 0.3818 1
O3 O f 8 0.3039 0.1258 0.134 1
Li3 Li f 8 0.3205 0.3799 0.1388 1
Li2 Li f 8 0.5425 0.1073 0.1263 1

_exptl_crystal_colour ?
_exptl_crystal_density_meas ?
_cell_measurement_temperature 293
_cell_measurement_radiation 'X-rays, Mo Ka'
_cell_measurement_reflns_used 63939
_diffrn_ambient_temperature 293
_diffrn_measurement_device 'automatic diffractometer'
_diffrn_measurement_device_type 'Rigaku R-AXIS RAPID'
_diffrn_radiation_type 'X-rays, Mo Ka'
_diffrn_reflns_number 10260
_exptl_absorpt_coefficient_mu 36.24
_exptl_absorpt_correction_type analytical

_computing_structure_solution 'starting values from the literature'
_refine_ls_number_parameters 74
_refine_ls_number_reflns 2422
_refine_ls_R_factor_all 0.033
_refine_ls_wR_factor_all 0.026
_computing_structure_refinement XTAL-3.7
End of data set 120004
****

$LiTa_3O_8$:

Li-O-Ta # LiTa3O8ht1 # 1408067
data_1408067
_audit_creation_date 2013-05-21
_audit_creation_method;
Pearson's Crystal Data browser;
#_database_code_PCD 1408067
Entry summary

_chemical_formula_structural M-LiTa3O8
_chemical_formula_sum LiO8Ta3
_chemical_name_mineral ?
_chemical_compound_source ?
_chemical_name_structure_type LiTa3O8,mS48,15
_chemical_formula_weight 677.8
_chemical_melting_point ?
Bibliographic data
_
publ_section_title;
The Crystal Structure of M-LiTa3O8 and Its Relationship to the Mineral Wodginite;
_journal_coden_ASTM JSSCBI
_journal_year 1976
_journal_volume 18
_journal_page_first 1
_journal_page_last 7
_journal_language English
loop_
_publ_author_name
_publ_author_address
'Gatehouse B.M.';
Monash University
Department of Chemistry
Clayton
Australia;
'Negas T.';
Monash University
Department of Chemistry
Clayton
Australia;
'Roth R.S.';
National Bureau of Standards
Materials Division
Washington
U.S.A. Washington D.C.;

Standardized crystallographic data

_cell_length_a 9.413
_cell_length_b 11.522
_cell_length_c 5.05
_cell_angle_alpha 90
_cell_angle_beta 91.05
_cell_angle_gamma 90
_cell_volume 547.6
_cell_formula_units_Z 4

```
_symmetry_Int_Tables_number 15
_symmetry_space_group_name_H-M C12/c1
loop_
_symmetry_equiv_pos_site_id
_symmetry_equiv_pos_as_xyz
1 'x, y, z'
2 '-x, -y, -z'
3 '-x, y, 0.5-z'
4 'x, -y, 0.5+z'
5 '0.5+x, 0.5+y, z'
6 '0.5-x, 0.5-y, -z'
7 '0.5-x, 0.5+y, 0.5-z'
8 '0.5+x, 0.5-y, 0.5+z'
loop_
_atom_type_symbol
_atom_type_oxidation_number
O 0
Ta 0
Li 0
loop_
_atom_site_label
_atom_site_type_symbol
_atom_site_Wyckoff_symbol
_atom_site_symmetry_multiplicity
_atom_site_fract_x
_atom_site_fract_y
_atom_site_fract_z
_atom_site_occupancy
O2 O f 8 0.1154 0.1788 0.573 1
O4 O f 8 0.1185 0.3033 0.1069 1
O3 O f 8 0.1332 0.0625 0.0792 1
Ta1 Ta f 8 0.2415 0.4136 0.2466 1
O1 O f 8 0.3541 0.0484 0.4413 1
Ta2 Ta e 4 0 0.1701 0.25 1
Li Li e 4 0 0.6966 0.25 1
_exptl_crystal_colour ?
_exptl_crystal_density_meas ?
_cell_measurement_temperature ?
_cell_measurement_radiation 'X-rays, Mo Ka'
_cell_measurement_wavelength 0.7107
_cell_measurement_reflns_used ?
_diffrn_ambient_temperature ?
_diffrn_measurement_device 'automatic diffractometer'
_diffrn_measurement_device_type 'Philips PW1100'
_diffrn_radiation_type 'X-rays, Mo Ka'
_diffrn_radiation_wavelength 0.7107
_diffrn_reflns_number 754
_exptl_absorpt_coefficient_mu 62.8
_exptl_absorpt_correction_type spherical
_computing_structure_solution 'Patterson and Fourier synthesis'
_refine_ls_number_parameters ?
_refine_ls_number_reflns 714
_refine_ls_R_factor_all 0.043
_refine_ls_wR_factor_all 0.055
_computing_structure_refinement ORFLS

# End of data set 140806
```

****

A.2.2 Parameters used for Rietveld structural refinement of equilibration powders

The estimation of *c* and *a* lattice parameters and the analysis of content of secondary phase in two phase powders was done by Rietveld structural refinement.

For *single phase powders* ($Li_{1-x}Ta_{1-x}O_{3-2x}$), were x=0.07-1, having molar ratio of $46.5 \leq X_{Li2O} \leq 50$ mol%. The program run in Fullprof interface is given in the following text:

```
COMM LiTaO3
#Current global Chi2 (Bragg contrib.) =     26.28
#Files => DAT-file: p3lt50av.uxd,  PCR-file: p3lt50av
#Job Npr Nph Nba Nex Nsc Nor Dum Iwg Ilo Ias Res Ste Nre Cry Uni Cor Opt Aut
  0  7  1  0  1  0  1  1  0  0  1  0  0  0  0  0  0  0  1
#Ipr Ppl Ioc Mat Pcr Ls1 Ls2 Ls3 NLI Prf Ins Rpa Sym Hkl Fou Sho Ana
  0  0  0  0  2  0  4  0  0  1  9  0  0  0  0  0  0
#Lambda1  Lambda2    Ratio    Bkpos   Wdt    Cthm     muR   AsyLim   Rpolarz  2nd-muR -> Patt# 1
 1.540560 1.540560  0.51400   40.000 10.0000  0.9897  0.0000   60.00    0.0000  0.0000
#NCY  Eps  R_at  R_an  R_pr  R_gl    Thmin      Step      Thmax    PSD   Sent0
 10  0.20  1.00  1.00  1.00  1.00    10.0000   0.023678   150.0080   0.000   0.000
# Excluded regions (LowT  HighT) for Pattern#  1
      5.00      20.10
# 13 Number of refined parameters
#  Zero    Code    SyCos    Code   SySin    Code  Lambda     Code MORE ->Patt# 1
 0.02757   11.0  0.00000    0.0  0.00000    0.0 0.000000    0.00   0
#  Background coefficients/codes  for Pattern#  1  (Polynomial of 6th degree)
   391.099   -364.618    117.159     -3.282      0.870      0.000
    21.00      31.00      41.00       0.00       0.00       0.00
#------------------------------------------------------------------------------
# Data for PHASE number:   1  ==> Current R_Bragg for Pattern#  1:    16.24
#------------------------------------------------------------------------------
Name: LiTaO3
#Nat Dis Ang Pr1 Pr2 Pr3 Jbt Irf Isy Str Furth      ATZ    Nvk Npr More
  3   0   0 2.0 0.0 0.0   0   0   0   0   0       235.810   0   5   0
R 3 c                 <--Space group symbol
#Atom   Typ      X       Y       Z     Biso      Occ     In Fin N_t Spc /Codes
LI     LI     0.00000  0.00000  0.27266  0.00000   0.33300   0  0  0    0
            0.00     0.00     0.00     0.00      0.00
TA     TA     0.00000  0.00000  0.00067  0.00000   0.33300   0  0  0    0
            0.00     0.00     0.00     0.00      0.00
O      O      0.04947  0.34337  0.06980  0.00000   1.00000   0  0  0    0
            0.00     0.00     0.00     0.00      0.00
-------> Profile Parameters for Pattern #  1
 Scale      Shape1      Bov      Str1      Str2      Str3   Strain-Model
0.27708E-03  0.00983   0.00000   0.00000   0.00000   0.00000      0
```

```
 51.00000   81.000    0.000    0.000    0.000    0.000
   U       V       W       X       Y      GauSiz  LorSiz Size-Model
 0.012802 -0.010593  0.011534  0.008596  0.000000  0.000000  0.000000   0
  91.000   101.000   111.000    0.000    0.000    0.000    0.000
  a       b       c      alpha    beta     gamma    #Cell Info
 5.151854  5.151854 13.774160 90.000000 90.000000 120.000000
 61.00000  61.00000  71.00000   0.00000   0.00000  61.00000
Pref1   Pref2    Asy1    Asy2    Asy3    Asy4
1.00000 0.00000 0.00000 -0.26432 0.42714 0.52547
  0.00    0.00    0.00    0.00  131.00  121.00
2Th1/TOF1   2Th2/TOF2  Pattern # 1
   35.000    130.006     1
************************************************
```

In the case of two phase equilibration powders (Li-poor powders) with X_{Li2O} ≤46.5 mol%, ($Li_{1-x}Ta_{1-x}O_{3-2x}$ +$LiTa_3O_8$) were x<0.07, the program was modified in order to take into account the presence of the secondary phase. Thus, it is as following:

```
COMM LiTaO3+LiTa3O8
! Current global Chi2 (Bragg contrib.) =     6.810
! Files => DAT-file: p3lt40avant.uxd,  PCR-file: p3lt40avant
!Job Npr Nph Nba Nex Nsc Nor Dum Iwg Ilo Ias Res Ste Nre Cry Uni Cor Opt Aut
  0   7   2   0   1   0   1   1   0   0   1   0   0   0   0   0   0   0   1
!Ipr Ppl Ioc Mat Pcr Ls1 Ls2 Ls3 NLI Prf Ins Rpa Sym Hkl Fou Sho Ana
  0   0   0   0   2   0   4   0   0   1   9   0   0   0   0   0   0
! Lambda1  Lambda2   Ratio   Bkpos   Wdt   Cthm    muR   AsyLim   Rpolarz  2nd-muR -> Patt# 1
 1.540560 1.540560  0.51400   40.000 10.0000  0.9897  0.0000   60.00    0.0000  0.0000
!NCY  Eps  R_at  R_an  R_pr  R_gl    Thmin     Step     Thmax    PSD    Sent0
 10  0.20  1.00  1.00  1.00  1.00    10.0000  0.023678   150.0080   0.000   0.000
! Excluded regions (LowT  HighT) for Pattern#  1
      5.00      20.10
    18   !Number of refined parameters
! Zero    Code    SyCos    Code   SySin    Code  Lambda     Code MORE ->Patt# 1
 0.03482   11.0  0.00000    0.0  0.00000    0.0 0.000000    0.00   0
!  Background coefficients/codes  for Pattern#  1  (Polynomial of 6th degree)
   350.313   -482.363    305.888    -60.181      0.870      0.000
    21.00      41.00      31.00     141.00       0.00       0.00
!-------------------------------------------------------------------------------
!  Data for PHASE number:   1  ==> Current R_Bragg for Pattern#  1:    8.29
!-------------------------------------------------------------------------------
Name: LiTaO3
!Nat Dis Ang Pr1 Pr2 Pr3 Jbt Irf Isy Str Furth      ATZ    Nvk Npr More
  3   0   0 2.0 0.0 0.0   0   0   0   0   0      235.810   0   5   0
R 3 c                 <--Space group symbol
!Atom   Typ      X       Y       Z     Biso      Occ     In Fin N_t Spc /Codes
```

```
LI    LI     0.00000  0.00000  0.22024  0.00000   0.33300   0   0   0    0
             0.00     0.00     0.00     0.00      0.00
TA    TA     0.00000  0.00000  0.00000  0.00000   0.33333   0   0   0    0
             0.00     0.00     0.00     0.00      0.00
O     O      0.01681  0.30781  0.09358  0.00000   1.00000   0   0   0    0
             0.00     0.00     0.00     0.00      0.00
!-------> Profile Parameters for Pattern #  1
! Scale      Shape1     Bov     Str1     Str2     Str3   Strain-Model
 0.18940E-03  0.01800  0.00000  0.00000  0.00000  0.00000      0
   51.00000   81.000    0.000    0.000    0.000    0.000
!     U        V        W        X        Y      GauSiz   LorSiz Size-Model
  0.023382  -0.012734  0.012186  0.008596  0.000000  0.000000  0.000000   0
    0.000     0.000     0.000     0.000     0.000     0.000     0.000
!    a        b        c       alpha     beta      gamma     #Cell Info
  5.156867  5.156868  13.781966  90.000000  90.000000 120.000000
  61.00000  61.00000  71.00000   0.00000   0.00000   61.00000
! Pref1    Pref2     Asy1     Asy2     Asy3     Asy4
 1.00000  0.00000  0.00000  0.00000  0.41794 -0.01201
   0.00     0.00     0.00     0.00   161.00   151.00
!------------------------------------------------------------------------------
! Data for PHASE number:   2  ==> Current R_Bragg for Pattern#  1:    18.28
!------------------------------------------------------------------------------
Name: LiTa3O8
!Nat Dis Ang Pr1 Pr2 Pr3 Jbt Irf Isy Str Furth      ATZ    Nvk Npr More
  7   0   0 2.0 0.0 0.0   0   0   0   0   0       677.560   0   5   0
C 2/c                 <--Space group symbol
!Atom   Typ      X       Y       Z     Biso      Occ     In Fin N_t Spc /Codes
LI    LI     0.00000  0.69660  0.25000  0.00000   0.50000   0   0   0    0
             0.00     0.00     0.00     0.00      0.00
TA1   TA     0.24150  0.41360  0.24660  0.00000   1.00000   0   0   0    0
             0.00     0.00     0.00     0.00      0.00
TA2   TA     0.00000  0.17010  0.25000  0.00000   0.50000   0   0   0    0
             0.00     0.00     0.00     0.00      0.00
O1    O      0.35410  0.04840  0.44130  0.00000   1.00000   0   0   0    0
             0.00     0.00     0.00     0.00      0.00
O2    O      0.11540  0.17880  0.57300  0.00000   1.00000   0   0   0    0
             0.00     0.00     0.00     0.00      0.00
O3    O      0.13320  0.06250  0.07920  0.00000   1.00000   0   0   0    0
             0.00     0.00     0.00     0.00      0.00
O4    O      0.11850  0.30330  0.10690  0.00000   1.00000   0   0   0    0
             0.00     0.00     0.00     0.00      0.00
!-------> Profile Parameters for Pattern #  1
```

```
! Scale      Shape1     Bov     Str1     Str2     Str3   Strain-Model
 0.36490E-04 -0.01929  0.00000  0.00000  0.00000  0.00000     0
   91.00000  131.000    0.000    0.000    0.000    0.000
!     U       V       W       X       Y      GauSiz  LorSiz Size-Model
  0.023382 -0.012734  0.012186  0.008596  0.000000  0.000000  0.000000   0
    0.000    0.000    0.000    0.000    0.000    0.000    0.000
!   a       b       c      alpha    beta     gamma     #Cell Info
  9.414388 11.528296  5.051814 90.000000 91.050537 90.000000
 101.00000 111.00000 121.00000   0.00000   0.00000   0.00000
! Pref1   Pref2    Asy1    Asy2    Asy3    Asy4
 1.00000  0.00000  0.00000  0.00000  0.35771 -0.03963
   0.00    0.00    0.00    0.00   181.00   171.00
! 2Th1/TOF1   2Th2/TOF2  Pattern # 1
    20.100    150.008     1
************************************************
```

Finally, in the case of two phase equilibration powders (Li-rich powders) with X_{Li2O} >50 mol%, ($LiTaO_3$ +Li_3TaO_4), the program used was:

```
COMM LiTaO3+Li3TaO4
! Current global Chi2 (Bragg contrib.) =     11.53
! Files => DAT-file: p3lt54av.uxd,  PCR-file: p3lt54av
!Job Npr Nph Nba Nex Nsc Nor Dum Iwg Ilo Ias Res Ste Nre Cry Uni Cor Opt Aut
  0   7   2   0   1   0   1   1   0   0   1   0   0   0   0   0   0   0   1
!Ipr Ppl Ioc Mat Pcr Ls1 Ls2 Ls3 NLI Prf Ins Rpa Sym Hkl Fou Sho Ana
  0   0   0   0   2   0   4   0   0   1   9   0   0   0   0   0   0
! Lambda1  Lambda2   Ratio   Bkpos   Wdt   Cthm    muR   AsyLim   Rpolarz  2nd-muR -> Patt# 1
 1.540560 1.540560  0.51400   40.000 10.0000  0.9897  0.0000   60.00    0.0000  0.0000
!NCY  Eps  R_at  R_an  R_pr  R_gl    Thmin      Step      Thmax    PSD    Sent0
 10  0.20  1.00  1.00  1.00  1.00    10.0000   0.023678   150.0080   0.000   0.000
! Excluded regions (LowT  HighT) for Pattern#  1
      5.00      20.10
    19   !Number of refined parameters
! Zero   Code   SyCos   Code   SySin   Code  Lambda    Code MORE ->Patt# 1
 0.01813   11.0  0.00000    0.0  0.00000    0.0 0.000000    0.00   0
!  Background coefficients/codes  for Pattern#  1  (Polynomial of 6th degree)
   433.160   -640.556    410.720    -80.964      0.870      0.000
    21.00      41.00      31.00     141.00       0.00       0.00
!-------------------------------------------------------------------------------
!  Data for PHASE number:   1  ==> Current R_Bragg for Pattern#  1:    14.72
!-------------------------------------------------------------------------------
Name: LiTaO3
!Nat Dis Ang Pr1 Pr2 Pr3 Jbt Irf Isy Str Furth      ATZ    Nvk Npr More
  3   0   0 2.0 0.0 0.0   0   0   0   0   0       235.810   0   5   0
R 3 c                 <--Space group symbol
```

```
!Atom   Typ      X       Y       Z     Biso      Occ     In Fin N_t Spc /Codes
LI    LI     0.00000  0.00000  0.28080  0.00000   0.33300   0   0   0    0
           0.00     0.00     0.00     0.00     0.00
TA    TA     0.00000  0.00000  0.00090  0.00000   0.33333   0   0   0    0
           0.00     0.00     0.00     0.00     0.00
O     O      0.04947  0.34337  0.06980  0.00000   1.00000   0   0   0    0
           0.00     0.00     0.00     0.00     0.00
!-------> Profile Parameters for Pattern #  1
! Scale      Shape1     Bov     Str1     Str2     Str3   Strain-Model
 0.23572E-03  -0.15447   0.00000   0.00000   0.00000   0.00000      0
   51.00000    81.000    0.000    0.000    0.000    0.000
!     U        V        W        X        Y      GauSiz   LorSiz Size-Model
  0.006235  -0.006856   0.008450   0.008596   0.000000   0.000000   0.000000    0
   141.000    151.000    161.000     0.000     0.000     0.000     0.000
!    a        b        c       alpha      beta      gamma     #Cell Info
  5.151226   5.151226  13.774823  90.000000  90.000000 120.000000
  61.00000   61.00000   71.00000    0.00000    0.00000   61.00000
! Pref1    Pref2     Asy1     Asy2     Asy3     Asy4
 1.00000  0.00000  0.00000 -0.26432  0.36880  0.45519
   0.00     0.00     0.00     0.00     0.00     0.00
!------------------------------------------------------------------------------
! Data for PHASE number:   2  ==> Current R_Bragg for Pattern#  2:    79.88
!------------------------------------------------------------------------------
Name: Li3TaO4
!Nat Dis Ang Pr1 Pr2 Pr3 Jbt Irf Isy Str Furth      ATZ    Nvk Npr More
  8   0   0 2.0 0.0 0.0   0   0   0   0   0       265.800   0   5   0
C 2/c                 <--Space group symbol
!Atom   Typ      X       Y       Z     Biso      Occ     In Fin N_t Spc /Codes
LI    LI     0.18360  0.38160  0.38180  0.00000   1.00000   0   0   0    0
           0.00     0.00     0.00     0.00     0.00
LI1   LI     0.54250  0.10730  0.12630  0.00000   1.00000   0   0   0    0
           0.00     0.00     0.00     0.00     0.00
LI2   LI     0.32050  0.37990  0.13880  0.00000   1.00000   0   0   0    0
           0.00     0.00     0.00     0.00     0.00
TA1   TA     0.07894  0.14081  0.12484  0.00000   1.00000   0   0   0    0
           0.00     0.00     0.00     0.00     0.00
O1    O      0.16430  0.12280  0.36080  0.00000   1.00000   0   0   0    0
           0.00     0.00     0.00     0.00     0.00
O2    O      0.06060  0.36110  0.11780  0.00000   1.00000   0   0   0    0
           0.00     0.00     0.00     0.00     0.00
O3    O      0.30390  0.12580  0.13400  0.00000   1.00000   0   0   0    0
           0.00     0.00     0.00     0.00     0.00
```

```
O4   O     0.05640  0.11060  0.61140  0.00000   1.00000  0  0  0   0
           0.00    0.00    0.00    0.00     0.00
!-------> Profile Parameters for Pattern #  2
! Scale      Shape1     Bov     Str1     Str2     Str3   Strain-Model
 0.53064E-05 -0.90929   0.00000  0.00000  0.00000  0.00000     0
   91.00000  131.000    0.000    0.000    0.000    0.000
!    U       V        W        X        Y      GauSiz   LorSiz Size-Model
  0.248329 -0.231351  0.073791  0.008596  0.000000  0.000000  0.000000   0
   171.000   181.000   191.000    0.000    0.000    0.000    0.000
!   a       b       c       alpha     beta      gamma     #Cell Info
  8.507891  8.508671  9.347748 90.000000 116.870743  90.000000
 101.00000 111.00000 121.00000   0.00000   0.00000   0.00000
! Pref1   Pref2    Asy1    Asy2    Asy3    Asy4
 1.00000  0.00000  0.00000 -0.25659  0.07597  0.46169
   0.00    0.00    0.00    0.00    0.00    0.00
! 2Th1/TOF1   2Th2/TOF2  Pattern # 1
    20.100    150.008
```

A.2.3 Table of function error used for estimation of Li+ diffusivity.

Table 6.1 Tabulation of Error Function Values

z	*erf(z)*	*z*	*erf(z)*	*z*	*erf(z)*
0	0	0.55	0.5633	1.3	0.9340
0.025	0.0282	0.60	0.6039	1.4	0.9523
0.05	0.0564	0.65	0.6420	1.5	0.9661
0.10	0.1125	0.70	0.6778	1.6	0.9763
0.15	0.1680	0.75	0.7112	1.7	0.9838
0.20	0.2227	0.80	0.7421	1.8	0.9891
0.25	0.2763	0.85	0.7707	1.9	0.9928
0.30	0.3286	0.90	0.7970	2.0	0.9953
0.35	0.3794	0.95	0.8209	2.2	0.9981
0.40	0.4284	1.0	0.8427	2.4	0.9993
0.45	0.4755	1.1	0.8802	2.6	0.9998
0.50	0.5205	1.2	0.9103	2.8	0.9999

A.3.1 Program in MATLAB for the estimation of the frequency and K^2 dependence of elastic and piezoelectric constants

The program give the dependence of frequency on the elastic constants (df/dC_{ij}) and the dependence of K^2 of piezoelectric coefficients (dK^2/de_{ij})for crystals of LT. The algorithm can be summarized as follows:

We start with the values of the six independent elastic constants of LT: $C_{11}, C_{13}, C_{14}, C_{44}, C_{66}$, given in the first matrix.

The matrix is rotated in a "Y" direction that we can define, the same is done with piezoelectric coefficients and permittivity. In this program, psideg, thetadeg and phideg corresponds to the Euler angles (ψ, θ, φ).

Estimation of stiffened elastic constants.

1) Estimation of velocity (V_o) and polarization by using the eigenvalues of the propagation of plane waves.
2) The frequency and K^2 are estimated from the velocity previously found.
3) The initial values of elastic (C_{ij}) and piezoelectric constants (e_{ij}) are increased by $1x10^{-3}$. Then, the frequencies and K^2 of the three modes are re-estimated with these new values of elastic and piezoelectric constants.

This estimation is done three times: f0, f1 and f2 and then the df/dC_{ij} is estimated. The same processes is done for the estimation of dK^2/de_{ij}

The details of the program are given below:

```
%PI=3.14159265358979324;
rho = 7465; //rho en kg/m3//
function c0=remplit(indeps)
c11=indeps(1);
c13=indeps(2);
c14=indeps(3);
c33=indeps(4);
c44=indeps(5);
c66=indeps(6);

c12 = c11-2*c66
c0=[ c11   c12  c13  c14   0   0
     c12   c11  c13 -c14   0   0
     c13   c13  c33   0    0   0
     c14  -c14   0   c44   0   0
       0     0    0    0   c44  c14
       0     0    0    0   c14  c66 ];
endfunction

function a=cosdir(phideg, thetadeg, psideg)
  phi=phideg*%pi/180
  theta=thetadeg*%pi/180
```

```
  psi=psideg*%pi/180

  c1=cos(phi)
  c2=cos(theta)
  c3=cos(psi)
  s1=sin(phi)
  s2=sin(theta)
  s3=sin(psi)
  // matrix to rotate a vector
a=[ c1*c3-s1*s2*s3  s1*c3+c1*s2*s3  -c2*s3
  -s1*c2        c1*c2          s2
  c1*s3+s1*s2*c3  s1*s3-c1*s2*c3   c2*c3 ] ;
endfunction

function M=rot_matrix_C(phideg, thetadeg, psideg)
a=cosdir(phideg,thetadeg,psideg);
B1=[ a(1,1)^2 a(1,2)^2 a(1,3)^2
   a(2,1)^2 a(2,2)^2 a(2,3)^2
   a(3,1)^2 a(3,2)^2 a(3,3)^2 ];

B2=[ a(1,2)*a(1,3)  a(1,1)*a(1,3) a(1,1)*a(1,2)
   a(2,2)*a(2,3)  a(2,1)*a(2,3) a(2,1)*a(2,2)
   a(3,2)*a(3,3)  a(3,1)*a(3,3) a(3,1)*a(3,2) ] ;

B3=[ a(2,1)*a(3,1) a(2,2)*a(3,2) a(2,3)*a(3,3)
   a(1,1)*a(3,1) a(1,2)*a(3,2) a(1,3)*a(3,3)
   a(1,1)*a(2,1) a(1,2)*a(2,2) a(1,3)*a(2,3) ] ;

B4=[ a(2,2)*a(3,3)  a(2,3)*a(3,1)  a(2,1)*a(3,2)
   a(3,2)*a(1,3)  a(3,3)*a(1,1)  a(3,1)*a(1,2)
   a(1,2)*a(2,3)  a(1,3)*a(2,1)  a(1,1)*a(2,2)] ;

B5=[ a(3,2)*a(2,3)  a(3,3)*a(2,1)  a(3,1)*a(2,2)
   a(1,2)*a(3,3)  a(1,3)*a(3,1)  a(1,1)*a(3,2)
```

```
   a(1,3)*a(2,2)  a(1,1)*a(2,3)  a(2,1)*a(1,2)] ;

M=[ B1, 2*B2;  B3, B4+B5 ] ;
Endfunction

//Rotated matrix of elastic constants//
function c=tourne_elast(phideg, thetadeg, psideg, c0)
  M=rot_matrix_C(phideg,thetadeg,psideg);
  c=M*(c0*M');
endfunction

function [X0, V0]=valP(c)
C=[ c(6,6)  c(2,6) c(4,6)
  c(2,6)  c(2,2) c(2,4)
  c(4,6)  c(2,4) c(4,4) ]
X0=[]
vals0=[]
 [X0,vals0]=spec(C)
 V0=sqrt(vals0*1e9/rho);
endfunction
 //Estimation of frequency in Hz//
  function f=freq(c)
  [X,V] = valP(c);
  V0= [V(1,1), V(2,2), V(3,3)];
  f=V0/(2*thick)
endfunction
// Complementary functions of piezoelectricity
function e0=remplit_e(coef)
e15=coef(1);
e22=coef(2);
e31=coef(3);
e33=coef(4);
e0 =[ 0.0   0.00   0.00  0.00  e15   -e22
   -e22   e22    0.00  e15   0.00  0.00
```

```
    e31  e31   e33   0.00  0.00  0.00];
endfunction

function epr0=remplit_perm(permitivite)
epr11=permitivite(1);
epr33=permitivite(2);
epr0= [epr11  0    0
      0   epr11  0
      0    0  epr33 ];
endfunction
//Rotated matrix of piezoelectric coeffcients//
function e=tourne_piezo(phideg, thetadeg, psideg, e0)
      M=rot_matrix_C(phideg, thetadeg,psideg);
      a=cosdir(phideg, thetadeg,psideg);
      e=a*(e0*M');
endfunction
//Rotated matrix of relative permittivity//
function epr=tourne_perm(phideg, thetadeg, psideg, epr0)
      a=cosdir(phideg, thetadeg,psideg);
      epr=a*(epr0*a');
endfunction

//Estimation of K²//
function [X, V]=valP_durcis(C, e, epr)
//eps_factor=36*%pi
epr22=epr(2,2)
D66=c(6,6)+e(2,6)**2/epr22*100
D44=c(4,4)+e(2,4)**2/epr22*100
D22= c(2,2)+e(2,2)**2/epr22*100
D26=c(2,6)+e(2,2)*e(2,6)/epr22*100
D24=c(2,4)+e(2,2)*e(2,4)/epr22*100
D46=c(4,6)+e(2,4)*e(2,6)/epr22*100

Cd=[ D66  D26 D46
```

```
    D26  D22 D24
    D46  D24 D44 ];
[X,Vals] =spec(Cd)
V=sqrt(Vals*1e9/rho);
endfunction

function K2=coefcouplage(c, e, eps)
   [X0,Y]=valP(c)
   V0= [Y(1,1), Y(2,2), Y(3,3)];
   [X1,Z]=valP_durcis(c,e,eps);
   V= [Z(1,1), Z(2,2), Z(3,3)];
   K2=[(V(1,1)**2-V0(1,1)**2)/V(1,1)**2,  (V(1,2)**2-V0(1,2)**2)/V(1,2)**2,  (V(1,3)**2-
V0(1,3)**2)/V(1,3)**2 ]
endfunction

//=========================================================

//Frequency dependence of elastic constants (df/dC_ij) in GPa//
c110=233.1
c120=46.4
c130=85.2
c140=-16.1
c250=0
c330=276
c440=102.9

c660=(c110-c120)*0.5;

elast0=[c110, c130, c140, c330, c440, c660 ];
thick = 250e-6;

dC = 1e-3;
dC2 = 2*dC;

c0 = remplit(elast0);
```

```
thetadeg = 42;
phideg=0;
psideg=0;

c = tourne_elast(phideg,thetadeg,psideg,c0);
[X0,V0]=valP(c)
f0=freq(c)
df = [];

for i=1:6
  elast1 = elast0;
  elast1(i)=elast0(i)*(1+dC);
  c10=remplit(elast1);
  c1 = tourne_elast(phideg,thetadeg,psideg,c10);
  f1=freq(c1);
  elast2 = elast0;
  elast2(i)=elast0(i)*(1+dC2);
  c20=remplit(elast2);
  c2 = tourne_elast(phideg,thetadeg,psideg,c20);
  f2=freq(c2);
  df(i,:)=(4*f1-f2-3*f0)/(2*dC*elast0(i));
end
//.....//
//Piezoelectric constants in C/m²//
  e150=2.63
  e220=1.84
  e310=-0.11
  e330=1.93
//Permittivity in F/m//
epc=1/(36*%pi*1e9)
//epr=ep/epc//
ep110=47 // *e-11
ep330=38.3 // *e-11
```

```
//Relative permittivity, ep/epc//
//epr110=53.1
//epr330=43.3
//Dependence of coupling factor on piezoelectric coefficients//
piezo0=[e150,e220,e310,e330];
perm0 = [ ep110, ep330 ]

dC=1e-03;
dC2=2*dC;

e0=remplit_e(piezo0);
epr0=remplit_perm(perm0);
thetadeg=42;
phideg=0;
psideg=0;
c=tourne_elas(phideg, thetadeg,psideg,c0)
ee=tourne_piezo(phideg,thetadeg,psideg,e0);
epr=tourne_perm(phideg,thetadeg,psideg,epr0);

[X0,speed0]=valP_durcis(c,ee,epr)
K20=coefcouplage(c,ee,epr)
dK=[];

for i=1:4
  piezo1=piezo0;
  piezo1(i)=piezo0(i)*(1+dC);
  e10=remplit_e(piezo1);
  e1=tourne_piezo(phideg,thetadeg,psideg,e10);
  K1=coefcouplage(c,e1,epr)

  piezo2=piezo0;
  piezo2(i)=piezo0(i)*(1+dC2);
  e20=remplit_e(piezo2);
  e2=tourne_piezo(phideg,thetadeg,psideg,e20);
```

```
K22=coefcouplage(c,e2,epr)
dK(i,:)=(4*K1-K22-3*K20)/(2*dC*piezo0(i));
    end
```

A 3.2 Estimation of the energy trapping of a BAW resonator based on 42RY-LT

Considering a resonator in a piezoelectric plate, where the wave propagates in direction normal to the plate (X_2). It have two electrodes: on the front and on the backside, as is indicated in the figure A4.1 a).

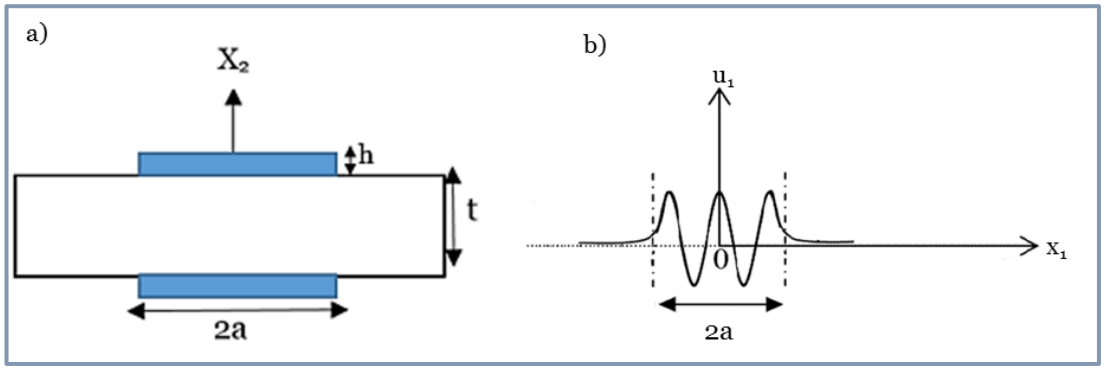

Fig. A 3.1 a) Schematic representation of a BAW resonator in TFE, b) distribution of vibration along x_1

If we consider that inside an outside of electrodes there a different behavior, the resonance frequency can be obtained with the following expressions:

In the case of a plate with shortcut electrodes:

$$\rho(\omega_1^e)^2 \approx \frac{\pi^2 \bar{C}_{ij}}{4h_0^2}\left(1 - \frac{8k^2}{\pi^2} - 2\hat{R}\right) = \frac{\pi^2 \hat{C}_{ij}}{4h_0^2}, \qquad (1)$$

$$\text{where} \quad \hat{R} = 2\left(\frac{\rho_{f1}h_{f1} + \rho_{f2}h_{f2}}{\rho_0 t_0}\right)$$

$\rho_0 t_0$ are the density and the thickness of the plate, $\rho_{f1}h_{f1}$ and $\rho_{f2}h_{f2}$ are the density and the thickness of the electrode 1 and the electrode 2, respectively.

- In the case of the plate without electrode:

$$\rho(\omega_1^f)^2 \approx \frac{\pi^2 \bar{C}_{ij}}{4h_0^2} \qquad (2)$$

On the other hand, the dispersion curves of plates with an without electrodes are similar in the region when $\xi \to 0$, where ξ is the wave number, then, for guided propagation, the resonance frequency can be expressed in terms of dispersion constants:

$$\rho\omega^2 = \rho(\omega_1^e)^2 + M_1\xi^2 \qquad \text{region in the plate with shortcut electrodes} \qquad (3)$$

$$\rho\omega^2 = \rho(\omega_1^f)^2 + M_1\bar{\xi}^2 \qquad \text{region in the plate without electrodes} \qquad (4)$$

In order to have an energy trapping, the wave should be trapped in the center of the structure and then it diminishes its intensity, which means that in the center the wavenumber is real and outside of electrodes it's imaginary. Then the wave displacement along the x_1 axis can be expressed by:

$$u_1 = A\cos(\xi x_1)\sin\frac{\pi x_2}{2h_0}e^{-i\omega t} \qquad \text{under shortcut electrodes} \tag{5}$$

$$u_1 = B\exp(-\bar{\xi}x_1)\sin\frac{\pi x_2}{2h_0}e^{-i\omega t} \qquad \text{outside of electrode} \tag{6}$$

The limit between the electrode and unelectroded areas is placed at x_1=b and the displacement is continuous across this frontier, then, by substituting x_1 by b, at the frontier, the equations 5 and 6 become:

$$A\cos(\xi b) = B\,exp(-\bar{\xi}b) \tag{7}$$

$$A\cos(\xi b) - B\,exp(-\bar{\xi}b) = 0 \tag{8}$$

Equating to zero the determinant of this equation, we obtain:

$$\xi\tan\xi a = \bar{\xi} \tag{9}$$

Since ω should be the same under and outside the electrodes, equating the equation 3 and 4 and simplifying, we have:

$$\bar{\xi}^2 + \xi^2 = \frac{\rho}{M_1}\left[\left(\omega_1^f\right)^2 - (\omega_1^e)^2\right] \tag{10}$$

By substituting $\bar{\xi}$ in equation 9, we obtain:

$$\xi\tan\xi a = \sqrt{\frac{\rho}{M_1}\left[\left(\omega_1^f\right)^2 - (\omega_1^e)^2\right] - \xi^2} \tag{11}$$

$$\delta^2 = \frac{\rho\left(\left(\omega_1^f\right)^2 - \left(\omega_1^e\right)^2\right)}{M_1} = \frac{\pi^2}{4h_0}\frac{\bar{C}_{ij} - \hat{C}_{ij}}{M_1},$$

$$\xi\tan\xi a = \sqrt{\delta^2 - \xi^2}$$

The last equation allows the estimation of wavenumber ξ, which can be obtained by using a graphic method, the value of ξ will be limited to values between 0 and δ because of the square root. Firstly, the value of δ is estimated from the values of angular ω frequency and dispersion constant M1 (which was obtained by an external program realized by M. Bernard Dulmet). Once δ and b are known, the follow graph (fig. A 3.1 a) may be traced, which provides the values of the roots in terms of ξ. Several thickness of electrodes (h) were tested, as is shown in the figure A 4.2, it can be seen that when the thickness is 50 nm, there are only one intersection between the two curves, which give the main mode. When higher thickness were used, other modes can be trapped as well. Therefore, is better to use electrodes with a thickness (h) between 50 and 150 nm in order to trap only the mode of interests. Then, with the values of δ, we can estimated $\bar{\xi}$=$\sqrt{\delta^2 - \xi^2}$. In order to determine the coefficient of exponential decay outside of electrodes, as well as the amplitude B, by using:

$$B = A\cos(\xi b)\exp(-\bar{\xi}b) \tag{12}$$

From equation 12, we can take A=1 in order to facilitate the comparison of curves. Finally, the amplitude distribution of 3 inharmonic modes can be represented in the figure A 3.1 b). The

mode with the Fo function will be better trap the energy, then, a better response is expected during the wave excitation.

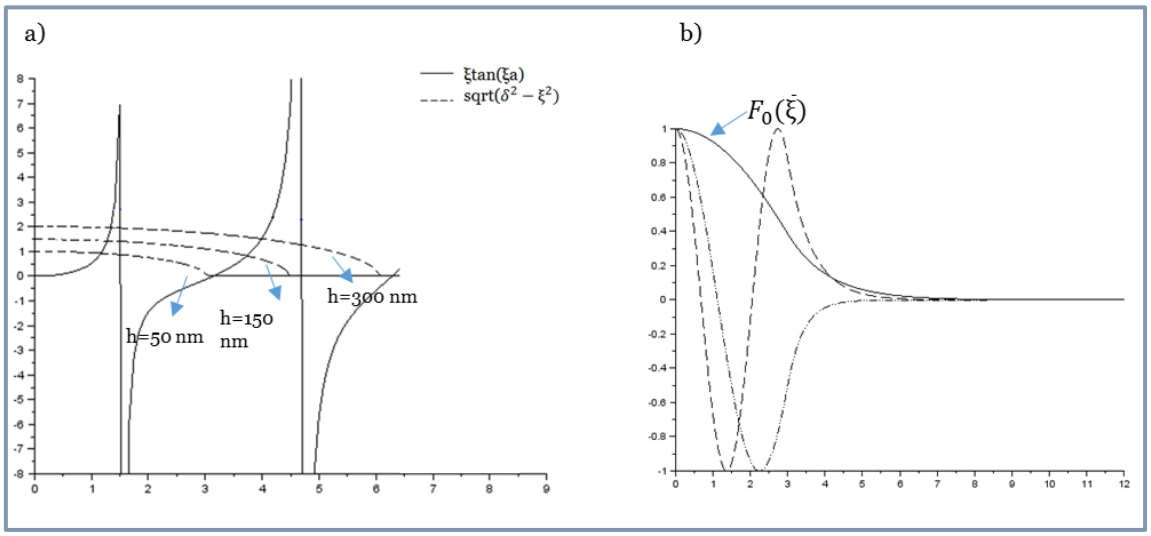

Fig. A3.2 a) Distribution of the wave number for different thickness of electrodes, b) amplitude distribution of the anharmonic modes for a plate having a diamtre electrode of 6 mm and a thickness of 50 nm.

The program realized in Scilab for the estimation of energy trapping is given below:

```
// basic program to obtain dispersion curves Omega=f(gamma)
phi=0.0
theta=42
psi=0

coef=%pi/180;
phi=phi*coef
theta=theta*coef

psi=psi*coef
c1=cos(phi)
c2=cos(theta)
c3=cos(psi)

s1=sin(phi)
s2=sin(theta)
s3=sin(psi)
// matrix to rotate a vector
a=[ c1*c3-s1*s2*s3  s1*c3+c1*s2*s3   -c2*s3
      -s1*c2         c1*c2      s2
  c1*s3+s1*s2*c3  s1*s3-c1*s2*c3    c2*c3 ] ;
// matrices to rotate a tensor of the fourth order
// which establishes a linear relation between two symmetric tensors
```

```
// the second order
B1=[ a(1,1)^2 a(1,2)^2 a(1,3)^2
   a(2,1)^2 a(2,2)^2 a(2,3)^2
   a(3,1)^2 a(3,2)^2 a(3,3)^2 ];

B2=[ a(1,2)*a(1,3)  a(1,1)*a(1,3) a(1,1)*a(1,2)
   a(2,2)*a(2,3)  a(2,1)*a(2,3) a(2,1)*a(2,2)
   a(3,2)*a(3,3)  a(3,1)*a(3,3) a(3,1)*a(3,2) ] ;

B3=[ a(2,1)*a(3,1) a(2,2)*a(3,2) a(2,3)*a(3,3)
   a(1,1)*a(3,1) a(1,2)*a(3,2) a(1,3)*a(3,3)
   a(1,1)*a(2,1) a(1,2)*a(2,2) a(1,3)*a(2,3) ] ;

B4=[ a(2,2)*a(3,3)  a(2,3)*a(3,1)  a(2,1)*a(3,2)
  a(3,2)*a(1,3)  a(3,3)*a(1,1)  a(3,1)*a(1,2)
  a(1,2)*a(2,3)  a(1,3)*a(2,1)  a(1,1)*a(2,2)] ;

B5=[ a(3,2)*a(2,3)  a(3,3)*a(2,1)  a(3,1)*a(2,2)
   a(1,2)*a(3,3)  a(1,3)*a(3,1)  a(1,1)*a(3,2)
   a(1,3)*a(2,2)  a(1,1)*a(2,3)  a(2,1)*a(1,2)] ;

M=[ B1, 2*B2;  B3, B4+B5 ] ; // to rotate 6-stress
N=[ B1, B2;  2*B3, B4+B5 ] ; // to rotate 6-strain

// Material constants for LiTaO3 in crystallographic axes
c0=[  233.1   46.4  85.2 -16.1   0.0  0.0
     46.4  233.1  85.2  16.1     0.0  0.0
     85.2   85.2 276.0   0.0     0.0  0.0
    -16.1   16.1   0.0 102.9     0.0  0.0
     0.0    0.0   0.0   0.0 102.9 -16.1
     0.0    0.0   0.0   0.0 -16.1  (233.1-46.4)*0.5 ] ;// en GPa

e0 =[ 0.0   0.00   0.00  0.00  2.63 -1.84
   -1.84  1.84   0.00  2.63  0.00  0.00
   -0.11  0.11   1.93  0.00  0.00  0.00]; // piezo cristallo(C/m2)

eps0= [53.6  0    0
     0   53.6  0
     0    0  43.4 ]; //permitivity relative ti epsilon zero(dimensionless)

epsilon_zero = 1/(36*%pi)  //  in GF/m ; in F/m it would be  1/(36*%pi*1e9)
```

```
// it is convenient to use GF/m because same 1e9 factor as elastic constants
rho = 7465;   // LiTaO3 kg/m3
rho_f1 = 8908;  // Ni density kg/m3
rho_f2= 8908;   //Ni density kg/m3
G0 = [ c0, c0(:,4), c0(:,5), c0(:,6)] ;
G1 = [G0 ; G0(4,:) ; G0(5,:) ; G0(6,:) ] ;

c = M*(c0*M');        // eq 66 tutorial  - here in GPa
e = a*(e0*M');        // eq 67 - in C/m2
eps = a*(eps0*a');     // eq 68 relative permittivities
eps = epsilon_zero*eps  // here in GF/m
de1 = sqrt((c(2,2)-c(4,4))**2+4*c(2,4)**2);

c3 = (c(2,2)+c(4,4)+de1)*0.5;

c2 = c(6,6);
c1 = (c(2,2)+c(4,4)-de1)*0.5;
Mn_B1 = 116.7322  // Gpa,   from external program
Mn_A5 = 74.6499  // idem
Mn_C2 =  281.3924  // idem

//===================================
Mn_A5 =74.6499; // enter value of Mn or Pn
h0 = 0.260;   // thickness of plate (mm)
hf1 = 0.000100;  // half thickness of electrode 1 (en mm)
hf2 = 0.000100; // half thickness of electrode 2 (en mm)
k2 =0.0810776;
n=5;

function out=R_hat(hf1, hf2)
out = (2*(rho_f1*hf1+rho_f2*hf2))/(rho*h0);
endfunction

c_bar =313.5938// valeur propre durcie de la propagation (zone externe)

// c_hat = c_bar*(1-8*e(2,6)**2/(c_bar*eps(2,2)*%pi^2)-2*R_hat)  // electroded region
function out=c_hat(hf1, hf2) // electroded region
out = c_bar*(1-8*k2/(n**2*%pi**2)-2*R_hat(hf1,hf2))
endfunction
```

```
function out=delta2(hf1, hf2)
out = %pi^2*(c_bar-c_hat(hf1,hf2))/(Mn_A5*4*h0^2)
endfunction

function out=courbe(x, hf1, hf2)
 ni=x/b
 out = sqrt(delta2(hf1,hf2)-ni*ni);
endfunction

b = 3  // location of electrode end
edge = 12  // for resonator length 6mm

function y=equ(alpha)
xi=alpha/b
y = xi*tan(xi*b)-sqrt(delta2(hf1,hf2)-xi**2)
endfunction

del2=delta2(hf1,hf2)
delta = sqrt(del2)

ni = [0:delta/100:delta];
A =  ni.*tan(ni*b);     // term by term multiplication because xi is a vector
B =  sqrt(del2-ni**2);

plot2d([ni*b;ni*b]',[A;B]',rect=[0,-8,9,8]);
deff('[y]=f(x)','y=courbe(x,hf1,hf2)')

xgrid();
        pause;

al0 = fsolve(1.3,equ)
ni0=al0/b;
ni0b = sqrt(del2-ni0^2)
ni1b = sqrt(del2-ni1^2)

b0 = cos(ni0*b)*exp(ni0b*b)
b1 = cos(ni1*b)*exp(ni1b*b)

z1=[0:1/100:b];
z2=[b:1/100:edge];  // cf. remarks at the end.
```

```
// I forced the scale between other curves will use a different one
plot2d([z1,z2]', [cos(ni0*z1),b0*exp(-ni0b*z2)]',rect=[0,-1,edge,1]);
xgrid();

plot2d([z1,z2]', [cos(ni1*z1),b1*exp(-ni1b*z2)]',[2 2]);

plot2d([z1,z2]', [cos(ni2*z1),b2*exp(-ni2b*z2)]',[3 3]);

xtitle('The three trapped modes b=1');

// Multiple curves in a single plot using transposed row vectors
//  plot2d([x',x',x'],[y',z',w']); xtitle('Combined plot 1')
//  plot2d([x, x, x]',[y, z, w]'); xtitle('Combined plot 1') // equivalent
// Multiple curves in a single plot using column vectors
// x = (-2*%pi:%pi/100:2*%pi);
// y = sin(2.*x); z = cos(x); w = exp(-abs(0.1*x)).*sin(x);
// plot2d([x,x,x],[y,z,w]); xtitle('Combined plot 2')
//  I used this method to plot both parts of u1 across x=a as different functions
```

Effet de la non-stœchiométrie en Li sur la performance des dispositifs à ondes élastiques à base de monocristaux de $LiTaO_3$ et $LiNbO_3$

Résumé:

Les technologies de filtres, résonateurs, oscillateurs et capteurs sont des éléments essentiels dans les industries des télécommunications, automobile, militaire, médical, etc. Les monocristaux de $LiTaO_3$ (LT) et $LiNbO_3$ (LN) sont les matériaux les plus utilisés pour la fabrication de filtres de radiofréquence à ondes élastiques des téléphones portables, car ils possèdent un facteur de couplage électromécanique (K^2) élevé. Cependant, ils présentent une problématique liée à la variation de la fréquence de fonctionnement avec la température (CTF), dont la valeur est environ de -40 à -95 ppm/°C. D'autre part, il a été démontré dans la littérature que les propriétés de LT et LN changent avec la non-stœchiométrie du Li.

L'objectif de cette thèse a été l'étude de l'effet de la concentration en Li_2O sur la performance des dispositifs acoustiques à ondes élastiques de surface, utilisant comme substrat piézoélectrique des monocristaux de LT coupe YXl/42 (42 RY-LT) et LN coupe YXl/128 (128 RY-LT). Cette étude vise à l'amélioration du CTF sans la dégradation d'autres propriétés (K^2 et pertes d'insertion) dans le cas du 42 RY-LT et la stabilité de dispositifs utilisés à haute densité de puissance dans le cas du 128 RY-LN. Tout d'abord, nous avons préparé des monocristaux de LT et LN avec différente concentration en Li_2O :48.5-50 mol%, en utilisant la méthode d'équilibration par transport en phase vapeur (VTE). Ensuite, nous avons fabriqué et caractérisé des dispositifs à ondes élastiques de volume et de surface à base de LT et LN, traités par VTE, afin d'étudier l'effet de la non-stœchiométrie de Li et l'effet des domaines ferroélectriques sur leur performance.

Mots clés : Coefficient de Température de la Fréquence (CTF), stœchiométrie, monocristaux de LT et LN, facteur de couplage electromécanique (K^2), équilibration par transport en phase vapeur (VTE).

Impact of Li non-stoichiometry on the performance of acoustic devices on $LiTaO_3$ and $LiNbO_3$ single crystals

Abstract:

The filter technologies, resonators, oscillators and sensors are essential elements for telecommunications, automotive, military, medical industries. The most of radio frequency surface acoustic wave (RF-SAW) filters, present in mobile phones, are based in $LiNbO_3$ (LN) and $LiTaO_3$ (LT) single crystals because they have high electromechanical coupling factor (K^2). However, these materials have a problem related to the variation of the operating frequency with temperature (TCF), whose value is about -40 to -95 ppm / ° C. On the other hand, it has been previously shown in the literature that the physical and structural properties of LT and LN change with Li non-stoichiometry, including elastic properties.

The aim of this work was the investigation of the impact of Li_2O concentration on the performance of SAW devices based on YXl/42 (42 RY-LT) and YXl/128 (128 RY-LN) single crystals. In the case of 42 RY-LT, we focused in the reduction of TCF without the degradation of other properties (K^2 and insertion losses) and in the case of 128 RY-LN crystals we focused in the stability of devices at high power densities. First, single crystals of LT and LN with different Li_2O concentration: 48.5-50 ml% were prepared, by using the Vapor Transport Equilibration (VTE) method. Afterwards, SAW and bulk acoustic wave (BAW) devices based on LT and LN VTE treated crystals, were fabricated and characterized, in order to study the effect of Li non-stoichiometry and the effect of ferroelectric domains on the performance of devices.

Key words: Temperature coefficient frequency (TCF), stoichiometry, LT and LN single crystals, electromechanical coupling factor (K^2), vapor transport equilibration (VTE).

SPIM

■ École doctorale SPIM 16 route de Gray F - 25030 Besançon cedex

■ tél. +33 (0)3 81 66 66 02 ■ ed-spim@univ-fcomte.fr ■ www.ed-spim.univ-fcomte.fr

UFC UNIVERSITÉ DE FRANCHE-COMTÉ